In-situ Far Ultraviolet Optical Characterization of Atomic Layer Deposited Oxides and Fluorides

by

Zhiyu Huang

A Dissertation Presented in Partial Fulfillment
of the Requirements for the Degree
Doctor of Philosophy

Approved April 2021 by the
Graduate Supervisory Committee:

Robert Nemanich, Chair
Fernando Ponce
Jose Menendez
Zachary Holman

ARIZONA STATE UNIVERSITY

May 2021

ABSTRACT

In this dissertation, far UV spectroscopy is applied to investigate the optical properties of dielectric thin films grown by atomic layer deposition. The far UV (120 – 200 nm) reflectance for several dielectric oxides and fluorides, including AlF_3, Al_2O_3, Ga_2O_3, HfO_2, and SiO_2, was measured at variable angles and thicknesses. Multiple optical calculation methods were developed for accurate determination of the optical constants from the reflectance. The deduced optical constants were used for optical designs, such as high-reflectivity coatings, and Fabry-Perot bandpass interference filters. Three filters were designed for use at 157 nm, 212 nm, and 248 nm wavelengths, based on multilayer structures consisting of SiO_2, Al_2O_3, HfO_2, and AlF_3. A thorough error analysis was made to quantify the non-idealities of the optical performance for the designed filters. Far UV spectroscopy was also applied to analyze material mixtures, such as AlF_3/Al and h-BN/c-BN mixtures. Using far UV spectroscopy, different phases in the composite can be distinguished, and the volume concentration of each constituent can be determined. A middle UV reflective coating based on A_2O_3 and AlF_3 was fabricated and characterized. The reflective coating has a smooth surface (R_q < 1 nm), and a peak reflectance of 25 – 30 % at a wavelength of 196 nm. The peak reflectance deviated from the design, and an analysis of the AlF_3 layer prepared by plasma enhanced atomic layer deposition (PEALD) indicated the presence of Al-rich clusters, which were associated with the UV absorption. Complementary techniques, such as spectroscopic ellipsometry, and X-ray photoelectron spectroscopy, were used to verify the results from far UV spectroscopy.

In conclusion, this Dissertation demonstrated the use of in-situ far UV spectroscopy to investigate the optical properties of thin films at short wavelengths. This work extends

the application of far UV spectroscopy to ultrawide band gap semiconductors and insulators. This work supports a path forward for far UV optical filters and devices. Various errors have been discussed with solutions proposed for future research of methods and materials for UV optics.

DEDICATION

To my grandmother and the whole family

ACKNOWLEDGMENTS

During my Ph.D. career, there were a lot of challenges and obstacles. I want to show my sincere acknowledgment to my advisor, Dr. Robert Nemanich, who helped me overcome the challenges I faced and guided me to achieve this success. Dr. Nemanich is always willing to listen to the ideas and thoughts from his students and trying to help every student succeed. I appreciate the opportunities Dr. Nemanich provided for me. I learnt a lot from him, not only for the research, but also his personality. Dr. Nemanich is diligent and puts efforts to his work. This also inspires me to get through the hardships in life and keep moving forward!

I would like to thank my Ph.D. committee members: Dr. Fernando Ponce, Dr. Jose Menendez, and Dr. Zachary Holman. I appreciate their time and suggestions for helping me identify the innovation in my research and helping me improve my dissertation.

I would like to thank all the group members in our research group. I worked with Daniel Messina for my NASA project. He is always helpful when I have questions. He helped me fix the far UV spectrometer, which is the foundation for this dissertation. I learnt a lot from him on the principles of atomic layer deposition and etching, which greatly helped me when I search for positions in the semiconductor industry. I also want to thank Jesse Brown, Kevin Hatch and Yichen Yao, for helping me familiarize the instruments in the lab, and providing me samples for the optical measurements. I want to extend my thanks to Franz Koeck, Manpuneet Kaur, Brianna Eller, Anna Zaniewski, Robert Mecham, Kari Slotten, Ali Yekta, and Avani Patel, for their support and help during my Ph.D. career.

I want to show my thanks to all my friends in the past 5 years at ASU. First, I want to thank my roommate, Jing Hu. He is the best roommate I have ever met. I also want to thank my classmate, Kentaro Yumigeta. I learnt a lot from the discussions with him for the coursework and my research. I also want to thank my other friends, include Peiyuan (Boki) Wang, Shule Yu, Jianlan Ye, Mingze Wu, and Hezi Ji, for the weekly party to cook food and play Mahjong. It is one of my best memories in ASU.

Besides, I want to thank all the faculties and staffs who helped me in my Ph.D. career. Specifically, thanks to Avaceli Vizcarra for guiding me to complete my Ph.D. exams. Thanks to Diana Convey in Eyring Materials Center for training me to use the optical instruments and offering me license to use the optical software. Thanks to Jamie Quintero for providing ALD Al_2O_3, HfO_2, and PECVD SiO_2 for the optical measurements.

Last, I would like to thank my families, especially to my grandmother, Xiuzhen Liu, my farther, Chunsheng Huang, my stepmom Chunxia Wang. Besides, I also want to thank my mother Xidong Wang, for her financial support during my undergraduate study. In the end, I would like to thank to my girlfriend, Shengnan Zhang, for her understanding and support during my Ph.D. study. I will never achieve this without all the support from you!

TABLE OF CONTENTS

Page

CHAPTER Page

CHAPTER Page

LIST OF TABLES

LIST OF FIGURES

Figure Page

Figure Page

Figure Page

Figure Page

Figure Page

Figure Page

Figure Page

Figure Page

Figure Page

Figure Page

Figure Page

CHAPTER 1

INTRODUCTION

1.1 Significance of the Study

Optical constants, including the refractive index and extinction coefficient, are the fundamental optical properties of a material. For thin film materials, the optical constants can determined using spectroscopic ellipsometry due to its high sensitivity and precision.[1-3] However, at shorter wavelengths, especially in the far UV region (120 – 200 nm), spectroscopic ellipsometry is not fully developed because of the shortage of wideband polarizers and phase retarders.[4] In this study, we employed far UV optical spectroscopy to investigate the optical properties of thin film materials. The far UV spectrometer is directly coupled with thin film deposition chambers, which enables the *in-situ* optical measurements. This advantageous set-up limits atmospheric contamination on the surface of the as-grown films, which significantly improves the accuracy of the optical measurements. The inter-band transitions and the excitonic effects of the semiconductors and insulators were also studied using *in-situ* far UV spectroscopy. To the best of our knowledge, we are among one of the few groups capable of *in-situ* far UV optical measurements of as-grown thin film materials.

Optical coating design highly relies on the optical constants of the materials measured at each wavelength. *In-situ* optical measurements allow us to accurately determine the spectroscopic optical constants of the thin film materials. In this study, we have developed several methods for determination of optical constants based on spectroscopic reflectance measurements. An optical coating was then designed using the

determined optical constants. The filter was fabricated using atomic layer deposition (ALD). As far as we know, we are pioneering the use of ALD is used to fabricate a middle UV reflective coating based on the dielectrics Al_2O_3 and AlF_3. The advantages using ALD for the optical coating growth include precise thickness control, high conformality and uniformity, and sub-nanometer root-mean-square surface roughness (R_q). In this study, we demonstrated the benefits and advantages of using metal fluorides for the next-generation far UV optics.

Far UV spectroscopy is further extended to study the optical properties of material mixtures. For mixtures containing constituents with distinct optical spectral properties, the spectroscopic measurements can be used to quantitatively determine the concentration of each constituent by considering the effective optical constants of the mixtures. In this study, we analyzed mixtures of hexagonal and cubic BN based on their distinct inter-band transitions in the far UV range. This work provides a new method to distinguish the hexagonal phase that forms during cubic BN growth. The results should foster the deposition of pure phase cubic BN for application in next-generation electronics.

In this study, several dielectric thin films grown by ALD are studied using custom-developed far UV spectroscopy. Reflectance has been measured at variable incident angles and for various thicknesses. Optical calculation methods based on iso-reflectance curves, and optical dispersion models have employed to determine the optical properties of each material, including optical constants, cut-off wavelength, and inter-band transitions. UV bandpass filters have been designed using the ALD grown dielectrics, and the non-idealities in the films have been analyzed. A middle UV highly reflective coating based on Al_2O_3 and AlF_3 has been designed, fabricated, and characterized.

1.2 Dissertation Approach

In Chapter 2, the relationship between the band structures and optical properties are discussed. The commonly used methods for measuring far UV optical constants measurements are reviewed, with a focus on the reflectance measurements which were used in this study. The basic components of far UV spectroscopy are introduced. The common types of optical coatings and filters used in far UV are reviewed.

In Chapter 3, the experimental and theoretical methods used in this study are described. The experimental methods include atomic layer deposition, spectroscopic ellipsometry, atomic force microscopy, and X-ray photoelectron spectroscopy. The theoretical methods include transfer-matrix method, optical calculation methods, and effective medium approximation.

In Chapter 4, the custom-built and developed *in-situ* variable angle far UV spectrometer system is described.

In Chapter 5, far UV optical constants of dielectric thin films grown by ALD are determined using far UV spectroscopy. Thin film dielectrics studied in this study include AlF_3, Al_2O_3, HfO_2, and Ga_2O_3. Optical calculation methods based on iso-reflectance curves and optical dispersion models are used for each material. The optical constants, and cut-off wavelength of each material are measured and discussed. For each material, the relation between band structure and the measured optical properties are discussed. Spectroscopic ellipsometry is used as a complement for verification of the results from spectroscopy.

In Chapter 6, the application of far UV spectroscopy in the analysis of material mixtures is introduced. AlF_3/Al mixtures grown by plasma enhanced ALD, and h-BN/c-BN mixtures grown by ECR-PECVD are used as examples. Far UV spectroscopy is used

for the phase distinguishment and volume concentration calculation. For BN, the relation between band structure and the measured optical properties are discussed.

In Chapter 7, optical coatings and filters are designed using the far UV optical constants determined from far UV spectroscopy. High-reflectivity coatings and bandpass interference filters are designed based on dielectric thin films SiO_2, Al_2O_3, HfO_2, and AlF_3. Three Fabry-Perot filters are designed for use at wavelengths of 157 nm, 212 nm, and 248 nm. Fabry-Perot filters with single- and multi-cavity structures are designed, and the difference between them is discussed. The non-idealities and the effects on the optical performance are analyzed. The non-idealities include incident angle variation, thickness variation, interface roughness, refractive index inhomogeneity, and atmospheric contaminations.

In Chapter 8, a multilayer high-reflectivity coating, based on AlF_3 and Al_2O_3, has been designed and fabricated. Spectroscopic ellipsometry measurements of the reflective coating suggested the presence of an absorbing compound inside the plasma enhance ALD AlF_3 layer. The volume concentration of the Al-rich clusters is determined to be 2.4 – 4.8% from the spectroscopic ellipsometry and X-ray photoelectron spectroscopy measurements. The Al impurities in the coating result in a discrepancy on the reflectance curve in the middle UV wavelength.

In Chapter 9, the main results in this study are summarized. Future work is proposed to extend the research into far UV optical properties of cubic and hexagonal BN, optical coating design with improved efficiency, and fabrication of the designed optical filters.

In Appendix, the maintenance, and operational procedures of the *in-situ* far UV spectrometer are described.

References

[1] H. G. Tompkins and J. N. Hilfiker, *Spectroscopic Ellipsometry: Practical Application to Thin Film Characterization*. (Momentum Press, LLC, New York, 2016).

[2] D. E. Aspnes, "Spectroscopic ellipsometry — Past, present, and future," Thin Solid Films **571**, 334 (2014).

[3] H. Fujiwara, "*Principles of Ellipsometry*," in Spectroscopic Ellipsometry for Photovoltaics, Vol. 1, Ch. 1.1.1, edited by H. Fujiwara and R. W. Collins (Springer International Publishing AG, Cham, Switzerland, 2018).

[4] J. I. Larruquert, "*Optical properties of thin film materials at short wavelengths*," in Optical Thin Films and Coatings, Ch. 7, edited by A. Piegari and F. Flory (Woodhead Publishing, 2018).

CHAPTER 2

FAR ULTRAVIOLET OPTICS AND SPECTROSCOPY

In this chapter, we introduce the basics of optics and spectroscopy at shorter wavelength. The methods used to determine the optical constants are reviewed, with a focus on the reflectance intensity measurements. The basics of the far UV spectroscopy are introduced, with a focus on the commonly used optical components. Finally, the common types of the optical coatings and filters are reviewed, with a focus for far UV applications.

2.1 Far UV Optical Constants

2.1.1 Optical Constants Basics

The optical properties of materials are described by refractive index n, and the extinction coefficient k, which are called "optical constants".[1] If light passes from vacuum to a medium with a speed of v, the refractive index can be described by Eq. (2.1). Here, c is the speed of light in vacuum.

$$n = \frac{c}{v} \qquad \text{(Eq. 2.1)}$$

When light passes through the material, the intensity is attenuated. The extinction coefficient k is used to describe the absorption of light in the medium, which is directly proportional to the absorption coefficient α.

$$\alpha = \frac{4\pi k}{\lambda} \qquad \text{(Eq. 2.2)}$$

The absorption of light follows the Beer-Lambert law, Eq. (2.3). The characteristic penetration depth z of light in a medium is given by, $z = \frac{1}{\alpha} = \frac{\lambda}{4\pi k}$, with the light intensity decreased by e^{-1} (~ 37 %) and described by Eq. (2.3):

$$\frac{I}{I_0} = e^{-\alpha z} \qquad \text{(Eq. 2.3)}$$

The optical constants, n and k, are also commonly referred as complex refractive index in the literature and are written as Eq. (2.4):

$$\tilde{n} = n + ik \qquad \text{(Eq. 2.4)}$$

The wavelength dependence of the refractive index is the dispersion. For dielectric materials, the dispersive properties of the refractive index can be derived from the classical harmonic oscillator model by considering the electric dipole from bound electrons.[2] By considering s oscillators in one atom, with each oscillator having a strength g_s and damping constant γ_s, the frequency (wavelength) dependent refractive index can be described by, $n(\omega) \equiv \sqrt{1 - \frac{e^2 N_a}{\varepsilon_0 m} \sum_s \frac{g_s}{\left(\omega^2 - \omega_s^2\right)^2 + i\gamma_s \omega}}$.[2] Here, N_a is the number of oscillators per unit volume

The above equation can be plotted in Fig. 2.1, with resonance frequency is in the infrared (IR), the ultraviolet (UV), and the X-ray regions. The resonances in IR, UV, and X-ray regions are due to molecular vibrations, electron transitions, and photoionization of atoms.[3] In the regions without resonance absorption, the relation between refractive index and frequency is called “normal dispersion”, while in the resonance region, it is called “anomalous dispersion”, as shown in the shaded area in Fig. 2.1.

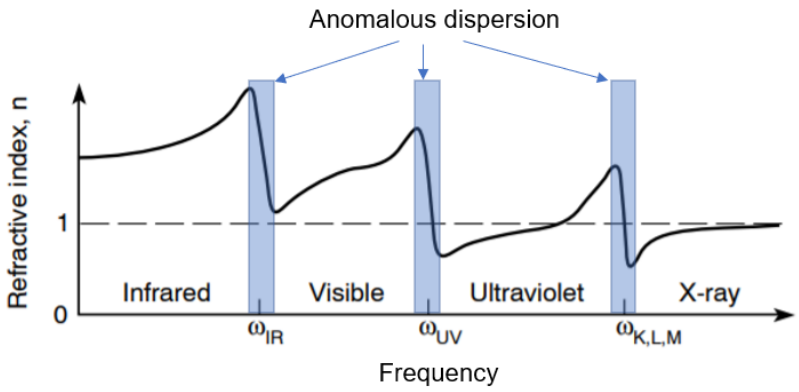

Figure 2.1. Refractive index vs frequency. Anomalous dispersion happens in resonance regions.[3] Copyright © 1999, Cambridge University Press.

From the perspective of the wave property of light, by solving the electromagnetic wave equation (Eq. 2.5), the electric field strength E_x has a solution which contains the complex refractive index $\tilde{n}$, Eq. (2.6).[2]

$$c^2 \frac{\partial^2 E_x}{\partial z^2} = \varepsilon \frac{\partial^2 E_x}{\partial t^2} + \frac{\sigma}{\varepsilon_0} \frac{\partial E_x}{\partial t} \qquad \text{(Eq. 2.5)}$$

If we write Eq. (2.6) in two parts, containing n and k separately, it is clear that k describes the damping of the light wave, while n only affects the light propagation without damping. This behavior is shown in Fig. 2.2.

$$E_x = E_0 e^{i\omega\left(t + \frac{z(n+ik)}{c}\right)} \qquad \text{(Eq. 2.6)}$$

$$E_x = E_0 e^{\left(-\frac{\omega k}{c} z\right)} e^{i\omega\left(t + \frac{zn}{c}\right)} \qquad \text{(Eq. 2.7)}$$

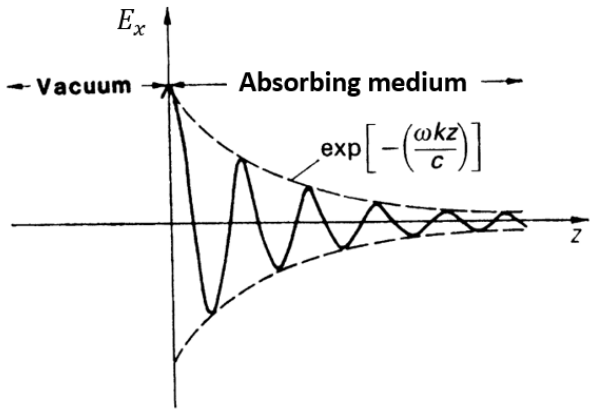

Figure 2.2. Light propagation in absorbing medium.[2] Copyright © 2011, Springer Science Business Media, LLC.

By plugging Eq. (2.7) into Eq. (2.5), one can obtain the relations between the complex dielectric function and the complex refractive index, shown in Eq. 2.8 and 2.9.[2] This relation assumes the materials are non-magnetic, i.e., $\mu_r = 1$.

$$n = \frac{1}{\sqrt{2}}\sqrt{\varepsilon_1 + \sqrt{\varepsilon_1^2 + \varepsilon_2^2}} \quad \text{(Eq. 2.8)}$$

$$k = \frac{1}{\sqrt{2}}\sqrt{-\varepsilon_1 + \sqrt{\varepsilon_1^2 + \varepsilon_2^2}} \quad \text{(Eq. 2.9)}$$

2.1.2 Band Structures and Optical Properties

For semiconductors and insulators, optical absorption occurs due to band transition and exciton formation.[2, 4-6] Band transitions include inter-band and intra-band transitions, depending on if the transition occurs in the same band. Exciton formation occurs when the electron-hole pair forms due to the Coulomb interaction. Electronic transitions and exciton formation can cause absorption of light, which can be modeled with *ab-initio* methods and measured using optical techniques. Below, we introduce electronic transitions in the materials of interest, and relate the optical properties to the band structures.

2.1.2.1 Inter-band and Intra-band Transitions

In semiconductors and insulators, an inter-band transition occurs between an occupied band and an unoccupied band.[5] This transition occurs when there is an electron in the initial state in the lower band and the upper band is empty. For a direct transition, an electron is excited from the filled band to the empty band by absorbing a photon, Fig. 2.3a.[2] As for the indirect transition, a phonon is involved because of the conservation of momentum, Fig. 2.3b.[2]

Different from inter-band transitions, an intra-band transition occurs within the same band with the participation of a phonon, Fig. 2.3c.[2] Intra-band transitions usually cannot occur in semiconductors or insulators, as the bands are completely filled or empty. However, for semiconductors with a high doping level, or at high temperature, intra-band transitions can occur if the bands are partially filled. As for the insulators, defects could also cause intra-band transitions.

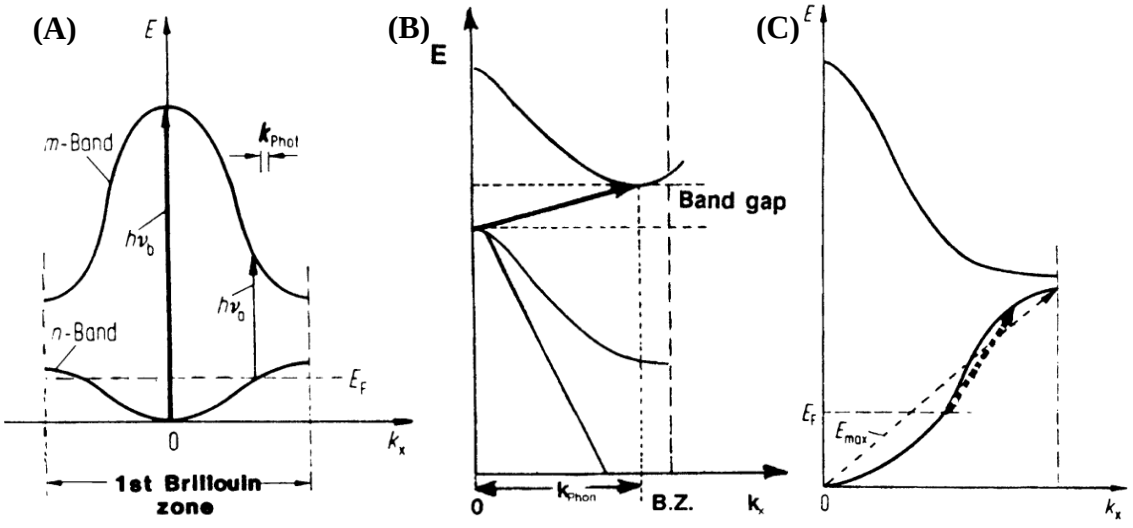

Figure 2.3. Inter-band and intra-band transition. (A) Direct inter-band transition; (B) Indirect inter-band transition; (C) Intra-band transition.[2] Copyright © 2011, Springer Science Business Media, LLC.

2.1.2.2 Excitons

Exciton is a neutral electron-hole pair bound by the Coulomb interaction.[6] An exciton can be formed when an electron is excited to the unoccupied band in an inter-band transition. Two types of exciton are considered here, one is based on strong electron-hole attraction, forming a tightly bound exciton, Fig.2.4b, called a Frenkel exciton.[6] Another type is called Wannier-Mott exciton, which is a weakly bound electron-hole pair, Fig. 2.4a.[6] Frenkel excitons are usually observed in insulators and molecular crystals, while Wannier-Mott excitons usually occur in semiconductors. For Wannier-Mott excitons, they are typically observed in direct bandgap semiconductors during inter-band excitation, especially in the spectral region near the fundamental band gap, Fig. 2.5a.[6] Frenkel excitons usually occur in insulators with small dielectric constants and large effective masses. These excitons have a higher binding energy than the Wannier-Mott excitons, and are usually stable at room temperature, Fig. 2.5b.[6] For the metal fluorides with large direct band gap, such as AlF_3, Frenkel excitons are readily observable in the optical spectra. This can be seen in Chapter 4 for the results of AlF_3.

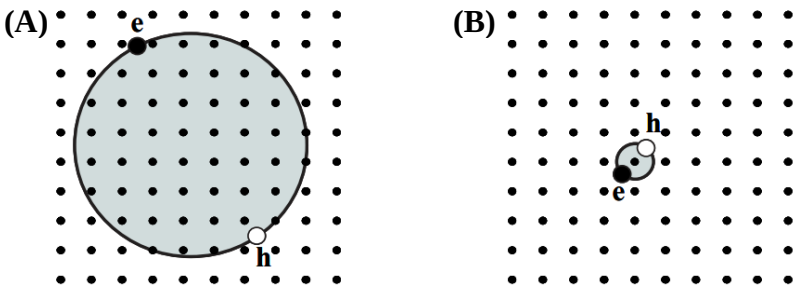

Figure 2.4. Exciton types. (A) Wannier-Mott exciton, weakly bound; (B) Frenkel exciton, tightly bound.[6] Copyright © 2010, Oxford University Press.

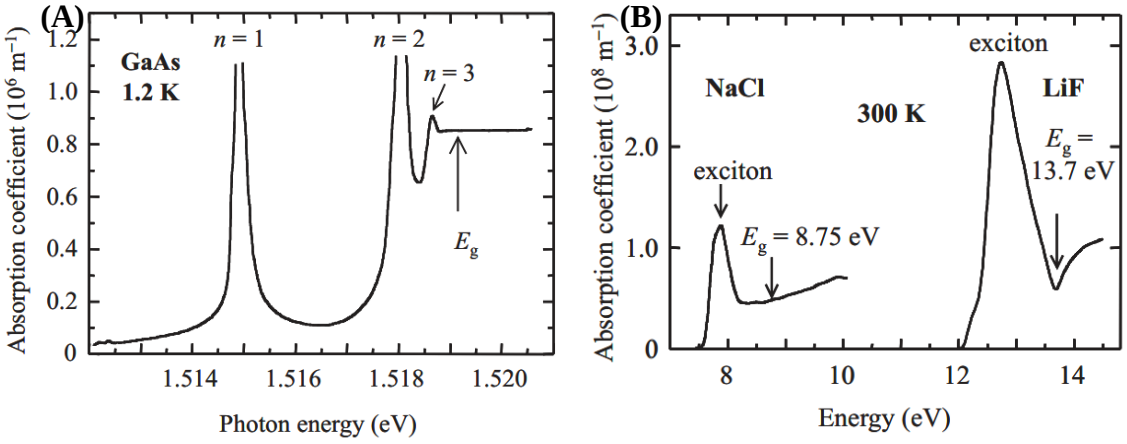

Figure 2.5. Wannier-Mott and Frenkel excitons. (A) Wannier-Mott excitons occur in GaAs at low temperature; (B) Frenkel excitons occur in alkali halide crystals, stable at room temperature.[6] Copyright © 2010, Oxford University Press.

2.1.2.3 Optical Properties from Band Structures

The optical properties of the materials can be calculated from the band structure, using inter-band momentum matrix elements, Eq. (2.10).[4, 7] Here, e, and m_e are the electron charge, and mass; ω is the electromagnetic radiation frequency; V is the unit cell volume; $\mathbf{p}$ is the momentum operator; $\mathbf{k}\,n\rangle$ is the crystal wave function, with eigenvalue $E_{\mathbf{k}\,n}$; and $f_{\mathbf{k}\,n}$ is the Fermi distribution function ensuring that only transitions from occupied to unoccupied states are counted. Specifically, for insulators, intra-band transitions ($m = n$) are not allowed, as $f_{\mathbf{k}\,n}(1 - f_{\mathbf{k}\,m}) = 0$.

$$\varepsilon_2(\omega) = \frac{4\pi^2 e^2}{V(m_e)^2\,\omega^2} \int d^3\mathbf{k} \sum_{nm} |\langle \mathbf{k}\,n|\mathbf{p}|\mathbf{k}\,m\rangle|^2 f_{\mathbf{k}\,n}(1 - f_{\mathbf{k}\,m}) \times \delta(E_{\mathbf{k}\,n} - E_{\mathbf{k}\,m} - \hbar\omega) \quad \text{(Eq. 2.10)}$$

The real part of the dielectric constant can be obtained using the Kramers-Kronig relation.[4]

$$\varepsilon_1(\omega) = 1 + \frac{4\pi e^2}{V(m_e)^2} \int d^3\mathbf{k} \sum_{nm} \left(\frac{2}{m\hbar\omega_{nm}}\right) \frac{|\langle \mathbf{k}\, n|\mathbf{p}|\mathbf{k}\, m\rangle|^2}{\omega_{nm}^2 - \omega^2} \qquad \text{(Eq. 2.11)}$$

If we define $g_{nm} = \left(\frac{2}{m\hbar\omega_{nm}}\right)|\langle \mathbf{k}\, n|\mathbf{p}|\mathbf{k}\, m\rangle|^2$, Eq. (2.11) can be re-written as,

$$\varepsilon_1(\omega) = 1 + \frac{4\pi e^2}{V(m_e)^2} \int d^3\mathbf{k} \sum_{nm} \frac{g_{nm}}{\omega_{nm}^2 - \omega^2} \qquad \text{(Eq. 2.12)}$$

Equation 2.12 represents the classical Lorentz oscillator model for optical dispersion, and g_{nm} corresponds to the oscillator strength.[2, 4] Eq. (2.11) and (2.12) are the physical foundation for the empirical Tauc-Lorentz model used in this study, which is used to model the absorption due to inter-band transitions.[8] However, this formulism ignores the absorption due to excitons. The Bethe-Salpeter method was used to account for the exciton effects, which have been reported for the calculation of insulators, such as AlF_3.[9]

2.1.3 Far UV Optical Constants for Dielectrics

Commonly used dielectric materials include oxides (such as SiO_2), nitrides (such as SiN*x*), and fluorides (such as MgF_2). Most dielectrics are transparent at longer wavelength, but start absorbing when they approach their cut-off wavelength, which is usually at UV wavelengths. For the dielectrics in the transparent region, i.e., above the cut-off wavelength, the refractive index of the materials follows normal dispersion, i.e., refractive index increases at shorter wavelength, and can be described by the Cauchy equation, Eq. (2.13).[10]

$$n = \mathrm{A} + \frac{\mathrm{B}}{\lambda^2} + \frac{\mathrm{C}}{\lambda^4} \ (\lambda \text{ in } \mu\mathrm{m}) \qquad \text{(Eq. 2.13)}$$

The electromagnetic radiation spectrum is shown in Fig. 2.6, with the UV wavelength region highlighted. Far UV is the UV wavelength between 122 – 200 nm. In

the far UV region, many dielectrics are absorbing, except some ultrawide bandgap oxides and fluorides, such as SiO_2, Al_2O_3, MgF_2, AlF_3, and LiF.[10]

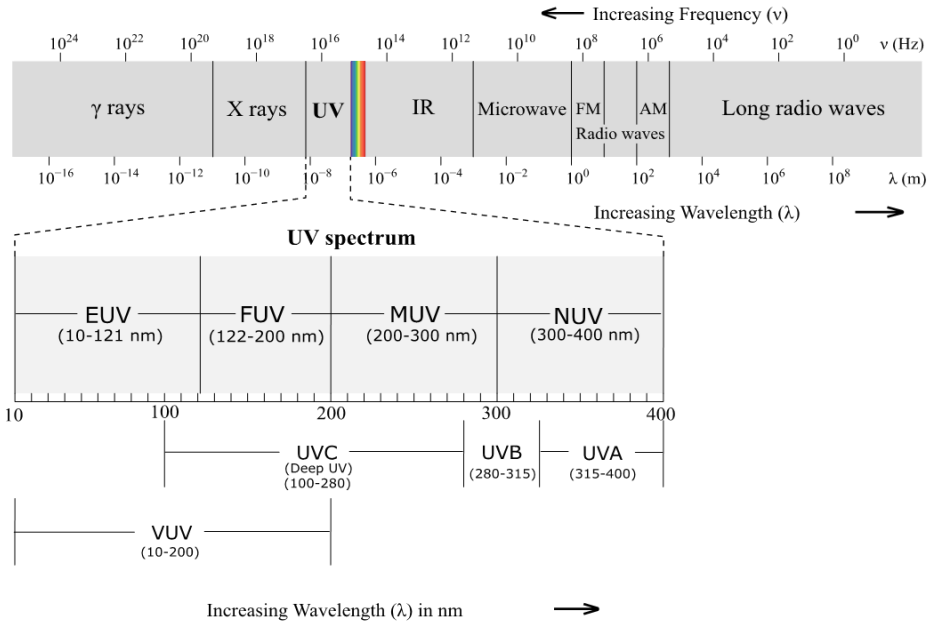

Figure 2.6. Electromagnetic radiation spectrum with UV regions highlighted. EUV-Extreme UV; FUV-Far UV; MUV-Middle UV; NUV-Near UV; VUV-Vacuum UV. Copyright © CC BY-SA 3.0, reproduced from the figure made by Gringer. P. Ronan (cited in Electromagnetic radiation, Wikipedia).

Here, we use Ta_2O_5 and MgF_2 as examples for an introduction of dielectrics in the Far UV region. The oxide Ta_2O_5 has a bandgap of ~ 3.8 eV, which corresponds to a cut-off wavelength of ~ 330 nm.[11] As for MgF_2, its bandgap is ~ 10.8 eV, and maintains transparency down to ~ 115 nm.[12] The optical constants for both materials are plotted in Fig. 2.7, with different UV regions labeled. For both materials, the Cauchy model can be used to fit the refractive index in the transparent region, and the fitted parameters are shown in Table 2.1. Root-mean-square-error (RMSE) is used to quantify the fitting, where for an ideal fit the RMSE tends to 0.[13]

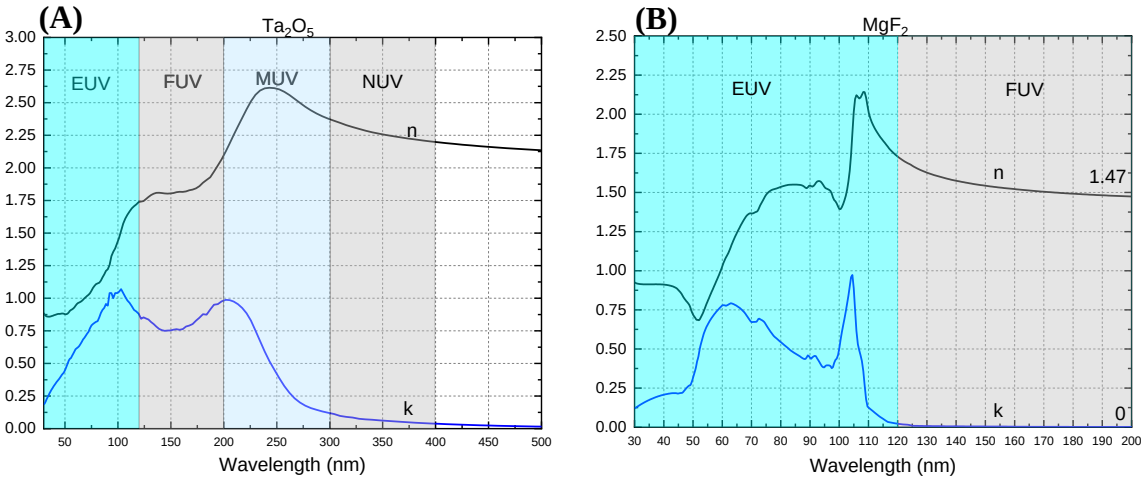

Figure 2.7. Optical constants of Ta_2O_5 and MgF_2. (A) Ta_2O_5, (B) MgF_2.

Table 2.1. Cauchy parameters fitted for refractive indices in Fig. 2.7.

	A	B	C	Fitted wavelength	RMSE
MgF_2	1.416	0.00185	1.8032×10^{-5}	200-400nm	0.00161
Ta_2O_5	2.038	0.02078	7.8469×10^{-4}	400-800nm	0.0951

Besides Ta_2O_5 and MgF_2, many other dielectric materials are transparent in the UV wavelength range and follow normal dispersion as described by the Cauchy model. Refractive index of a set of representative dielectrics has been plotted in Fig. 2.8, with cut-off wavelength above 200 nm.

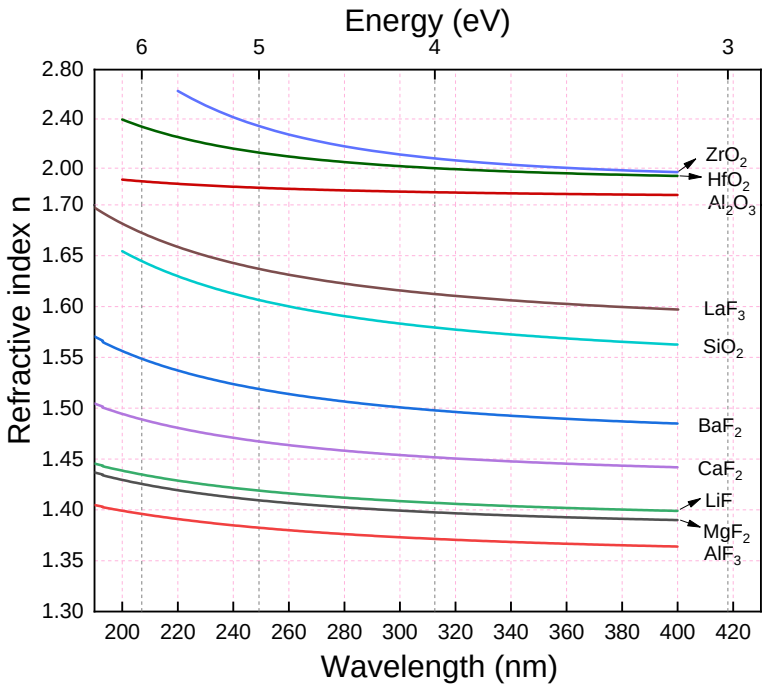

Figure 2.8. Refractive index vs wavelength for UV coating materials, from various references.[14-20]

For dielectric materials, the cut-off wavelength λ_c marks the boundary for absorption in the materials. The cut-off wavelengths for commonly used dielectric materials are shown in Fig. 2.9. It shows that many fluorides are among the materials with the shortest cut-off wavelength, which corresponds to their ultra-wide bandgap. The relation between cut-off wavelength, and the bandgap can be estimated from Eq. (2.14) below.

$$\lambda_c = \frac{hc}{E_g} = \frac{1239.8\ (\text{eV·nm})}{E_g} \qquad \text{(Eq. 2.14)}$$

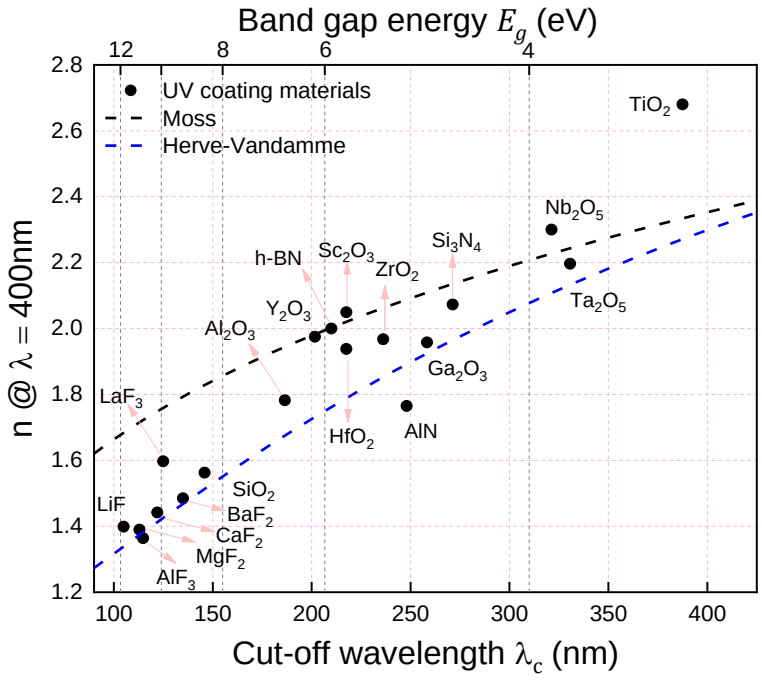

Figure 2.9. Refractive index (at $\lambda = 400$ nm) vs λ_c and E_g for UV coating materials, from various references.[10, 14-32]

Even though the Cauchy model describes well the optical constants for metal fluorides in the Far UV (FUV) region, it fails for many other oxides due to the absorptions. For example, Ta_2O_5 shows anomalous dispersion for the refractive index in the FUV, and the extinction coefficients are not 0, as shown in Fig. 2.7a. For amorphous dielectrics and semiconductors below the cut-off wavelength, the Lorentz model with modifications has been used to describe the optical properties.[8] The following describes the classical Lorentz oscillator model and their modifications.[2]

Lorentz proposed the classical theory of dielectric materials which assumes the electrons are bonded to their respective nuclei. The Lorentz oscillator theory gives the dispersive characteristics of dielectric functions $\tilde{\varepsilon} = \varepsilon_1 + i\varepsilon_2$ with frequency ν,

$$\varepsilon_1 = 1 + \frac{e^2 m N_a (\nu_0^2 - \nu^2)}{\varepsilon_0 [4\pi^2 m^2 (\nu_0^2 - \nu^2)^2 + \gamma^2 \nu^2]} \quad \text{(Eq. 2.15)}$$

$$\varepsilon_2 = \frac{e^2 N_a \gamma \nu}{2\pi\varepsilon_0 [4\pi^2 m^2 (\nu_0^2 - \nu^2)^2 + \gamma^2 \nu^2]} \quad \text{(Eq. 2.16)}$$

Here, γ is the damping parameter, N_a is the number of all dipoles. This formula assumes there is one oscillator per atom. The plots of dielectric functions vs frequency are shown below in Fig. 2.10. The relations between $\tilde{\varepsilon}$ and $\tilde{n}$ are given in Eq. (2.17) and (2.18), assuming the materials are non-magnetic, i.e., $\mu_r = 1$.

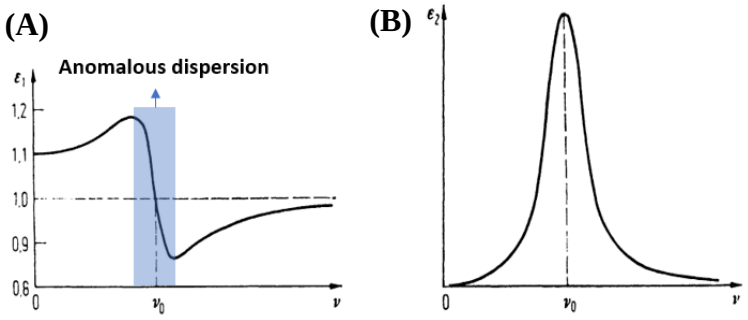

Figure 2.10. Dielectric functions vs frequency. Anomalous dispersion occurs around resonance wavelengths. (A) Real part, (B) Imaginary part.[2] Copyright © 2011, Springer Science Business Media, LLC.

$$\varepsilon_1 = n^2 - k^2 \quad \text{(Eq. 2.17)}$$

$$\varepsilon_2 = 2nk \quad \text{(Eq. 2.18)}$$

In the special case of small damping case, i.e., low absorption (with small damping constant γ), $\gamma^2\nu^2 \ll 4\pi^2 m^2 (\nu_0^2 - \nu^2)^2$, the Lorentz model can be simplified as Eq. (2.19) and (2.20) and plotted in Fig. 2.11.

$$\varepsilon_1 = 1 + \frac{e^2 N_a}{4\pi^2 \varepsilon_0 m^2 \left(\nu_0^2 - \nu^2\right)^2} \quad \text{(Eq. 2.19)}$$

$$\varepsilon_2 = \frac{e^2 N_a}{2\pi \varepsilon_0 \gamma' \nu_0} \quad \text{(Eq. 2.20)}$$

When the frequency is below the resonance frequency, i.e., the wavelength is above the cut-off wavelength, the real part of the dielectric function $\varepsilon_1 = n^2$ follows the normal dispersion, which can be described by the Cauchy model. However, the symmetric shape of the imaginary dielectric function ε_2 can not correctly describe the absorption of dielectric materials in the inter-band region. To better describe ε_2, a few modifications of the Lorentz oscillator model have been developed, and Lorentz models with the Tauc and Cody modifications are commonly used.[8, 33]

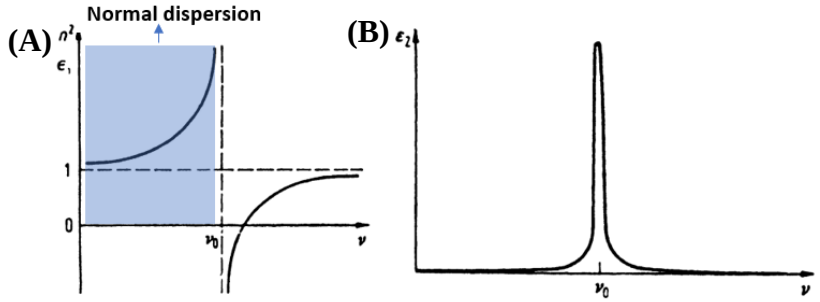

Figure 2.11. Dielectric functions vs frequency. With low absorption.[2] Copyright © 2011, Springer Science Business Media, LLC.

G. E. Jellison and F. A. Modine proposed a parameterization of the dielectric function for amorphous semiconductors and insulators in the inter-band region, which is called the Tauc-Lorentz (T-L) model.[8, 34] The T-L model combines the Lorentz model for ε_2, with the Tauc joint density of states, Eq. (2.21), which were proposed by Tauc to describe the imaginary part of the dielectric function,

$$\varepsilon_{2\mathrm{T}}(E) = A_T \left(E - E_g\right)^2 / E^2 \quad \text{(Eq. 2.21)}$$

The T-L form of the imaginary dielectric function is shown in Eq. (2.22) below. The boundary that marks the absorption is called the Tauc optical bandgap, E_g. Here, A, C, E_0, E_g are treated as fitting parameters.

$$\varepsilon_{2\mathrm{TL}}(E) = \begin{cases} \frac{AE_0C(E-E_g)^2}{(E^2-E_0^2)^2+C^2E^2} \cdot \frac{1}{E}, & E > E_g \\ 0 & E \leq E_g \end{cases} \quad \text{(Eq. 2.22)}$$

The real part of the dielectric function can be obtained from Kramers-Kronig integration, and the full analytical form of ε_1 can be found in Ref. 33 and 34, where it is a function with five parameters, i.e., $\varepsilon_{1\mathrm{TL}} = \varepsilon_1(\varepsilon_{1\mathrm{TL}}(\infty), A, C, E_0, E_g)$. In practical data analysis with the T-L model, the imaginary part of the dielectric function will first be fit with Eq. (2.22) to obtain the parameters (A, C, E_0, E_g) and the real part will be fitted second for the determination of $\varepsilon_{1\mathrm{TL}}(\infty)$.

$$\varepsilon_{1\mathrm{TL}} = \varepsilon_{1\mathrm{TL}}(\infty) + \frac{2}{\pi} P \int_{E_g}^{\infty} \frac{\xi \varepsilon_2(\xi)}{\xi^2 - E^2} d\xi \quad \text{(Eq. 2.23)}$$

Where P stands for the Cauchy principal part of the integral.

The above equations used the assumption of one oscillator per atom. If there are multiple oscillators occurring, the forms can be modified to:

$$\varepsilon_{2\mathrm{TL}}(E) = \begin{cases} \sum_{i=1}^{N} \frac{A_i E_i C_i (E-E_g)^2}{(E^2-E_i^2)^2+C_i^2E^2} \cdot \frac{1}{E}, & E > E_g \\ 0 & E \leq E_g \end{cases} \quad \text{(Eq. 2.24)}$$

$$\varepsilon_{1\mathrm{TL}} = \varepsilon_{1\mathrm{TL}}(\infty) + \sum_{i=1}^{N} \frac{2}{\pi} P \int_{E_g}^{\infty} \frac{\xi \varepsilon_i(\xi)}{\xi^2 - E^2} d\xi \quad \text{(Eq. 2.25)}$$

For the Tauc-Lorentz model, the limitation requires ε_2 to be 0 for energies less than the band gap. Consequently, the absorption due to intra-band absorption was neglected in this model. In this case, the defects or intra-band absorption increases below the band gap

and generates poor fits in that region. The valid spectral range for this model is when the energies $E \leq E_i$, where E_i is the transition energy of the oscillator of the highest order.[35]

We use Ta_2O_5 as an example for the application of T-L model, with different oscillators considered in different wavelength regions. The experimental values of (n, k) for Ta_2O_5 in the UV wavelength have been fit with Tauc-Lorentz with 1 oscillator (at longer wavelength 200 – 400 nm), with 2 oscillators (at shorter wavelength 150 – 200 nm), and 3 oscillators (100 – 150 nm). Different oscillators were chose based on the inter-band transitions and the shapes of the optical constants. The number of the oscillators correspond to the possible inter-band transitions, which can be calculated from the density function theory (DFT). As for the amorphous thin films, the inter-band transitions occur at different energy level might be overlapped, thus the number of the classical oscillators used does not necessarily equal to the number of inter-band transitions in the spectral range studied.

The optical constants fit with the Tauc-Lorentz model are shown in Fig. 2.12. With the increase of the number of oscillators in the different wavelength region, the optical constants of Ta_2O_5 can be well described by the Tauc-Lorentz model, and the RMSE from the fittings has been reduced from 0.0812 for 1 oscillator, to 0.0171 for 2 oscillators, and 0.00651 for 3 oscillators.

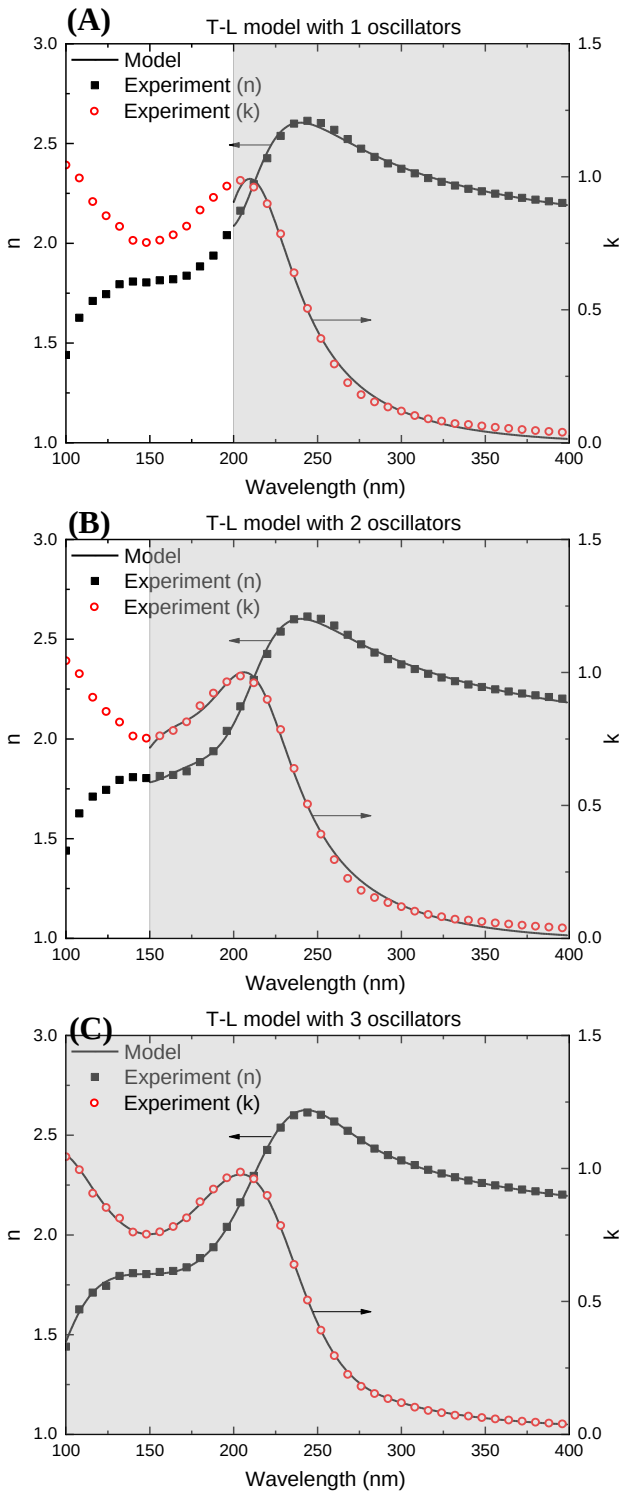

Figure 2.12. Tauc-Lorentz model for Ta_2O_5 in the inter-band region. Different oscillator numbers need to be considered for different wavelength regions. (A) 1 oscillator, (B) 2 oscillators, and (C) 3 oscillators.

Besides the Tauc-Lorentz model, A. S. Ferlauto *et al* proposed a modified Lorentz model with Cody joint density of states, called Cody-Lorentz (C-L) model.[33] In this model, the imaginary part of the dielectric function has a different form, Eq. (2.26), compared with the form used for Tauc model, Eq. (2.21). Compared with the T-L model, the C-L model uses an Urbach exponential absorption tail to describe the imaginary part of the dielectric function above the cut-off wavelength, which is set to be 0 for T-L model. However, compared with the T-L model, the C-L needs at least six parameters, which increases the fitting complexities.

$$\varepsilon_{2C}(E) \propto \left(E - E_g\right)^2 \qquad \text{(Eq. 2.26)}$$

2.1.4 Far UV Optical Constants Measurements

Optical constants can be determined from spectroscopic reflectance, transmission, and ellipsometry measurements.[10, 36] At shorter UV wavelengths, the measurements become more challenging as it usually requires vacuum condition to minimize the atmospheric absorption, especially from O_2. Besides, the lack of a FUV transparent substrate also prevents the transmission measurements. In this section, we will review the commonly used methods for optical constant measurements at shorter wavelengths and focus on methods based on reflectance intensity measurements.

2.1.4.1 Reflectance Intensity Measurements

For a two-layer structure with a single interface, Fig. 2.13, Fresnel equations are used to calculate the reflectance and transmission using the complex refractive index,

incident angles and refractive angles. As for the reflectance, it can be calculated from the Fresnel coefficients shown in Eq. (2.27) and (2.28). The reflected intensity can be calculated by, $R = |r|^2$ for each of the polarization where $\perp$ and $\parallel$ stand for s- and p-polarized light, respectively.[37]

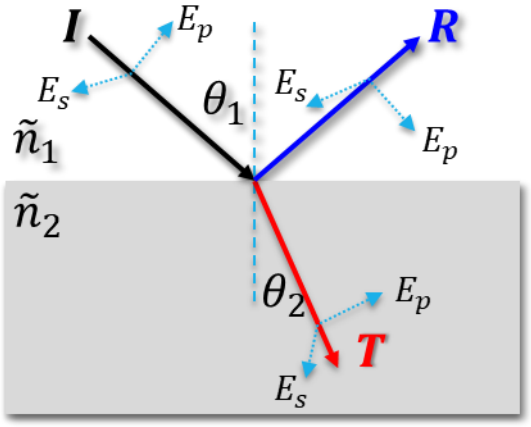

Figure 2.13. Two-layer structure with a single interface.

$$r_{1,2\perp} = \frac{\tilde{n}_1 \cos\theta_1 - \tilde{n}_2 \cos\theta_2}{\tilde{n}_1 \cos\theta_1 + \tilde{n}_2 \cos\theta_2} \quad \text{(Eq. 2.27)}$$

$$r_{1,2\parallel} = \frac{\tilde{n}_2 \cos\theta_1 - \tilde{n}_1 \cos\theta_2}{\tilde{n}_2 \cos\theta_1 + \tilde{n}_1 \cos\theta_2} \quad \text{(Eq. 2.28)}$$

For completely non-polarized light, the reflectance equals to the average of the two polarized intensities, as shown in Eq. (2.29).

$$R_a = \frac{1}{2}\left(R_s + R_p\right) = \frac{1}{2}\left(|r_\perp|^2 + |r_\parallel|^2\right) \quad \text{(Eq. 2.29)}$$

With known incident angle and the thickness, the reflectance R_a is a function of the optical constants, Eq. (2.30). Thus, it requires at least two independent measurements to uniquely determine both n and k. In this chapter, we discuss the reflectance vs incident angles, and reflectance vs thickness methods, for the determination of Far UV optical constants of thin films.

$$R_a = R_a(\tilde{n}) = R_a(n, k) \qquad \text{(Eq. 2.30)}$$

2.1.4.1.1 Reflectance vs Two Incident Angles

For non-polarized light, the reflectance varies with the incident angles. Fig. 2.14 shows the simulated polarized reflectance for different 20 nm films on a single crystal silicon substrate. Nine plots are made by varying the n and k with n = 1.0, 2.0, 3.0 and k = 0.2, 1.2, 2.2. For each combination of (n, k), the reflectance (s-, p-, and non-polarized) was plotted in the incident angles from 0° to 90°.

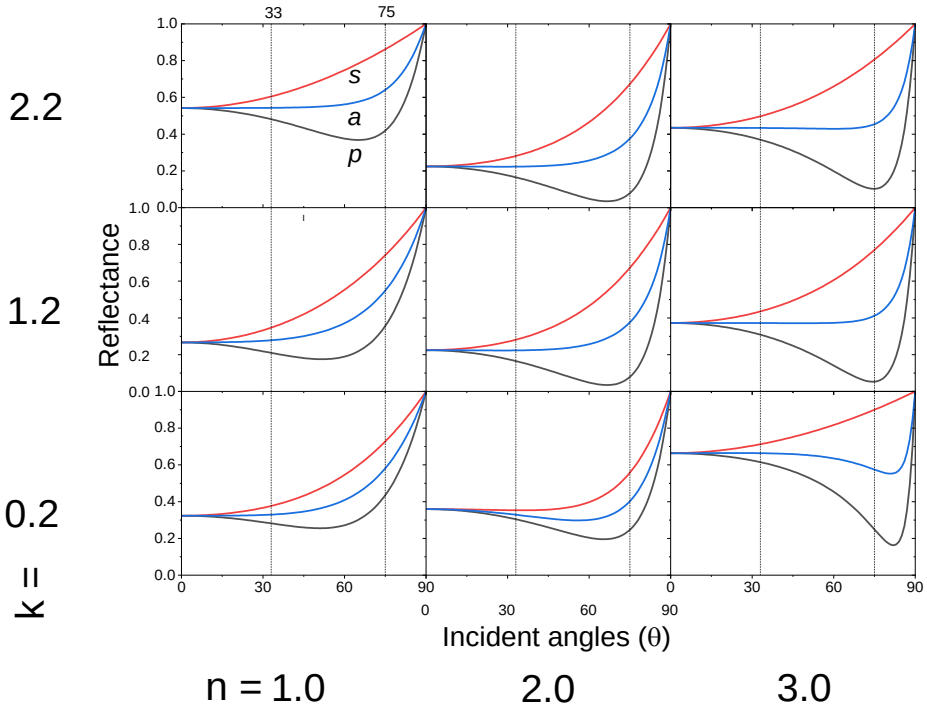

Figure 2.14. Reflectance vs incidents angles with different (n, k) combinations.

For the reflectance vs incident angles method, the reflectance measured at at least two incident angles is required. The larger the difference of the measured reflectance at different angles, the more accurate this method is to determine (n, k). In this research, the

light source used is un-polarized, and the reflectance remains constant until 30 – 50°, as shown in Fig. 2.14. Based on this consideration, we choose 33° and 75° as the two incident angles, which guarantee the measured reflectance are different for different (n, k) combinations, shown in Fig. 2.14.

When the reflectance at one incident angle is known, the locus of possible (n, k) combinations forms an "iso-reflectance" curve, as shown in Fig. 2.15.[36] Another iso-reflectance curve forms from the measurement at a different angle, and these two curves have intersection points, shown in Fig. 2.15. These intersection points are the possible solutions of (n, k). In some cases, more than one intersection points can be achieved, for example in Fig. 2.15, both (2.00, 1.20) and (1.46, 0.11) are the possible solutions. In this situation, one needs to access which value has physical meaning, thus the other solution can be ruled out. If there is no reference information available, one needs to do another measurement at a third incident angle which will result in an additional iso-reflectance curve to uniquely determine the intersection points.

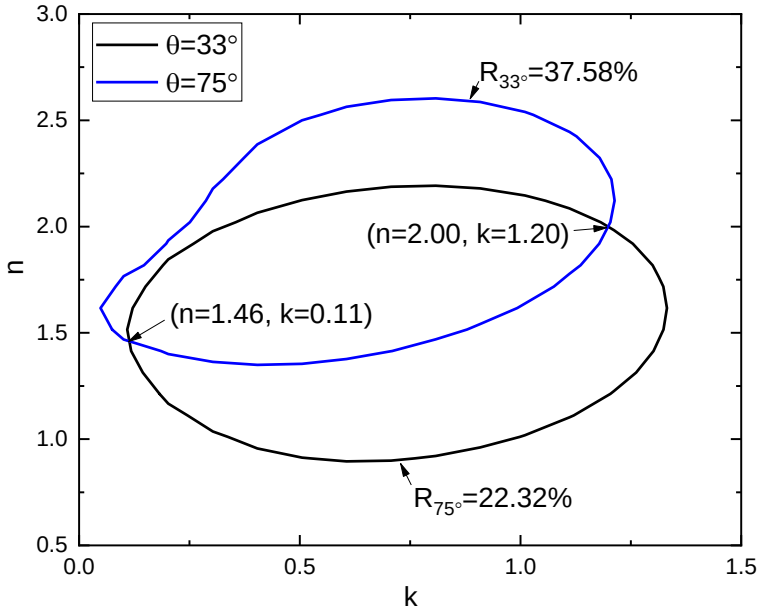

Figure 2.15. Iso-reflectance curves for reflectance vs two incident angles method.

For different values of (n, k), the iso-reflectance curve method may have different sensitivity and accuracy.[36] For example, for a material with $(n = 2.0, k = 0.2)$, the iso-reflectance curves from incident angles 33° and 75° are almost parallel, the intersection points become difficult to distinguish, Fig. 2.16. In this case, a small error on the reflectance measurement may cause a large shift of the intersection points, and thus increase the uncertainty for the measured values of (n, k). As a comparison, for a larger value of k, for example, $(n = 2.0, k = 1.2)$, the iso-reflectance curves become more distinguishable, and the determination of (n, k) becomes easier.

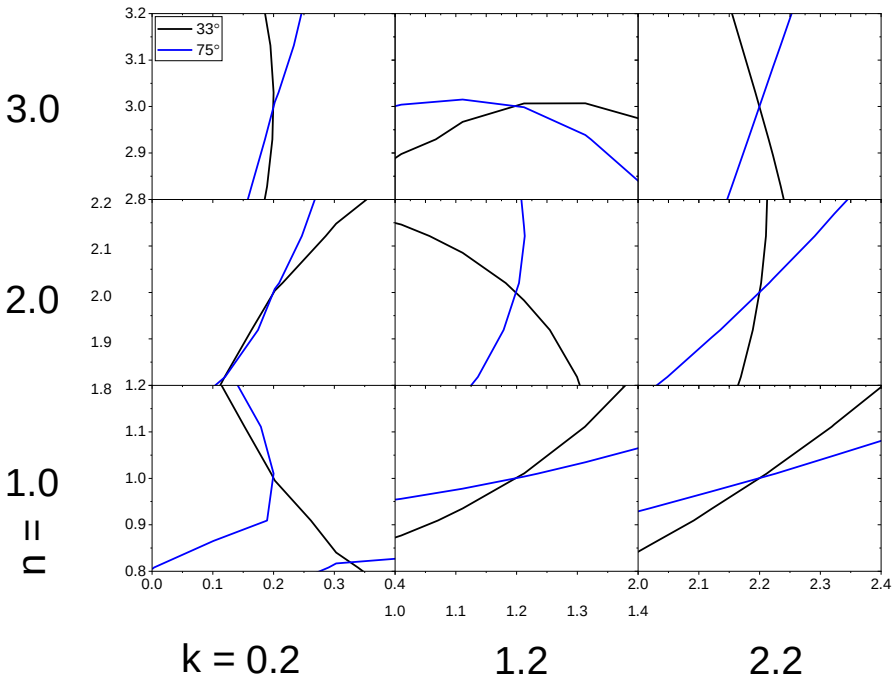

Figure 2.16. Iso-reflectance method with two incident angles. With different (n, k) combinations.

To quantify the effects from the errors in the reflectance measurements, an estimation on the error range has been made for the measurements of a film with ($n = 2.0$, $k = 1.2$), shown in Fig. 2.17. It shows that if the measured reflectance is shifted within 1% of the magnitude, the determined (n, k) has an uncertainty of ($n = 2.00 \pm 0.03$, $k = 1.20 \pm 0.02$). If the error is increased to 5%, the uncertainty increases to ($n = 1.99 \pm 0.16$, $k = 1.17 \pm 0.13$). The iso-reflectance method is strongly affected by the accuracy of the reflected intensity measurements, which is less accurate than the ellipsometry measurements, where the ratio of the complex reflectance is measured.

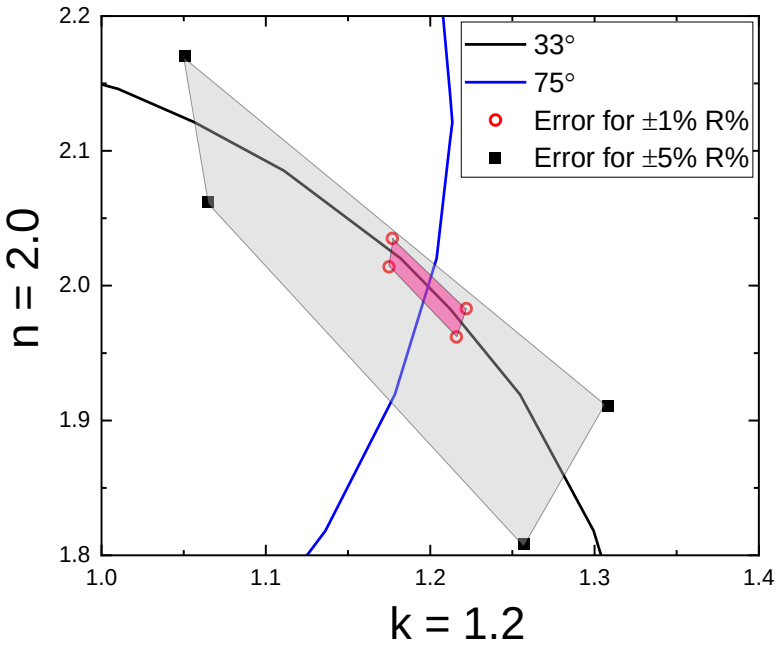

Figure 2.17. Error estimation on the reflectance vs two incident angles methods.

2.1.4.1.2 Reflectance vs Two Thicknesses

Similarly, reflectance vs two thicknesses can also be used to determine (n, k). The intersection points on the iso-reflectance curve correspond to the values of (n, k) for this material. Fig. 2.18 shows the simulated (n, k) for a single layer film on single crystal Si substrate, with two thicknesses of 20 nm and 40 nm. Nine plots are made in which each corresponds to a film with different (n, k), with $n = 1.0$, 2.0, 3.0 and $k = 0.2$, 1.2, 2.2. Different from the two incident angles method, this method does not work well for the materials with a large value of k. For example, for the $k = 2.2$, the iso-reflectance curves from these two measurements are nearly overlapped, which increases the uncertainty of the intersection points of (n, k).

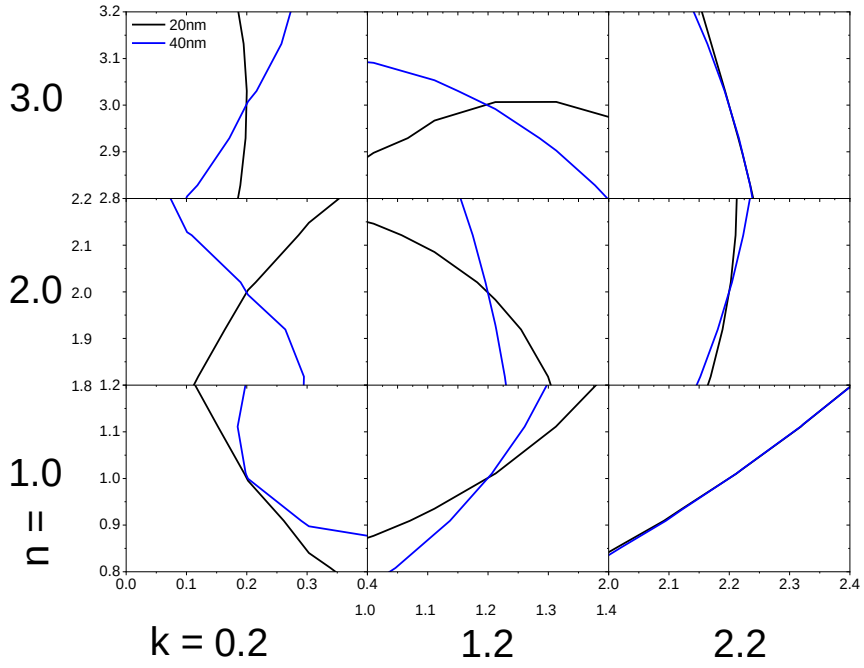

Figure 2.18. Iso-reflectance method with two thicknesses. With different (n , k) combinations.

The errors due to the uncertainty in the reflectance measurements have also been made for the two thicknesses method, as shown in Fig. 2.19. It shows that if the measured reflectance is shifted within 1% in the magnitude, the determined (n, k) has an uncertainty of $(n = 2.00 \pm 0.03, k = 1.20 \pm 0.02)$. If the error increases to 5%, the uncertainty increases to $(n = 2.00 \pm 0.12, k = 1.19 \pm 0.09)$. With an increase of the uncertainty of the reflectance measurements, the uncertainty for the determined (n, k) also increases.

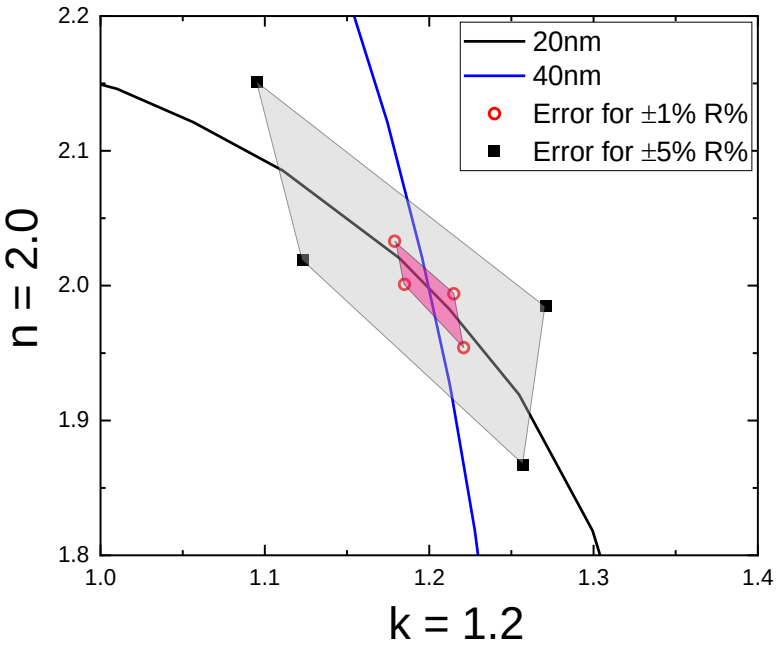

Figure 2.19. Error estimation on the reflectance vs two thicknesses methods.

2.1.4.1.3 Kramers-Kronig Integration Method

Another commonly used method is based on Kramers-Kronig (K-K) integration, which is used to describe the relations for complex quantities.[10] Both refractive index and reflectance are complex quantities, and described by, $\tilde{n} = n + ik$ (complex refractive index) and $r = \sqrt{R}e^{i\phi}$ (complex reflectance). For the complex refractive index, the K-K integration gives,[10]

$$n(E) = 1 + \frac{2}{\pi} P \int_0^\infty \frac{E' k(E')}{E'^2 - E^2} dE' \qquad \text{(Eq. 2.30)}$$

$$k(E) = -\frac{2E}{\pi} P \int_0^\infty \frac{n(E') - 1}{E'^2 - E^2} dE' \qquad \text{(Eq. 2.31)}$$

As a practical point of view, extinction coefficient k is easier to be obtained by transmission measurements. With the determination of k from transmission measurements, refractive index n can be obtained by K-K integration. In theory, the integration shown in

Eq. (2.30) is taken over the full spectrum, which is impossible in practice. Extrapolations and interpolations are usually applied to complete the full integration.[10]

K-K integration can also be used for the complex reflectance, with the modulus $\sqrt{R}$ and phase ϕ following the relation,[10]

$$\phi(E) = -\frac{E}{\pi} P \int_0^{\infty} \frac{\ln[R(E')/R(E)]}{E'^2 - E^2} dE' \quad \text{(Eq. 2.32)}$$

The complex refractive index $\tilde{n}$ can be obtained from the complex reflectance r, Eq. (2.33).[10] This method requires there is only a single interface, thus it is not applicable for multilayer structures.

$$\tilde{n} = \frac{1+r}{1-r} \quad \text{(Eq. 2.33)}$$

For the K-K integration, two methods have been commonly used.

2.1.4.1.3.1 Reflectance over a Wide Spectrum

If the reflectance intensity can be measured over a wide spectrum, i.e., from extreme UV to infrared, the phase of the reflectance can be obtained from the K-K integration. This method has been applied to study fluoride films by Juan I. Larruquert.[18, 29, 38]

2.1.4.1.3.2 Transmission over a Wide Spectrum

Alternatively, one can measure the transmission measurements over a wide spectrum, and the absorption coefficients α can be obtained. The extinction coefficient k is related to α with $k = \frac{\lambda\alpha}{4\pi}$. Then, the refractive index n can be obtained from K-K integration. This method has also been used in Juan. I. Larruquert's work, especially in the far UV optical constants for metal fluorides.[18, 38]

2.1.4.2 Ellipsometry Measurements

Spectroscopic ellipsometry for far UV measurements is not well developed due to the lack of the wideband polarizers and phase retarders for use at shorter wavelengths.[10] Currently, the commercially available vacuum UV ellipsometer can cover wavelengths down to 146 nm from J.A. Woollam (VUV-VASE), and 147 nm from Horiba (UVISEL 2 VUV). For the wavelengths shorter than 140 nm, some synchrotron beamlines have been used to perform the ellipsometry measurements, but only very narrow bands are available. J. Barth et al reported the use of VUV spectrometer with the synchrotron beamlines at BESSY, Berlin to perform the ellipsometry measurements in the wavelength 35 – 200 nm.[39]

2.2 Far UV Spectroscopy

In this section, we introduce the basic instrumentation for optical spectroscopy. We use the commonly used ultraviolet-visible-near infrared (UV-vis-NIR) spectroscopy as a starting point and jump to the vacuum UV and far UV spectroscopy for detailed descriptions of the commonly used light sources, monochromators, and detectors.

2.2.1 UV-vis-NIR Spectroscopy

For commonly used UV-vis-NIR spectroscopy, one of the instrumental set-ups is shown in Fig. 2.20 below.[40] This optical system consists of three components, namely, the lamp, monochromator, and detector. For this system, a deuterium lamp is used to cover the UV wavelengths, while a halogen lamp is used for visible and near infrared wavelengths. Diffraction gratings are used in the monochromator to produce a continuous

spectrum, with one single wavelength output at each time. For the detectors, a photomultiplier is used in the UV/vis range, while a lead sulfide (PbS) detector is used in the NIR range.[40] The specifications for the Lambda 950 optical system are shown below in Table 2.2.

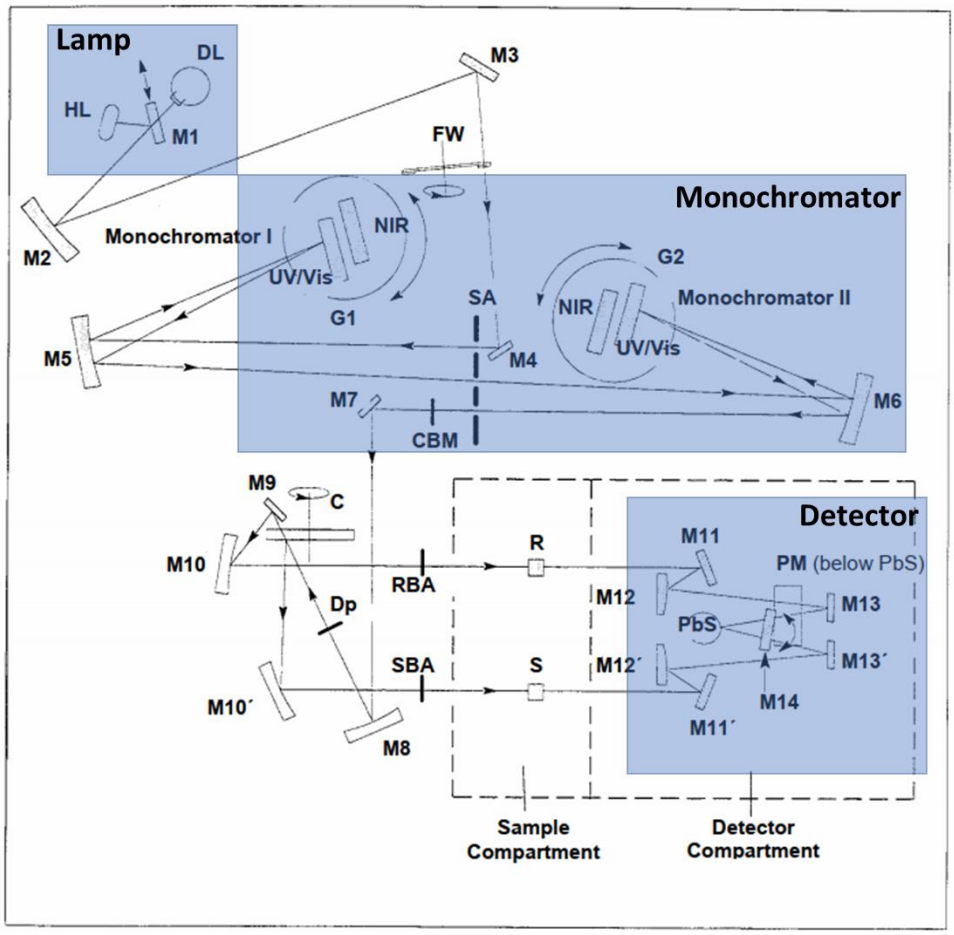

Figure 2.20. Instrumental set-up for Lambda 950 UV-vis-NIR spectrometer.[40]

Table 2.2 Lambda 950 UV-vis-NIR spectrometer specifications.[40]

Specification	Lambda 950
Principle	Double beam, double monochromator, ratio recording UV/Vis/NIR spectrophotometer with microcomputer electronics.
Optical system	All reflecting optical system (SiO_2 coated) with holographic grating monochromator with 1440 lines/mm UV/Vis blazed at 240 nm and 360 lines/mm NIR blazed at 1100 nm. Littrow mounting, sample thickness compensated detector.
Beam Splitting System	Chopper (46+ Hz, Cycle: Dark/Sample/Dark/ Reference, Chopper Segment Signal Correction CSSC).
Detector	Photomultiplier R6872 for high energy in the whole UV/Vis wavelength range. Peltier cooled PbS detector for NIR.
Source	Pre-aligned tungsten-halogen and deuterium.
Wavelength Range	175 nm–3300 nm (N_2 purge required below 185 nm)
UV/Vis Resolution	≤0.05 nm
NIR Resolution	≤0.20 nm

The monochromator is an essential component in any spectroscopy, as continuous wavelength output is required for the optical measurements. Diffraction gratings have been commonly used in the monochromator. The basic grating equation for the reflective diffraction (Fig. 2.21) is shown in Eq. (2.34). Here, m is the spectral order of diffraction; k is the distance between the grating lines; α is the incident angle; and β is the diffracted angle.[41]

$$m \times \lambda = k \times (\sin\alpha \pm \sin\beta) \qquad \text{(Eq. 2.34)}$$

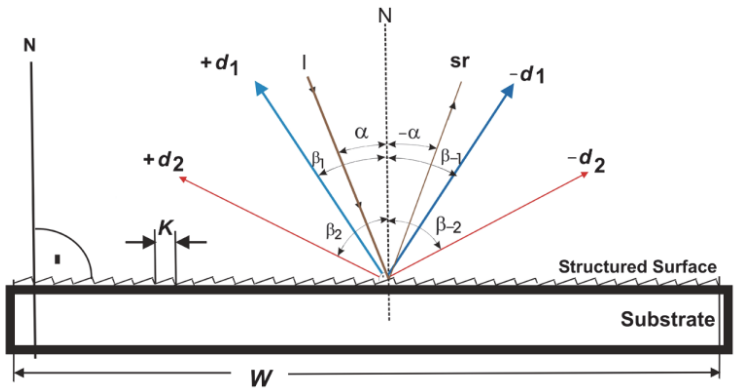

Figure 2.21. Reflective diffraction gratings.[41]

A single diffraction grating may not be sufficient for the experimental wavelength range, and the combination with other mirrors in different configurations have been proposed. For the optical system shown in Fig. 2.20, the monochromator used is based on the Littrow mounting, which consists of a spherical mirror (Fig. 2.22).[41] The spherical mirror in this configuration is used for both collimating and focusing. This system is compact since the entrance and exit slits are placed nearby, but it also has the disadvantages related to internal reflections.[42]

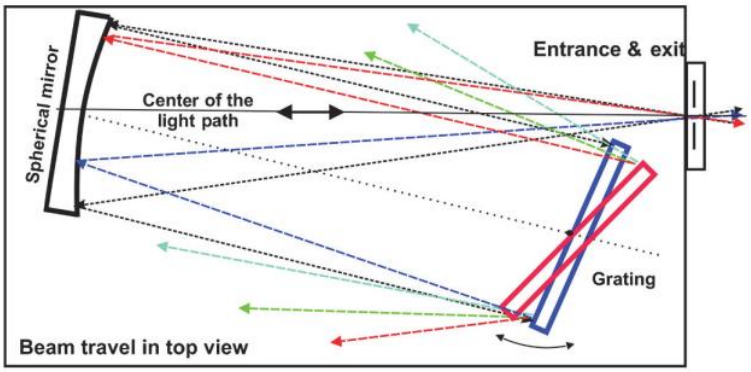

Figure 2.22. Littrow mount used in Lambda 950 optical system, shown in Fig. 2.20.[41]

2.2.2 Far UV Spectroscopy Basics

For far UV spectroscopy, the light sources, monochromators, and detectors should be optimized and customized for the use in shorter wavelengths. This section will review the commonly used light sources, monochromator set-ups, and detectors.

2.2.2.1 Light Source

The light sources used in far UV are mainly based on gas discharges, high-pressure arcs, and low-pressure and vacuum sparks.[42] Synchrotron beamlines and X-ray free electron laser are also used as far UV light sources. In this section, we will introduce the

two commonly used sources, one is the deuterium lamp, and another is the hollow cathode lamp.

2.2.2.1.1 Deuterium Lamp

A deuterium lamp is a low-pressure gas discharge light source, and commonly used in UV spectroscopy due to its advantages of high radiant efficiency, modest power assumption, and simple operation conditions.[43] For the deuterium lamp, the visible and infrared emission is negligible, which makes deuterium lamps ideal sources for UV spectroscopy. The commercially available deuterium lamp can cover the wavelength down to 115 nm, with MgF_2 window (Hamamatsu Photonics, L1835).

2.2.2.1.2 Hollow Cathode Lamp

For wavelengths below 105 nm (the lowest cut-off wavelength for existing window material, LiF), the windowless lamp needs to be used. Windowless Hollow cathode lamps use the gas discharge with inter gases to generate spectra down to a wavelength of 20 nm.[42] As an example, the commercially available hollow cathode lamp can cover the UV wavelength range of 30 – 160 nm (McPherson Inc., Model 629).

2.2.2.2 Monochromator

The commonly used designs for FUV monochromators are based on concave gratings and planar gratings. In this section, we describe the Seya-Namioka configuration as an example for concave gratings and the Czerny-Turner configuration as an example for planar gratings.

2.2.2.2.1 Seya-Namioka mount

The Seya-Namioka mount was designed by Seya and constructed by Namioka, as shown in Fig. 2.23.[42, 44] In this system, the entrance and exit slits are fixed, and the wavelength scanning is performed by rotation of the grating. The directions of the incident and exiting beams remain unchanged while the wavelengths are scanned. The angle between entrance and exit light beams (called included angle) is fixed at 70°15', which allows to satisfy the horizontal focal condition over a wide wavelength range (e.g., 0 – 700 nm with a 600 grooves/mm grating).[42]

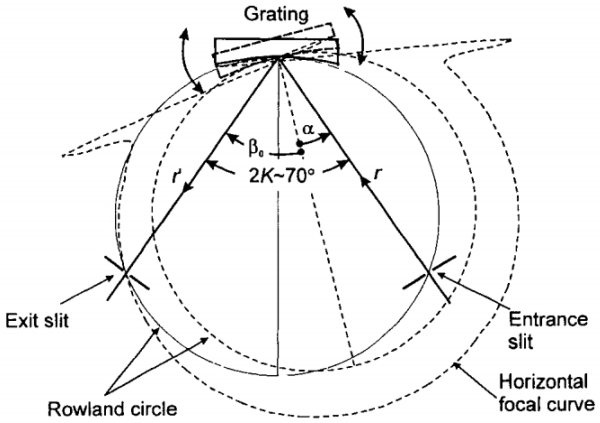

Figure 2.23. Seya-Namioka mount for the monochromator.[42]

For the Seya-Namioka configuration, the relation between wavelength and the angle is given by, $\lambda = \left(\frac{2\sigma}{m}\right) \cos K \sin \theta$. Here, $2K$ is the included angle between the principal incident and exiting rays, and σ is the distance between the grating grooves (called the grating constant). A number of modifications of the Seya-Namioka design have been made to reduce the astigmatism.[42]

2.2.2.2.2 Czerny-Turner mount

Different from the Seya-Namioka mount, the Czerny-Turner mount uses a plane grating instead of a concave grating (Fig. 2.24).[42] The incident light beam is collimated with a concave mirror, while the diffracted light is focused into the exit slit by another concave mirror. Similar to the Seya-Namioka mount, the wavelength scanning for the Czerny-Turner mount is also performed by the rotation of the grating on its axis parallel to the ruling.

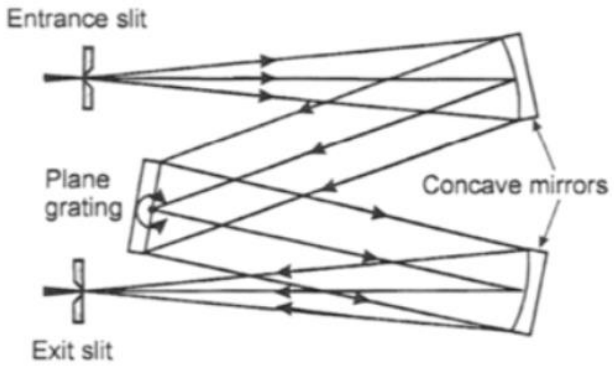

Figure 2.24. Czerny-Turner mount for the monochromator.[42]

2.2.2.3 Detector

The commonly used detectors for FUV spectroscopy include photodiodes, photomultiplier tubes, and charge-coupled devices.[42] For the detailed description of the detectors commonly used in vacuum and far UV, please refer to the review articles.[42, 45-47]

2.2.2.3.1 Photodiode

A photodiode is a p-n junction or a PIN junction that converts light into a current using the inner photoelectric effect. Silicon photodiode is commonly used due to the advantages include lightweight, low noise, wide spectral range, and long lifetime.[48] The traditional silicon photodiodes at far UV wavelengths can be degraded by the outer protective SiO_2 layer due to the formation of charge carrier traps.[45] To solve this issue, alternative photodiodes are developed, such as n-p junction photodiodes.[49] The commercial nitridated Silicon photodiode (Model 423, McPherson Inc.) can measure the wavelength down to 1 nm.

2.2.2.3.2 Photomultiplier Tube

A photomultiplier tube (PMT) is a vacuum tube consists a photocathode, focusing electrodes, multiple dynode stages, and an anode.[42] PMT uses several dynodes as electron multipliers, thus is highly sensitive to low incident flux. The current produced by the low incident light can be multiplied as much as 10^8.[50] Besides the high sensitivity, PMT also has the advantages include low noise, large collection area, and ultra-fast response.[45, 50] For the use in far UV, sapphire, fused silica, MgF_2, and LiF are used as the window materials to enhance the high transparency in the 105 – 200 nm range. For the wavelength below 105 nm, a scintillator needs to be equipped to convert the vacuum UV light to a visible light and detected by the PMT.[42, 45] The commercial PMT used for far UV can cover the wavelength down to 30 nm (Model 658, McPherson Inc.).

2.2.2.3.3 Charge-Coupled Device

Charge-coupled devices (CCD) are scientific grade cameras containing an array of coupled capacitors, and can be used as the photon detectors.[51] CCD detectors have the

advantages include high quantum efficiencies, high sensitivity, multi-channel operations, rapid data collection, and linear outputs.[51-53] For the use in far UV, the front-illuminated open electrode CCD detector with Lumogen coating, can be used down to 120 nm. For the wavelengths lower than 120nm, a windowless back-illuminated CCD needs to be used.[42, 53] The commercial CCD detector used in far UV can cover the wavelength down to 1 nm (Model CCD, McPherson Inc.).[53]

2.2.3 Far UV Spectroscopy Application

Far UV spectroscopy has the potential to be used for the study of electronic transitions and the structure of molecules. For example, one can explore Rydberg transitions of liquids with far UV spectroscopy. Besides, it is also possible to investigate the transitions concerning σ electrons of molecules and the $\pi - \pi^*$ transitions.[54]

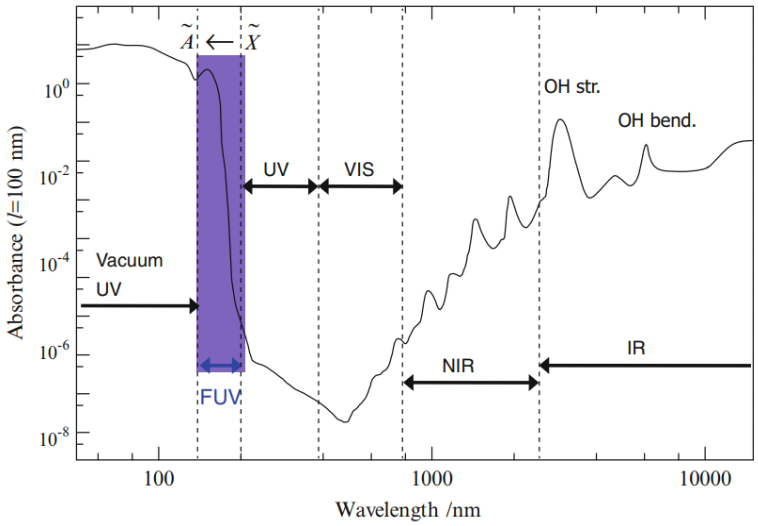

Figure 2.25. Absorption spectrum of water from IR to FUV region. The first electronic transition occurs in FUV region.[54] Copyright © 2015, Springer Japan.

Besides the potential applications for liquids and small molecules, far UV spectroscopy can be used study the electronic transitions in wide bandgap materials, such

as the inter-band transitions of hexagonal boron nitride (h-BN) at 6.1 eV and 6.95 eV,[55] and the excitonic effects of Al_2O_3 at 9.5 eV.[56] In this study, we demonstrated the use of far UV spectroscopy for the determination of the optical constants of thin films, in Chapter 5. We further extend the use of far UV spectroscopy to study the material mixtures, for the determination of the volume concentration of each constituent, in Chapter 6.

2.3 Far UV Optical Coatings

Optical coatings are used to enhance the reflection, transmission, or polarization for the optical components. The basic types of optical coatings include high-reflectivity (HR), and anti-reflective (AR) coatings, depending on if they are highly reflecting or transmitting to the light beam.[57] Using optical coatings, different optical devices can be made, including optical filters and polarizers. In this section, we will review the commonly used optical coatings, and their applications in the Far UV wavelength range.

2.3.1 Basic Far UV Optical Coatings

2.3.1.1 High-Reflectivity Coatings

The high-reflectivity optical coatings used at shorter wavelength can be divided into two categories, with metal-dielectric structures, and all-dielectric structures.[58] The metal-dielectric structure, usually uses Al as the reflecting metal layer, which is overcoated with transparent dielectrics to prevent oxidation. Figure 2.26 shows the reflectance for commonly used metal materials, where Au and Ag can maintain a high reflectance in visible and infrared region while they suffer a significant drop at UV wavelengths. The ideal Al metal can still have >90% reflectance in the Far UV wavelength range, but Al metal is easily oxidized and the formed Al_2O_3 layer will significantly degrade the optical

performance. To prevent oxidation, Far UV transparent metal fluorides, such as MgF_2, AlF_3, and LiF have been used as overcoating layers on Al to enhance the reflectance.[12] The advantage of a metal reflective coating is that a single layer thin metallic film can result in a relatively high reflectance over a wide spectrum, but it is not feasible for optical design, as absorption exists in Al. To overcome the Far UV absorption, all-dielectric structures should be considered as candidates for HR coatings.

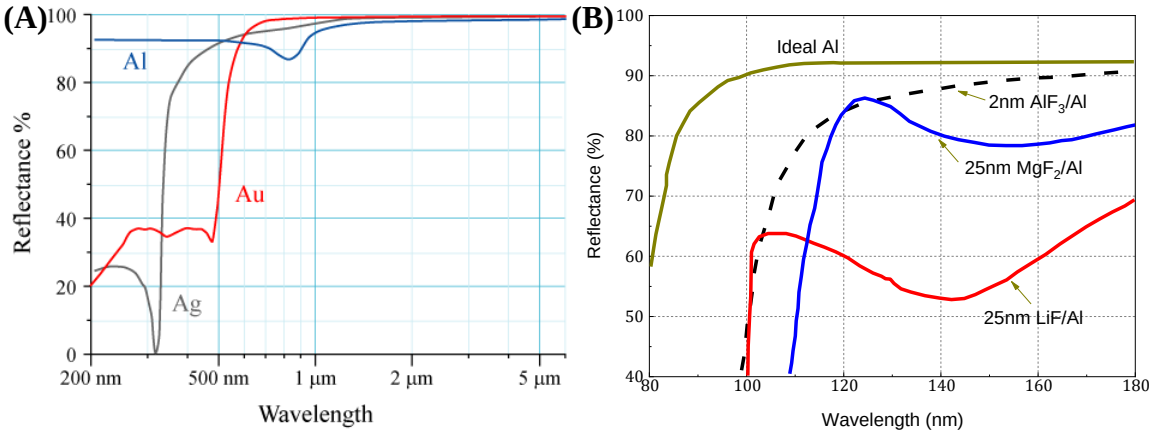

Figure 2.26. Metal reflective coatings. (A) Metal coatings; Copyright © CC BY-SA 3.0).[59] (B) Al overcoated with metal fluorides, reproduced from various sources.[12, 60]

All-dielectric high-reflectivity coatings can be achieved from quarter-wave structures, as shown in Fig. 2.27. With each thickness fixed at quarter wavelength optical thickness (QWOT), constructive interference can be achieved from this structure. Figure 2.27b shows an example design with LaF_3 as the high-index layer, and MgF_2 as the low-index layer. With increase of the number of layers, the reflectance curve becomes sharper and higher, with ultimate reflectance approaching 100%.

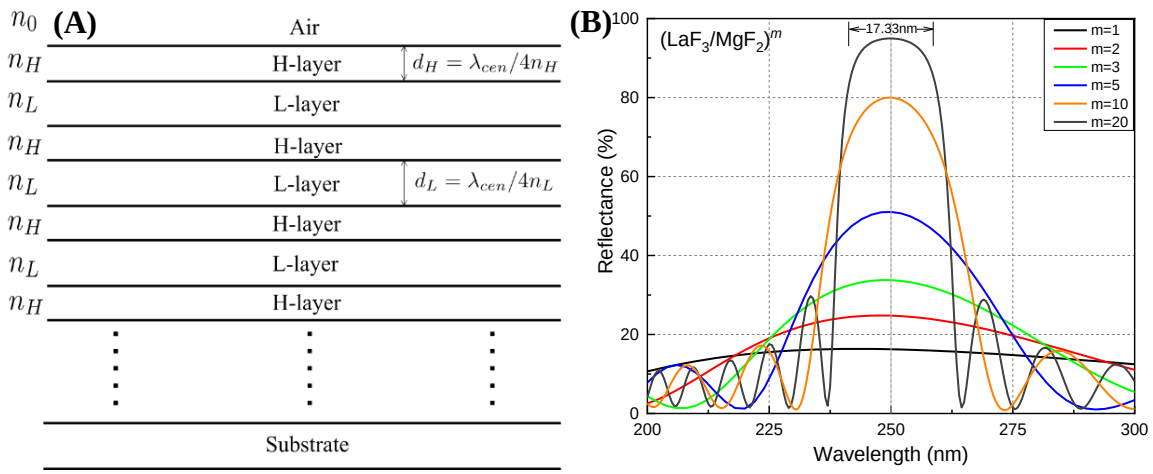

Figure 2.27. All-dielectric reflective coatings. (A) Quarter-wave high-reflectivity structure; (B) Example design with LaF_3/MgF_2.

For use in the UV and FUV ranges, the materials should have a wide bandgap to minimize absorption. For oxides, the commonly used high refractive index layers are Al_2O_3,[61-63] and HfO_2,[64-66] with low refractive index layers (L-layers) normally of SiO_2.[63, 66, 67] Besides oxides, metal fluorides have ultrawide bandgap (>10eV), and thus maintain high transparency in the FUV wavelength range. For UV optical coatings, BaF_2,[68] LaF_3,[62, 68, 69] or GdF_3,[70] have been used as H-layers, while MgF_2,[62, 68, 69] and AlF_3[61, 70] have been used as L-layers. It is also worth noting that SiO_2 has also been used as H-layers when paired with metal fluorides, such as MgF_2.[68]

Figure 2.28 shows an example for an HR coating based on quarter-wave structures. Multilayer high-reflectivity all-dielectric coatings based on HfO_2/SiO_2, and LaF_3/MgF_2 have been designed and fabricated, with the measured reflectance curves, shown in Fig. 2.29.[10, 71]

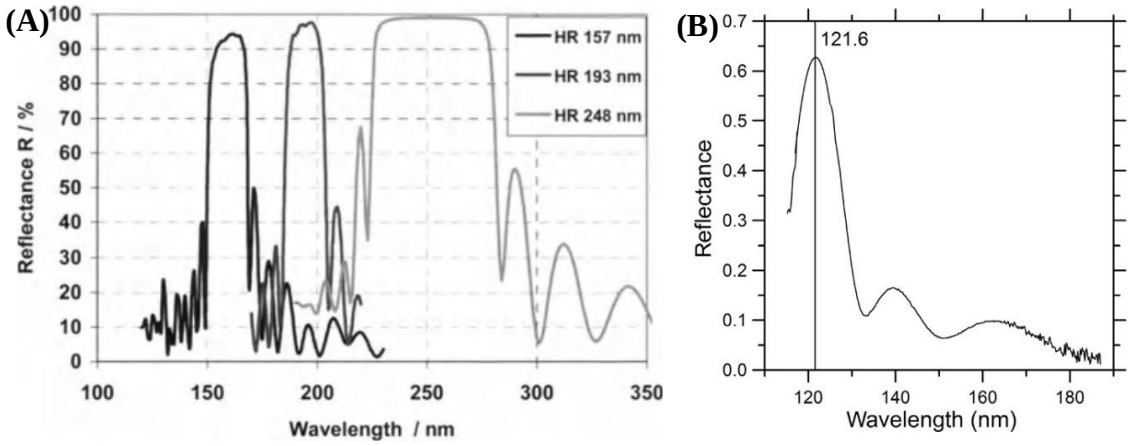

Figure 2.28. Measured reflectance of quarter-wave all-dielectric mirrors. (A) Design based on HfO_2/SiO_2 and LaF_3/MgF_2 for the use at 157, 193, and 248 nm. Copyright © 2003, Springer-Verlag Berlin Heidelberg.[71] (B) Design based on LaF_3/MgF_2 for the use at 121.6 nm. Copyright © 2018, Elsevier Ltd.[10]

2.3.1.2 Anti-Reflective Coatings

Antireflective coatings have different designs, from a single layer to a multilayer structure, Fig. 2.29.[57, 72, 73] The simplest design is a single layer structure, with a quarter-wave thickness, Fig. 2.29a. To achieve a high transmission coating, the refractive index of the film should satisfy the relation, Eq. (2.35).[57, 72] Here, n_s is the refractive index of the substrate. n_0 is the refractive index of air.

$$n_1 = \sqrt{n_0 n_s} \qquad \text{(Eq. 2.35)}$$

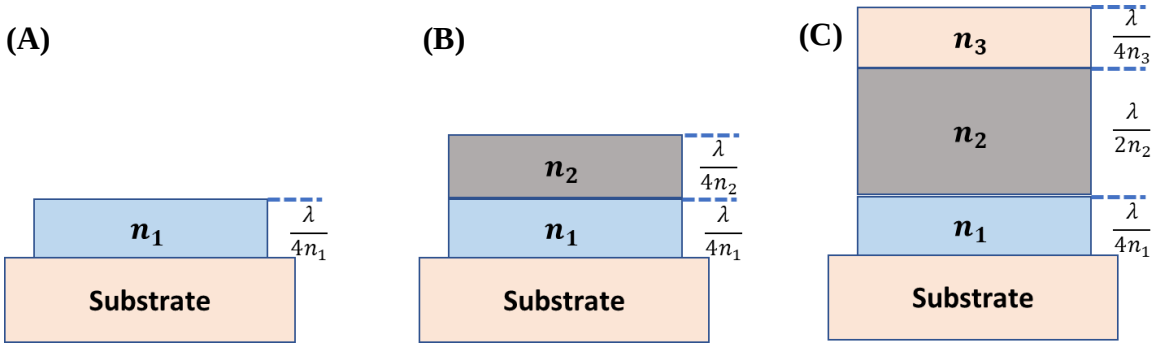

Figure 2.29. Antireflective coating structures. (A) Single layer, (B) Double layer (V-coat), (C) Multilayer structure (triple layer).

As for a double layer structure, each layer should be at quarter-wave thickness, with refractive indices satisfying the Eq. (2.36).[72] This structure is also called V-coat due to its V-shape profile on the transmission spectra, as shown in Fig. 2.30.[71]

$$n_1 n_2 = n_0 n_s \qquad \text{(Eq. 2.36)}$$

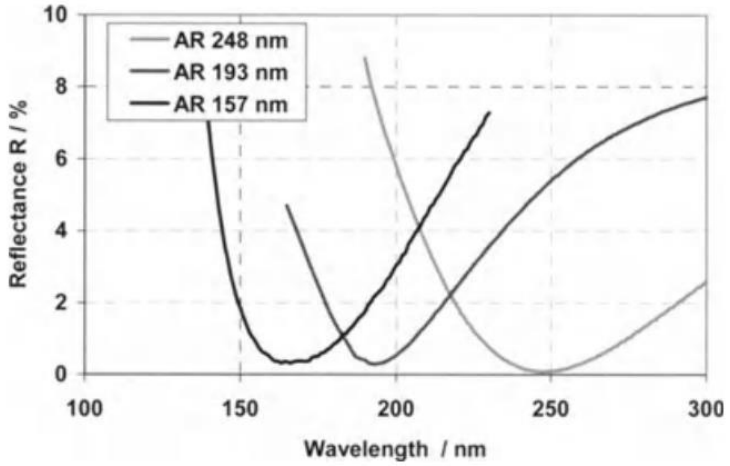

Figure 2.30. Measured reflectance of CaF_2 on both sides for an anti-reflective V-coated design at 248 nm, 193 nm, and 157 nm. Copyright © 2003, Springer-Verlag Berlin Heidelberg. [71]

As for the multilayer structure, the three-layer structure can be achieved with alternating quarter-wave and half-wave structures. In order to achieve destructive interference, the relation between the refractive indices is,[57]

$$\frac{n_1}{n_0} = \frac{n_2}{n_1} = \frac{n_3}{n_2} = \frac{n_s}{n_3} \qquad \text{(Eq. 2.37)}$$

2.3.2 Far UV Optical Filters

Based on high-reflectivity and anti-reflective coatings, optical filters can be made with more complex structures. The commonly used bandpass filters are mainly based on metal-dielectric and all-dielectric Fabry-Perot structure, with a single cavity or multiple cavities, shown in Fig. 2.31.[57]

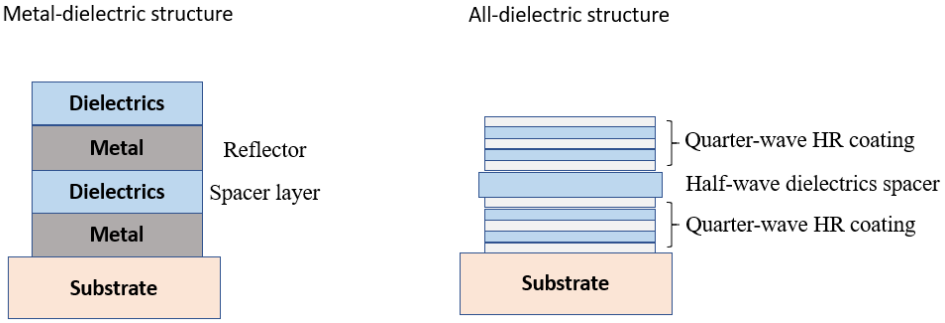

Figure 2.31. Fabry-Perot type bandpass filter structures. (A) Metal-dielectric structure, (B) All-dielectric structure.

2.3.2.1 Metal-Dielectric Structure

In the metal-dielectric structure, a thin metal layer, usually Al, serves as the reflector. A high-transparency dielectric layer is the spacer layer, i.e., the cavity for the Fabry-Perot interferometer.[57] Figure 2.32 shows a bandpass filter based on Al/MgF_2 structure on fused silica substrate. Five different designs were made with different central wavelengths in the far and middle UV wavelength range.[57]

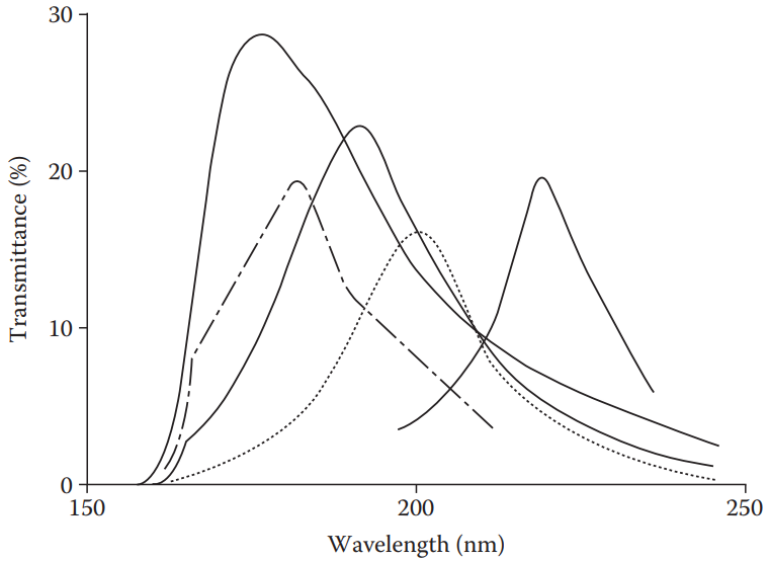

Figure 2.32. Al/MgF_2 bandpass filters on fused silica substrate. Copyright © 2010, Taylor & Francis Group LLC – Books.[57]

2.3.2.2 All-Dielectric Structure

An all-dielectric bandpass filter has the structure shown in Fig. 2.31b and 2.33. In this design, the multilayer quarter-wave high-reflectivity coatings will be used as the reflector for Fabry-Perot interferometer, and a half-wave dielectric layer serves as the cavity. A simulation was done for the design of bandpass filter based on SiO_2/AlF_3, for the use at 157nm, Fig. 2.34. It shows that with increasing number of high-reflectivity coating layers, the transmission for the filter becomes sharper, with the bandwidth reduced to 0.2 nm.

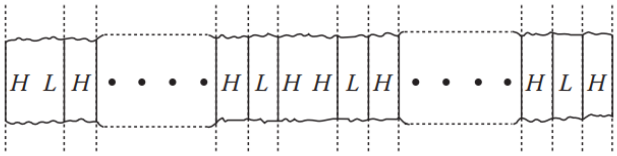

$(\mathrm{HL})^m|\mathrm{HH}|(\mathrm{LH})^m$

Figure 2.33. Structure of the all-dielectric single-cavity filter. Copyright © 2010, Taylor & Francis Group LLC – Books. [57]

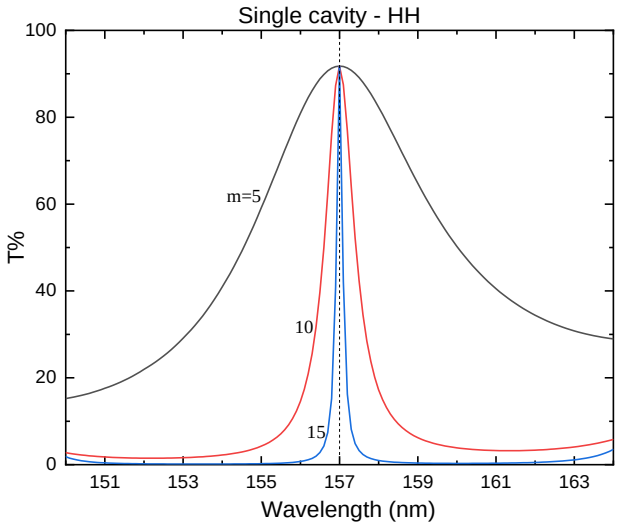

Figure 2.34. Simulated transmission for the bandpass filter based on SiO_2/AlF_3.

Yang *et al* designed and fabricated an all-dielectric bandpass filter based on LaF_3/MgF_2 from evaporation method, for use at a wavelength of 193 nm. They designed a multilayer structure with $m = 10$, i.e., $(\mathrm{HL})^{10}|\mathrm{HH}|(\mathrm{LH})^{10}$, with LaF_3 and MgF_2 as the high- and low-index layers, respectively.[74]

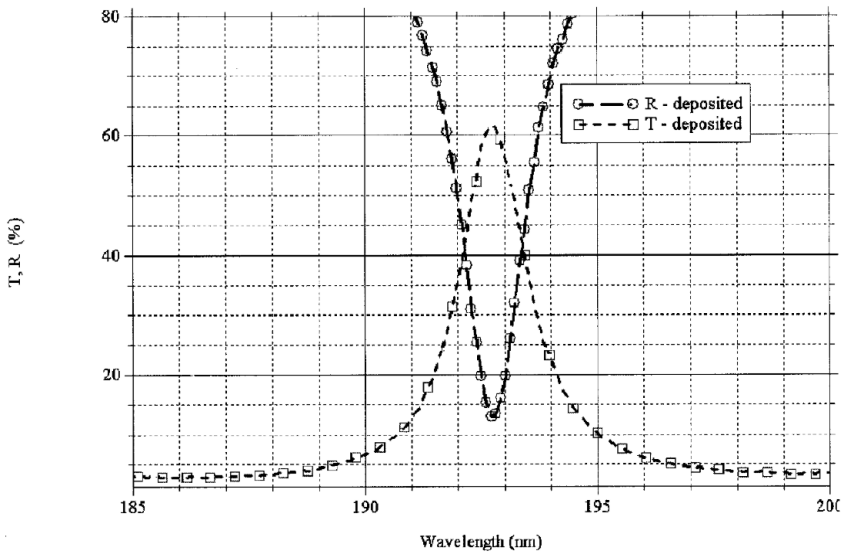

Figure 2.35. Measured transmission of the deposited FUV bandpass filter with a single-cavity structure. Copyright © 2006, The Optical Society. [74]

References

[1] R. E. Hummel, "*The Optical Constants*," in Electronic Properties of Materials, Ch. 10, pp. 215, edited by R. E. Hummel (Springer 2010).

[2] R. E. Hummel, "*Quantum Mechanical Treatment of the Optical Properties*," in Electronic Properties of Materials, Ch. 12, pp. 247, edited by R. E. Hummel (Springer, 2010).

[3] M. Tryus, "Extreme Ultraviolet Reflectometry for Structural and Optical Characterization of Thin Films and Layer Systems," RWTH Aachen University, 2018.

[4] P. Y. Yu and M. Cardona, "*Optical Properties I*," in Fundamentals of Semiconductors - Physics and Materials Properties, Ch. 6, pp. 243, edited by P. Y. Yu and M. Cardona (Springer, 2010).

[5] M. Fox, "*Interband absorption*," in Optical Properties of Solids, Ch. 3, pp. 62 (Oxford University Press, 2010).

[6] M. Fox, "*Excitons*," in Optical Properties of Solids, Ch. 4, pp. 95 (Oxford University Press, 2010).

[7] A. Delin, P. Ravindran, O. Eriksson and J. M. Wills, "Full-potential optical calculations of lead chalcogenides," Int. J. Quantum Chem. **69**, 349 (1998).

[8] G. E. Jellison and F. A. Modine, "Parameterization of the optical functions of amorphous materials in the interband region," Appl. Phys. Lett. **69**, 371 (1996).

[9] J. L. Navarro, E. A. Albanesi, R. Vidal and J. Ferrón, "A study on the structural, electronic and optical properties of the α-AlF3 compound," Mater. Res. Bull. **83**, 615 (2016).

[10] J. I. Larruquert, "*Optical properties of thin film materials at short wavelengths*," in Optical Thin Films and Coatings, Ch. 7, edited by A. Piegari and F. Flory (Woodhead Publishing, 2018).

[11] E. S. Field, J. C. Bellum and D. E. Kletecka, "Laser damage comparisons of broad-bandwidth, high-reflection optical coatings containing TiO_2, Nb_2O_5, or Ta_2O_5 high index layers," Proc. SPIE **8885**, 88851X (2013).

[12] B. Fleming, M. Quijada, J. Hennessy, A. Egan, J. Del Hoyo, B. A. Hicks, J. Wiley, N. Kruczek, N. Erickson and K. France, "Advanced environmentally resistant lithium fluoride mirror coatings for the next generation of broadband space observatories," Appl. Opt. **56**, 9941 (2017).

[13] J. A. W. Co., "*"Goodness" of Fit: definition of the MSE*," in CompleteEASE Software Manual, Ch. 3.1 (J.A. Woollam Co., Lincoln, NE, 2014).

[14] M. Jerman, Z. Qiao and D. Mergel, "Refractive index of thin films of SiO_2, ZrO_2, and HfO_2 as a function of the films' mass density," Appl. Opt. **44**, 3006 (2005).

[15] M. F. Al-Kuhaili, "Optical properties of hafnium oxide thin films and their application in energy-efficient windows," Opt. Mater. **27**, 383 (2004).

[16] M. J. Dodge, "*Refractive index*," in Handbook of Laser Science and Technology, Vol. IV, pp. 30 (CRC Press, Boca Raton, 1986).

[17] G. Ghosh, "Dispersion-equation coefficients for the refractive index and birefringence of calcite and quartz crystals," Opt. Commun. **163**, 95 (1999).

[18] L. V. Rodriguez-de Marcos, J. I. Larruquert, J. A. Mendez and J. A. Aznarez, "Self-consistent optical constants of MgF_2, LaF_3, and CeF_3 films," Opt. Mater. Express **7**, 989 (2017).

[19] H. H. Li, "Refractive index of alkaline earth halides and its wavelength and temperature derivatives," J. Phys. Chem. Ref. Data **9**, 161 (1980).

[20] J. Hennessy, A. Jewell, K. Balasubramanian and S. Nikzad, "Ultraviolet optical properties of aluminum fluoride thin films deposited by atomic layer deposition," J. Vac. Sci. Technol., A **34**, 01A120 (2016).

[21] D. König, R. Scholz, D. R. T. Zahn and G. Ebest, "Band diagram of the $AlF_3/SiO_2/Si$ system," J. Appl. Phys. **97**, 093707 (2005).

[22] A. Belosludtsev, K. Juškevičius, L. Ceizaris, R. Samuilovas, S. Stanionytė, V. Jasulaitienė and S. Kičas, "Correlation between stoichiometry and properties of scandium oxide films prepared by reactive magnetron sputtering," Appl. Surf. Sci. **427**, 312 (2018).

[23] R. K. Choudhary, P. Mishra, A. Biswas and A. C. Bidaye, "Structural and Optical Properties of Aluminum Nitride Thin Films Deposited by Pulsed DC Magnetron Sputtering," ISRN Materials Science **2013**, 1 (2013).

[24] I. Bhaumik, R. Bhatt, S. Ganesamoorthy, A. Saxena, A. K. Karnal, P. K. Gupta, A. K. Sinha and S. K. Deb, "Temperature-dependent index of refraction of monoclinic Ga_2O_3 single crystal," Appl. Opt. **50**, 6006 (2011).

[25] S.-L. Ku and C.-C. Lee, "Optical and structural properties of silicon nitride thin films prepared by ion-assisted deposition," Opt. Mater. **32**, 956 (2010).

[26] K.-N. Chen, C.-M. Hsu, J. Liu, Y.-C. Liou and C.-F. Yang, "Investigation of Antireflection Nb_2O_5 Thin Films by the Sputtering Method under Different Deposition Parameters," Micromachines **7**, 151 (2016).

[27] T. Siefke, S. Kroker, K. Pfeiffer, O. Puffky, K. Dietrich, D. Franta, I. Ohlídal, A. Szeghalmi, E. B. Kley and A. Tünnermann, "Materials Pushing the Application Limits of Wire Grid Polarizers further into the Deep Ultraviolet Spectral Range," Adv. Opt. Mater. **4**, 1780 (2016).

[28] F. Z. Tepehan, F. E. Ghodsi, N. Ozer and G. G. Tepehan, "Determination of optical properties of amorphous Ta_2O_5 films deposited by spin- and dip-coating methods," Sol. Energy Mater. Sol. Cells **46**, 311 (1997).

[29] L. V. Rodríguez-de Marcos, J. I. Larruquert, J. A. Méndez and J. A. Aznárez, "Self-consistent optical constants of SiO_2 and Ta_2O_5 films," Opt. Mater. Express **6**, 3622 (2016).

[30] J.-K. Yang, W. S. Kim and H.-H. Park, "Chemical bonding states and energy band gap of SiO_2-incorporated La_2O_3 films on n-GaAs (001)," Thin Solid Films **494**, 311 (2006).

[31] M. L. Huang, Y. C. Chang, C. H. Chang, T. D. Lin, J. Kwo, T. B. Wu and M. Hong, "Energy-band parameters of atomic-layer-deposition Al_2O_3 / InGaAs heterostructure," Appl. Phys. Lett. **89**, 012903 (2006).

[32] E. R. Zakirov, V. G. Kesler, G. Y. Sidorov, I. P. Prosvirin, A. K. Gutakovsky and V. I. Vdovin, "XPS investigation of the ALD Al_2O_3/HgCdTe heterointerface," Semicond. Sci. Technol. **34**, 065007 (2019).

[33] A. S. Ferlauto, G. M. Ferreira, J. M. Pearce, C. R. Wronski, R. W. Collins, X. Deng and G. Ganguly, "Analytical model for the optical functions of amorphous semiconductors from the near-infrared to ultraviolet: Applications in thin film photovoltaics," J. Appl. Phys. **92**, 2424 (2002).

[34] G. E. Jellison and F. A. Modine, "Erratum: ‘‘Parameterization of the optical functions of amorphous materials in the interband region’’ [Appl. Phys. Lett. 69, 371 (1996)]," Appl. Phys. Lett. **69**, 2137 (1996).

[35] M. T. Aguilar-Gama, E. Ramírez-Morales, Z. Montiel-González, A. Mendoza-Galván, M. Sotelo-Lerma, P. K. Nair and H. Hu, "Structure and refractive index of thin alumina films grown by atomic layer deposition," Journal of Materials Science: Materials in Electronics **26**, 5546 (2015).

[36] W. R. Hunter, "Measurement of optical properties of materials in the vacuum ultraviolet spectral region," Appl. Opt. **21**, 2103 (1982).

[37] S. J. Byrnes, "Multilayer optical calculations," arXiv:1603.02720 (2016).

[38] M. Vidal-Dasilva, A. L. Aquila, E. M. Gullikson, F. Salmassi and J. I. Larruquert, "Optical constants of magnetron-sputtered magnesium films in the 25-1300 eV energy range," J. Appl. Phys. **108**, (2010).

[39] J. Barth, R. L. Johnson and M. Cardona, "*Spectroscopic Ellipsometry in the 6–35 eV Region*," in Handbook of Optical Constants of Solids, pp. 213 (Elsevier, 1997).

[40] "Lambda 650/850/950 Hardware Guide." https://cmdis.rpi.edu/sites/default/files/UVVis-PerkinElmer-Lambda950-HardwareGuide.pdf (accessed 4/2/2021)

[41] W. Neumann, "*Spectrometer Concepts*," in Fundamentals of dispersive optical spectroscopy systems, Ch. 2, pp. 13, edited by W. Neumann (SPIE—The International Society for Optical Engineering, 2014).

[42] J. A. Samson and David L. EDERER, *Vacuum Ultraviolet Spectroscopy*. (Academic Press, 1998).

[43] U. Finkenzeller and D. Labs, "Deuterium lamp as a UV continuum source from 160 nm to 320 nm for space applications," Appl. Opt. **18**, 3938 (1979).

[44] T. Namioka, "Theory of the Concave Grating. III. Seya-Namioka Monochromator," J. Opt. Soc. Am. **49**, 951 (1959).

[45] W. Zheng, L. Jia and F. Huang, "Vacuum-Ultraviolet Photon Detections," iScience **23**, 101145 (2020).

[46] "VUV system: Detector." Horiba Ltd. https://www.horiba.com/gbr/technology/measurement-and-control-techniques/spectroscopy/vacuum-ultra-violet-spectroscopy/vuv-system-detector/ (accessed)

[47] L. Jia, W. Zheng and F. Huang, "Vacuum-ultraviolet photodetectors," PhotoniX **1**, (2020).

[48] "Si Photodiodes Selection Guide - April 2020." Hamamatsu Photonics K.K. https://www.hamamatsu.com/resources/pdf/ssd/si_pd_kspd0001e.pdf (accessed)

[49] M. Richter, U. Kroth, A. Gottwald, C. Gerth, K. Tiedtke, T. Saito, I. Tassy and K. Vogler, "Metrology of pulsed radiation for 157-nm lithography," Appl. Opt. **41**, 7167 (2002).

[50] "Photomultiplier Tube." Wikipedia. https://en.wikipedia.org/wiki/Photomultiplier_tube (accessed)

[51] "Charge-coupled device." Wikipedia. https://en.wikipedia.org/wiki/Charge-coupled_device (accessed)

[52] "What is a CCD Detector?" Horiba Ltd. https://www.horiba.com/en_en/technology/measurement-and-control-techniques/spectroscopy/detectors/what-is-a-ccd-detector/ (accessed)

[53] "Windowless, back illuminated CCD." McPherson Inc. https://mcphersoninc.com/detectors/directDetectionCCD.html (accessed)

[54] Y. Ozaki, Y. Saito and S. Kawata, "*Introduction to FUV and DUV Spectroscopy*," in Far and Deep Ultraviolet Spectroscopy, Ch. 1, pp. 1, edited by Y. Ozaki and S. Kawata (Springer 2015).

[55] C. Tarrio and S. E. Schnatterly, "Interband transitions, plasmons, and dispersion in hexagonal boron nitride," Physical Review B **40**, 7852 (1989).

[56] E. T. Arakawa and M. W. Williams, "Optical properties of aluminum oxide in the vacuum ultraviolet," J. Phys. Chem. Solids **29**, 735 (1968).

[57] H. A. Macleod, "Thin-Film Optical Filters."

[58] H. A. Macleod, "*Multilayer high-reflectance coatings*," in Thin-Film Optical Filters, Ch. 6, edited by E. R. Pike and R. G. W. Brown (CRC Press, Boca Raton, 2018).

[59] "Reflectance." Wikipedia. https://en.wikipedia.org/wiki/Reflectance (accessed)

[60] H. A. MacEwen, J. B. Breckinridge, K. Balasubramanian, J. Hennessy, N. Raouf, S. Nikzad, M. Ayala, S. Shaklan, P. Scowen, J. Del Hoyo and M. Quijada, in *UV/Optical/IR Space Telescopes and Instruments: Innovative Technologies and Concepts VII* (2015).

[61] J. Sun, X. Li, W. L. Zhang, K. Yi and J. D. Shao, "High-reflectivity mirrors by Al_2O_3, LaF_3 and AlF_3 for 193 nm application," Opt. Laser Technol. **56**, 65 (2014).

[62] S. Gunster, D. Ristau, A. Gatto, N. Kaiser, M. Trovo and M. Danailov, "Storage ring free-electron lasing at 176 nm-dielectric mirror development for vacuum ultraviolet free-electron lasers," Appl. Opt. **45**, 5866 (2006).

[63] V. S. P. Kumar, M. Kumar, N. Kumari, V. Karar and A. L. Sharma, "Fabrication of Al_2O_3/SiO_2 multilayer reflective filters with excellent uniformity for demanding optical interference filters," Mater. Res. Express **6**, 066410 (2019).

[64] P. Torchio, A. Gatto, M. Alvisi, G. Albrand, N. Kaiser and C. Amra, "High-reflectivity HfO_2/SiO_2 ultraviolet mirrors," Appl. Opt. **41**, 3256 (2002).

[65] L. Yuan, Y. N. Zhao, C. J. Wang, H. B. He, Z. X. Fan and J. D. Shao, "Effect of SiO_2 protective layer on the femtosecond laser-induced damage of HfO_2/SiO_2 multilayer high-reflective coatings," Appl. Surf. Sci. **253**, 3450 (2007).

[66] F. Réveret, L. Bignet, W. Zhigang, X. Lafosse, G. Patriarche, P. Disseix, F. Médard, M. Mihailovic, J. Leymarie, J. Zúñiga-Pérez and S. Bouchoule, "High reflectance dielectric distributed Bragg reflectors for near ultra-violet planar microcavities: SiO_2/HfO_2 versus SiO_2/SiNx," J. Appl. Phys. **120**, 093107 (2016).

[67] S. F. Pellicori, C. L. Martinez, P. Hausgen and D. Wilt, "Development and testing of coatings for orbital space radiation environments," Appl. Opt. **53**, A339 (2014).

[68] M. Zukic, D. G. Torr, J. F. Spann and M. R. Torr, "Vacuum ultraviolet thin-films. 2: Vacuum ultraviolet all-dielectric narrowband filters," Appl. Opt. **29**, 4293 (1990).

[69] X. D. Wang, B. Chen and L. Yao, "Design and fabrication of Far-ultraviolet reflective broadband filter based on dielectric materials," Appl. Spectrosc. **72**, 943 (2018).

[70] M. C. Liu, C. C. Lee, B. H. Liao, M. Kaneko, K. Nakahira and Y. Takano, "Fluoride antireflection coatings deposited at 193 nm," Appl. Opt. **47**, C214 (2008).

[71] R. Thielsch, "*Optical Coatings for the DUV/VUV*," in Optical Interference Coatings, pp. 257, edited by N. Kaiser and H. K. Pulker (Springer, 2003).

[72] H. K. Raut, V. A. Ganesh, A. S. Nair and S. Ramakrishna, "Anti-reflective coatings: A critical, in-depth review," Energy Environ. Sci. **4**, 3779 (2011).

[73] M. Keshavarz Hedayati and M. Elbahri, "Antireflective Coatings: Conventional Stacking Layers and Ultrathin Plasmonic Metasurfaces, A Mini-Review," Materials **9**, 497 (2016).

[74] M. H. Yang, A. Gatto and N. Kaiser, "Design and deposition of vacuum-ultraviolet narrow-bandpass filters for analytical chemistry applications," Appl. Opt. **45**, 1359 (2006).

CHAPTER 3

EXPERIMENTAL AND THEORETICAL METHODS

In this chapter, we introduce the experimental and theoretical methods used for the design, fabrication, and characterization of the optical coatings. We start from a brief description of atomic layer deposition, which is used for the thin film optical coating depositions. Then, we describe the techniques used for characterizing the optical coatings, including far UV spectroscopy, spectroscopic ellipsometry (SE), atomic force microscopy (AFM), and X-ray photoelectron spectroscopy (XPS). Finally, we will describe the commonly used theoretical methods for the optical simulations, and optical constants calculations from the reflectance measurements.

3.1 Atomic Layer Deposition

Atomic layer deposition is a deposition method which allows atomic layer control and conformal growth.[1] ALD uses sequential pulsing of the precursors, with inert gas purge between each pulse cycle, to ensure self-limiting growth, as shown in Fig. 3.1. For plasma enhanced ALD, radical species generated from the plasma are used as the co-reactant. For a detailed description of ALD, please see review articles.[1-4]

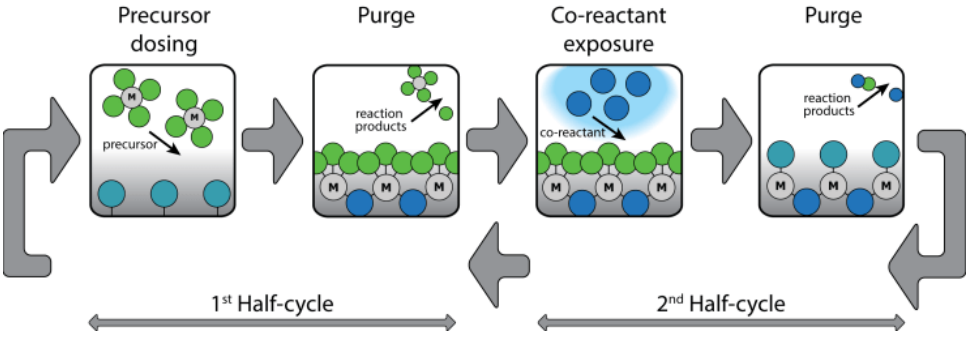

Figure 3.1. Self-limiting growth mechanism for ALD. Copyright © 2019, Atomic Limits.[5]

At lower wavelengths, surface roughness becomes increasingly important as surface scattering can significantly degrade the optical performance of the designed coating.[6] Even though ultra-smooth surfaces ($R_q \approx 0.2\text{nm}$) have been achieved using techniques such as sputtering, incorporation of un-wanted impurities may occur.[7] However, the self-limiting growth mechanism for ALD allows for minimal build-up of roughness for amorphous oxide films.[8] The smooth surface and precise thickness control benefits thin-film coating design, fabrication, and characterization. As discrete precursor exposures are used in ALD to obtain self-limiting surface reactions, longer deposition times are to be expected in comparison to other growth methods.[2, 4]

In this research, a custom-built PEALD, Fig. 3.2, was used for the deposition of AlF_3, with Trimethylaluminum (TMA) and HF-pyridine as the precursors. The Ga_2O_3 was grown in a similar custom-built chamber with Trimethylgallium (TMG) and O_2 plasma as precursors, with a substrate temperature of 150 °C. For the Al_2O_3, and HfO_2, a commercial tool (Cambridge, Savannah S100) with TMA, Tetrakis(dimethylamino)hafnium (TDAHF) and H_2O, as precursors, and a substrate temperature of 185 °C, and 200 °C, respectively.

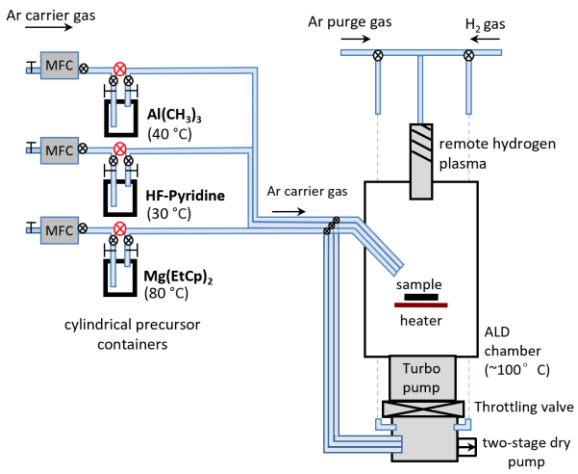

Figure 3.2. Custom-built PEALD system for metal fluorides deposition. [1] Courtesy of Daniel C. Messina in Nanoscience Laboratory, ASU.

3.2 Far UV Spectroscopy

A custom-built vacuum UV spectrometer, that operates at 2×10^{-7} Torr, was used for *in-situ* characterization of the optical properties spanning 120 – 300 nm. The UV spectrometer, described in Chapter 4 of this Dissertation, has three primary components: UV light source, monochromator, and detector. The light source used is a water-cooled deuterium lamp (Hamamatsu Photonics, L1835) with a MgF_2 window. In this research, this spectrometer was used to measure the reflectance at variable incident angles (33° and 75°). A single crystal Si wafer was used as a calibration standard to calibrate the measured reflectance curves. For details on the instrumentation and operation of this system, please refer the Chapter 4.

[1] Metal fluorides PEALD system was built by Daniel C. Messina in NSL lab.

3.3 Spectroscopic Ellipsometry

Spectroscopic ellipsometry (SE) uses polarized light to measure the optical constants (n, k) and thickness of materials. The complex reflectance ratio, ρ, of the mutually perpendicular components of the light beam (s-, and p-waves) can be measured by ellipsometry, and is defined as $\rho = \frac{R_p}{R_s} = \tan\Psi\, e^{i\Delta}$, where Ψ (Psi) and Δ (Delta) are related to the change in amplitude, and phase shift, respectively.[9] The ellipsometer (J. A. Woollam, M-2000DI) allows for use of wavelengths ranging from 193.7 nm to 1689.4 nm with incident angles spanning 45°-85°. Multiple incident angles, around a substrates' Brewster angle, are used for more accurate measurements. An ellipsometry software package (J. A. Woollam, CompleteEASE v6.51) was used to analyze Ψ and Δ, for the determination of thickness, and optical constants. Cauchy and B-Spline dispersion models were applied for transparent and absorbing films, respectively. The root mean square error (MSE) was used to quantify the "goodness of fit" where an RMSE of 1 indicates an ideal fit.[10]

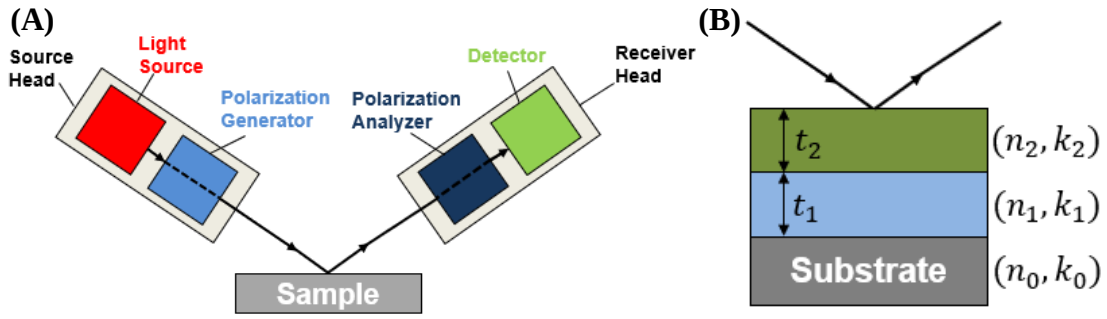

Figure 3.3. Spectroscopic ellipsometry. (A) Instrumental set-up for standard ellipsometer. Image reproduced from N. Hong.[11] Copyright © 2014, J.A. Woollam Co., Inc. (B) Data analysis allows for the measurements of optical constants and thickness of each layer.

3.4 Atomic Force Microscopy

AFM consists of a cantilever with a sharp tip at its end that is used to scan the sample surface. The cantilever used is n-type Si (AppNano, ACT-200) with a tip radius less than 10 nm. When the tip is brought into proximity of a sample surface, forces between the tip and the sample lead to a deflection of the cantilever. The back of the cantilever is illuminated with the laser light, and the reflection is observed on a position-sensitive detector, Fig. 3.4.[12] Alternating contact mode was used in this research, and the scans were taken over a 5 µm × 5 µm area with a scan rate of 0.5 Hz and 1024 points and lines. The root mean square (rms) roughness, R_q, is defined by $R_q = \sqrt{\frac{1}{n}\sum_{i=1}^{n} y_i^2}$, where n is the total number of points and y_i is the height of the *i*-th point.

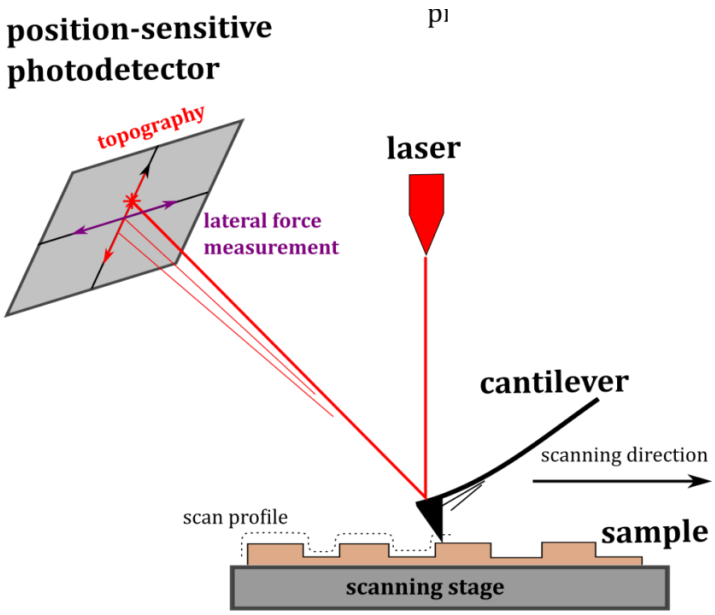

Figure 3.4. Principles of Atomic Force Microscopy. Copyright © 2021, MAX IV Laboratory.[12]

3.5 X-ray Photoelectron Spectroscopy

X-ray photoelectron spectroscopy (XPS) is a surface-sensitive quantitative spectroscopic technique based on the photoelectric effect that can identify and determine the surface film composition, bonding states, defect configurations, and band gap. The XPS instrument (VG Scientia, R3000) uses a monochromatic Al K_α source with a photon energy of 1482.35 eV. Data acquisition was performed using the manufacturer supplied software (VG Scientia, SES Software). The system pressure was below 7×10^{-10} Torr during measurements. Peak analysis was performed using an XPS software package (Casa Software LTD, CasaXPS). The photoelectron transitions can be modeled with Gaussian-Lorentzian line shapes with Tougaard backgrounds.[13] Relative atomic concentrations were calculated using a standard method based on the ratio of peak areas and atomic sensitivity factors.[14] Fig. 3.5 shows the basic operation principle for XPS. [15]

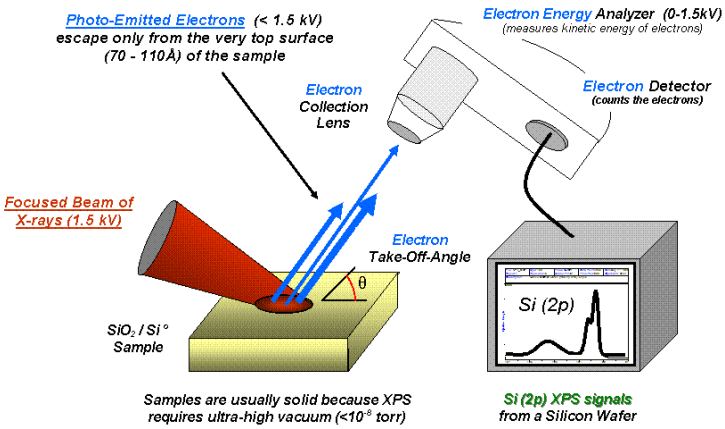

Figure 3.5. Principles of X-ray Photoelectron Spectroscopy.

Copyright © Public Domain.[15]

3.6 Transfer-Matrix Method

The optical properties of a multilayer thin-film optical coating can be calculated using the transfer-matrix method (TMM).[16, 17] For multilayer structures with isotropic and homogeneous properties, TMMs use a product of matrices to represent the superposition of the complex reflection and transmission Fresnel coefficients. For a two-layer structure with a single interface, the Fresnel coefficients can be represented by equations shown in Fig. 3.6b. The reflected and transmitted intensity can be calculated by, $R = |r|^2$, and $T = \frac{n_2 \cos\theta_2}{n_1 \cos\theta_1}|t|^2$, respectively.[18]

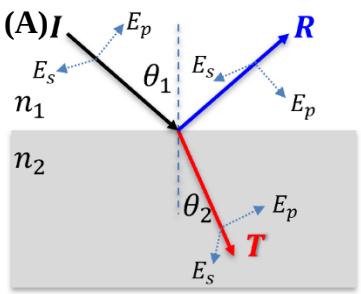

(B)

s-polarized light

$$r_{1,2_\perp} = \frac{n_1 \cos\theta_1 - n_2 \cos\theta_2}{n_1 \cos\theta_1 + n_2 \cos\theta_2}$$

$$t_{1,2_\perp} = \frac{2n_1 \cos\theta_1}{n_1 \cos\theta_1 + n_2 \cos\theta_2}$$

***p*-polarized light**

$$r_{1,2_\parallel} = \frac{n_2 \cos\theta_1 - n_1 \cos\theta_2}{n_2 \cos\theta_1 + n_1 \cos\theta_2}$$

$$t_{1,2_\parallel} = \frac{2n_1 \cos\theta_1}{n_2 \cos\theta_1 + n_1 \cos\theta_2}$$

Figure 3.6. Single interface reflection and transmission. (A) Illustration diagram, (B) Fresnel coefficients for *s*, and *p*-polarized light.

As for a multilayer structure, shown in Fig. 3.7a, multiple reflections and refractions occur at the interfaces, which introduces more complexities for the calculation of the Fresnel coefficients. The transfer-matrix method, by considering the superposition of Fresnel coefficients at each interface, can be used to simplify the multilayer optical calculation, shown in Fig. 3.7b. For example, at the interface between Layer 1 (with refractive index $\tilde{n}_1$) and 2, the Fresnel coefficients have the relationships shown in Eq. (3.1) and (3.2).[18]

$$v_2 = v_1 t_{1,2} e^{i\delta_1} + w_2 r_{2,1} \tag{3.1}$$

$$w_1 = w_2 t_{2,1} e^{i\delta_1} + v_1 r_{1,2} \tag{3.2}$$

Here $\delta_1 = \frac{2\pi}{\lambda}\tilde{n}_1 d_1 \cos\theta_1$, is the phase change by traveling Layer 1. $\tilde{n} = n + ik$ is the complex refractive index for absorbing materials. Written in a matrix form, Eq. (3.1) and (3.2) become,

$$\begin{pmatrix} v_1 \\ w_1 \end{pmatrix} = \frac{1}{t_{1,2}} \begin{pmatrix} e^{-i\delta_1} & e^{-i\delta_1} r_{1,2} \\ e^{i\delta_1} r_{1,2} & e^{i\delta_1} \end{pmatrix} \begin{pmatrix} v_2 \\ w_2 \end{pmatrix} \tag{3.3}$$

Here, we define $M_{1,2} = \frac{1}{t_{1,2}} \begin{pmatrix} e^{-i\delta_1} & e^{-i\delta_1} r_{1,2} \\ e^{i\delta_1} r_{1,2} & e^{i\delta_1} \end{pmatrix}$ as the transfer matrix between Layer 1 and 2.

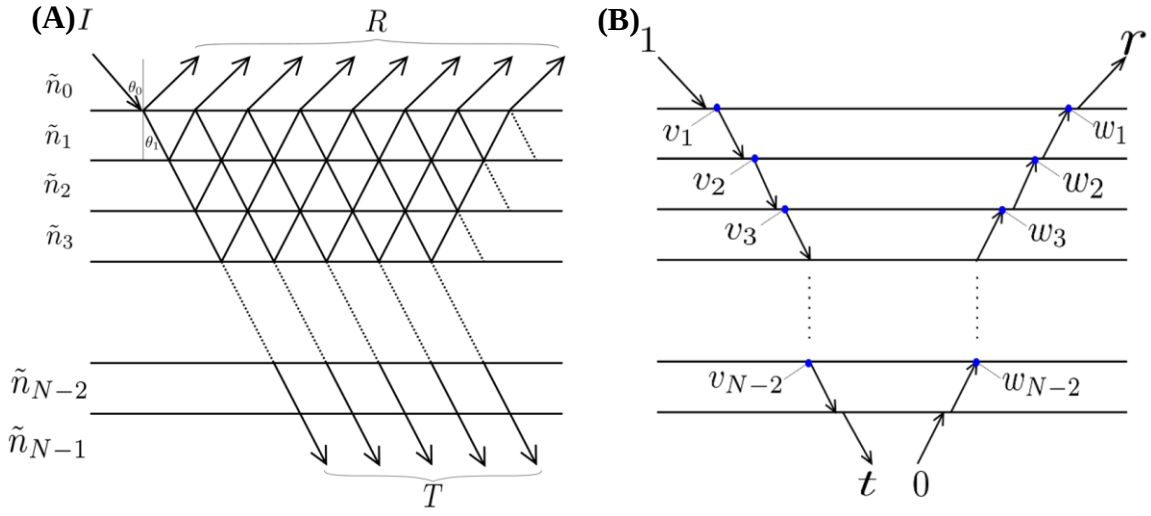

Figure 3.7. Multilayer reflection and transmission. (A) Illustration diagram, (B) Simplified model for transfer-matrix method.

By multiplying the transfer matrices, the final Fresnel coefficients r, and t, can be described by Eq. (3.4).

$$\begin{pmatrix} 1 \\ r \end{pmatrix} = \tilde{M} \begin{pmatrix} t \\ 0 \end{pmatrix} \tag{3.4}$$

Here, $\widetilde{M} := M_{0,1}M_{1,2}M_{2,3}\cdots M_{N-2,N-1}$, with $M_{n,n+1}$ described by Eq. (3.5),[18]

$$M_{n,n+1} = \frac{1}{t_{n,n+1}}\begin{pmatrix} e^{-i\delta_n} & e^{-i\delta_n}r_{n,n+1} \\ e^{i\delta_n}r_{n,n+1} & e^{i\delta_n} \end{pmatrix} \tag{3.5}$$

The Fresnel coefficients can be calculated from the transfer matrix of the entire system, $\widetilde{M}$, by Eq. (3.6). Thus, the reflection intensity, R, and transmission intensity, T, can be calculated accordingly.[18]

$$r = \frac{\widetilde{M}_{10}}{\widetilde{M}_{00}} \qquad t = \frac{1}{\widetilde{M}_{00}} \tag{3.6}$$

3.7 Optical Constants Calculation Methods

Determination of the optical constants from ellipsometry and reflectivity is a reverse engineering problem. Data analysis for the ellipsometry and reflection measurements is needed to extract the optical constants. In this research, we used two different approaches. The first approach is based on the iso-reflectivity curve, which requires no prerequisite information except the thickness of the material in interest.[19, 20] The second approach is based on optical dispersion model, which significantly reduces the parameters used for the curve fitting and minimizes the noise from the experimental data.[10]

3.7.1 Iso-Reflectivity Curve Method

The iso-reflectance curve method has been introduced in Chapter 2. To use this method, the (n, k) of all layers except the unknown layer should be known, Fig. 3.8. Besides, the thickness of each layer (including the unknown layer) should also be known. Thus, there are only two unknowns need to be solved, i.e., n, and k.

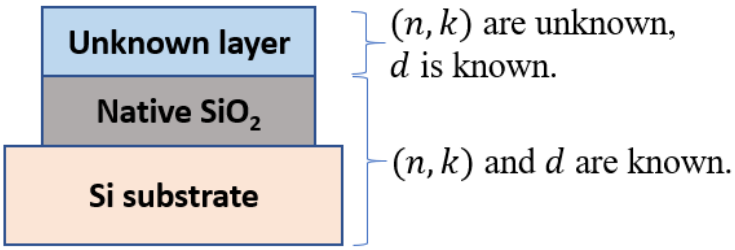

Figure 3.8. Well-defined structure with only (n, k) of the top layer unknown.

For a detailed explanation of this method, we will use Ga_2O_3 films grown on Si substrate as an example, but it also applies for other materials. The Ga_2O_3 film has a thickness of 19.42 nm, on the substrate of 2.65 nm SiO_2/Si. The (n, k) of SiO_2 and Si are known. For this structure, if the measured reflectivity is 15.47% at a wavelength of 130.5 nm and incident angle 33°, the solutions for (n, k) are not unique. Instead, the locus of all possible (n, k) values form an iso-reflective curve, as shown in Fig. 3.9. Figure 3.9a is the simulated reflectance assuming the (n, k) of the unknown layer ranges from (0, 10). Figure 3.9b is the iso-reflectance curve where the reflectance equals the experimental value 15.47%.

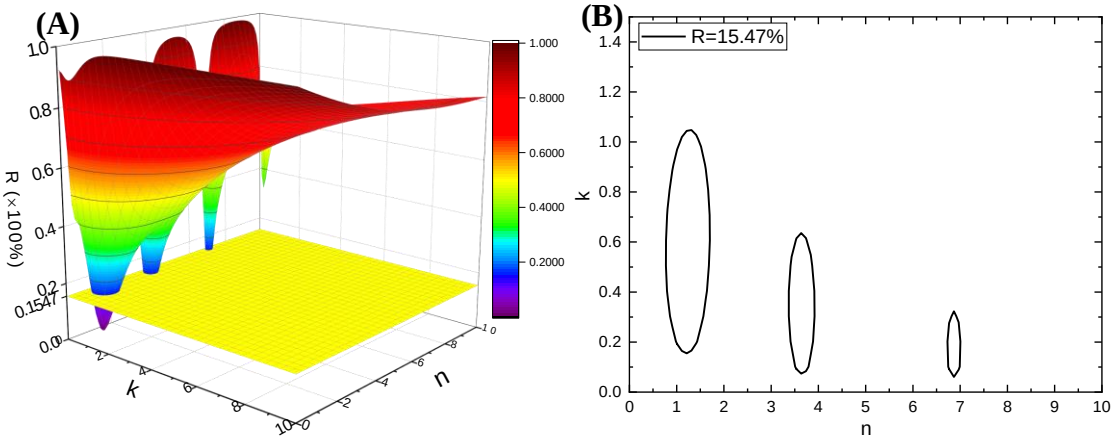

Figure 3.9. Iso-reflectivity curve method. (A) 3D drawing of the simulated reflectivity vs (n, k) from (0, 10), (B) Intersection between simulated and experimental curves forms the "iso-reflectivity" curve.

As it is shown in Fig. 3.9, one single reflectivity measurement is not adequate to uniquely determine both n and k. This can be explained by the Fresnel equations, where at each wavelength, the reflectivity is a function of (n, k), thickness d, incident angles θ, and polarization P, as written in Eq. (3.7).

$$R(\lambda) = R(n(\lambda), k(\lambda), d, \theta, P) \quad \text{(Eq. 3.7)}$$

Figure 3.9 and Equation 3.7 show that, at least two independent reflectivity measurements are needed to uniquely determine both n and k. In this research, we carried out measurements at two different incident angles θ, and on the same material with two different thicknesses d.

3.7.1.1 Reflectance vs Two Thicknesses

Measurements for two Ga_2O_3 films have been made at the same incident angle 33°. The thicknesses of Ga_2O_3 are 11.42 nm and 19.42 nm. The resultant iso-reflectivity curves are shown in Fig. 10a, at the wavelength of $\lambda = 130.5$ nm. There are two intersection points, (1.164, 1.033) and (1.461, 0.223), which corresponds to two possible (n, k) for Ga_2O_3. From the knowledge of the optical properties of Ga_2O_3 at Far UV, only one of the solutions, (1.164, 1.033), has more physical meaning, and is the unique solution of (n, k) for Ga_2O_3 at $\lambda = 130.5$ nm.

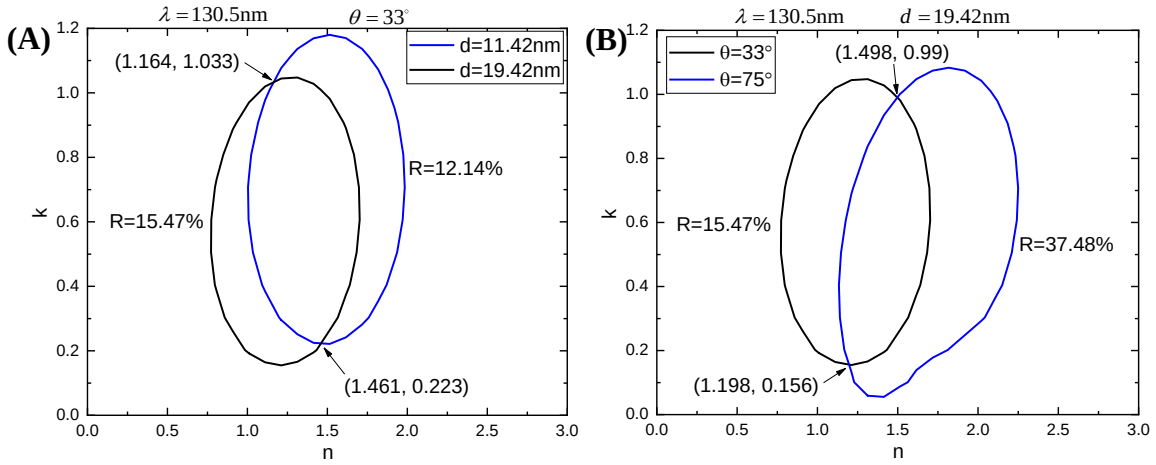

Figure 3.10. Iso-reflectance curve methods with two independent measurements. (A) Measurements on the same materials with two different thicknesses, (B) Measurements on the same sample at two different angles. Intersection points are the possible solutions of (n, k).

3.7.1.2 Reflectance vs Two Incident Angles

For each sample, measurements can be done at two different angles, 33° and 75°. Figure 3.10b shows an example for the iso-reflectivity curve of Ga_2O_3 with $d = 19.42$ nm measured at two angles. Similar to the first method, two intersection points can be achieved, but only one of them, (1.498, 0.99), is the unique solution of (n, k) for Ga_2O_3 at $\lambda =$ 130.5 nm.

3.7.2 Optical Dispersion Model Method

Besides iso-reflectivity curve methods, optical dispersion models have also been applied in the data analysis. Dispersion models consider wavelength-dependent characteristics of the $\tilde{n}$, and use analytical mathematical formulas derived from empirical or theoretical models. The advantage of this method is it maintains the consistence of the

(n, k) between adjacent points, and can guarantee the Kramers–Kronig constraint depending on the models used.[6] The commonly used dispersion models include Cauchy, Sellmeier, Lorentz, Drude, and so on.[10] The detailed descriptions of the Cauchy model and modified Lorentz models can be found in Chapter 2.

In this research, we developed an algorithm based on the dispersion equations to fit the measured reflectance and ellipsometry curves. The Levenberg–Marquardt least-square algorithm is used to find the solutions by minimizing the root-mean-square-error (RMSE).[10] Depending on the optical properties of the materials, we applied Cauchy model to ultrawide bandgap material AlF_3, and modified Lorentz models to HfO_2, Al_2O_3, Ga_2O_3, and SiO_2, to describe the inter-band transitions in the far UV wavelength range.

3.8 Effective Medium Approximation

For the material mixtures, the effective optical constants can be estimated with the effective medium approximation method. Figure 3.11 shows possible versions of the mixtures of two or more materials.[21] If we know the volume concentration p_j of the *j*-th constituent in the mixtures, the effective dielectric constant has the form,[21]

$$\frac{\varepsilon_{eff}-\varepsilon_h}{\varepsilon_h+(\varepsilon_{eff}-\varepsilon_h)L} = \sum_j p_j \frac{\varepsilon_j-\varepsilon_h}{\varepsilon_h+(\varepsilon_j-\varepsilon_h)L} \quad \text{(Eq. 3.8)}$$

Here, L is the depolarization factor, which depends on the morphology of the mixtures. ε_h is the dielectric function of the host materials, and ε_{eff} represents the effective dielectric constant.

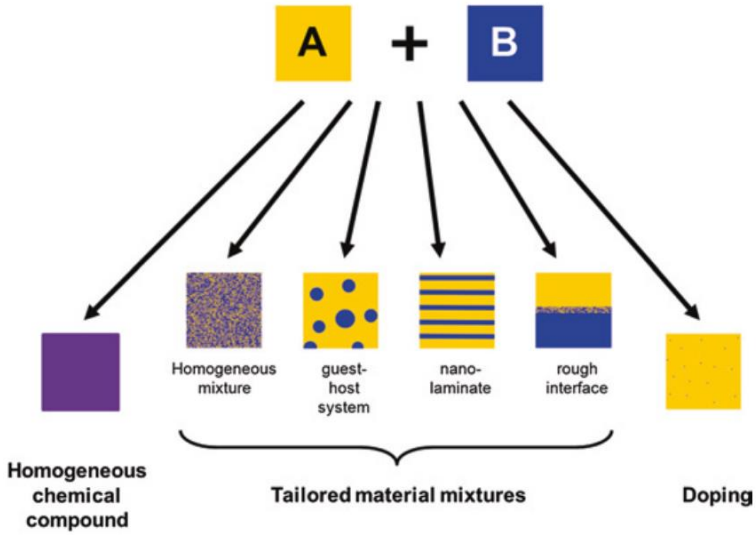

Figure 3.11. Possible versions of mixing materials A and B. Copyright © 2014, Springer-Verlag Berlin Heidelberg. [21]

Depending on the possible versions of the material mixtures, different approaches have been developed. The commonly used methods include Maxwell-Garnett and Bruggeman methods.

3.8.1 Maxwell-Garnett Method

In M-G approach, one of the constituents is considered as the host material, as the "guest-host" mixture shown in Fig. 3.11. The effective dielectric constant calculated in Eq. (3.8) is simplified as Eq. (3.9) shown below,[21]

$$\frac{\varepsilon_{eff}-\varepsilon_l}{\varepsilon_l+(\varepsilon_{eff}-\varepsilon_l)L} = \sum_{j\neq l} p_j \frac{\varepsilon_j-\varepsilon_l}{\varepsilon_l+(\varepsilon_j-\varepsilon_l)L} \qquad \text{(Eq. 3.9)}$$

In the special case for two materials, Eq. (3.9) simplifies as shown in Eq. (3.10). Here h and g represent "host" and "guest" materials, respectively.

$$\frac{\varepsilon_{eff}-\varepsilon_h}{\varepsilon_h+(\varepsilon_{eff}-\varepsilon_h)L} = p_g \frac{\varepsilon_g-\varepsilon_h}{\varepsilon_h+(\varepsilon_g-\varepsilon_h)L} \qquad \text{(Eq. 3.10)}$$

3.8.2 Bruggeman Method

The Bruggeman method assumes the mixture itself is the host medium for the inclusions, as the "homogeneous mixture" case in the Fig. 3.11. This leads to the following mixing formula,[21]

$$0 = \sum_j p_j \frac{\varepsilon_j - \varepsilon_{eff}}{\varepsilon_{eff} + (\varepsilon_j - \varepsilon_{eff})L} \quad \text{(Eq. 3.11)}$$

In this study, the Bruggeman EMA was used for the characterization of material mixtures, especially for the AlF_3/Al mixtures grown by PEALD, and h-BN/c-BN mixtures grown by ECR-PECVD.

References

[1] S. M. George, "Atomic layer deposition: an overview," Chem. Rev. **110**, 111 (2010).

[2] P. O. Oviroh, R. Akbarzadeh, D. Pan, R. A. M. Coetzee and T.-C. Jen, "New development of atomic layer deposition: processes, methods and applications," Sci. Technol. Adv. Mater. **20**, 465 (2019).

[3] P. French, G. Krijnen and F. Roozeboom, "Precision in harsh environments," Microsyst. Nanoeng. **2**, 16048 (2016).

[4] S. Zhuiykov, T. Kawaguchi, Z. Hai, M. Karbalaei Akbari and P. M. Heynderickx, "Interfacial engineering of two-dimensional nano-structured materials by atomic layer deposition," Appl. Surf. Sci. **392**, 231 (2017).

[5] M.F.J. Vos, A. J. M. Mackus and W. M. M. Kessels. "Atomic Layer Deposition Process Development – 10 steps to successfully develop, optimize and characterize ALD recipes." Atomic Limits. https://www.atomiclimits.com/2019/02/12/atomic-layer-deposition-process-development-10-steps-to-successfully-develop-optimize-and-characterize-ald-recipes/ (accessed)

[6] J. I. Larruquert, "*Optical properties of thin film materials at short wavelengths*," in Optical Thin Films and Coatings, Ch. 7, edited by A. Piegari and F. Flory (Woodhead Publishing, 2018).

[7] C. Q. Hu, J. Z. Cai, Y. K. Li, C. B. Bi, Z. Q. Gu, J. Q. Zhu, J. F. Zang and W. T. Zheng, "In situ growth of ultra-smooth or super-rough thin films by suppression of vertical or horizontal growth of surface mounds," J. Mater. Chem. C **8**, 3248 (2020).

[8] P. A. Premkumar, A. Delabie, L. N. J. Rodriguez, A. Moussa and C. Adelmann, "Roughness evolution during the atomic layer deposition of metal oxides," J. Vac. Sci. Technol., A **31**, 061501 (2013).

[9] H. Fujiwara, "*Principles of Ellipsometry*," in Spectroscopic Ellipsometry for Photovoltaics, Vol. 1, Ch. 1.1.1, edited by H. Fujiwara and R. W. Collins (Springer International Publishing AG, Cham, Switzerland, 2018).

[10] J. A. W. Co., "*"Goodness" of Fit: definition of the MSE*," in CompleteEASE Software Manual, Ch. 3.1 (J.A. Woollam Co., Lincoln, NE, 2014).

[11] N. Hong. "1A: Introduction to WVASE Data Analysis." J. A. Woollam Co., Inc. https://www.seas.upenn.edu/~nanosop/documents/Session1A_UPenn_WVASE_Feb_2014.pdf (accessed)

[12] "AFM scanning modes." MAX IV Laboratory. https://www.maxiv.lu.se/accelerators-beamlines/support-labs-microscopy/atomic-force-microscopy/afm-scanning-modes/ (accessed)

[13] S. Tougaard, "Universality Classes of Inelastic Electron Scattering Cross‐sections " Surf. Interface Anal. **25**, 137 (1997).

[14] J. F. Moulder, W. F. Stickle, P. E. Sobol and K. D. Bomben, "*Handbook of X-ray Photoelectron Spectroscopy*," Ch. 1, pp. 25 (Perkin-Elmer Corporation, Eden Prairie, Minnesota, USA 1979).

[15] L. C. d. Carvalho. "X-ray photoelectron spectroscopy - Basic components of a monochromatic XPS system." Wikipedia. https://en.wikipedia.org/wiki/X-ray_photoelectron_spectroscopy (accessed)

[16] C. C. Katsidis and D. I. Siapkas, "General transfer-matrix method for optical multilayer systems with coherent, partially coherent, and incoherent interference," Appl. Opt. **41**, 3978 (2002).

[17] B. Harbecke, "Coherent and incoherent reflection and transmission of multilayer structures," Appl. Phys. B **39**, 165 (1986).

[18] S. J. Byrnes, "Multilayer optical calculations," arXiv:1603.02720 (2016).

[19] F. Bridou, M. Cuniot-Ponsard and J.-M. Desvignes, "Experimental determination of optical constants in the vacuum ultra violet wavelength region between 80 and 140nm: A reflectance versus thickness method and its application to ZnSe," Opt. Commun. **271**, 353 (2007).

[20] F. Bridou, M. Cuniot-Ponsard, J.-M. Desvignes, M. Richter, U. Kroth and A. Gottwald, "Experimental determination of optical constants of MgF2 and AlF3 thin films in the vacuum ultra-violet wavelength region (60–124nm), and its application to optical designs," Opt. Commun. **283**, 1351 (2010).

[21] O. Stenzel, "*Basic Knowledge on Optical Constants*," in Optical Coatings Material Aspects in Theory and Practice, Ch. 2, pp. 21, edited by O. Stenzel (Springer 2014).

CHAPTER 4

IN-SITU VARIABLE ANGLE FAR ULTRAVIOLET SPECTROMETER

In this Chapter, the custom-built *in-situ* Far UV spectrometer is described in detail. The basic instrumental set-up, operation procedure, and reflectance calibration are described. The maintenance on the spectrometer, including deuterium lamp windows cleaning, diffraction grating calibration, and vacuum vent/pumping, are not covered in this Chapter, but can be found in the Appendix A. The details of the operation procedures can be found in Appendix B of this Dissertation.

This spectrometer is connected in vacuum with the chambers for thin film growth, Fig. 4.1. Dielectric oxide and fluoride films can be grown using oxide and fluoride ALD. Cubic and hexagonal boron nitride can be grown using ECR-PECVD. The far UV (120 – 200 nm) reflectance can be measured for as-grown films without breaking the vacuum. The in-situ capabilities can significantly reduce the atmospheric contaminations and improve the accuracy for the experimental measurements.

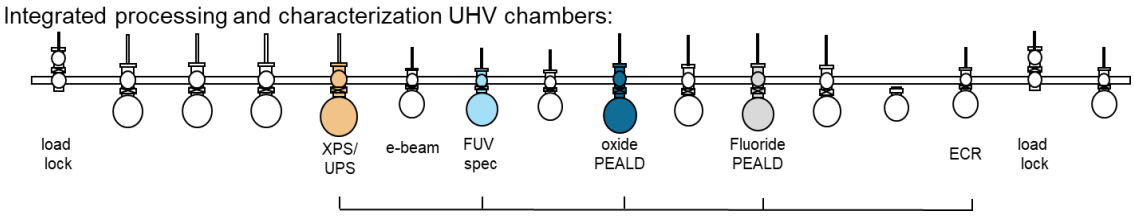

Figure **4.1** In-situ capabilities for the thin film growth and characterization.

XPS (UPS): X-ray (Ultraviolet) Photoelectron Spectroscopy; UPS: Ultraviolet Photoelectron Spectroscopy; FUV Spec: Far UV Spectrometer. PEALD: plasma enhance atomic layer deposition; ECR: Electron Cyclotron Resonance.

4.1 Instrumental Set-up

This *in-situ* variable angle Far UV spectrometer, Fig. 4.2, with a base pressure 4×10^{-7} Torr, was built for characterization of the spectroscopic intensity (reflectivity or transmission), spanning 120 – 300 nm. This system has six primary components: UV light source, reflective condenser, monochromator, toroidal mirror, sample stage, and detector. The details of each component will be described below.

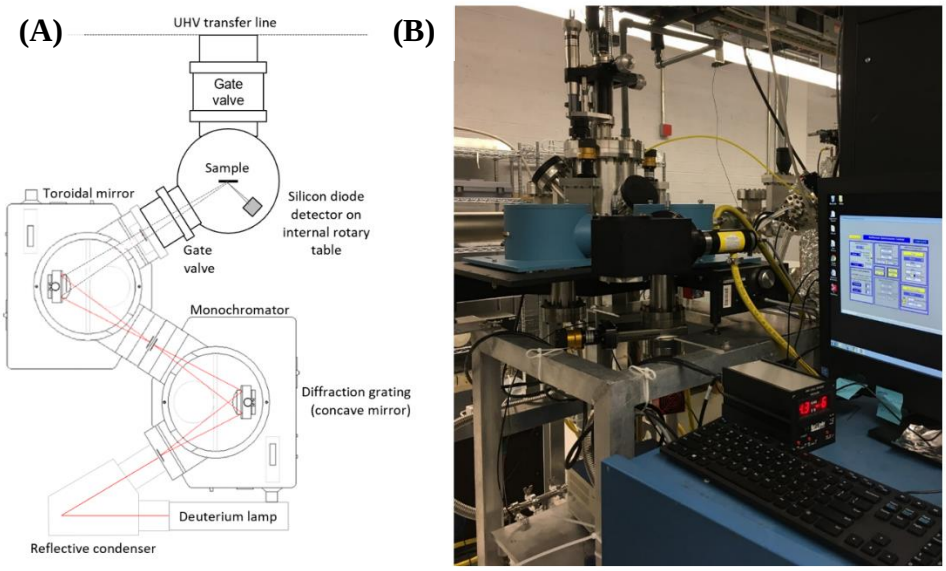

Figure 4.2. Far UV spectrometry. (A) Illustration diagram, (B) Custom-built FUV spectrometer.

4.1.1 UV Light source

The light source used is a water-cooled 150 W Deuterium lamp (Hamamatsu Photonics, L1835) with a MgF_2 window, with spectral distribution from 115 to 400 nm. The aperture size for this lamp is 2.5 mm diameter. A power supply (Hamamatsu Photonics, Model C3150) is used for the operation of the lamp. It takes 20 s of warm-up time before the lamp stabilizes. Figure 4.3 shows the deuterium lamp installed in our

system. The cooling water is used during the operation of the lamp. The water is flowing in from the bottom and out from the top.

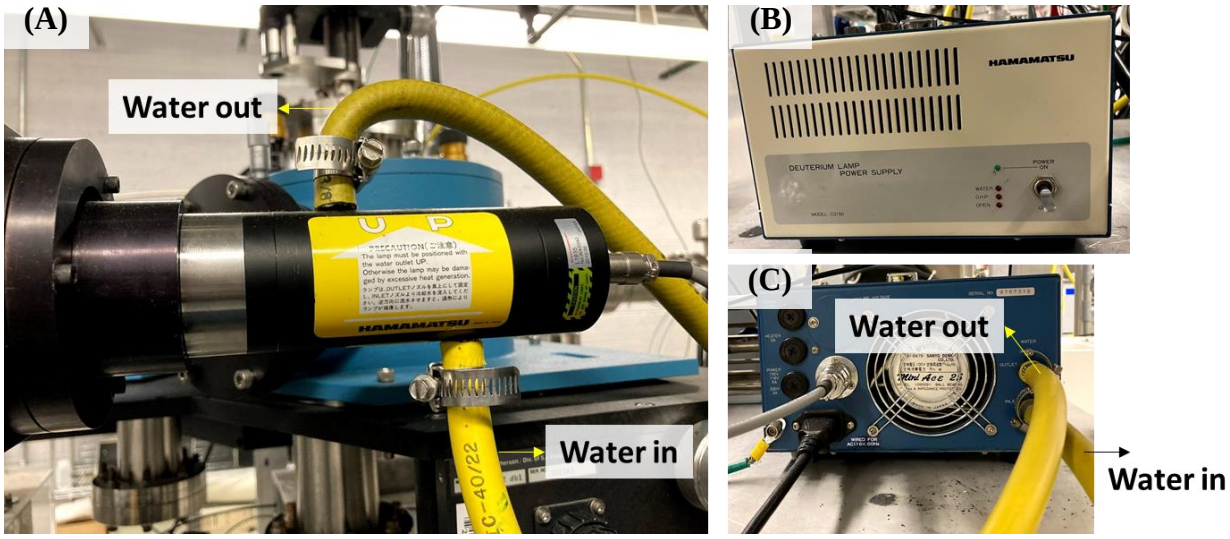

Figure 4.3. Deuterium lamp and water-cooled power supply. (A) Deuterium lamp with MgF_2 window. Power supply, (B) Front and (C) Back side.

The emission spectrum of the deuterium lamp in the UV wavelength is shown in Fig. 4.4. The characteristic peaks (especially the double peaks at 160.8 nm) in the Far UV range were used during the calibration of the diffraction gratings. For the details of the calibration of the grating, please see the Appendix A.

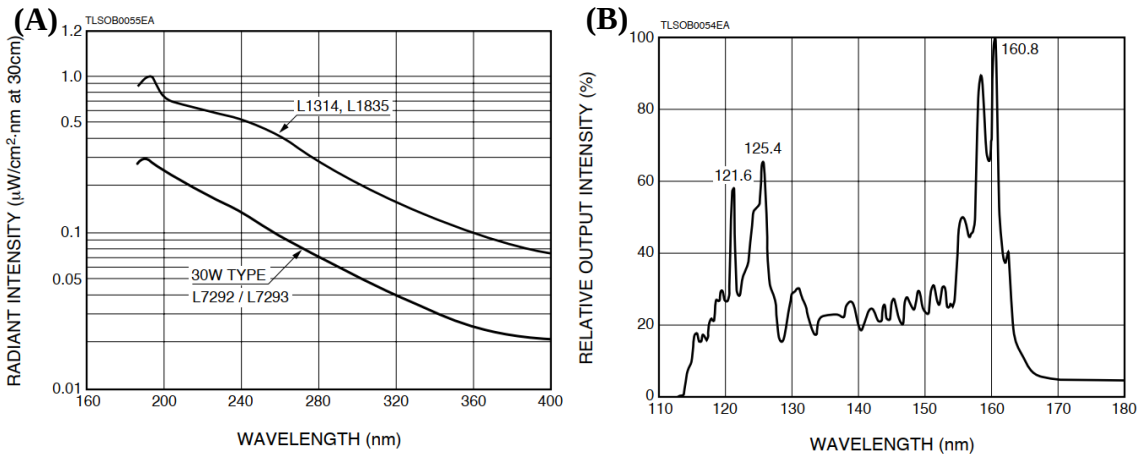

Figure 4.4. Spectroscopic radiant intensity of the L1835 deuterium lamp. (A) 160 – 400 nm, (B) 115 – 180 nm.[1] Copyright © 1998, Hamamatsu Photonics K.K.

4.1.2 Reflective Condenser

A spherical reflective condenser (focal length 250 mm, Model 615) is installed between the lamp and the entrance slit of the monochromator, Fig. 4.5.

Figure 4.5. Reflective condenser installed between the lamp and monochromator. (A) Side view, (B) Top view.

4.1.3 Monochromator

The monochromator (McPherson Inc, Model 234/302) is a 200 mm focal length, f/4.5, aberration corrected vacuum monochromator. It has 0.1 nm FWHM spectral resolution with 1200 g/mm grating. The precision slits are micrometer adjustable from 0.01 to 3 mm. The 234/302 features a wavelength counter, and manually operable sine drive providing accurate and reproducible wavelength positioning. The scan controller provides computer/software control. The compact housing is easily adapted to most experiments.

This monochromator, Fig. 4.6, is based on aberration corrected Seya-Namioka design,[2] with an incident angle of 32°. This design allows for a simple rotation of the diffraction grating, which is a concave grating with Al overcoated MgF_2 and a grove density of 1200 g/mm. The wavelength reproducibility is +/-0.05nm. The grating size is 40×45 mm. The dispersion of a 1200 g/mm grating is 4 nm/mm, and the wavelength range is up to 550 nm.

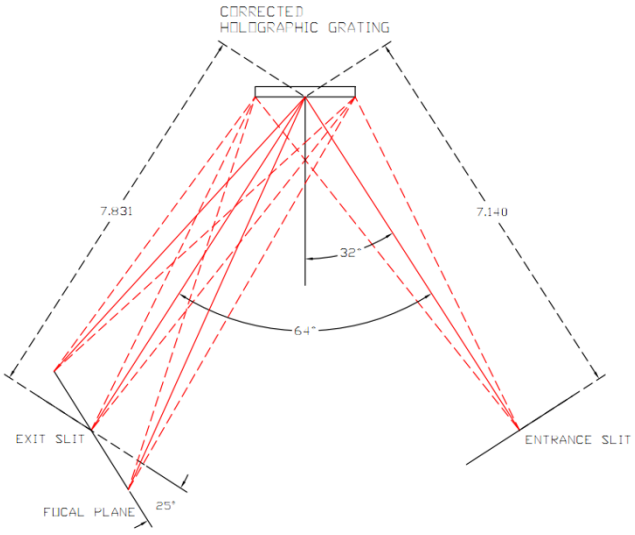

Figure 4.6. Aberration-corrected Seya-Namioka mount for the monochromator. Concave reflective grating is used in this system.[3] Copyright © 2021, McPherson Inc.

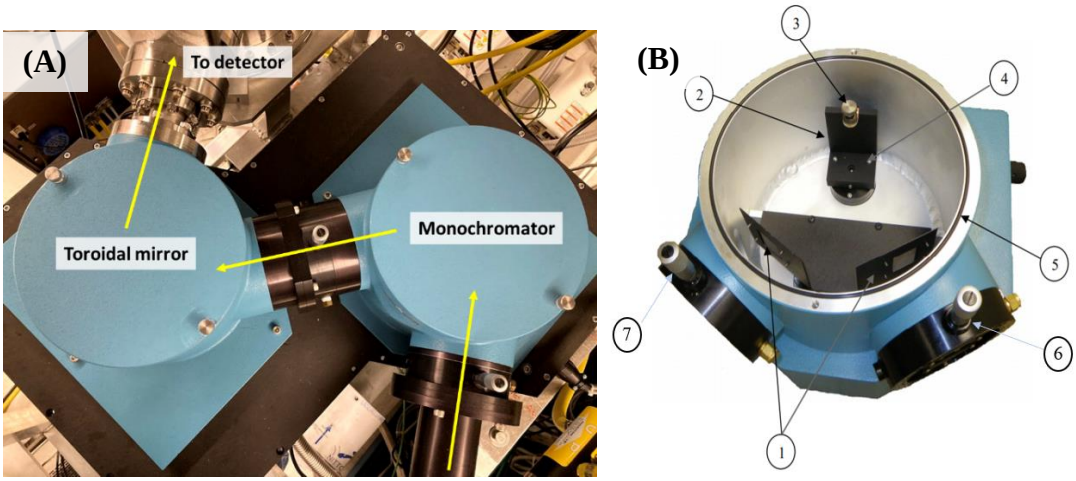

Figure 4.7. Monochromator in the spectrometer. (A) Outside view, (B) Inside view. Note: 1. Baffles, 2. Grating holder, 3. Retaining screw, 4. Half balls, 5. "O" ring, 6. Entrance slit, 7. Exit slit.

A control software, Fig. 4.8, is used to control the stepper drive for the movement of the grating. The stepper drive is controlled by the Motion Parameters, where the Begin, End, and Point Increment need to be specified before use. Under the Monochromator on the software, the motion velocity can be adjusted.

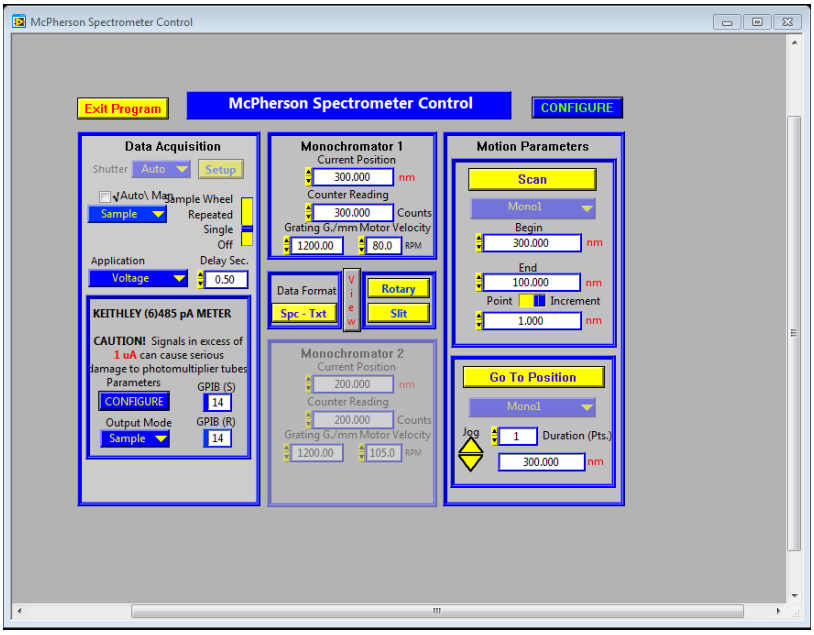

Figure 4.8. Spectrometer software interface for the control of stepper drive.

Scan speed can be selected between 1 to 99 Å/minute, from the stepper drive controller, Fig. 4.9. The motor button allows to engage stepper motor for scanning and disengage motor if manual adjustment of wavelength is desired. With the Motor button on the controller off, the manual adjustment knob will be unlocked, and the wavelength can be adjusted accordingly, Fig. 4.10.

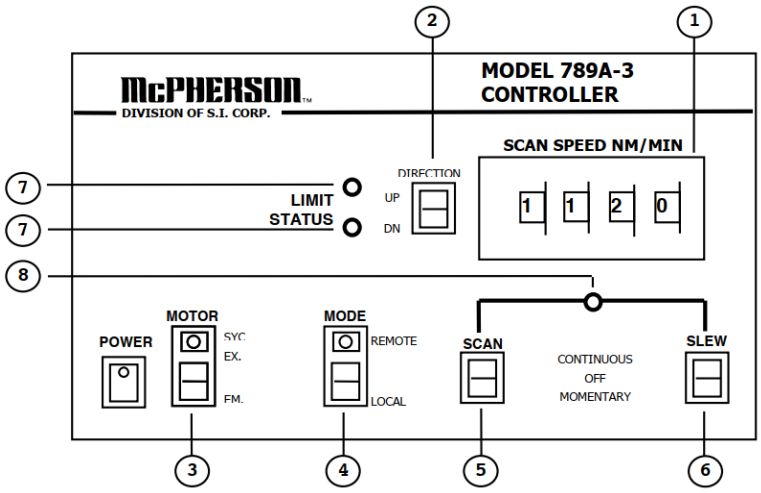

Figure 4.9. Model 789A-3 stepper drive controller.[4] Copyright © 2021, McPherson Inc.

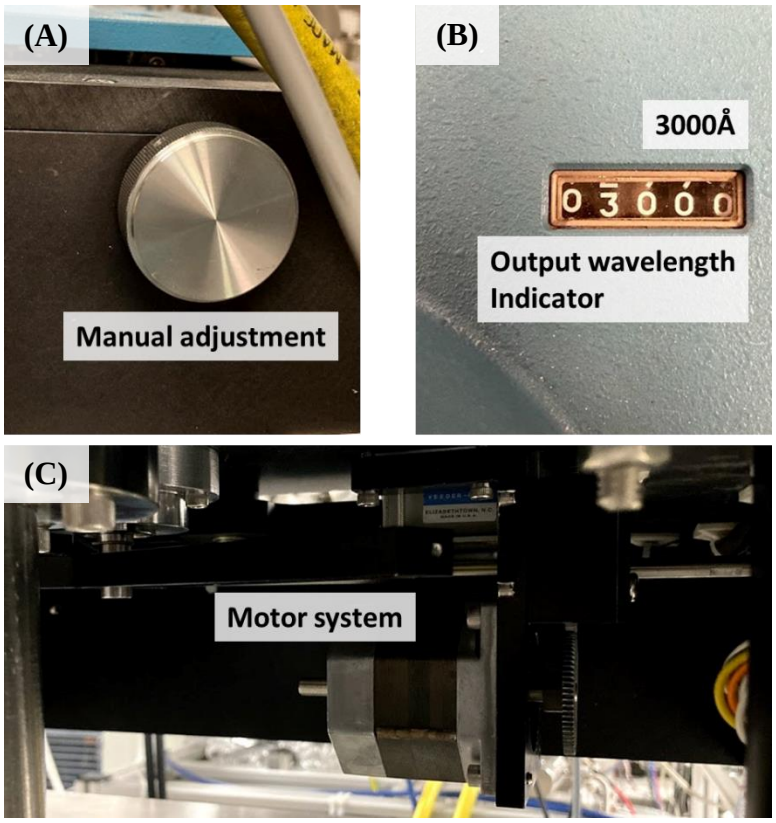

Figure 4.10. Stepper drive system. (A) Manual adjustment knob for the wavelength output, (B) Output wavelength indicator, (C) Motor system underneath the monochromator for the control of the diffraction grating rotation.

4.1.4 Toroidal Mirror

A toroidal mirror is installed between the monochromator and the sample stage chamber to focus the light onto the sample position. This mirror is coated with Al protected with MgF_2. The radius of this mirror is R = 335.6 mm and r = 241.3 mm, Fig. 4.11. This mirror is used to focus light from the monochromator to the sample position, however, it will result an image of 10×10 mm due to magnification of the 1 mm source.

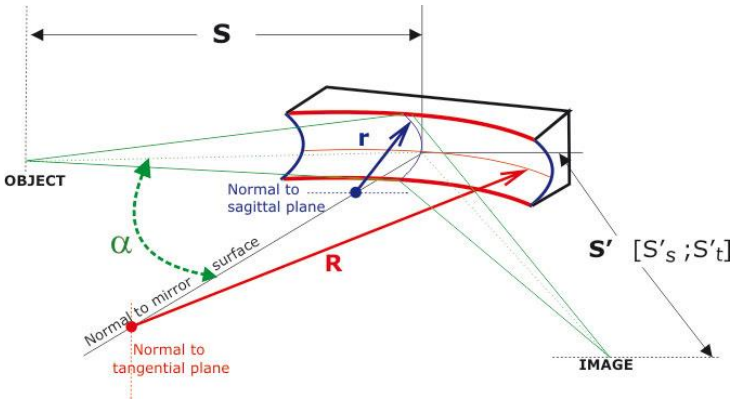

Figure 4.11. A toroidal mirror.[5] Copyright © 2019, Lithuania European Union.

For the toroidal mirror, one can determine the required incident angle for the value of radius R and r. From Eq. (4.1), plugging the values of radius for this mirror, the determined incident angle $\alpha = 32°$, which agrees with the instrumental design, half of the angle between entrance and exit slit (64°), Fig. 4.6.

$$\frac{r}{R} = \cos^2 \alpha \qquad \text{(Eq. 4.1)}$$

Between the toroidal mirror and the sample stage chamber, an aperture is installed to reduce the beam spot size on the sample, with compensation of the beam intensity.

4.1.5 Sample Stage

The sample stage, Fig. 4.12a, is placed in a separate stainless-steel chamber which is also open to the monochromator vacuum. The dimensions of the sample stage in (x, y, z) directions can be adjusted to let the light beam have the best coverage on the sample surface. The angle of the sample surface can be adjusted to allow the specular reflected beam to be detected by the detector, which can be rotated with a different manipulator stage installed underneath the sample chamber, Fig. 4.12b.

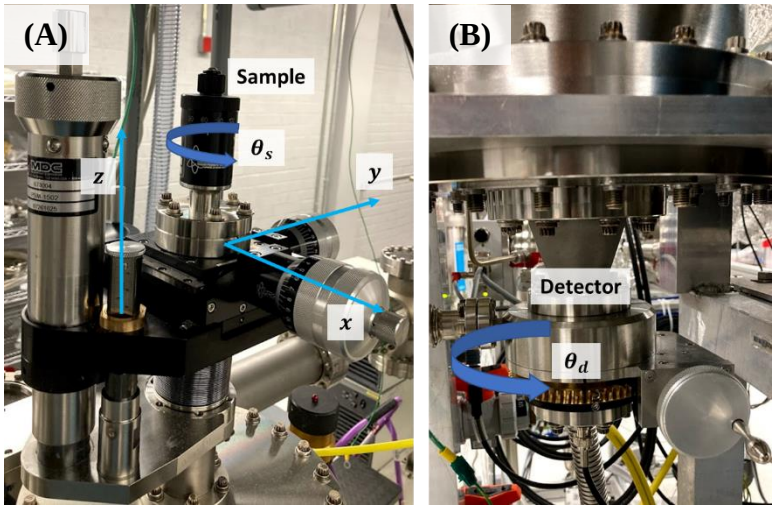

Figure 4.12. Sample stage and detector. (A) Adjustable sample stage, in adjustable dimensions in x, y, z directions and adjustable angles in the range of 360°, (B) Adjustable detector stage, with 360° variable angles. s and d stand for sample and detector.

4.1.6 Detector

A National Instruments of Standards and Technology (NIST) calibrated silicon photodiode detector (McPherson Inc, VUV Si Detector) connected with a pico-ammeter (Keithley Instruments, Model 6485) was used to detect the intensity of the transmitted or reflected light beams. Incident angles of 33° and 75° were used in this research. A vacuum-compatible Silicon photodiode detector (10×10mm), Fig. 4.13, is used. This photodiode detector has a large detection area, and 100% internal quantum efficiency.

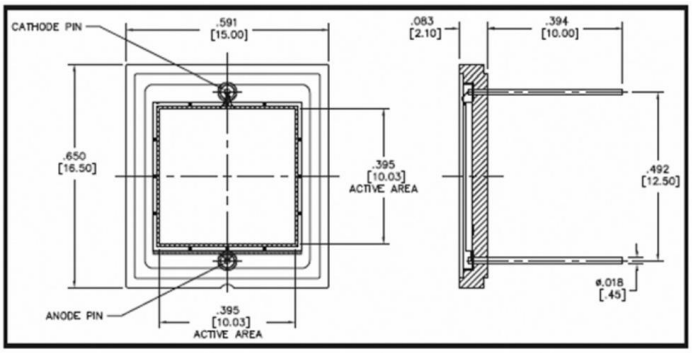

Figure 4.13. Dimensions of the Si photodiode detector (in inch).[6] Copyright © 2021, McPherson Inc.

Figure 4.14 shows the photon responsivity for the Si photodiode detector. The photon responsivity is a function of the wavelength of the incident radiation and of the sensor properties, such as the bandgap of the material the photodetector is made of. The responsivity R of a photodetector in which an optical signal is converted into an electric current (known as a photocurrent) can be expressed by Eq. 4.2. Here, η is the quantum efficiency (the conversion efficiency of photons to electrons) of the detector of a given wavelength, q is the electron charge, f is the frequency of the light beam, and h is the plank constant.[7]

$$R = \frac{\eta q}{hf} \approx \eta \frac{\lambda\,(\mathrm{nm})}{1239.85\,(\mathrm{nm}\times\ W/A)} \qquad \text{(Eq. 4.2)}$$

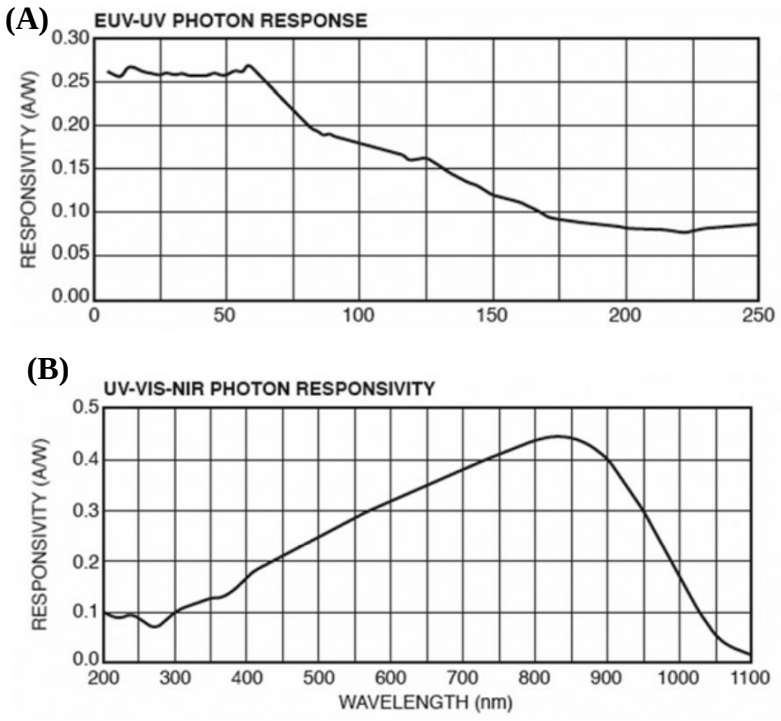

Figure 4.14. Photon responsivity for the Si photodiode detector.[6]

For the pico-ammeter, it can be used within one minute after it is turned on. However, the instrument should be turned on and allowed to warm up for at least one hour before use to achieve rated accuracy.

4.1.7 Other Accessories

To maintain the high vacuum condition in the spectrometer, two turbomolecular pumps (Pfeiffer Vacuum, HiPace 80), were installed in this system. A cold-cathode gauge (Model 943, MKS Instruments) is installed in the sample chamber to monitor the pressure inside the system.

$$\text{Reflectance} = \frac{\text{Reflected intensity}}{\text{Baseline intensity}} \times 100\% \qquad \text{(Eq. 4.3)}$$

4.2 Data Calibration

After the reflectance measurements are complete, the experimental data needs to be calibrated before use. The first calibration is the correction of the wavelength shift. This can be done by comparing the baseline intensity data with the reference spectra from the manufacturer, as shown in Fig. 4.15 below. By comparing the strongest peak, ~161 nm, one can calibrate the wavelength position by comparing with the reference value 160.8 nm, Fig. 4.4b. In the case shown in Fig. 4.15, the wavelength of the measured reflectance can be calibrated by deducting 0.6 nm (161.4 – 160.8 nm) for each of the wavelength.

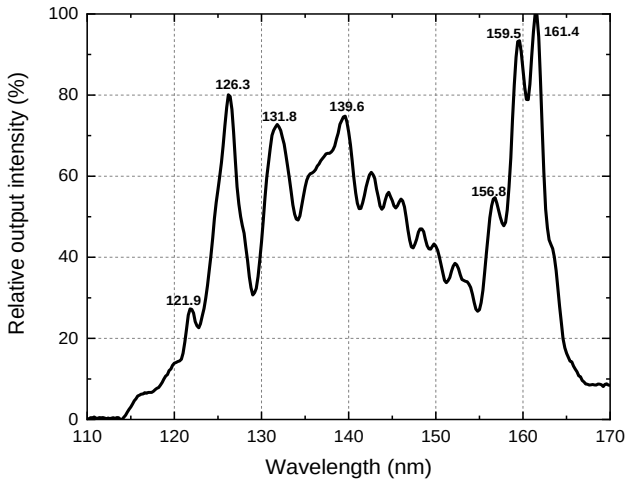

Figure 4.15. Baseline intensity measurements.

Besides the calibration of the wavelength position, the magnitude of the measured reflectance also needs to be calibrated as it is affected by the environmental noises. This can be done by measuring the reflectance with a standard sample, such as a single crystal silicon wafer. In this research, the correction factors are determined from a Si standard wafer, with Eq. (4.4) shown below. The reference values for the Si wafer is from the literature.[8] The correction factors are wavelength dependent, and also dependent on the incident angles. In this research, we determined the correction factors with incident angles of 33° and 75°, shown in Fig. 4.16.

$$\text{Correction Factors} = \frac{\text{Reference values}}{\text{Measured reflectance}} \qquad \text{(Eq. 4.4)}$$

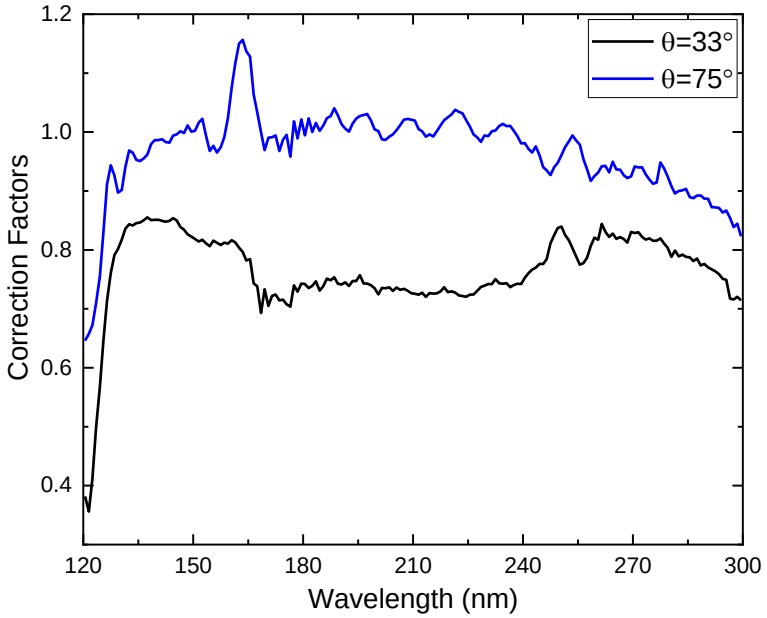

Figure 4.16. Correction factors determined with Si wafer. For incident angles of 33° and 75°.

With the correction factors determined, the reflectance measurements for other samples should have the same relation with the reference sample, from Eq. (4.5). Here, R_{cal}, and R_{meas} are the calibrated, and measured reflectance for the sample under test. R_{ref}, and R_{meas_Si} are the reference, and measured reflectance the standard sample used, i.e., Si wafer.

$$\frac{R_{cal}}{R_{meas}} = \frac{R_{ref}}{R_{meas\_Si}} \qquad \text{(Eq. 4.5)}$$

Thus, the calibrated reflectance can be determined from Eq. (4.5), and re-written in Eq. (4.6), with correction factors explicitly included. By multiplying the measured reflectance with the correction factors (C. F.), the reflectance can be calibrated.

$$R_{cal} = \frac{R_{ref}}{R_{meas\_Si}} \times R_{meas} = \text{C. F.} \times R_{meas} \qquad \text{(Eq. 4.6)}$$

To investigate if the correction factors depend on the size and shape of the samples. Si wafers with different sizes of caps were used for the measurements. A 0.90×0.90 cm Si wafer was prepared to study if a different shape matters for the correction factors, as shown in Fig. 4.17.

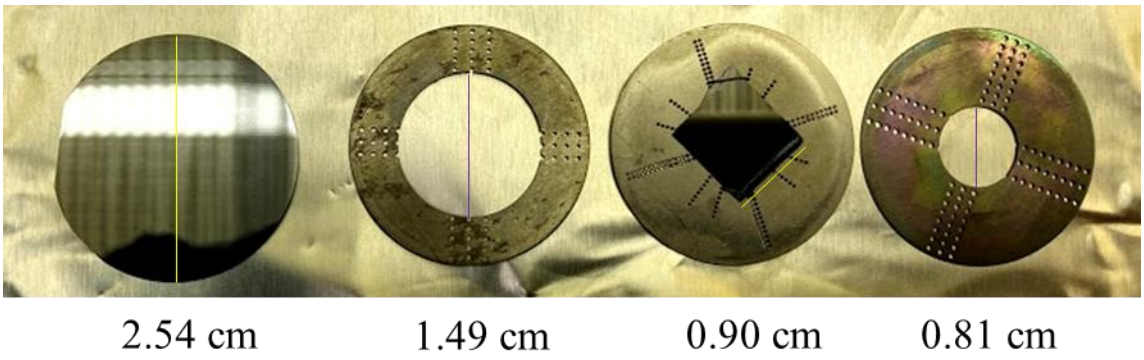

Figure 4.17. Si wafers with different sizes and shapes.

For each of the Si wafers, the reflectance measurements have been made with all other variables the same. The determined correction factors are shown in Fig. 18. As is shown below, the correction factors for the Si wafer with size 2.54 cm and 1.49 cm are nearly identical at longer UV wavelength. Even though they have some discrepancies at shorter wavelength, we can still say they should have same correction factors, and this means the beam spot size is smaller than 1.49 cm, thus there is no difference on the reflectance measurements if the size of the Si wafer is reduced to 1.49 cm.

However, for Si wafer with sizes of 0.81 and 0.90 cm, the correction factors are significantly different from the Si wafer with larger sizes. This indicates that the beam spot size is greater than 0.90 cm, that only part of the light beam is reflected, so the correction factors will be higher because the measured reflectance will be lower, explained from Eq. (4.4).

All of these indicate that the beam spot size for the spectrometer used is 0.90 – 1.5 cm. A refined determination requires Si wafers with sizes between 0.90 – 1.49 cm.

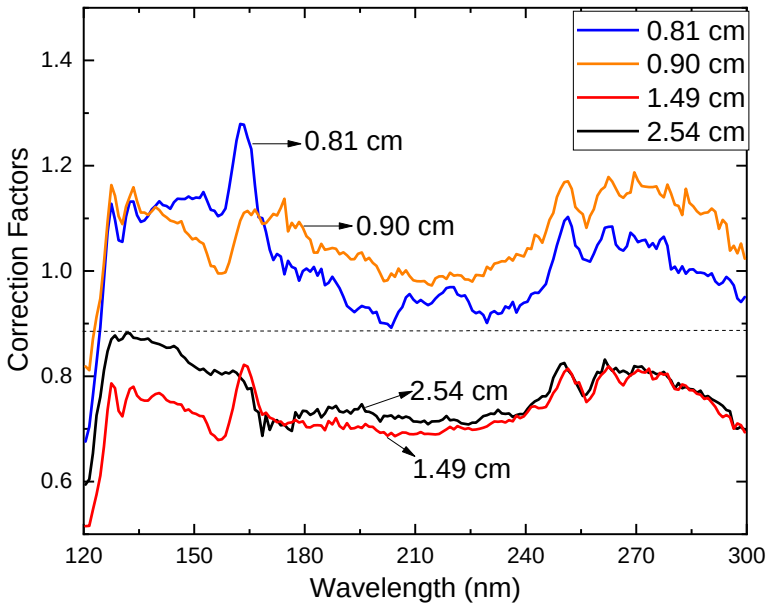

Figure 4.18. Correction factors from Si wafers with different sizes and shapes.

References

[1] "High Intensity, 150 W Type, Vacuum UV (from 115 nm) Light Source - L1835." Hamamatsu Photonics K.K. https://www.hamamatsu.com/resources/pdf/etd/L1314_L1835_TLSO1012E.pdf (accessed)

[2] T. Namioka, "Theory of the Concave Grating. III. Seya-Namioka Monochromator," J. Opt. Soc. Am. **49**, 951 (1959).

[3] "Aberration Corrected Vacuum Monochromator." McPherson Inc. https://mcphersoninc.com/spectrometers/vuvuvvis/model234302.html (accessed)

[4] "Model 789A-3 Scan Controller." McPherson Inc. https://nstx.pppl.gov/nstxhome/DragNDrop/Operations/Diagnostics_&_Support_Sys/DIMS/789A3%20Manual.pdf (accessed)

[5] "Toroidal Mirrors (Definitions)." ZILTA Co., Inc. http://www.lasertechn.com/index.php/toroidal-mirrors (accessed)

[6] "VUV Si Detector." McPherson Inc. https://mcphersoninc.com/detectors/vuv-si-diode.html (accessed)

[7] "Responsivity." Wikipedia. https://en.wikipedia.org/wiki/Responsivity (accessed)

[8] E. D. Palik, *Handbook of Optical Constants of Solids*. (Academic Press, 1985).

CHAPTER 5

FAR ULTRAVIOLET OPTICAL CONSTANTS MEASUREMENTS FOR ATOMIC LAYER DEPOSITED AlF_3, Al_2O_3, HfO_2, AND Ga_2O_3

5.1 Introduction

Optical constants are commonly measured using ellipsometry and spectroscopy.[1] To extract the values of (n, k), optical dispersion models are usually used to fit the experimental data using least-squared algorithms.[2] However, for the measurements of (n, k) in far UV wavelength (120 – 200 nm), the ellipsometry was limited due to the shortage of efficient wideband polarizers and retarders.[3] In this case, spectroscopy becomes one of the commonly used methods to measure (n, k) at shorter UV wavelength.

For the designs for the thin-film optical coatings, the optical constants (n, k) of the materials should be known. Thin films are usually amorphous and the refractive index varies for the materials grown using different processing.[4] For an effective optical design, the optical constants for the thin films should be measured. Dielectric thin films are commonly used as the coating materials, because of their high transparency and variable refractive indices. It is reported that the refractive indices for dielectric thin film vary with the thickness and density.[5-8] For the Al_2O_3 grown by thermal ALD, the refractive index increases until 50 nm thickness.[8] Higher refractive index can be achieved by increasing the film density, such as annealing and gas reactant pressures.[5-7, 9] For the HfO_2 and SiO_2 thin films grown by electron-beam evaporation, the refractive indices were found to increase with increasing packing densities.[5] Thus, it is necessary to measure the optical constants (n, k) of the thin films used for the optical coating designs and fabrications.

For the optical coatings used at UV wavelength, materials with wide bandgaps are preferred, such as SiO_2, Al_2O_3, HfO_2, and AlF_3. Metal fluorides, such as AlF_3, have an ultrawide bandgap >10 eV, which make them transparent in the far UV range. However, dielectric oxides and fluorides were reported to easily absorb water and carbon at atmosphere.[10, 11] For the AlF_3 thin films, the surface layer will be oxidized at atmosphere.[11] For the use at shorter wavelength, the impurities containing water and carbon will cause light absorption and degrade the optical performance of the optical devices, such as bandpass filters. For the use at the far UV, the oxidized AlF_3 will induce absorption and alter the refractive index of the optical coatings. Based on this consideration, the measurements of the thin films should be conducted *in-situ*, to minimize the atmospheric contamination.

In this study, the reflectance of AlF_3, Al_2O_3, HfO_2, and Ga_2O_3 was measured *in-situ* with far UV spectroscopy. All the materials were grown using ALD, with thickness ranges 10 – 50 nm. Optical constants were deduced using custom-developed calculation methods, based on iso-reflectance curves and optical dispersion models. Spectroscopic ellipsometry was used as a complement to verify the accuracy of the determined optical constants. It is shown that the complementary use of spectroscopic ellipsometry and far UV spectroscopy can provide more complete and accurate optical constants measurements.

5.2 Materials and methods

Ga_2O_3 have been utilized as transparent conducting oxides (TCOs) and passivating dielectrics for GaAs-based electronics, due to its wide bandgap (4.95 eV) and high refractive index (1.88 at 589 nm).[12] HfO_2 and Al_2O_3 were commonly used as the high-κ

gate dielectric layer due to their high refractive index, n = 1.9 for HfO_2 and 1.7 for Al_2O_3, at 589 nm wavelength.[13, 14] The bandgap measured for HfO_2 and Al_2O_3 grown using ALD are 5.6 eV and 6.7 eV.[10, 13, 15] For the AlF_3 material, it has a low refractive index of 1.3 at 589 nm wavelength, and a wide bandgap of 10.8 eV.[16, 17]

HfO_2 and Al_2O_3 were grown using the Cambridge ALD system in the ASU NanoFab. For HfO_2, the precursors used are tetrakis(dimethylamino)hafnium and water vapor, with a growth rate 1 Å/cycle. For Al_2O_3, the precursors are trimethylaluminum and water vapor, with a growth rate 1 Å/cycle. Ga_2O_3 and AlF_3 were grown using a custom-built ALD system in our lab. For Ga_2O_3, trimethylgallium and O_2 plasma are used as the precursors. AlF_3 was grown by thermal ALD, with TMA and HF-pyridine as the precursors. All the materials were grown on single-crystal (001) Si substrates.

Spectroscopic ellipsometer (J. A. Woollam, M-2000DI) was used for the ellipsometry measurements. A custom-built Far UV spectrometer was used for the in-situ reflectivity measurements. A commercially available software program CompleteEASE (J. A. Woollam, v6.51) was used to analyze the ellipsometry and reflectance data.

5.3 Optical Calculations

Different approaches were used to calculate the optical constants (n, k) from the measured ellipsometry and reflectance data. These methods are based on the iso-reflectivity curve and optical dispersion models. For the iso-reflectance curve methods, two reflectance measurements need to be done. The intersection points on the two iso-reflectance curves correspond to the value of (n, k).[18, 19] For the optical dispersion model,

it uses a few variables to model the dispersion relation between (n, k) and the wavelength. This method reduces the parameters used for curve fittings and the deduced (n, k) have a smooth shape than the first method.[2] Depending on the optical properties of the materials, each method has its advantages and limitations. The detailed descriptions of these methods were described in Chapter 3.7.

5.4 Results

Far UV reflectance and spectroscopic ellipsometry measurements have been done for Ga_2O_3, Al_2O_3, HfO_2, and AlF_3. For the UV reflectance measurements, two different incident angles were used, 33°and 75°, from the normal, in the wavelength of 120 – 300 nm. The measured reflectance was calibrated with the correction factors determined using a single crystal silicon wafer, described in Chapter 4. For the spectroscopic ellipsometry measurements, three different incident angles were used, 65°, 75°, and 85°, in the wavelength of 193 – 1689 nm. Different combinations of the methods were used for each material, summarized in Table 5.1.

Table 5.1. Methods used in this work for each material.

	Iso-reflectivity curve		**Optical dispersion model**			**Direct conversion ($k = 0$)**
	Two angles	Two thicknesses	Cauchy	Modified Lorentz		
				Tauc	Cody	
Ga_2O_3	✓	✓		✓		
Al_2O_3	✓				✓	
HfO_2	✓			✓		
AlF_3			✓			✓

5.4.1 AlF_3

5.4.1.1 Optical Properties from Band Structures

AlF_3 has several polymorphs, and the most stable phase, α-AlF_3, has a direct bandgap of 10.81 eV.[20] The band structure of the α-AlF_3 calculated by J. L. Navarro *et al*, using the density functional theory (DFT), is shown in Fig. 5.1.[20] The large band gap of AlF_3 shows a high UV transparency down to ~115 nm and has potential to be used in far UV optics.[17]

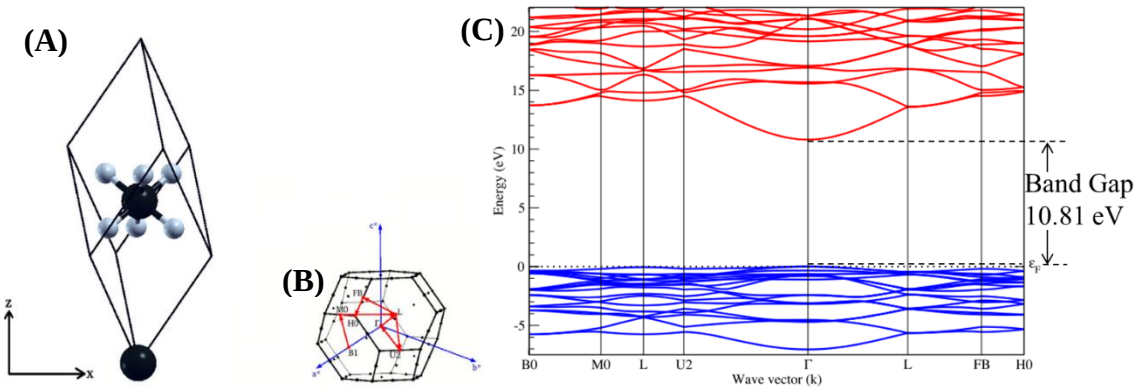

Figure 5.1. Band structure calculation of α-AlF_3. (A) Primitive cell of the R-3c rhombohedral structure of α-AlF_3 (dark blue: Al atoms; grey: F atoms), (B) First Brillouin zone, showing the *k*-point path (red lines) used in the band structure plot, (C) Band structure calculated with DFT, corrected with the GW method for the band gap, showing a direct band gap of 10.81 eV.[20] Copyright © 2016, Elsevier.

Optical properties of α-AlF_3 can be calculated from the band structure, with the inter-band momentum matrix for the inter-band transitions, and the Bethe–Salpeter equation to account for the excitonic effects. Fig. 5.2a shows the calculated dielectric constants from the inter-band transitions, in which the first transition (E_0) occurs slightly above the fundamental band gap (10.81 eV). Fig. 5.2b shows the excitonic effects calculated with Bethe-Salpeter equation, in which strong exciton absorption occurs at

around 11 eV, close to the direct band gap. The calculated excitonic effects are consistent with Frenkel excitons which are readily observed around the fundamental band gap of the insulators with large band gap, where the electron-hole pairs are tightly bound and stable at room temperature. In this study, 11 eV is beyond the detection limit of the far UV optical spectrometer (10.3 eV), thus both the inter-band transitions and excitonic effects could not be observed from our experiments.

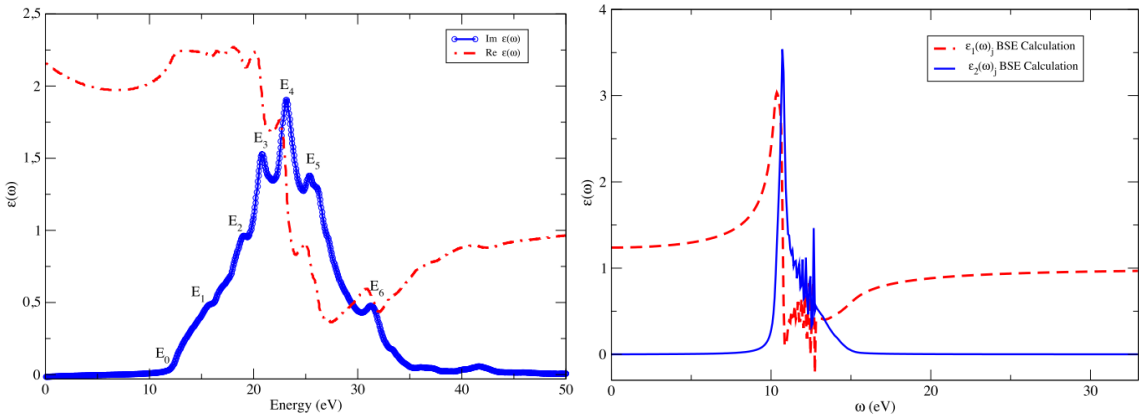

Figure 5.2. Optical properties of α-AlF_3 from band structures. (A) Dielectric constants considering inter-band transitions, (B) Dielectric constants considering excitonic effects.[20] Copyright © 2016, Elsevier.

5.4.1.2 Optical Properties from Reflectance Measurements

A ~25 nm AlF_3 layer grown by thermal ALD was used in this study. Since both the inter-band transitions and the excitonic effects occur beyond the far UV range, methods based on transparent materials are used in the calculation. Direction conversion (assuming $k = 0$) and Cauchy model methods were used to characterize the AlF_3 optical properties. Far UV reflectance (120 – 300 nm) for AlF_3 was measured at incident angles 33°, Fig. 5.3a.

5.4.1.2.1 Direct Conversion (assuming $k = 0$)

The direct conversion method can be used if the material is transparent material, where $k = 0$. In this case, only the value of n needs to be measured, which reduces the unknows from 2 to 1. The fitted data and the deduced values of n are shown in Fig. 5.3.

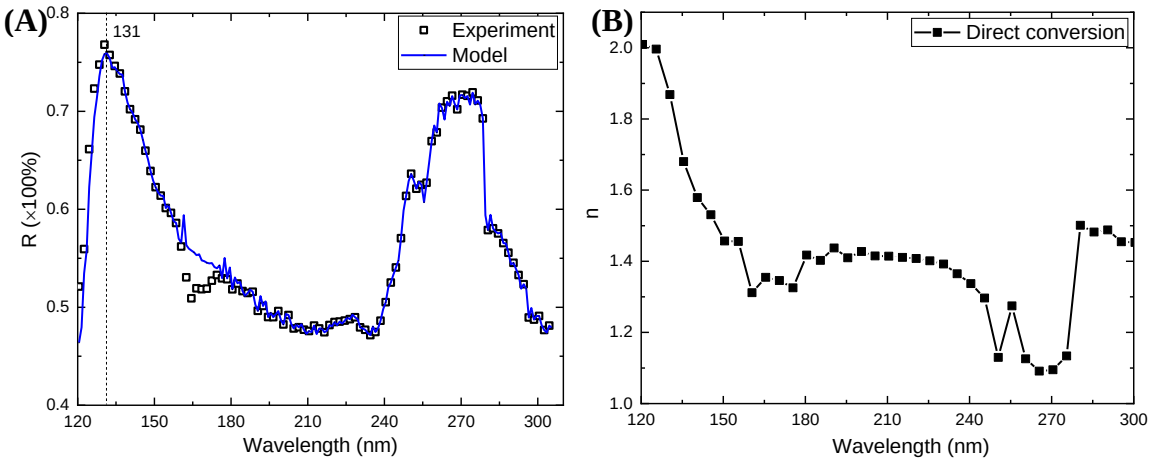

Figure 5.3. Direct conversion method for AlF_3. (A) Fitted far UV reflectance data; (B) Deduced values of n.

5.4.1.2.2 Cauchy Model Method

The Cauchy model, described in Chapter 3, was used to characterize the refractive index n of AlO_3. Cauchy model was used to fit the spectroscopic ellipsometry and far UV reflectance data, separately. Ellipsometry data was measured at three different incident angles (65°, 75°, and 85°), with three curves shown for Psi and Delta in Fig. 5.4a.

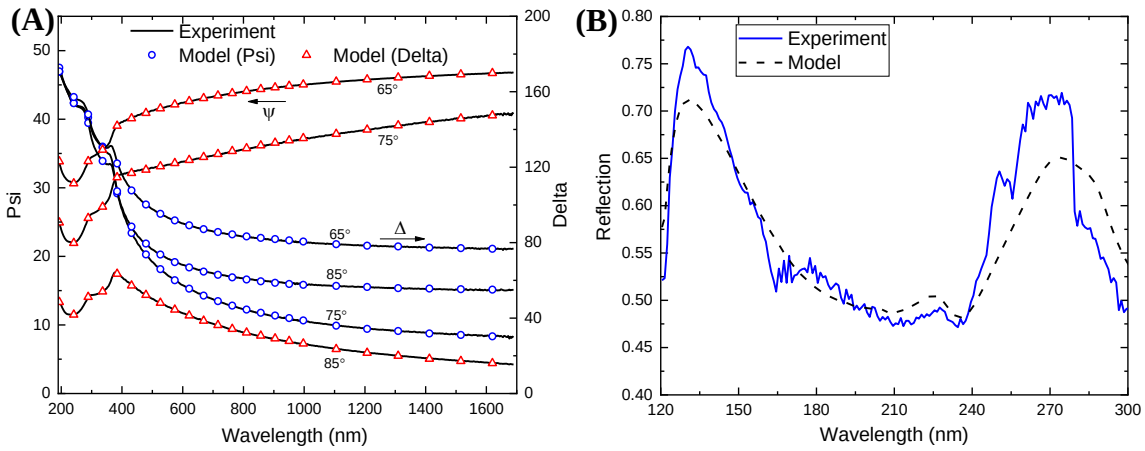

Figure 5.4. Curve fitting for AlF_3 with the Cauchy model.

(A) Fit spectroscopic data; (B) Fit far UV reflectance data (θ: 33°)

The measured values of refractive index n from the Cauchy model are shown in Fig. 5.5, together with the reference values reported by several groups, Table 5.2. Compared with the results from the literatures, our results agree well the references. The discrepancies could be due to the variation of the deposition and calculation methods.

Table 5.2. References for the refractive index of AlF_3 thin films, shown in Fig. 5.5.

	Growth	**Measurements**	**Method**	**Wavelength**
Ref. 1 [21]	ALD	SE	Cauchy	240 nm – IR
Ref. 2 [16]	ALD	SE	Cauchy	193 nm – IR
Ref. 3 [22]	ALD	R%	Iso-reflectance	90 – 190 nm
Ref. 4 [23]	Evaporation	R% + T%	Cauchy	120 nm – visible

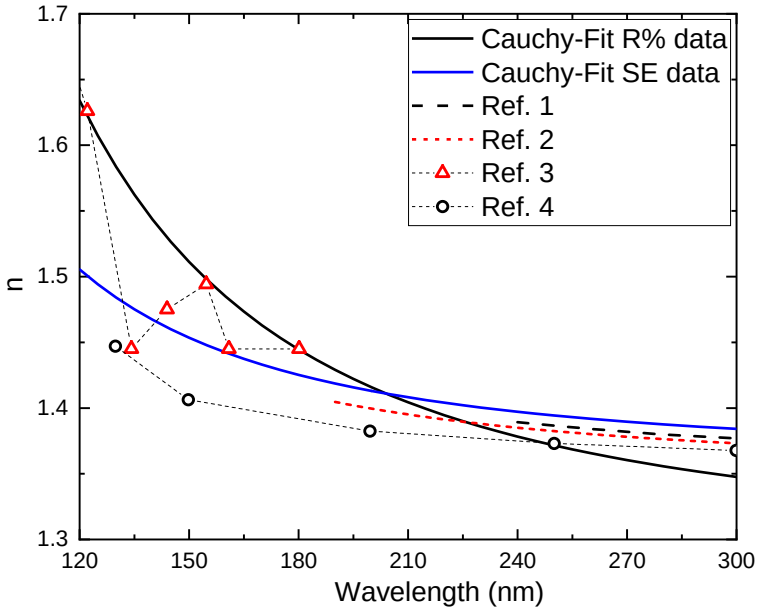

Figure 5.5. Refractive index determined for AlF_3 with Cauchy model.

5.4.2 Al_2O_3

5.4.2.1 Optical Properties from Band Structures

Al_2O_3 has several polymorphs, and the most stable phase, α-Al_2O_3, is an insulator with an indirect bandgap of 8.7 eV from experiment.[24] The band structure of α-Al_2O_3 was calculated by Y. N. Xu *et al*, using density functional theory (DFT), shown in Fig. 5.6.[25] The calculated indirect band gap, 6.29 eV, is lower than the experimental values. This is because the local density approximation (LDA) scheme used for the calculation underestimates the band gap in semiconductors and insulators, sometimes up to 50%. Optical properties were calculated from the band structures with the orthogonalized linear combination of atomic orbitals (OLCAO) method. Absorption due to inter-band transitions and excitons can be calculated from this method, shown in Fig. 5.11a.[25]

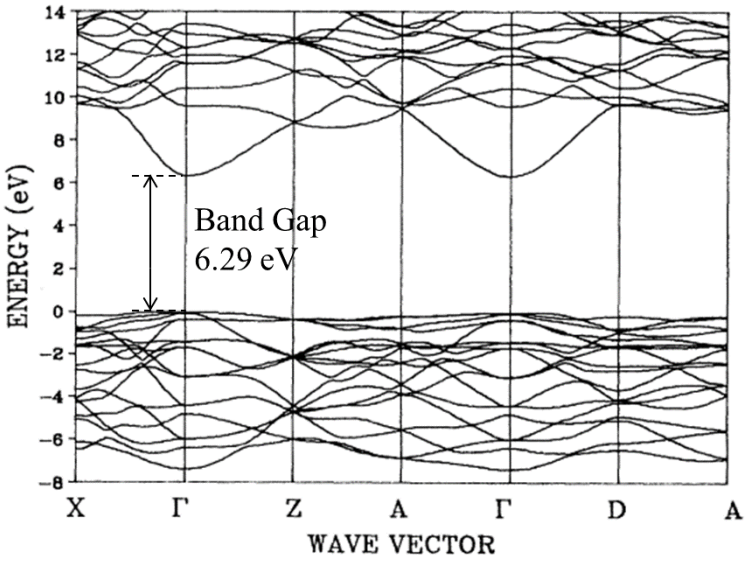

Figure 5.6. Band structure of α-Al_2O_3 calculated with DFT, showing an indirect band gap of 6.29 eV, which is 0.06 eV lower than the direct band gap at Γ point.[25] Copyright © 1991, American Physics Society.

5.4.2.2 Optical Properties from Reflectance Measurements

A ~50 nm Al_2O_3 layer grown by thermal ALD was used to determine (n, k) using both iso-reflectivity curve and Cody-Lorentz model methods. Far UV reflectance (120 – 300 nm) for Al_2O_3 was measured at incident angles 33°and 75°, Fig. 5.7. The reference spectrum for silicon substrate was also shown in Fig. 5.7.

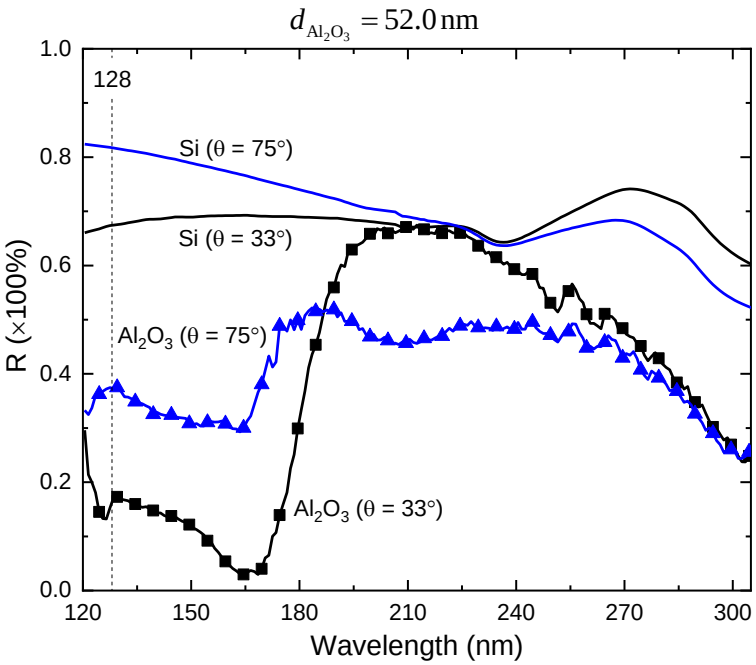

Figure 5.7. Far UV reflectance measurements for Al_2O_3 at incident angles 33°and 75°.

5.4.2.2.1 Iso-Reflectivity Curve Method

The determined (n, k) is shown in Fig. 5.8a. The value of n is determined in the 120 – 200 nm wavelength range. For wavelengths above 200 nm, there are no intersection points from the iso-reflectivity curves, because of $k = 0$. The cut-off wavelength can be determined to be 195 nm, from the value of k in Fig. 5.8a. The dielectric constants ($\varepsilon_1, \varepsilon_2$) converted from (n, k) are shown in Fig. 5.8b. For the imaginary dielectric constant, the peak at 130 nm, should correspond to absorption due to the formation of an exciton at 9.5 eV for Al_2O_3, Fig. 5.11.

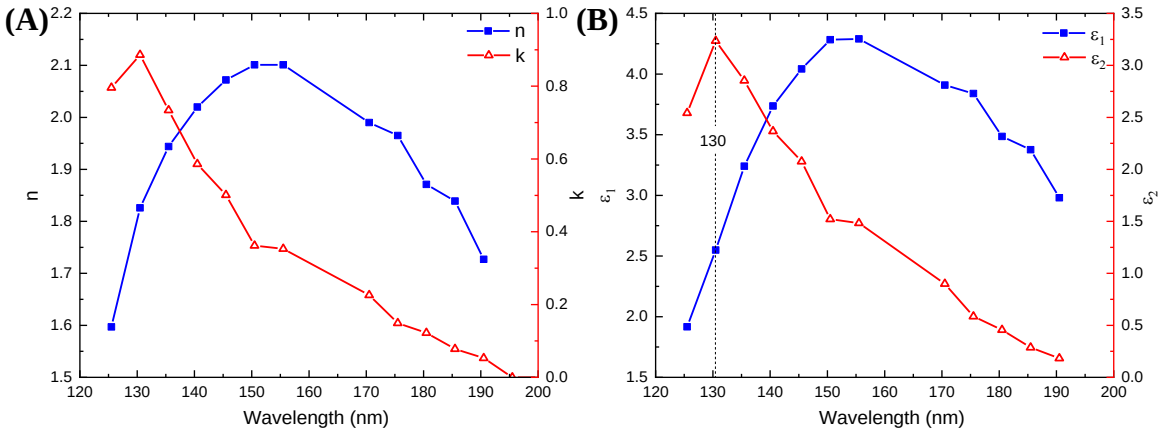

Figure 5.8. (n, k) and $(\varepsilon_1, \varepsilon_2)$ determined for Al_2O_3 using iso-reflectivity curve method. (A) (n, k), (B) $(\varepsilon_1, \varepsilon_2)$.

5.4.2.2.2 Cody-Lorentz Model Method

The Cody-Lorentz model, described in Chapter 3, was used to characterize the optical constants (n, k) of Al_2O_3. Cody-Lorentz model is similar to Tauc-Lorentz model, but using a Cody form to describe the imaginary dielectric constant in the inter-band transition region.[26] Cody-Lorentz model was used to fit spectroscopic ellipsometry and far UV reflectance data, separately. Ellipsometry data was measured at three different incident angles (65°, 75°, and 85°), with three curves shown for Psi and Delta in Fig. 5.9a.

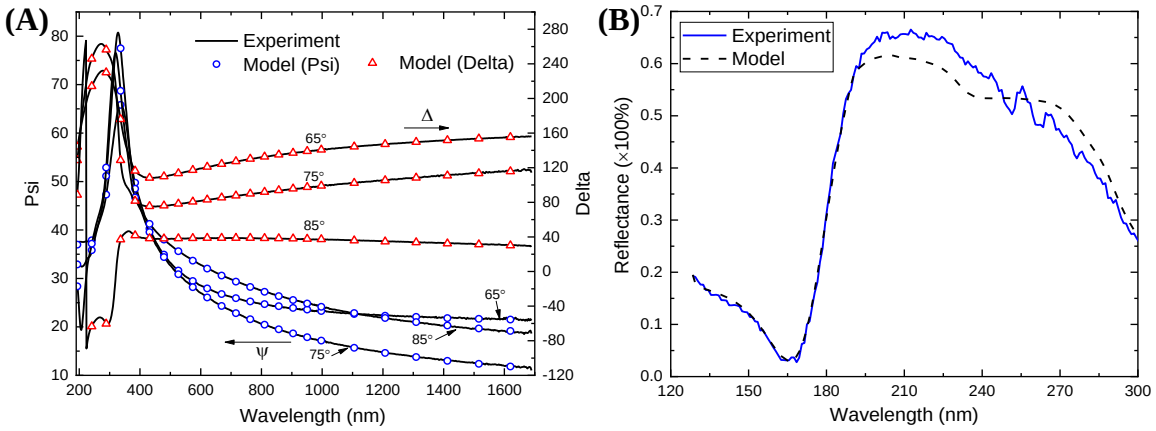

Figure 5.9. Curve fitting for Al_2O_3 with Cody-Lorentz model. (A) Fit spectroscopic ellipsometry data; (B) Fit far UV reflectance data (θ: 33°). The three different curves in (A) corresponds to the measurements at three different incident angles, 65°, 75°, and 85°.

The measured (n, k) from all methods, together with the reference values, are shown in Fig. 5.10. The measured values of (n, k) agree well with the results reported from several groups, Table 5.3. The discrepancies could be due to the variation of the deposition and calculation methods. Besides, the results from all methods showed that the cut-off wavelength is at 190 – 200 nm, which agrees with the measured bandgap for amorphous Al_2O_3 grown by ALD (E_g ~ 6.7 eV, λ_c ~ 185 nm).[15] The determined imaginary dielectric constant is shown in Fig. 5.11b, the peak at ~9.5 eV should correspond to the excitonic effects calculated from DFT, Fig. 5.11a.

Table 5.3. References for the refractive index of Al_2O_3 thin films, shown in Fig. 5.10.

	Growth	**Measurements**	**Method**	**Wavelength**
Ref. 1 [27]	ALD	SE	Cauchy	193 nm – IR
Ref. 2 [28]	PVD	SE + T%	Cauchy	150 nm – visible
Ref. 3 [29]	Evaporation	SE + R%	UDM	120 nm – IR

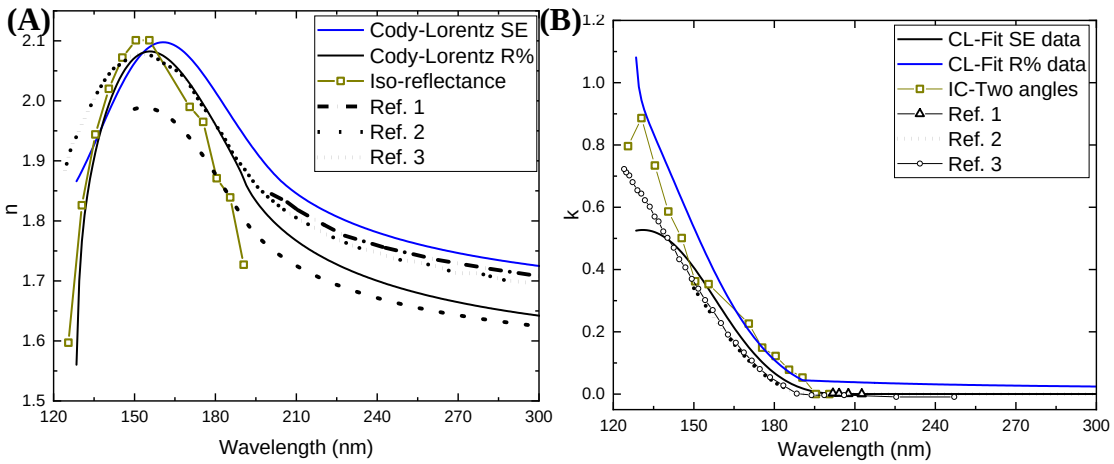

Figure 5.10. Optical constants determined for Al_2O_3 in this work.

(A) Refractive index n; (B) Extinction coefficient k.

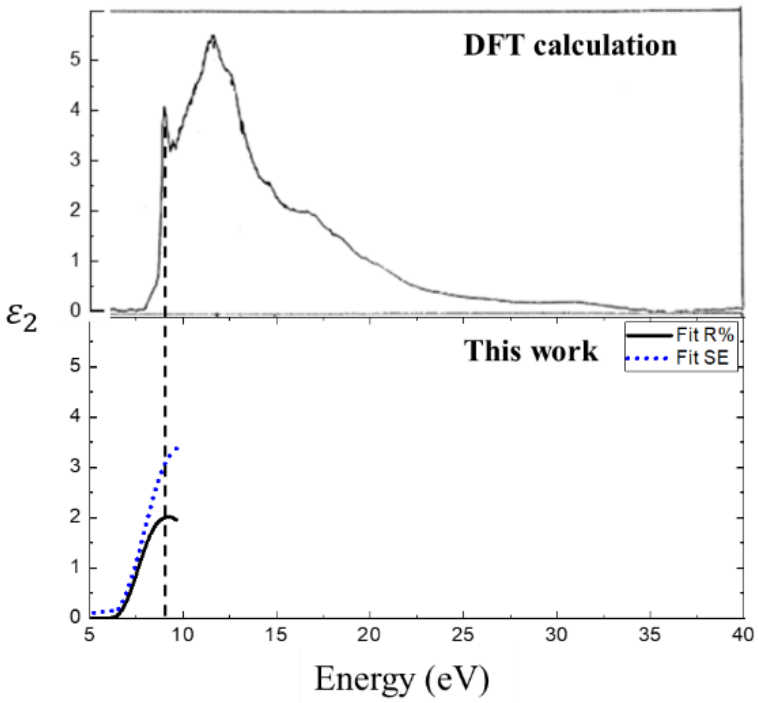

Figure 5.11. Imaginary dielectric constant of Al_2O_3. (A) DFT calculations from the band structure shown in Fig. 5.6;[25] Copyright © 1991, American Physics Society. (B) Measured in this work.

5.4.3 HfO_2

5.4.3.1 Optical Properties from Band Structures

HfO_2 has several polymorphs, and the most stable phase, m-HfO_2, is an insulator with an indirect bandgap of 5.68 eV from the experiment.[30] The DFT calculation shows an indirect band gap of 3.98eV, Fig. 5.12a. This is due to an underestimation of the conduction band energies in first-principles calculations.[31, 32] The optical absorption is calculated using inter-band momentum matrix elements, Fig. 5.12b. The peak A at 7.13 eV originates from the electronic transition between the O 2p states in the upper valence band and the Hf 5d states in the conduction band.[31]

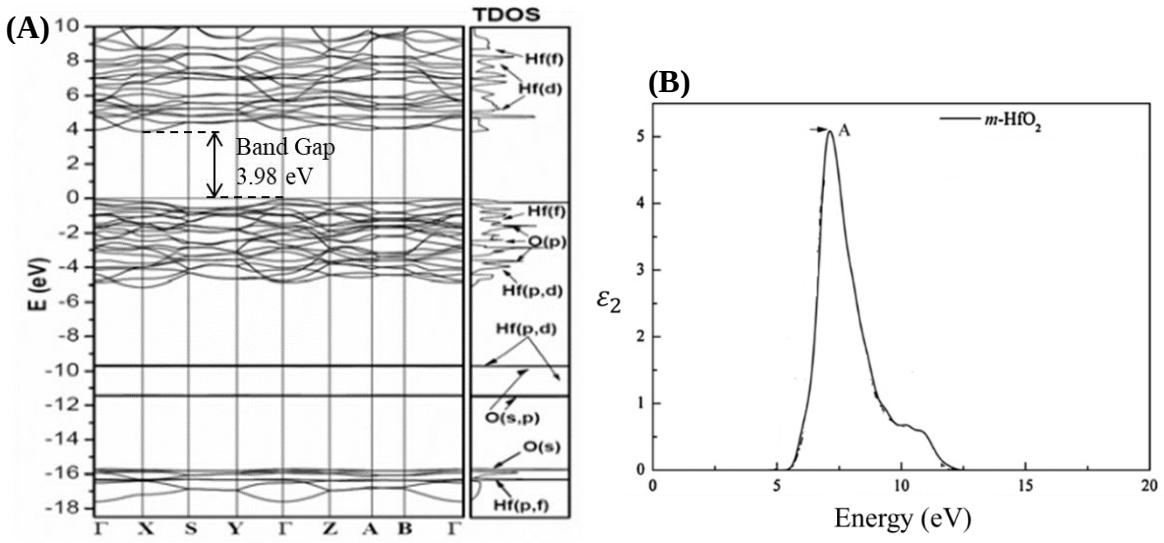

Figure 5.12. Band structure and optical properties of m-HfO_2 calculated with DFT. (A) Band structure shows an indirect band gap of 3.98 eV, which is 0.1 eV lower than the direct band gap at Γ and X point.[32] Copyright © 2005, American Institute of Physics. (B) Calculated imaginary part of the dielectric constants.[31] Copyright © 2011, Elsevier B.V.

5.4.3.2 Optical Properties from Reflectance Measurements

A ~50 nm HfO_2 layer grown by thermal ALD was used to determine (n, k) using both iso-reflectivity curve and Tauc-Lorentz model methods. Far UV reflectance (120 – 300 nm) for HfO_2 was measured at incident angles 33°and 75°, Fig. 5.13.

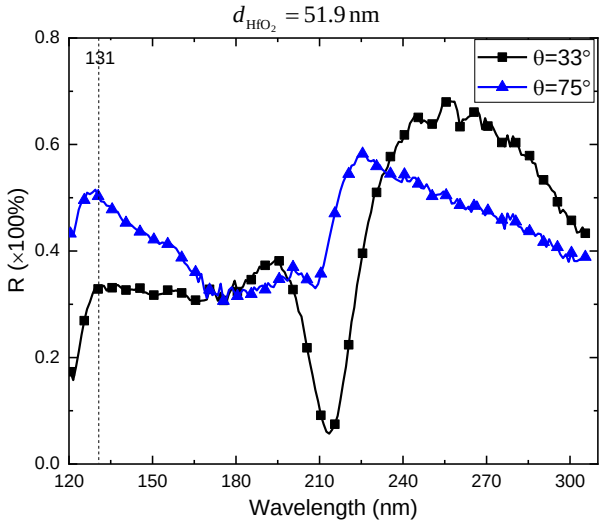

Figure 5.13. Far UV reflectance measurements for HfO_2 at incident angles 33°and 75°.

5.4.3.2.1 Iso-Reflectivity Curve Method

The determined (n, k) is shown in Fig. 5.14a. The value of n is determined in the 120 – 240 nm wavelength range. For wavelengths above 240 nm, there are no intersection points from the iso-reflectivity curves, because of $k = 0$. The cut-off wavelength can be determined to be 250 nm, from the value of *k* in Fig. 5.14a. The dielectric constants ($\varepsilon_1, \varepsilon_2$) converted from (n, k) are shown in Fig. 5.14b. For the imaginary dielectric constant, the peak at 151 nm (8.21 eV), should correspond to the inter-band transition (peak A at 7.13 eV) shown in Fig. 5.12b. The discrepancy between the DFT calculation and the measurement can be due to the underestimation of the conduction band energies from first principles calculations.[31]

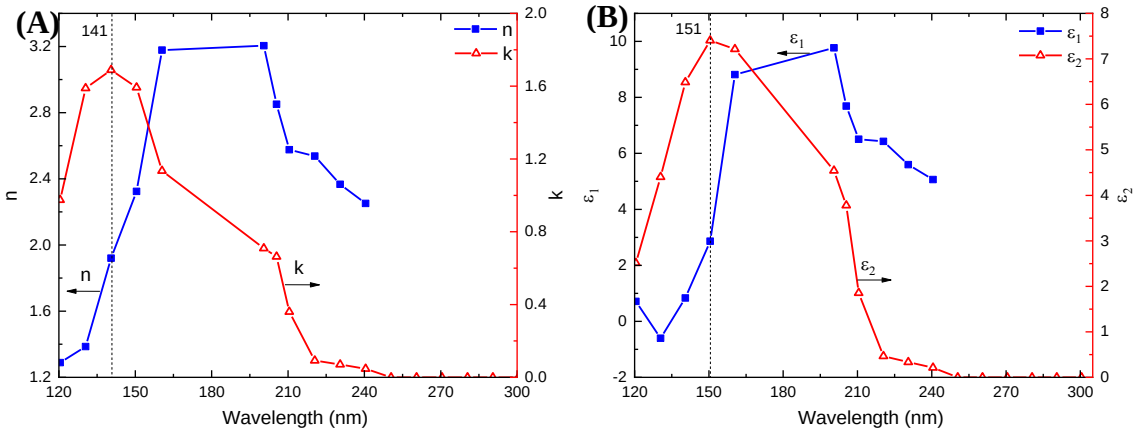

Figure 5.14. (n, k) and $(\varepsilon_1, \varepsilon_2)$ determined for HfO_2 using the iso-reflectivity curve method. (A) (n, k); (B) $(\varepsilon_1, \varepsilon_2)$.

5.4.3.2.2 Tauc-Lorentz Model Method

The Tauc-Lorentz model, described in Chapter 3, was used to characterize the optical constants (n, k) of HfO_2. The Tauc-Lorentz model was used to fit the spectroscopic ellipsometry and far UV reflectance data, separately. Ellipsometry data was measured at three different incident angles (65°, 75°, and 85°), with three curves shown for Psi and Delta in Fig. 5.15a. The sharp steps at 300 and 360 nm for the measured Delta data, Fig. 5.15a, were due to graphing artifact in the software program. When the value of Delta exceeds the maximum limit (270 for this software program), the data will enter the graph at the minimum range. If we select a different minimum value for Delta, it will change where this "step" appears.[33]

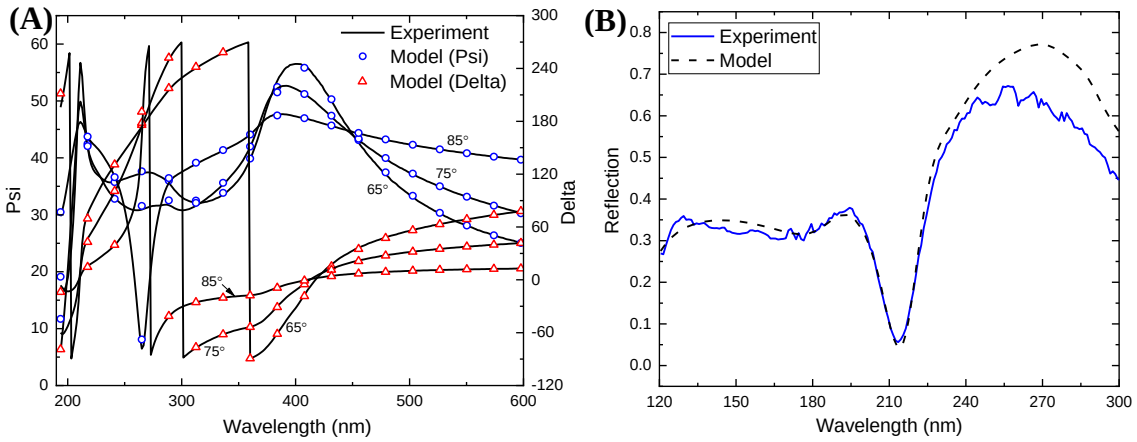

Figure 5.15. Curve fitting with Tauc-Lorentz model. (A) Fit spectroscopic ellipsometry data; (B) Fit far UV reflectance data (θ: 33°). The three different curves in (A) corresponds to the measurements at three different incident angles, 65°, 75°, and 85°.

The measured (n, k) from all methods, together with the reference values, are shown in Fig. 5.16. The measured values of (n, k) agree well with the results reported from several groups, Table 5.4. The discrepancies could be due to the variation of the deposition and calculation methods. Besides, the results from all methods showed that the cut-off wavelength is at 225 – 230 nm, which agrees with the measured bandgap for HfO_2 grown by ALD (E_g ~ 5.1eV, λ_c ~ 243nm).[34]

Table 5.4. References for the refractive index of HfO_2 thin films, shown in Fig. 5.16.

	Growth	**Measurements**	**Method**	**Wavelength**
Ref. 1 [35]	Evaporation	SE + R%	UDM	120 nm – IR
Ref. 2 [34]	PEALD	T%	Cauchy	250 nm – visible
Ref. 3 [36]	ALD	SE	Cauchy	245 nm – IR

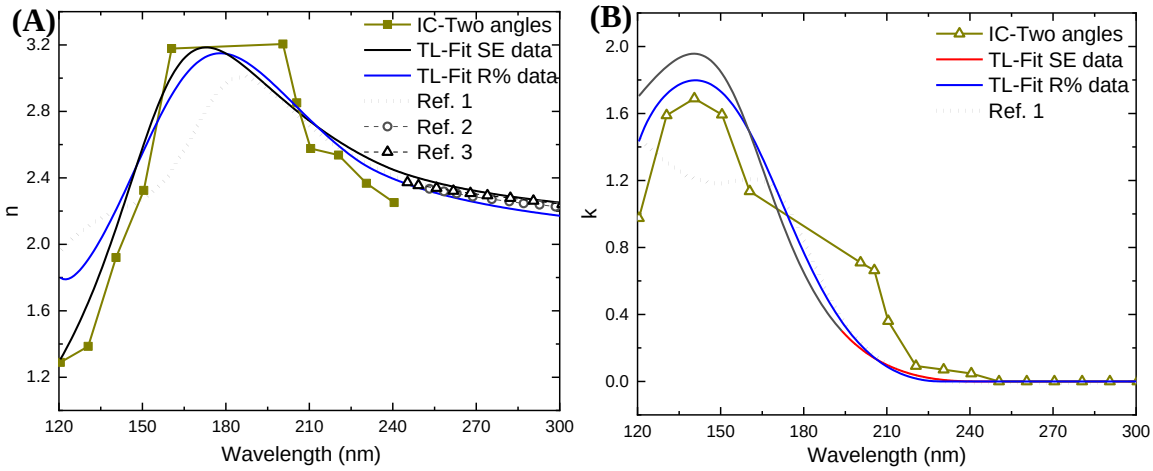

Figure 5.16. Optical constants determined for HfO_2 in this work.
(A) Refractive index n; (B) Extinction coefficient k.

5.4.4 Ga_2O_3

5.4.4.1 Optical Properties from Band Structures

Ga_2O_3 has several polymorphs, and the most stable phase, β-Ga_2O_3, is a semiconductor with an indirect bandgap of 4.8 eV from experiment.[37] DFT calculation shows an indirect band gap of 2.19 eV, Fig. 5.17a, which is due to an underestimation of the band gap in first-principles calculations.[38] The real and imaginary part of the dielectric constants are calculated and shown in Fig. 5.17b. The peaks in the imaginary dielectric constant spectrum correspond to inter-band transitions , which can be assigned with the help of the calculated density of states.[38]

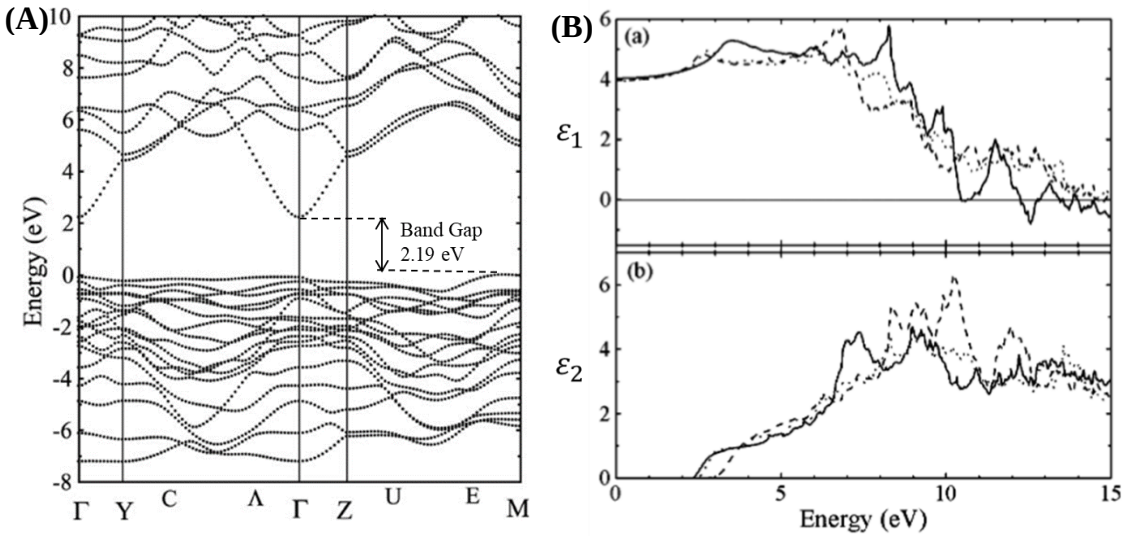

Figure 5.17. Band structure and optical properties of β-Ga_2O_3 calculated with DFT. (A) Band structure shows an indirect band gap of 2.19 eV; (B) Calculated dielectric constants. (a) real and (b) imaginary part. The dotted, broken, and solid lines represent the optical properties via the polarized dipoles along the x-, y-, and z-directions, respectively.[38] Copyright © 2004, Elsevier Ltd.

5.4.4.2 Optical Properties from Reflectance Measurements

UV (120 – 300 nm) reflectance were measured for Ga_2O_3 with thickness 11.4 nm and 19.4 nm grown on silicon substrate, at incident angles 33°and 75°, Fig. 5.18. The reference spectrum for the bare silicon is shown in this figure, for both 33°and 75°. For the Ga_2O_3, the reflectance peaks 126 – 135 nm are not visible on the silicon spectrum. These wavelengths correspond to an energy of 9.2 – 9.8 eV.

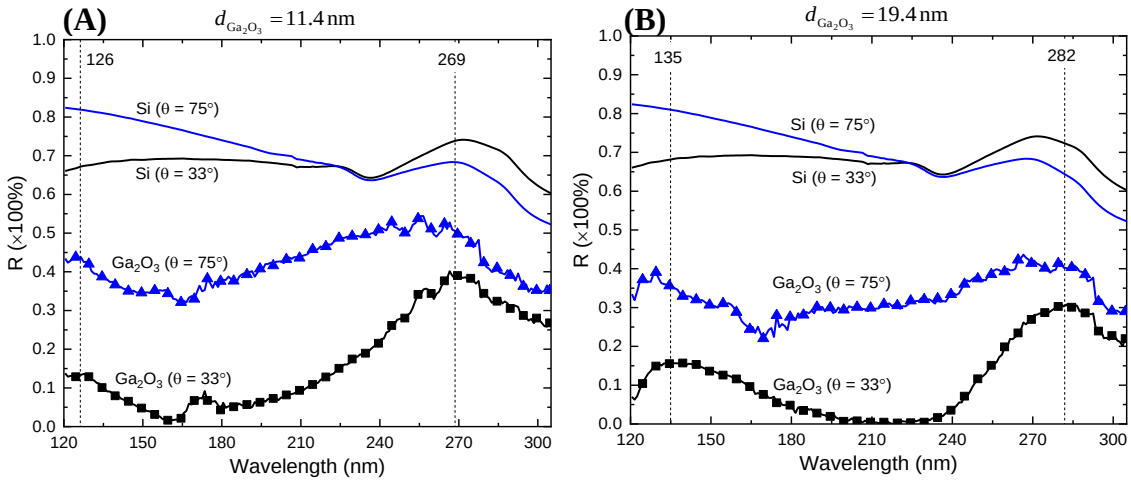

Figure 5.18. Far UV reflectance measurements for Ga_2O_3 with two different thicknesses at incident angles 33°and 75°. (A) 11.4 nm; (B) 19.4 nm.

5.4.4.2.1 Iso-Reflectivity Curve Method

The iso-reflectivity curve method was described in Chapter 3. Simply speaking, at each wavelength, two independent reflectance data were needed to draw the iso-reflectance curves. The intersection point on the iso-reflectance curves determines the value of (n, k) of Ga_2O_3 at this wavelength.

In this work, two methods were used based on the iso-reflectance curve. First, at same incident angle (33°), reflectance for Ga_2O_3 sample of two thicknesses were measured. Second, for the Ga_2O_3 of each thickness, reflectance at two incident angles 33° and 75° were measured. In total, there are three independent results for the (n, k) values of Ga_2O_3, in the wavelength 120 – 300 nm, Fig. 5.19. With the relations between dielectric and optical constants, Eq. (5.1) and (5.2), the dielectric constants $(\varepsilon_1, \varepsilon_2)$ can be obtained, Fig. 5.20. The peaks observed on the reflectance spectrum, ~130 nm, were also shown on the curve

of extinction coefficient k, Fig. 5.19b, and on the curve of imaginary dielectric constant ε_2, Fig. 5.20b. Besides, there are no peaks at ~280 nm at the curves of k and ε_2 of Ga_2O_3, while silicon has a provident peak at this position, Fig. 5.21. This suggests the Ga_2O_3 should have an inter-band transition at around ~130 nm (9.5 eV), Fig. 5.17b.

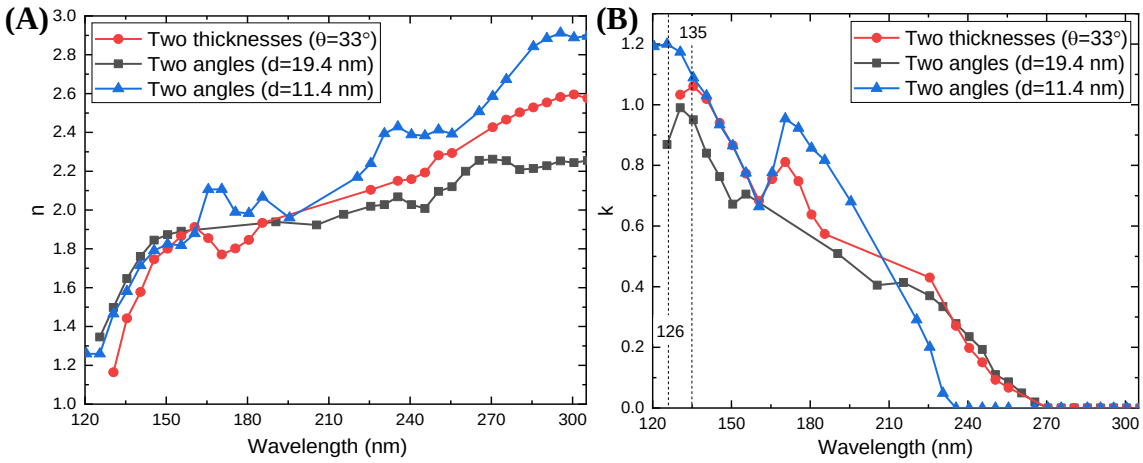

Figure 5.19. (n, k) determined for Ga_2O_3 from iso-reflectance curves. (A) Refractive index n; (B) Extinction coefficient k.

$$\varepsilon_1 = n^2 - k^2 \quad \text{(Eq. 5.1)}$$

$$\varepsilon_2 = 2nk \quad \text{(Eq. 5.2)}$$

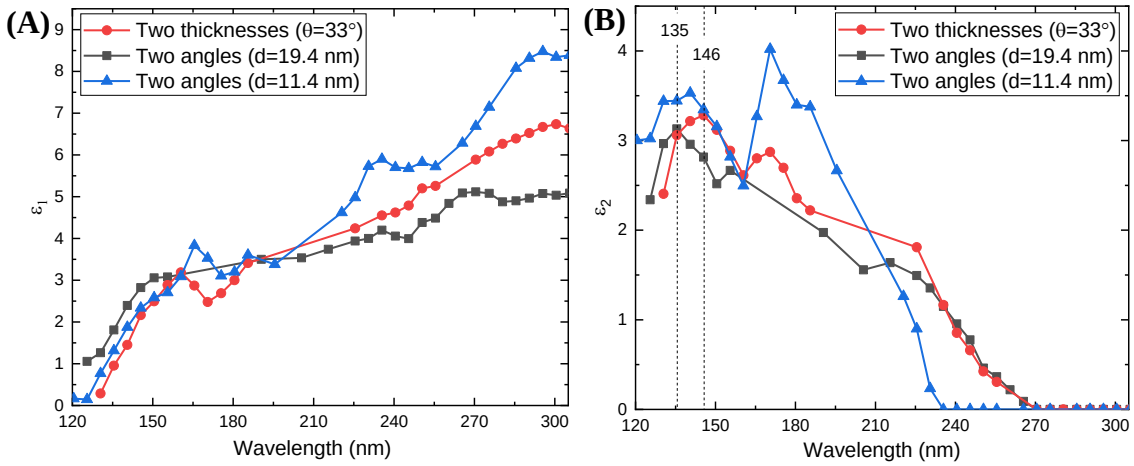

Figure 5.20. (ε_1, ε_2) for Ga_2O_3 converted from (n, k) in Fig. 5.2. (A) Real part ε_1; (B) Imaginary part ε_2.

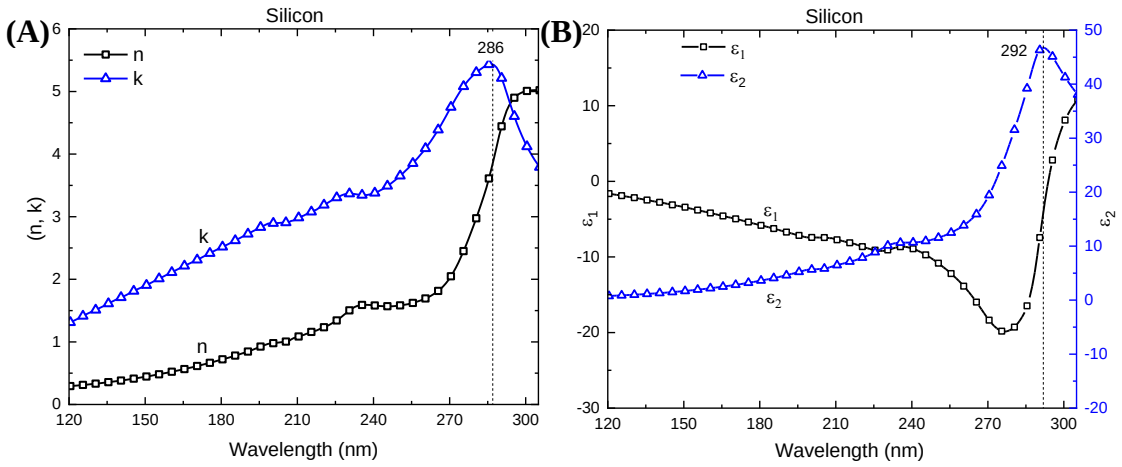

Figure 5.21. (n, k) and $(\varepsilon_1, \varepsilon_2)$ for silicon substrate. (A) (n, k); (B) $(\varepsilon_1, \varepsilon_2)$.

Fig. 5.19a shows that the refractive indices measured for both samples follow the same trend, with increasing discrepancies toward longer wavelength. This is because when $k \to 0$, the two iso-reflectivity curves become more parallel near the intersection points.[18, 19, 39] This brings a larger uncertainty for the determination of n. It was reported that, for AlF_3, this method works better when $k > 0.2$.[19] It needs to be mentioned here that, for the 19.4 nm Ga_2O_3 sample, it contains some AlF_3 residuals on the surface. This could cause a reduction of the refractive index, as AlF_3 is a low index material (1.4 @ $\lambda = 300$ nm). Fig. 5.19b shows k starts to increase at around 232 – 270 nm, which agrees with the cut-off wavelength for β-Ga_2O_3, 258 nm. [12]

5.4.4.2.2 Tauc-Lorentz Model Method

The calculation method based on optical dispersion models was described in Chapter 3.The Tauc-Lorentz model can be used to model the dispersion of optical constants in the inter-band transition regions, for amorphous semiconductors and dielectrics.[40] In Tauc-Lorentz model, the relations between (n, k) and wavelength can be described using 5

parameters, with one Lorentz oscillator considered. Tauc-Lorentz model was used to fit spectroscopic ellipsometry and far UV reflectance data, for the Ga_2O_3 sample of each thickness.

5.4.4.2.2.1 Fit the Spectroscopic Ellipsometry Data

The spectroscopic ellipsometry data was fitted with Tauc-Lorentz model in the wavelength 193 – 800 nm, for Ga_2O_3 with each thickness, Fig. 5.22. For each thickness, ellipsometry data was measured at three incident angles 65°, 75° and 85°. These angles ensure the Brewster angle of silicon substrate (76°) is within this range.

The deduced values of (n, k) are shown in Fig. 5.23. It shows the refractive index n of thicker Ga_2O_3 (19.8 nm) is lower than n of thinner Ga_2O_3 (11.4 nm). This agrees with the results from the iso-reflectivity curve method, Fig. 5.19a. As for the values of k, the 11.4 nm Ga_2O_3 layer shows higher absorption, which is also consistent with the iso-reflectivity results, Fig. 5.19b. The measured cut-off wavelength, from Fig. 5.23, is at around 300 nm, which is greater than the one determined from the iso-reflectivity method (232 – 270 nm) and the value for β-Ga_2O_3, 258 nm.[41-43] The dielectric constants converted from (n, k) are shown in Fig. 5.23b. The imaginary dielectric constant ε_2 shows there is a peak at around 136 – 152 nm, this is close to the results from iso-reflectance curve methods, Fig. 5.20b.

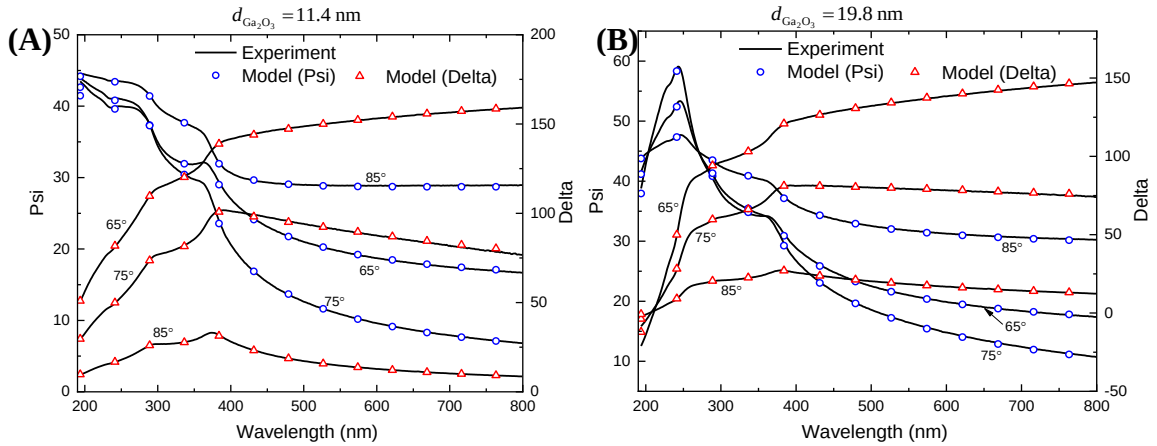

Figure 5.22. Fitted SE data with Tauc-Lorentz model. (A) For Ga_2O_3 with thickness 11.4 nm; (B) 19.8 nm. The three different curves in (A) and (B) correspond to the measurements at three different incident angles, 65°, 75°, and 85°.

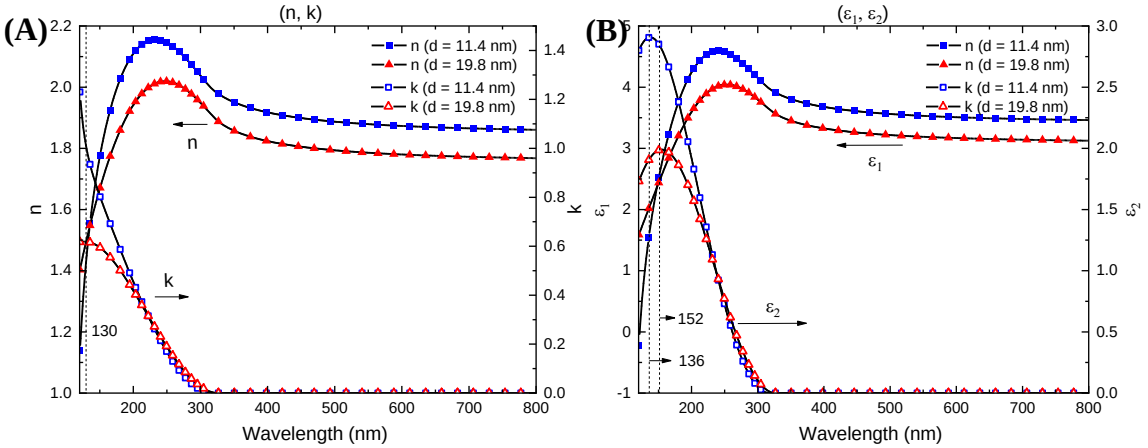

Figure 5.23. Measured (n, k) and $(\varepsilon_1, \varepsilon_2)$ for Ga_2O_3 with Tauc-Lorentz model. Fit spectroscopic ellipsometry data. (A) (n, k); (B) $(\varepsilon_1, \varepsilon_2)$.

5.4.4.2.2.2 Fit the Far UV Reflectance Data

The Tauc-Lorentz model was also applied to fit the far UV reflectance data, Fig. 5.24. The determined (n, k) for both samples are shown in Fig. 5.25. It shows that for the Ga_2O_3 with smaller thickness, the values of n and k are both higher than the thicker sample. This agrees with the iso-reflectivity method, and the Tauc-Lorentz method for

spectroscopic ellipsometry data. However, the cut-off wavelength cannot be determined from Fig. 5.24, as the value of k was not 0 in the wavelength 120 – 300 nm. This suggests that fitting reflectance data has limited accuracy. The complementary measurements with spectroscopic ellipsometry and far UV reflectance should be done to determine (n, k) in a broader wavelength range with a reliable accuracy.

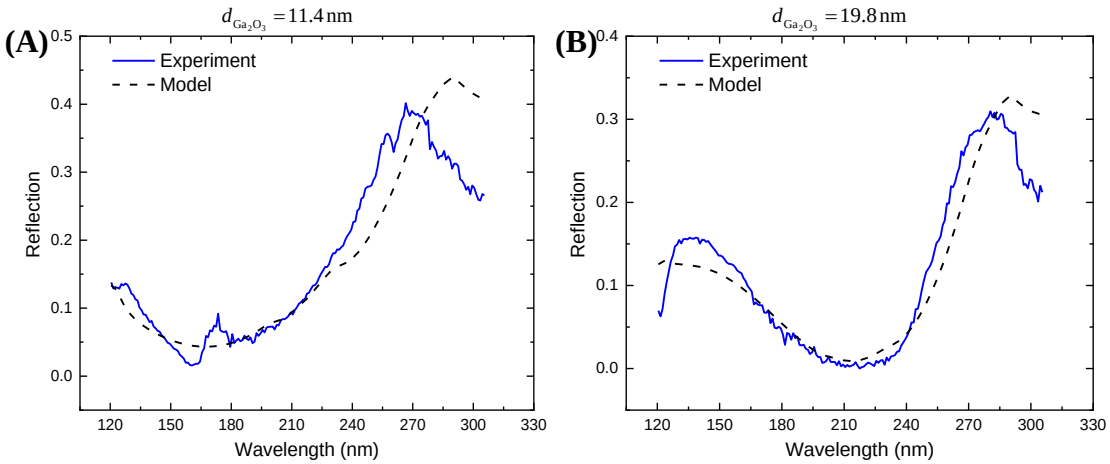

Figure 5.24. Fitted reflectance data with the Tauc-Lorentz model. (A) For Ga_2O_3 with thickness 11.4 nm; (B) 19.8 nm.

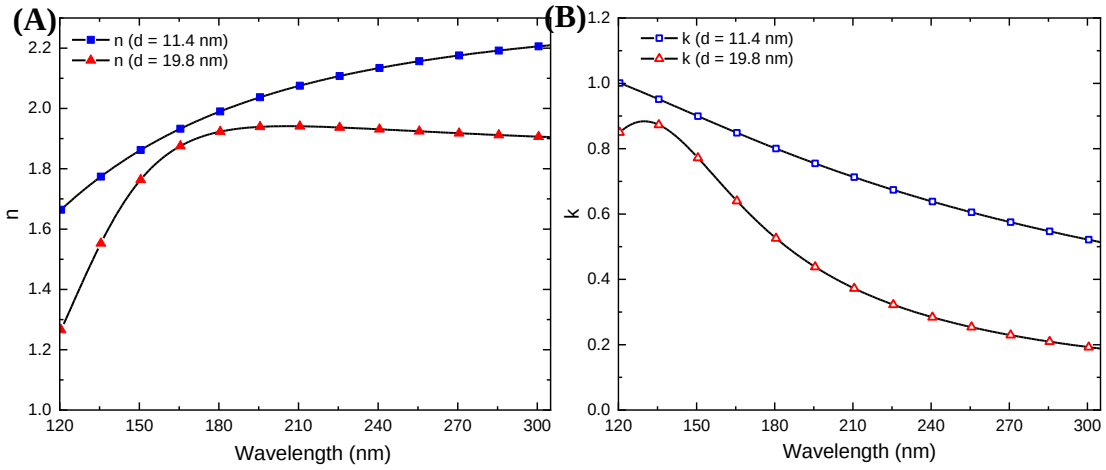

Figure 5.25. Measured (n, k) for Ga_2O_3 with Tauc-Lorentz model. Fit reflectance data. (A) Refractive index n; (B) Extinction coefficient k.

The dielectric constants (ε_1, ε_2) converted from (n, k) are shown in Fig. 5.26. The imaginary dielectric constant ε_2, Fig. 5.26b, shows a peak position at 135 – 142 nm, this agrees with the results from iso-reflectance curve method, and the Tauc-Lorentz model for SE data.

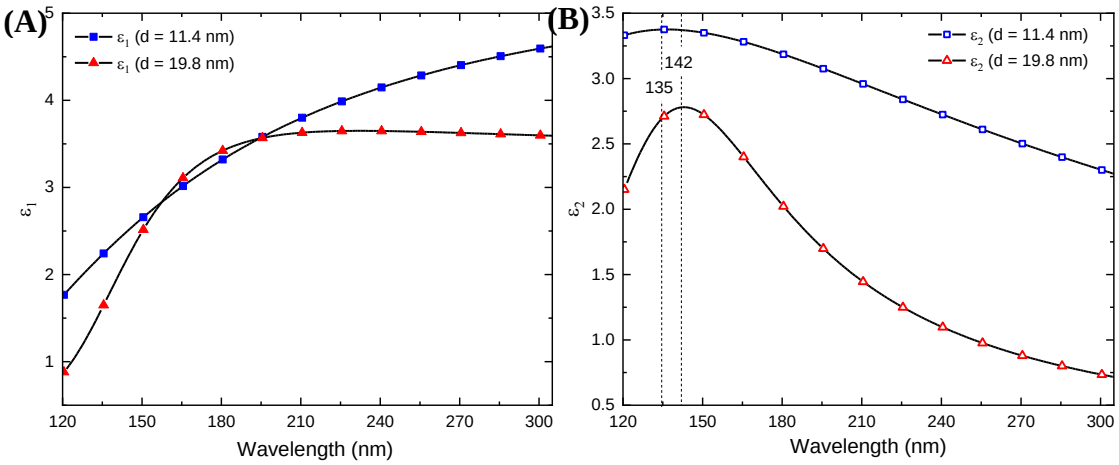

Figure 5.26. (ε_1, ε_2) for Ga_2O_3 converted from (n, k) in Fig. 5.25.
(A) Real part ε_1; (B) Imaginary part ε_2.

5.5 Comparison between Optical Calculation Methods

In this work, two optical calculation methods have been used, the iso-reflectance curve method, and the optical dispersion model method. The optical constants (n, k) determined from both methods were plotted together, for sample Ga_2O_3, Al_2O_3, and HfO_2, Fig. 5.27 – 5.29. For the AlF_3 sample, the results from the direct conversion and Cauchy dispersion model were plotted together, in Fig. 5.30.

For all four materials, it shows that the optical dispersion model resulted in a smoother curve of (n, k), which has more physical meaning and guarantees the Kramers-Kronig constraint. For the iso-reflectivity curve method, the fluctuation of the (n, k) comes

from the noise in the reflectance intensity measurements. The optical dispersion model is less sensitive to the environmental noise. However, each dispersion model has its limited spectral region and there is no such a model can work in the entire wavelength range. The iso-reflectance curve, in other hand, is independent of the dispersion models, and can be universally used for the determination of (n, k) with limited accuracy.

Regardless of the noise in the data, all the results gave the values of (n, k) with similar shapes and magnitude. It shows that for the iso-reflectance method, a larger uncertainty should be expected if the value of k is small. For the sample Ga_2O_3, Al_2O_3, and HfO_2, the cut-off wavelengths determined from both methods were similar, and agreed with the values reported from literature. It also shows that the dispersion model method could extrapolate the values of (n, k) into longer or shorter wavelengths, while the iso-reflectance curve can only calculate the (n, k) in the wavelength range where reflectance was scanned. Overall, both methods have their unique characteristics and the complementary use of them should give more accurate and complete results.

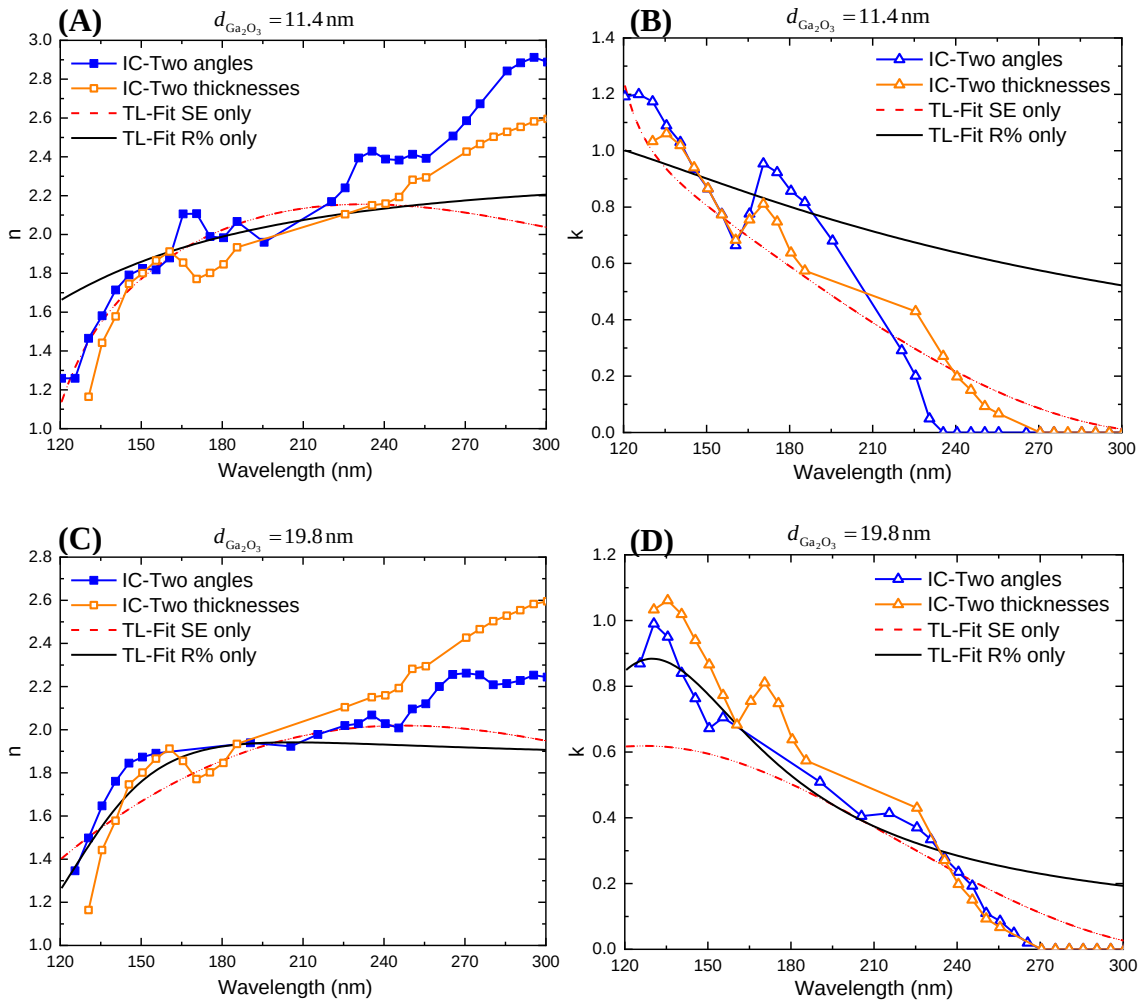

Figure 5.27. Determined (n, k) with all methods for Ga_2O_3 with each thickness. (A-B) (n, k) for 11.4 nm Ga_2O_3; (C-D) (n, k) for 19.8 nm Ga_2O_3.

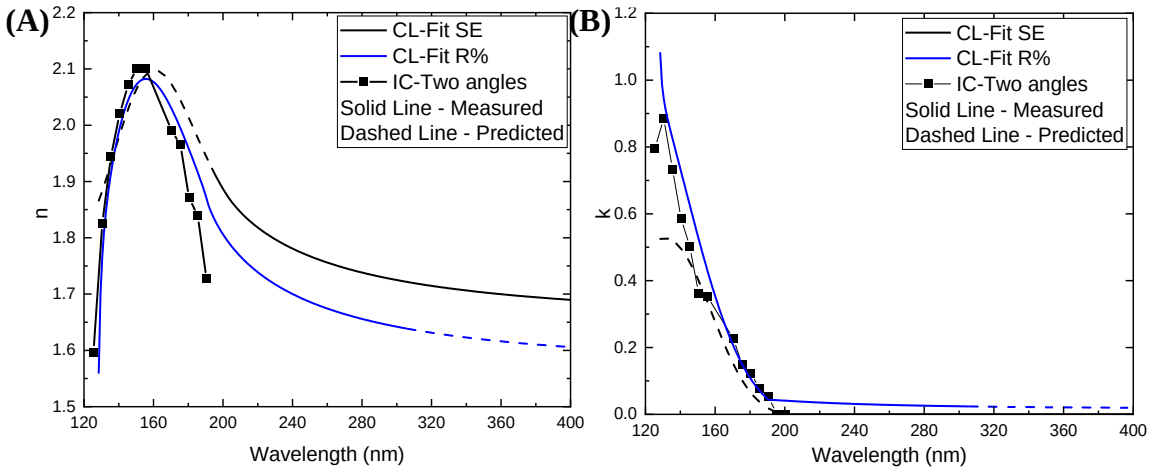

Figure 5.28. Determined (n, k) for Al_2O_3 with both methods.

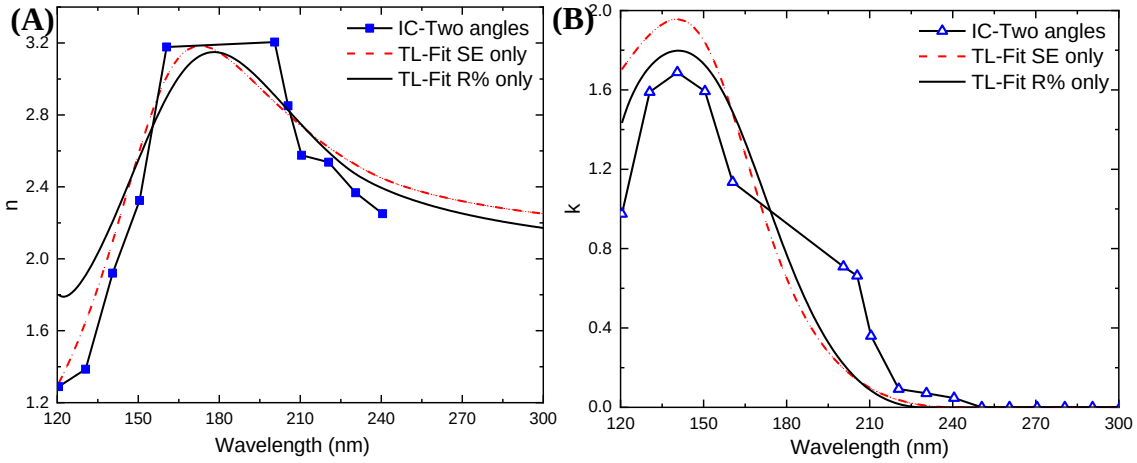

Figure 5.29. Determined (n, k) for HfO_2 with both methods.

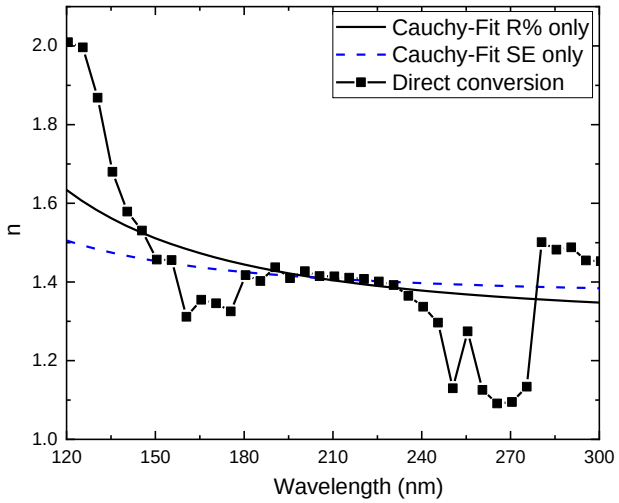

Figure 5.30. Determined (n, k) for AlF_3 with both methods.

5.6 Summary and Future Work

In summary, Ga_2O_3, Al_2O_3, HfO_2, and AlF_3 with 20 – 50 nm thickness have been grown on silicon wafer by atomic layer deposition. Far UV reflectance and spectroscopic ellipsometry measurements have been done for all the samples. The optical calculations methods based on iso-reflectivity curve and optical dispersion model have been developed

and used to determine the optical constants (n, k), in the far UV wavelength range (120 – 200 nm). For each material, the optical constants (n, k), dielectric constants (ε_1, ε_2), and cut-off wavelengths have been determined. For each material, results from both methods are consistent. Each method has its advantages and limitations, the complementary use of them can provide more accurate and complete information on the optical properties of the materials. From the measured imaginary dielectric constant ε_2, the inter-band transitions for each material were discussed. For the materials Ga_2O_3, Al_2O_3, and HfO_2, an inter-band transition or exciton is observed at 8 – 10 eV, which agrees with the calculated band structures and optical properties.

With the determination of the optical constants (n, k), the future work includes the application of these optical constants. Chapter 5 discusses the use of far UV spectroscopy for the study of material mixtures. With determined values of (n, k) for each constituent in the mixtures, the volume concentration of each phase can be determined. Chapter 6 discusses the use of (n, k) for the design of optical coatings and filters. Optical constants (n, k) measured for Al_2O_3, HfO_2, and AlF_3 are used for the design of bandpass interference filter, which can be used in far UV wavelength.

In conclusion, this work demonstrated a method based on far UV spectroscopy, for the study of the optical properties of thin films, including optical constants, cut-off wavelengths, and the inter-band transitions. Different optical calculation methods have been proposed, used, and discussed for their advantages and limitations. This method has been verified by comparison with more commonly used spectroscopic ellipsometry techniques. This work indicates that the complementary use of both far UV spectroscopy and spectroscopic ellipsometry provides more accurate and complete information for the

optical properties of the materials. Overall, this work developed a method based on far UV spectroscopy to investigate the optical properties of thin solid films grown by atomic layer deposition, which should be able to provide useful information for the optics and materials physics community.

References

[1] in *Handbook of Optical Constants of Solids*, edited by E. D. Palik (1991), Vol. 2, pp. 3.

[2] J. A. W. Co., "*"Goodness" of Fit: definition of the MSE*," in CompleteEASE Software Manual, Ch. 3.1 (J.A. Woollam Co., Lincoln, NE, 2014).

[3] J. I. Larruquert, "*Optical properties of thin film materials at short wavelengths*," in Optical Thin Films and Coatings, Ch. 7, edited by A. Piegari and F. Flory (Woodhead Publishing, 2018).

[4] O. Stenzel, "*Basic Knowledge on Optical Constants*," in Optical Coatings Material Aspects in Theory and Practice, Ch. 2, pp. 21, edited by O. Stenzel (Springer 2014).

[5] M. Jerman, Z. Qiao and D. Mergel, "Refractive index of thin films of SiO_2, ZrO_2, and HfO_2 as a function of the films' mass density," Appl. Opt. **44**, 3006 (2005).

[6] Z.-Y. Wang, R.-J. Zhang, H.-L. Lu, X. Chen, Y. Sun, Y. Zhang, Y.-F. Wei, J.-P. Xu, S.-Y. Wang, Y.-X. Zheng and L.-Y. Chen, "The impact of thickness and thermal annealing on refractive index for aluminum oxide thin films deposited by atomic layer deposition," Nanoscale Res. Lett. **10**, (2015).

[7] C. C. Lee, M. C. Liu, M. Kaneko, K. Nakahira and Y. Takano, "Influence of thermal annealing and ultraviolet light irradiation on LaF3 thin films at 193 nm," Appl. Opt. **44**, 6921 (2005).

[8] S. Shi, S. Qian, X. Hou, J. Mu, J. He and X. Chou, "Structural and optical properties of amorphous Al2O3 thin film deposited by atomic layer deposition," Adv. Condens. Matter Phys. **2018**, (2018).

[9] C. Barbos, D. Blanc-Pelissier, A. Fave, C. Botella, P. Regreny, G. Grenet, E. Blanquet, A. Crisci and M. Lemiti, "Al_2O_3 thin films deposited by thermal atomic layer deposition: Characterization for photovoltaic applications," Thin Solid Films **617**, 108 (2016).

[10] M. T. Aguilar-Gama, E. Ramírez-Morales, Z. Montiel-González, A. Mendoza-Galván, M. Sotelo-Lerma, P. K. Nair and H. Hu, "Structure and refractive index of thin alumina films grown by atomic layer deposition," Journal of Materials Science: Materials in Electronics **26**, 5546 (2015).

[11] C. C. Lee, M. C. Liu, M. Kaneko, K. Nakahira and Y. Takano, "Characterization of AlF3 thin films at 193 nm by thermal evaporation," Appl. Opt. **44**, 7333 (2005).

[12] D. J. Comstock and J. W. Elam, "Atomic Layer Deposition of Ga2O3 Films Using Trimethylgallium and Ozone," Chem. Mater. **24**, 4011 (2012).

[13] K. M. Kim, J. S. Jang, S. G. Yoon, J. Y. Yun and N. K. Chung, "Structural, Optical and Electrical Properties of HfO2 Thin Films Deposited at Low-Temperature Using Plasma-Enhanced Atomic Layer Deposition," Materials (Basel) **13**, (2020).

[14] C. Barbos, D. Blanc-Pelissier, A. Fave, E. Blanquet, A. Crisci, E. Fourmond, D. Albertini, A. Sabac, K. Ayadi, P. Girard and M. Lemiti, "Characterization of Al2O3 Thin Films Prepared by Thermal ALD," Energy Procedia **77**, 558 (2015).

[15] M. L. Huang, Y. C. Chang, C. H. Chang, T. D. Lin, J. Kwo, T. B. Wu and M. Hong, "Energy-band parameters of atomic-layer-deposition Al_2O_3 / InGaAs heterostructure," Appl. Phys. Lett. **89**, 012903 (2006).

[16] J. Hennessy, A. Jewell, K. Balasubramanian and S. Nikzad, "Ultraviolet optical properties of aluminum fluoride thin films deposited by atomic layer deposition," J. Vac. Sci. Technol., A **34**, 01A120 (2016).

[17] B. Fleming, M. Quijada, J. Hennessy, A. Egan, J. Del Hoyo, B. A. Hicks, J. Wiley, N. Kruczek, N. Erickson and K. France, "Advanced environmentally resistant lithium fluoride mirror coatings for the next generation of broadband space observatories," Appl. Opt. **56**, 9941 (2017).

[18] F. Bridou, M. Cuniot-Ponsard and J.-M. Desvignes, "Experimental determination of optical constants in the vacuum ultra violet wavelength region between 80 and 140nm: A reflectance versus thickness method and its application to ZnSe," Opt. Commun. **271**, 353 (2007).

[19] F. Bridou, M. Cuniot-Ponsard, J.-M. Desvignes, M. Richter, U. Kroth and A. Gottwald, "Experimental determination of optical constants of MgF2 and AlF3 thin films in the vacuum ultra-violet wavelength region (60–124nm), and its application to optical designs," Opt. Commun. **283**, 1351 (2010).

[20] J. L. Navarro, E. A. Albanesi, R. Vidal and J. Ferrón, "A study on the structural, electronic and optical properties of the α-AlF3 compound," Mater. Res. Bull. **83**, 615 (2016).

[21] Y. Lee, J. W. DuMont, A. S. Cavanagh and S. M. George, "Atomic Layer Deposition of AlF_3 Using Trimethylaluminum and Hydrogen Fluoride," J. Phys. Chem. C **119**, 14185 (2015).

[22] J. Hennessy, K. Balasubramanian, C. S. Moore, A. D. Jewell, S. Nikzad, K. France and M. Quijada, "Performance and prospects of far ultraviolet aluminum mirrors protected by atomic layer deposition," Journal of Astronomical Telescopes Instruments and Systems **2**, (2016).

[23] S. Günstera, H. Blaschkea, D. Ristaua, M. Danailovb, M. Trovób, A. Gattoc, N. Kaiserc, F. Sartod, D. Florid and F. Menchinid, "Radiation resistance of single- and multilayer coatings against synchrotron radiation," Proc. SPIE **5250**, 146 (2004).

[24] R. H. French, H. Müllejans and D. J. Jones, "Optical Properties of Aluminum Oxide: Determined from Vacuum Ultraviolet and Electron Energy-Loss Spectroscopies," J. Am. Ceram. Soc. **81**, 2549 (2005).

[25] Y.-N. Xu and W. Y. Ching, "Self-consistent band structures, charge distributions, and optical-absorption spectra in MgO, α-Al2O3, andMgAl2O4," Physical Review B **43**, 4461 (1991).

[26] A. S. Ferlauto, G. M. Ferreira, J. M. Pearce, C. R. Wronski, R. W. Collins, X. Deng and G. Ganguly, "Analytical model for the optical functions of amorphous semiconductors from the near-infrared to ultraviolet: Applications in thin film photovoltaics," J. Appl. Phys. **92**, 2424 (2002).

[27] F. Naumann, J. Reck, H. Gargouri, B. Gruska, A. Blümich, A. Mahmoodinezhad, C. Janowitz, K. Henkel and J. I. Flege, "In situ real-time and ex situ spectroscopic analysis of Al2O3 films prepared by plasma enhanced atomic layer deposition," J. Vac. Sci. Technol., B **38**, (2020).

[28] Bernhard von Blanckenhagen, Diana Tonova and J. Ullmann, "Application of the Tauc–Lorentz formulation to the interband absorption of optical coating materials," Appl. Opt. **41**, 3137 (2002).

[29] A. Duparré, R. Geyl, D. Franta, D. Nečas, I. Ohlídal and A. Giglia, in *Optical Systems Design 2015: Optical Fabrication, Testing, and Metrology V* (2015).

[30] M. Balog, M. Schieber, M. Michman and S. Patai, "Chemical vapor deposition and characterization of HfO2 films from organo-hafnium compounds," Thin Solid Films **41**, 247 (1977).

[31] T. Tan, Z. Liu and Y. Li, "First-principles calculations of electronic and optical properties of Ti-doped monoclinic HfO2," J. Alloys Compd. **510**, 78 (2012).

[32] J. C. Garcia, presented at the AIP Conference Proceedings, 2005 (unpublished).

[33] H. G. Tompkins and J. N. Hilfiker, *Spectroscopic Ellipsometry: Practical Application to Thin Film Characterization*. (Momentum Press, LLC, New York, 2016).

[34] R. Drazdys, L. Stasiūnas, K. Leinartas, R. Buzelis, T. Tolenis, K. Juškevičius, U. Gimževskis, A. Selskis and V. Jasulaitienė, "Optical Properties of HfO2 Thin Films Grown by Atomic Layer Deposition," Optical Interference CoatingsWB.2 (2016).

[35] D. Franta, D. Necas and I. Ohlidal, "Universal dispersion model for characterization of optical thin films over a wide spectral range: application to hafnia," Appl Opt **54**, 9108 (2015).

[36] S. Li, Y. Zhang, D. Yang, W. Yang, X. Chen, H. Zhao, J. Hou and P. Yang, "Structure and optical properties of HfO2 films on Si (100) substrates prepared by ALD at different temperatures," Physica B **584**, 412065 (2020).

[37] H. Xue, Q. He, G. Jian, S. Long, T. Pang and M. Liu, "An Overview of the Ultrawide Bandgap Ga2O3 Semiconductor-Based Schottky Barrier Diode for Power Electronics Application," Nanoscale Res. Lett. **13**, (2018).

[38] K. Yamaguchi, "First principles study on electronic structure of β-Ga2O3," Solid State Commun. **131**, 739 (2004).

[39] W. R. Hunter, "Measurement of optical properties of materials in the vacuum ultraviolet spectral region," Appl. Opt. **21**, 2103 (1982).

[40] G. E. Jellison and F. A. Modine, "Parameterization of the optical functions of amorphous materials in the interband region," Appl. Phys. Lett. **69**, 371 (1996).

[41] D. F. Edwards, "*Beta-Gallium Oxide (β-Ga2O3)*," in Handbook of Optical Constants of Solids, pp. 753 (Elsevier, 1997).

[42] S. Ghose, S. Rahman, L. Hong, J. S. Rojas-Ramirez, H. Jin, K. Park, R. Klie and R. Droopad, "Growth and characterization of β-Ga2O3 thin films by molecular beam epitaxy for deep-UV photodetectors," J. Appl. Phys. **122**, 095302 (2017).

[43] S. J. Hao, M. Hetzl, F. Schuster, K. Danielewicz, A. Bergmaier, G. Dollinger, Q. L. Sai, C. T. Xia, T. Hoffmann, M. Wiesinger, S. Matich, W. Aigner and M. Stutzmann, "Growth and characterization of β-Ga2O3 thin films on different substrates," J. Appl. Phys. **125**, 105701 (2019).

CHAPTER 6

FAR ULTRAVIOLET SPECTROSCOPY FOR MATERIAL MIXTURES: APPLICATION TO PEALD AlF_3 AND ECR-PECVD BN

6.1 Introduction

Incorporation of another phase into a pure phase material can be intentional, such as doping, or unwanted, such as impurities. Material mixtures have different types based on the formation of the mixtures, including homogenous mixture, guest-host system, nano-laminate, and rough interfaces.[1] Optical and X-ray techniques are commonly used to distinguish each constituent in the mixtures, including Raman spectroscopy, Fourier-transform infrared spectroscopy (FT-IR), spectroscopic ellipsometry, X-ray diffraction (XRD), and X-ray photoelectron spectroscopy (XPS). Each of these techniques has their own advantages and limitations. For example, FT-IR, Raman, and XRD are desirable to be used for crystalline materials; XPS can detect the elements and bonding states in the materials but is only sensitive to the top 5 – 10 nm of the materials. Spectroscopic ellipsometry is sensitive to the optical properties of the materials, but has limitations for the use in far UV wavelength due to the shortage of efficient wideband polarizers and retarders.[2] In this work, an optical method based on far UV (120 – 200 nm) spectroscopy was developed as a complement for the analysis of the material mixtures. The far UV reflectance measurements can be used to distinguish the constituents in the mixtures and determined the volume concentration of each one.

In semiconductors, inter-band transitions can be measured with optical spectroscopy. Wide bandgap semiconductors, such as diamond and cubic boron nitride, have a band gap of 5.5 eV and 6.4 eV, respectively.[3] Inter-band transition happens if the photonic energy of the light is greater than the band gap of the materials. Light in the far UV wavelengths correspond to the photonic energies in the range of 6.2 – 10.3 eV. For diamond, optical measurements showed it has a strong inter-band transitions at 7.4 eV, corresponding to the $\Gamma'_{25} \rightarrow \Gamma_{15}$ transition on the band structure.[4] Boron nitride has two common polytypes, the graphite-like hexagonal phase (h-BN) and the diamond-line cubic phase (c-BN). Inter-band transitions for BN have been measured using electron energy loss spectroscopy,[5, 6] luminescence excitation spectroscopy,[7] and transmission measurements.[5] Both measurements suggest several direct or indirect band transitions in the far UV range. Hexagonal BN has a strong transition at 6.1 eV related with the π-electron plasmon which is absent for the cubic BN.[5] π plasmon in the h-BN arises from the collective oscillations of bound electrons in its graphite-like structures. Optical absorption occurs during the inter-band transitions, which can be indicated on the imaginary dielectric constant of the materials. Optical spectroscopy can be used to measure the absorption and thus the imaginary dielectric function for the observation of inter-band transitions. Thus, the hexagonal and cubic boron nitride should be distinguishable using the far UV spectroscopy.

For the material mixtures, the volume concentration of each constituent can be determined using optical spectroscopy. For example, it is observed in our work that plasma enhanced ALD can produce AlF_3/Al mixture films. X-ray photoelectron spectroscopy (XPS) can be used to estimate the volume concentration, but XPS is only sensitive to the

top 5 nm of the material. Thus, XPS cannot make accurate estimations for the film with thickness greater than 5 nm. Metal dielectrics such as AlF_3 have an ultrawide bandgap >10 eV and are transparent in the far UV. For the materials with little absorption, the light beam can easily penetrate them and detect their optical properties by measuring the reflectance. For the AlF_3/Al mixtures, the Al concentration can be determined by fitting the measured reflectance with the effective medium approximation (EMA) method.[1] This method requires the measurements of the optical constants (n, k) for each constituent, which can be done with the reflectance methods described in Chapter 4. Thus, far UV spectroscopy can be used to determine the volume concentration for the materials with little absorption.

In this work, we demonstrated the use of far UV spectroscopy for the study of material mixtures. AlF_3/Al and h-BN/c-BN mixtures were grown for this study. Spectroscopic ellipsometry and X-ray photoelectron spectroscopy were used as complements tools to verify the results from the far UV spectroscopy.

6.2 Materials and Methods

The AlF_3 layers were grown on (0001) sapphire substrate by custom-built plasma-enhance ALD, with trimethylaluminum (TMA) and HF-pyridine as precursors. An H_2 plasma process was used during the deposition. The BN layers were grown on 10×10mm polycrystalline diamond substrate by custom-built ECR-PECVD, with BF_3 and NH_3 as precursors.

A custom-built far UV spectrometer was used for the UV reflectance measurements, at wavelengths 120 – 300 nm. A commercial spectroscopic ellipsometer (J. A. Woollam, M-2000DI) was used for the ellipsometry measurements, from 193 nm to 1689 nm wavelength. X-ray diffraction (Malvern PANalytical Aeris) and Raman

spectroscopy (custom built multi-wavelengths, Eyring Materials Center, ASU) were used to distinguish the phase in the BN films. A commercially available software program CompleteEASE (J. A. Woollam, v6.51) was used to analyze the ellipsometry and reflectance data. Bruggeman effective medium approximation was used for the determination of the volume concentration.

6.3 Effective Medium Approximation

For material mixtures with known compositions, the dielectric function for the mixtures can be estimated from the effective medium approximation (EMA), Eq. (6.1).[8]

$$\varepsilon_{\mathrm{EMA}} = f_a \varepsilon_a + f_b \varepsilon_b \qquad \text{(Eq. 6.1)}$$

with the constraint $f_a + f_b = 1$. Here (f_a, f_b) and $(\varepsilon_a, \varepsilon_b)$ are the volume fraction and dielectric functions of each constituent, respectively.

Bruggeman's method assumes that the mixtures are homogenous. The effective dielectric function can be calculated with Eq. (6.2). Here, p_j represents the volume concentration of the *j*-th constituent in the mixtures, ε_{eff} represents the effective dielectric function, and *L* is the depolarization factor, which depends on the morphology of the mixtures.

$$0 = \sum_j p_j \frac{\varepsilon_j - \varepsilon_{eff}}{\varepsilon_{eff} + (\varepsilon_j - \varepsilon_{eff})L} \qquad \text{(Eq. 6.2)}$$

In this work, the Bruggeman model was used for the data analysis. The EMA method requires input of the optical constants for each constituent, for the determination of the volume concentration of the constituents. A detailed description of the effective medium approximation can be found in Chapter 3.8.

6.4 Results

6.4.1 AlF_3/Al Mixtures

A 43 nm AlF_3 layer was grown on sapphire by plasma-enhance ALD. Spectroscopic ellipsometry data was measured in the wavelength 193 – 1689 nm, at incident angles 50°, 55° and 60°. Reflectance intensity data was measured in the wavelength 120 – 300 nm, at incident angle 33°. The optical constants (n, k) used for AlF_3 were deduced from the Cauchy method described in Chapter 5. For the Al and the sapphire substrate, the optical constants used are from the literature.[9] Two different approaches were used for the data analysis: i) fit the spectroscopic ellipsometry (SE) data with the EMA; and ii) fit the reflectance (R%) data with the EMA.

6.4.1.1 Fit spectroscopic ellipsometry data

Spectroscopic ellipsometry data were measured at three incident angles, 50°, 55° and 60°, Fig. 6.1. Fig. 6.1b shows sharp steps on the measured Delta data at 295 and 375 nm. These steps arise from the graphing artifact in the software program. If the Delta value exceeds the maximum limit (270 for this software program), the data will enter the graph at the minimum range.[18]

The structure of materials is 43 nm AlF_3/Al on sapphire. The volume concentration of the Al, and the depolarization factor *L* were varied to fit the ellipsometry data. The root mean square error (RMSE) was used to quantify the "goodness of fit". The results showed the volume concentration of Al is 2.6±0.01 vol. %, with a depolarization factor of 0.284±0.002.

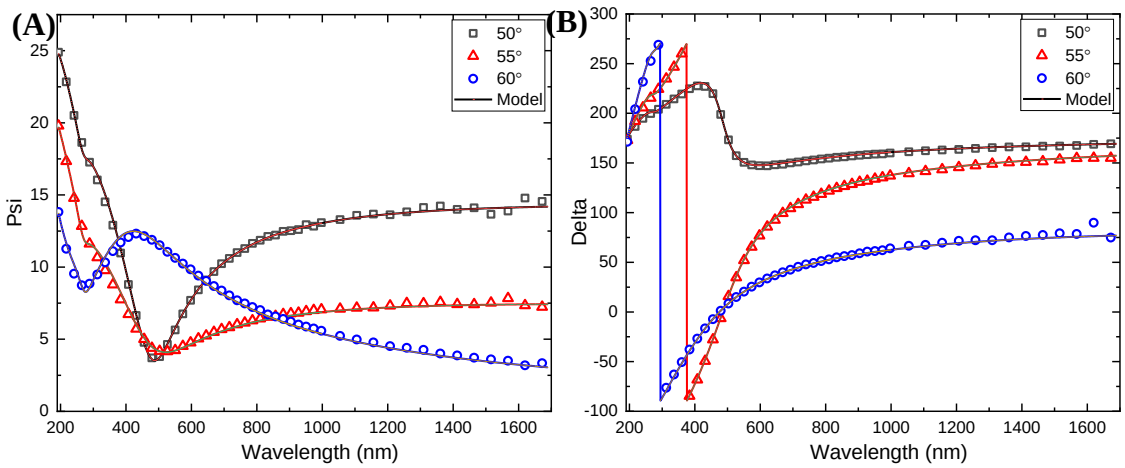

Figure 6.1. Fitted spectroscopic ellipsometry data with EMA method.

6.4.1.2 Fit reflectance data

Reflectance intensity data was measured with custom-built far UV spectrometer in the wavelength of 120 – 300 nm, at incident angle 33°. The reflectance was calibrated with the correction factors determined from a standard single crystal silicon wafer. Similar with the ellipsometry data analysis, only the Al concentration was varied to fit the reflectance curve. The results showed the volume concentration of Al is 1.6±0.16 vol. %, with a with a depolarization factor of 0.287±0.012. Fig. 6.2 shows there is a discrepancy between the data and model at shorter wavelength. This is because of the Al optical constants used may not be sufficiently accurate to describe the Al-clusters inside the AlF_3 films.

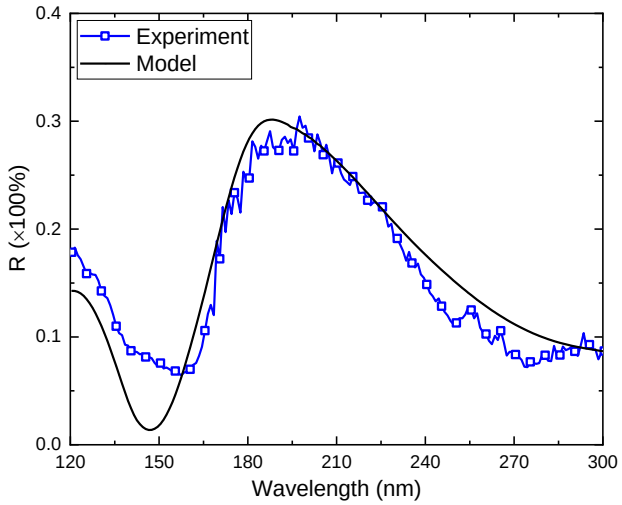

Figure 6.2. Fitted far UV spectroscopy data with EMA method.

6.4.1.3 Comparison between different methods

The results for the vol. % of Al inside the AlF_3 films from both methods are close, 2.6±0.01 vol. % and 1.6±0.16 vol. %. Compared with fitting spectroscopic ellipsometry data, fitting reflectance data gives a higher uncertainty. This is because ellipsometry measures both the intensity and the phase change of the reflected beam, while spectroscopy can only measure the intensity. Since ellipsometry measures the ratio of the complex reflectance between two polarized reflected beams, it is less sensitive the environmental noises.[10]

An additional 4 nm PEALD AlF_3 layer was grown on a 33 nm Al_2O_3/Si substrate for the XPS measurements. XPS spectra of the Al 2p region is shown in Fig. 6.3 for the PEALD AlF_3 films. The Al-Al bonding states shown in Fig. 6.3 indicates it has Al clusters in the AlF_3 films. The peak area of each Al bonding states was calculated, Table 6.1. The atomic concentration of the Al was determined to be 4.8±0.95 at. % by comparing the peak areas. The discrepancy between the XPS and the optical analysis can be due to the uncertainty of the optical constants used to describe the Al clusters inside the films. Besides,

the samples measured using XPS and optical methods were different, which might suggest the volume concentration of the Al is thickness dependent. Further experiments need to be done to confirm this statement.

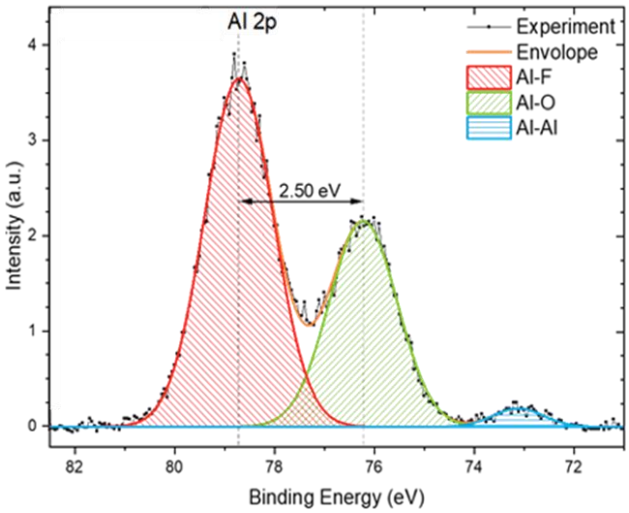

Figure 6.3. XPS Al 2p spectra of plasma enhance ALD AlF_3 films on 33 nm Al_2O_3/Si. The peaks associated with AlF_3 (red), Al_2O_3 (green), and Al clusters (blue) are shown. Courtesy of Daniel C. Messina in Nanoscience Laboratory, ASU.

Table 6.1. Comparison of the Al 2p XPS peak parameters for before and after deposition of PEALD AlF_3 film. Errors are calculated from peak fitting and instrument resolution. Unless listed, errors were less than 0.1 eV. Courtesy of Daniel C. Messina in Nanoscience Laboratory, ASU.

		Chemical State (Al 2p)	Peak Energy (eV)	Peak Width FWHM (eV)	Peak Area (eV-cts/s)
PEALD	Before	Al-O	75.9	1.5	11.3
	After	Al-O	76.2	1.6	3.7
		Al-F	78.7	1.6	6.3
		Al-Al	73.1 ± 0.1	1.2 ± 0.2	0.3

6.4.2 h-BN/c-BN mixtures

Epitaxial growth of cubic BN on crystalline diamond is challenging, and the hexagonal phase usually forms during the deposition.[11, 12] Cubic BN has a zinc-blende structure, and is isotropic on the optical properties, with a refractive index of 2.13 for bulk material. Hexagonal BN has graphite structure, and is anisotropic, with an ordinary refractive index of 2.17, and an extra-ordinary refractive index of 1.65.[13, 14]

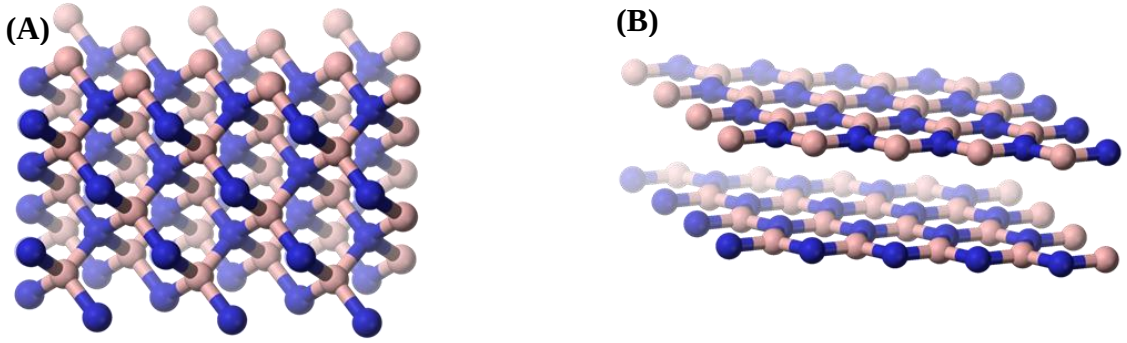

Figure 6.4. Crystal structures of boron nitride. (A) Cubic BN with zinc-blende structure, (B) Hexagonal BN with graphite structure.[15] Copyright © Public Domain.

6.4.2.1 Optical Properties from Band Structures

Hexagonal phase of BN (h-BN) has an indirect bandgap of 4.07 eV from the band DFT calculation, which is lower than the experimental value, 5.96 eV.[16] For the cubic phase of BN (c-BN), the calculated indirect band gap is 5.18 eV, which is also lower than the experimental value, 6.4 eV.[16] The calculated band gap is lower than the experimental values, this is because the local density approximation (LDA) method used in this calculation usually underestimates the band gap of semiconductors and insulators.[16]

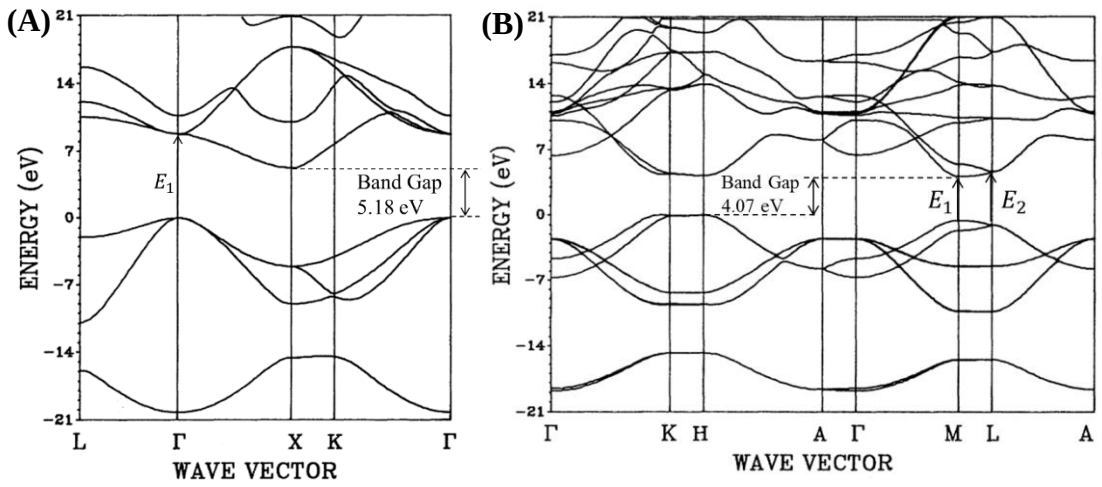

Figure 6.5. Band structures of boron nitride. (A) Cubic boron nitride; (B) Hexagonal boron nitride.[16] Copyright © 1991, The American Physical Society.

The optical properties calculated from the band structures are shown in Fig. 6.6.[16] Compared with the experimental values used in this study, there is a shift of the energy level for the electronic transitions, this is due to the underestimation of the conduction band energies from first principles calculations.[16] The peak positions in Fig. 6.6 are label in the band structures. For the h-BN, the first two strong transitions occur at 6.1 eV and 6.95 eV, are direct inter-band transition along the L and M point, labeled E_1 and E_2 in the Fig. 6.5b, respectively. For the c-BN, the first strong peak occurs at ~ 10 eV, this corresponds to inter-band transition along Γ point in Fig. 6.5a. Thus, both transitions in h-BN occur in far UV wavelength, which can be detected using far UV spectroscopy.

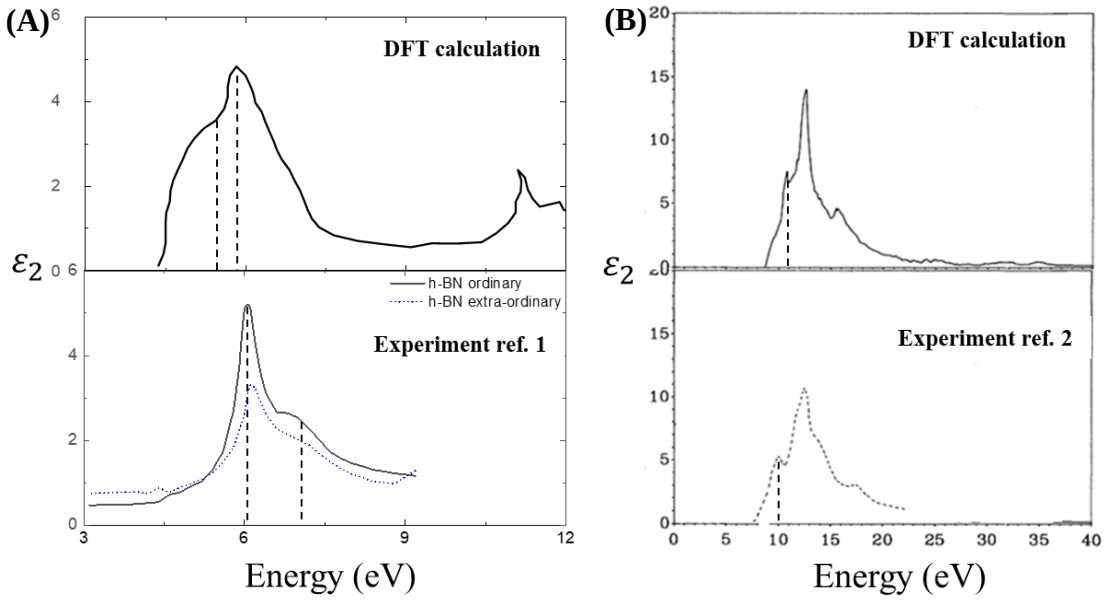

Figure 6.6. Imaginary dielectric constant of boron nitride calculated from the band structures in Fig. 6.5. (A) Hexagonal boron nitride; (B) Cubic boron nitride. In comparison with the experiment results ref. 1,[17] and ref 2.[16] Copyright © 1991, The American Physical Society.

Since the BN films are grown on diamond, the optical properties of diamond also need to be investigated. The calculated band structure of diamond is shown in Fig. 6.7a. It shows that diamond has an indirect band gap of 5.4 eV. The measured imaginary dielectric constants showed it has a strong transition at 7.4 eV, Fig. 6.7, which is related to the $\Gamma'_{25} \rightarrow \Gamma_{15}$ transition on the band structure, Fig. 6.7a.[4]

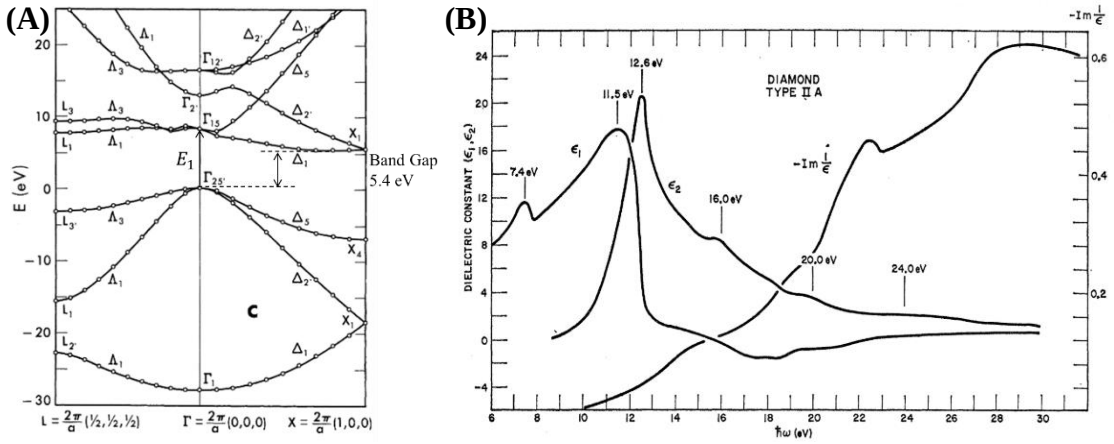

Figure 6.7. Band structure and optical properties of diamond. (A) Band structure calculated with DFT. (B) Dielectric constants measured from experiment.[4] Copyright © 1964, The American Physical Society.

6.4.2.2 Optical Constants of BN

6.4.2.2.1 Optical Constants of h-BN

For the h-BN, a 160 nm h-BN was grown on single crystal silicon wafer. The optical constants (n, k) of h-BN on silicon were measured by spectroscopic ellipsometry in the transparent region (1.25 – 3 eV). A bi-axial model was used to characterize the anisotropic refractive index of h-BN. For the ordinary and extra-ordinary index, Cauchy model was used for the dispersion. The measured refractive index, Fig 11a, is close to the results reported by M. Schubert et al.[18] For the extra-ordinary index, the "turning" point showed on the measurement indicates there might be some amorphous phase (a-BN) in the films, compared with Fig. 6.8b.

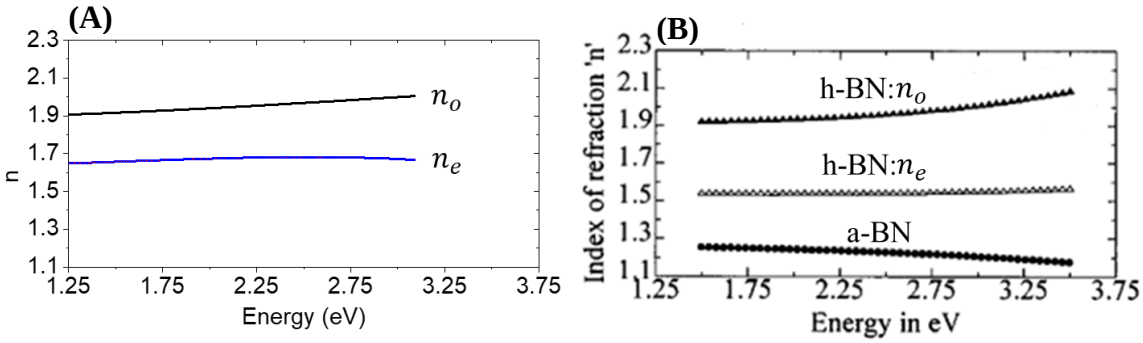

Figure 6.8. Refractive index of h-BN from spectroscopic ellipsometry measurements. (A) 160 nm h-BN grown on silicon; (B) Reference from M. Schubert et al. [18]

The far and middle UV reflectance measurements for 160 nm h-BN on silicon have been measured in the 120 – 300 nm wavelength, Fig. 6.9. Compared with the single crystal silicon, h-BN has several provident peaks on the reflectance spectrum. In the far UV range, two peaks at 175.7 and 200.2 nm correspond to the inter-band transitions at 6.1 and 6.9 eV, observed by C. Tarrio and S. E. Schnatterly.[5] These two peaks were also observed for the films grown on diamond, Fig. 6.9. There are also several peaks in the middle UV wavelength, these can be related with other inter-band transitions or due to the interference fringes. The details for the explanations of these peaks are still under investigation.

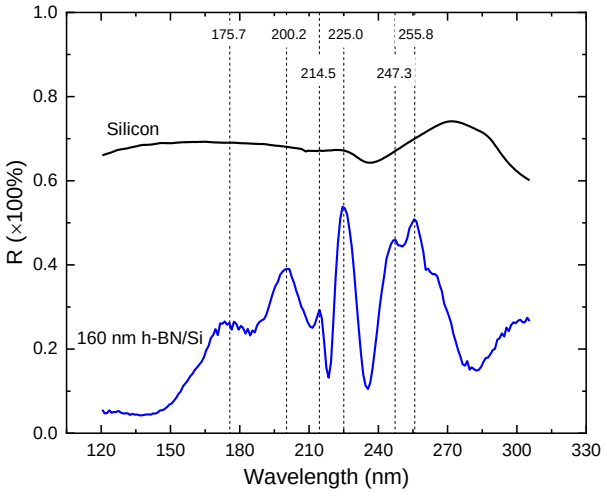

Figure 6.9. Far and middle UV reflectance measurements for h-BN grown on silicon.

6.4.2.2.2 Optical Constants for c-BN

For the c-BN grown on silicon, the films have poor adhesion to the substrate due to the high residual stress and have the chance to be delaminated. It was reported that the c-BN films on Si substrate started to partially peel off after 2-month storage.[19] In our work, the c-BN grown on silicon has a rough surface (R_q > 150 nm), which limited the specular reflectance measurements because of the light scatterings. In this case, the optical constants (n, k) were not able to be measured.

The deposition of c-BN on crystalline diamond substrate could resolve the poor adhesion, as c-BN and diamond have similar crystal structures and lattice parameters. However, the epitaxial growth of c-BN using ECR-PECVD usually induces hexagonal phase into the films. The growth of a pure c-BN on diamond is challenging, thus the far UV spectroscopy measurements for c-BN was not able to be conducted.

6.4.2.3 Volume Concentration Determination

The optical constants used in far UV for h-BN and c-BN are from the literature, Palik *et al*.[9] For the h-BN, both ordinary and extra-ordinary constants were used. The

simulated reflectance for a 10 nm BN/diamond and a diamond substrate are shown in Fig. 6.10. Fig. 6.10a shows that 10 nm c-BN on diamond has a peak position close to diamond, while 10 nm h-BN/diamond has a distinct peak at 203 nm (6.1 eV), this corresponds to the inter-band transition observed in h-BN only.[5] Both diamond and 10 nm h-BN/diamond curves showed the peaks at 173 nm, which corresponds to the inter-band transition (7.2 eV) in diamond. For the 10 nm c-BN/diamond, this peak was shifted from 173 nm to 177 nm, which indicates that the peaks from c-BN and diamond were overlapped.

Fig. 6.10b shows the simulated reflectance with increasing h-BN concentration in the 10 nm BN on diamond substrate. With increasing h-BN concentration, the peak at 203 nm becomes more prominent, which is absent on both diamond and c-BN reflectance curves. This suggests that far UV spectroscopy can be used to distinguish the c-BN/h-BN mixtures from reflectance measurements.

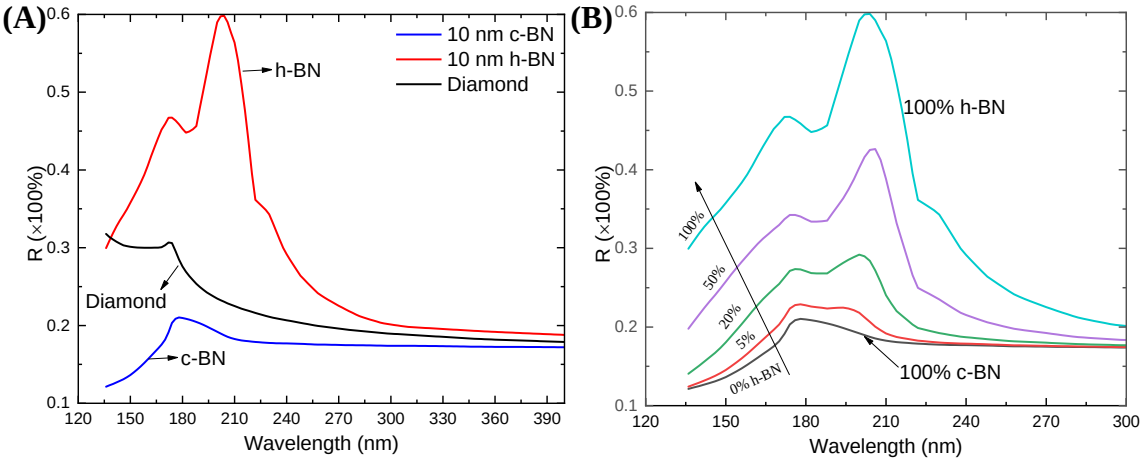

Figure 6.10. Simulated reflectance for diamond and BN. (A) Diamond substrate and pure BN films; (B) BN films with increasing h-BN concentration.

To verify the simulated reflectance in Fig. 6.11, a ~17 nm BN layer (~80±10 at. % h-BN, from XPS) on diamond was grown by ECR-PECVD. In-situ reflectance

measurements have been done in the 120 – 300 nm wavelength range, Fig. 6.11. The characteristic peak for h-BN at 203 nm is provident in the spectrum. The volume concentration of the h-BN in the mixtures is determined to be 54.0±1.87 vol. % using the EMA method.

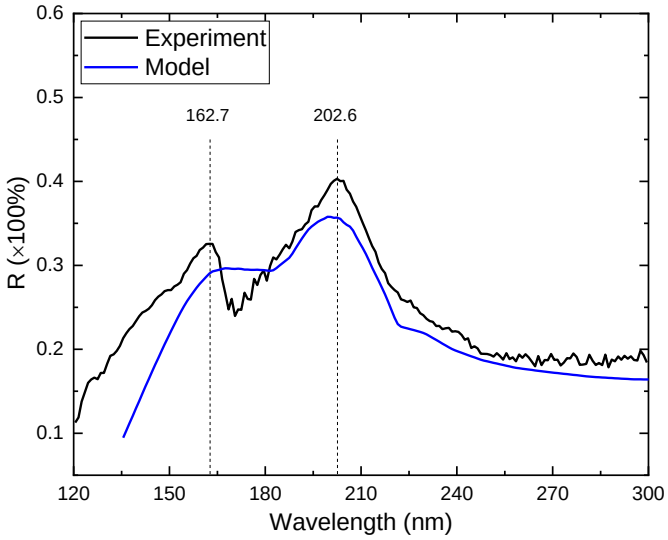

Figure 6.11. Far UV reflectance measurements for BN grown on diamond.

6.5 Discussion

6.5.1 AlF_3/Al Mixtures

For the AlF_3/Al mixtures, the Bruggeman effective medium approximation (EMA) method was used to fit the reflectance and ellipsometry data. Alternatively, we can measure the optical constants (n, k) for the mixtures, and then use Bruggeman method to fit the (n, k). In our work, we tried to measure the (n, k) of AlF_3/Al mixtures with the iso-reflectance curve method described in Chapter 5 at two different angles. However, the intersection points were not able to accurately be determined because of the value of extinction coefficient k is too small. If the mixtures have a larger value of k, the optical constants can

be measured, and the volume concentration of each constituent can be determined with the EMA method.

To improve the accuracy of this method, (n, k) of each constituent should be measured. For the AlF_3/Al mixtures, only the AlF_3 was measured. To improve the accuracy, a film containing pure Al can be grown in-situ with the electron beam evaporation method. The iso-reflectance curve method can be applied to measure the (n, k) of Al. Besides, the Bruggeman method assumes the mixtures are homogenous. For other mixture models, such as strongly porous films, and host-guest system, they should be modeled using Lorentz-Lorenz, and Maxwell-Garnett approaches, respectively.[1]

6.5.2 h-BN/c-BN Mixtures

In this work, far UV spectroscopy was used to distinguish the h-BN and c-BN phases using the provident reflectance peaks corresponding to the inter-band transitions at 6.1 and 6.95 eV. For the measurement of the concentration of each constituent, the optical constants (n, k) should be measured for h-BN and c-BN. For the h-BN, un-polarized spectroscopic measurements cannot measure the anisotropic refractive indices. In this case, ellipsometry measurements need to be used and the extrapolation of the optical constants into far UV wavelength range is needed. As for the c-BN, a pure phase c-BN films need to be grown for the optical measurements. The volume concentration of the c-BN phase in the mixtures can thus be determined with the EMA methods used for AlF_3/Al mixtures.

6.6 Summary and Future Work

In this work, we demonstrated a method based on far UV spectroscopy for the analysis of material mixtures. This method can be used to quantitatively determine the volume concentration of each constitute in the composite materials. AlF_3/Al and h-BN/c-BN mixtures have been used as examples. For the AlF_3/Al mixtures, the Al-clusters concentration was determined to be 1.6±0.16 vol. % from the far UV reflectance data, agrees with the 2.6±0.01 vol. % using the spectroscopic ellipsometry and 4.8±0.95vol. % using the XPS. For the h-BN/c-BN mixtures, the method for distinguishing the phases based on the inter-band transitions was proposed and verified with the experiments. Raman spectroscopy and XRD were used to identify the h-BN phase grown on silicon, and SE was used to measure the anisotropic refractive index in the transparent range.

The future work includes determination of the optical constants (n, k) of c-BN and h-BN using far UV spectroscopy. Inter-band transitions for other wide bandgap semiconductors, such as β-Ga_2O_3 and AlN, are also interesting to be investigated with far UV spectroscopy. For the AlF_3/Al mixtures, the processing parameters, such as plasma power, can be adjusted to vary the Al concentration inside the films. The far UV spectroscopy can be used as an in-situ monitoring tool for the measurement of the Al volume concentration.

In conclusion, this work demonstrated a method based on far UV spectroscopy for the study of material mixtures. Far UV spectroscopy is a non-destructive optical technique and can distinguish the crystalline phases based on the inter-band transitions occurring in the energy 6.2 – 10.3 eV. Quantitative determination of the volume concentration for each constituent in the mixtures can be done using the effective medium approximation method.

Overall, this work provided an application of far UV spectroscopy for the study of material mixtures, which is expected to benefit the optics and materials physics community.

References

[1] O. Stenzel, "*Basic Knowledge on Optical Constants*," in Optical Coatings Material Aspects in Theory and Practice, Ch. 2, pp. 21, edited by O. Stenzel (Springer 2014).

[2] J. I. Larruquert, "*Optical properties of thin film materials at short wavelengths*," in Optical Thin Films and Coatings, Ch. 7, edited by A. Piegari and F. Flory (Woodhead Publishing, 2018).

[3] J. Y. Tsao, S. Chowdhury, M. A. Hollis, D. Jena, N. M. Johnson, *et al.*, "Ultrawide-Bandgap Semiconductors: Research Opportunities and Challenges," Adv. Electron. Mater. **4**, 1600501 (2018).

[4] W. C. Walker and J. Osantowski, "Ultraviolet Optical Properties of Diamond," Physical Review **134**, A153 (1964).

[5] C. Tarrio and S. E. Schnatterly, "Interband transitions, plasmons, and dispersion in hexagonal boron nitride," Physical Review B **40**, 7852 (1989).

[6] K. P. Loh, I. Sakaguchi, M. Nishitani-Gamo, T. Taniguchi and T. Ando, "Surface structure of single-crystal cubic boron nitride (111) studied by LEED, EELS, and AES," Physical Review B **56**, R12791 (1997).

[7] D. A. Evans, A. G. Mcglynn, B. M. Towlson, M. Gunn, D. Jones, T. E. Jenkins, R. Winter and N. R. J. Poolton, "Determination of the optical band-gap energy of cubic and hexagonal boron nitride using luminescence excitation spectroscopy," J. Phys.: Condens. Matter **20**, 075233 (2008).

[8] J. N. Hilfiker, J. Sun and N. Hong, "*Data Analysis*," in Spectroscopic Ellipsometry for Photovoltaics, Vol. 1, Ch. 3, edited by H. Fujiwara and R. W. Collins (Springer International Publishing AG, Cham, Switzerland, 2018).

[9] E. D. Palik, *Handbook of Optical Constants of Solids*. (Academic Press, 1985).

[10] H. G. Tompkins and J. N. Hilfiker, *Spectroscopic Ellipsometry: Practical Application to Thin Film Characterization*. (Momentum Press, LLC, New York, 2016).

[11] J. Shammas, "Characterization of Cubic Boron Nitride Interfaces with in situ Photoelectron Spectroscopy," Arizona State University, 2016.

[12] J. Shammas, Y. Yang, X. Wang, F. A. M. Koeck, M. R. McCartney, D. J. Smith and R. J. Nemanich, "Band offsets of epitaxial cubic boron nitride deposited on polycrystalline diamond via plasma-enhanced chemical vapor deposition," Appl. Phys. Lett. **111**, (2017).

[13] M. Chubarov, H. Pedersen, H. Högberg, S. Filippov, J. A. A. Engelbrecht, J. O'Connel and A. Henry, "Boron nitride: A new photonic material," Physica B **439**, 29 (2014).

[14] R. Haubner, M. Wilhelm, R. Weissenbacher and B. Lux, "*Boron Nitrides — Properties, Synthesis and Applications*," in Struct. Bond., pp. 1 (Springer Berlin Heidelberg, 2002).

[15] "Boron nitride." Wikipedia. https://en.wikipedia.org/wiki/Boron_nitride (accessed)

[16] Y. N. Xu and W. Y. Ching, "Calculation of ground-state and optical properties of boron nitrides in the hexagonal, cubic, and wurtzite structures," Phys Rev B Condens Matter **44**, 7787 (1991).

[17] S. Adachi, *Optical Constants of Crystalline and Amorphous Semiconductors*. (1999).

[18] M. Schubert, B. Rheinländer, E. Franke, H. Neumann, J. Hahn, M. Röder and F. Richter, "Anisotropy of boron nitride thin-film reflectivity spectra by generalized ellipsometry," Appl. Phys. Lett. **70**, 1819 (1997).

[19] M. Ye and M. P. Delplancke-Ogletree, "Formation of cubic boron nitride thin films using ECR plasma enhanced CVD," Diamond Relat. Mater. **9**, 1336 (2000).

CHAPTER 7

OPTICAL DESIGN OF ULTRAVIOLET BANDPASS FILTERS WITH ATOMIC LAYER DEPOSITED OXIDES AND FLUORIDES

7.1 Introduction

Optical filters have been used to filter out the optical beams at specific wavelengths, which has applications in fields such as astronomy,[1, 2] optical lithography,[3, 4] and laser physics.[5-7] For example, UV light is used for lithography patterning in the microelectronic process. One of the commonly used sources is argon fluoride (ArF) laser at 193 nm. In the laser system, both high-reflectivity coatings and bandpass filters are used to enhance the intensity and the monochromaticity.[8] Metal oxides have been used as dielectric layers in filters, but they may not be suitable for the use at shorter UV wavelength due to light absorption. To overcome the absorption, metal fluorides have been considered as an alternative dielectric layer for bandpass filters in the UV or even Far UV wavelength ranges.[9]

Bandpass filters can be designed based on Fabry-Perot interferometer structure. The original form of Fabry-Perot design consists of two identical highly reflective surfaces spaced apart at distance d, with a transparent dielectric layer as the cavity.[10] In practical designs, metallic layers and multilayer dielectrics can be used to serve as the reflecting surfaces. These designs are called metal-dielectric or all-dielectric structures based on if metallics layers are used. Metal-dielectric structures are usually easier to be fabricated than all-dielectric designs, as a thin metallic layer can result a relatively high reflectance, while all-dielectric structure needs a thicker multilayer structure. However, metal-dielectric

designs suffer light absorption at shorter wavelength, and the effective light transmission is limited. To overcome the UV absorption and improve the light transmission, the all-dielectric structures should be considered for better optical performance.[9, 10]

A lot of non-idealities could exist in the fabricated optical costing, such as thickness variation, inhomogeneity, and impurities. Those non-idealities may cause a significant discrepancy between the actual performance and the original design. Impurities such as water or carbon adsorbed on the surfaces can cause absorption and limit the performance of the filters. Thickness variations and the inhomogeneity of the refractive index may cause a shift of the central wavelength and alter the shape of transmission curve.[10] Thus, it is important to analyze the effects of the non-idealities on the optical performance of the designed filters. This analysis can be used as to identify the most appropriate growth method for the fabrication of the optical coatings.

In this work, we designed bandpass interference filters based on all-dielectric Fabry-Perot structures.[10] Both single-cavity and multi-cavity designs are made for the comparison. The designed filters can be used in UV wavelength range, with central wavelength at 157 nm, 212 nm, and 248 nm. Refractive index from atomic layer deposited HfO_2, Al_2O_3, AlF_3, and plasma-enhanced chemical vapor deposition SiO_2, were used in the design. A thorough error analysis based on Monte Carlo method was made to investigate the non-ideal effects on the optical performance from thickness variation, interface and surface roughness, inhomogeneity, and atmospheric impurity.

7.2 Materials and Methods

Single-crystal (001) silicon wafers were used as the substrates for thin oxide and fluoride film growth. HfO_2 and Al_2O_3 were grown using Cambridge ALD system in the ASU NanoFab. A ~50 nm thick HfO_2 was grown using tetrakis(dimethylamino)hafnium and water vapor as precursors, with a growth rate of 1 Å/cycle. A ~50 nm thick Al_2O_3 was grown using precursors trimethylaluminum (TMA) and water vapor, with a growth rate of 1 Å/cycle. An AlF_3 layer with 25 nm thickness was grown using a custom-built ALD system, with TMA and HF-pyridine as precursors. A ~130 nm thick SiO_2 layer was grown using Oxford Plasmalab 100 PECVD system with SiH_4 and N_2O as the gas precursors.

The grown films were characterized by a spectroscopic ellipsometer (M-2000 XI, J. A. Woollam), and a custom-built Far UV spectrometer for the optical measurements. Tauc-Lorentz and Cody-Lorentz models were used to measure the optical constants (n, k) of all films, as described in Chapter 4. Fused silica and sapphire were used as the substrates in the design, with the refractive index from the literature.[11] A commercially available program, Essential Macleod (Thin Film Center, Inc.) was used for the bandpass filter design.

7.3 Optical Design

Bandpass interference filters based on all-dielectric structures can be designed as shown in Fig. 7.1. The structure is similar with a Fabry-Perot interferometer with the metallic reflecting layers replaced by quarter-wave dielectric layers.[10] The spacer layer in the Fabry-Perot interferometer is the cavity where only optical waves with the resonant

wavelength can pass through it. High transparency dielectrics are usually used as the spacer layer material to minimize the light absorption.[10]

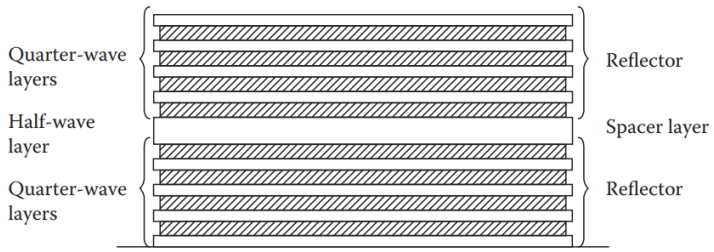

Figure 7.1. Structure of an all-dielectric single-cavity filter.

7.3.1 High-Reflectivity Coating

For the all-dielectric filter in Fig. 7.1, the reflectors are a stack of dielectric layers with alternating high and low refractive indices, with each layer fixed at quarter-wave optical thickness (QWOT), $\lambda_{\text{cen}}/4\text{n}$.[12] Here, λ_{cen} is the central wavelength with peak transmission, and n is the refractive index at central wavelength. Fig. 7.2 shows the multilayer structure for high-reflectivity (HR) coatings, (H-/L-layer)^m, where m denotes the number of repeating bilayers. For HR coatings, the top layer must be an high refractive index layer for constructive interference,[12] thus the lowest requirement for a reflective coating is a bilayer structure, i.e. $m = 1$.

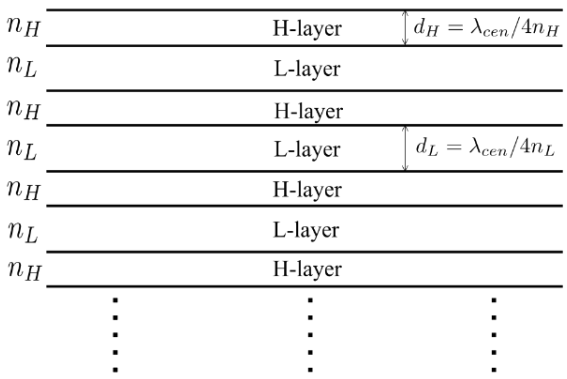

Figure 7.2. High-reflectivity coating design based on quarter-wave structure.

7.3.2 Bandpass Interference Filter

7.3.2.1 Single-Cavity Design

For a single-cavity design, the spacer layer (also called cavity layer) is a dielectric with half-wave thickness, $\lambda_{cen}/4n$. Depending on the spacer layer materials, the single cavity design can be "HH" type (spacer layer is a high index layer) or "LL" type (low index layer). It is shown that these two designs have similar results for the optical performance.[10, 13] In this work, we use the "LL" type for the design, Fig. 7.3. The structure is H $(LH)^m|LL|(HL)^m$ HS, with m denotes the repeating bilayers, and S denotes the substrate. In this design, each layer is at quarter-wave thickness. The substrate used should be transparent to maximize the transmission. In this work, we use fused silica and sapphire as the substrates.

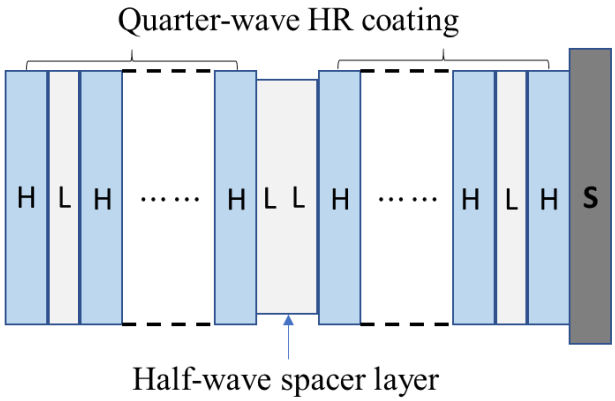

$$H(LH)^m|LL|(HL)^mH|S$$

Figure 7.3. Structure of all-dielectric single-cavity filter.

For a single-cavity structure, the peak transmission at the central wavelength can be calculated with Eq. (7.1).[10] Here, a and b represent those two high-reflectivity coatings, and s represents the substrate. In this work, the design is symmetric (Fig. 7.3), thus a and

b are identical. Eq. (7.1) can be simplified to Eq. (7.2). Further, the materials used in this work are transparent with no absorption at the central wavelength, i.e., $T + R = 1$. Equation (7.2) can be further simplified to Eq. (7.3). This indicates that the peak transmission is only dependent on the transmission of the substrate.

$$T_{peak} = \frac{T_a T_b}{\left(1-\sqrt{R_a R_b}\right)^2} T_s \quad \text{(Eq. 7.1)}$$

$$T_{peak} = \frac{T^2}{(1-R)^2} T_s \quad \text{(Eq. 7.2)}$$

$$T_{peak} = T_s \quad \text{(Eq. 7.3)}$$

Equation (7.3) indicates that the peak transmission of the filter can be enhanced if the substrate is coated with an anti-reflective coating. The simplest anti-reflective coating is a quarter-wave layer with lower refractive index than the substrate.[10, 14] Thus, the traditional single-cavity filter design shown in Fig. 7.3 can be improved with enhanced peak transmission, Fig. 7.4.

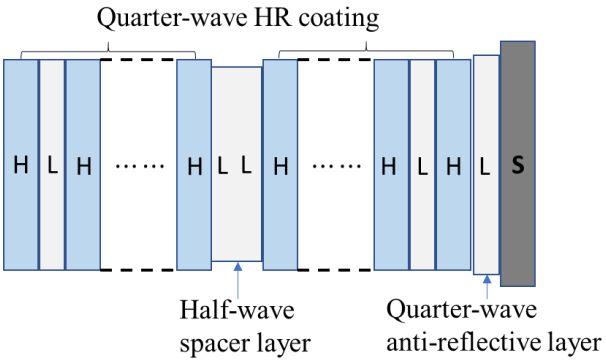

$$\mathrm{H(LH)}^m\mathrm{|LL|(HL)}^m\mathrm{H|LS}$$

Figure 7.4. Structure of all-dielectric single-cavity filter, with an anti-reflective coating.

7.3.2.2 Multi-Cavity Design

The single-cavity design does not give an ideal rectangular shape for the transmission curves. It is also shown that half of the energy transmitted lies outside of the bandwidth (full width half maximum, FWHM).[10] To get a more promising shape, two or more cavities need to be used. A double cavity design can be made from two single-cavity structures coupled with a quarter-wave dielectric layer, the coupling layer, Fig. 7.5. Three or more cavity structures can be made in series with the coupling layers. For the double-cavity design, the peak transmission equals the transmission of LS, i.e., a quarter-wave low-index layer on the substrate, Fig. 7.5a. This will enhance the peak transmission. As for the triple-cavity structure, two coupling layers are used. Thus, an extra quarter-wave layer needs to be inserted above the substrate, so the equivalent peak transmission will be equal to LLLS, which also serves as an anti-reflective coating, Fig. 7.5b.

The peak transmission of the multi-cavity structure can also be altered with the additional anti-reflective coating. In the design of the multi-layer filter, a single-layer antireflective coating will be added to enhance the peak transmission at the central wavelength.

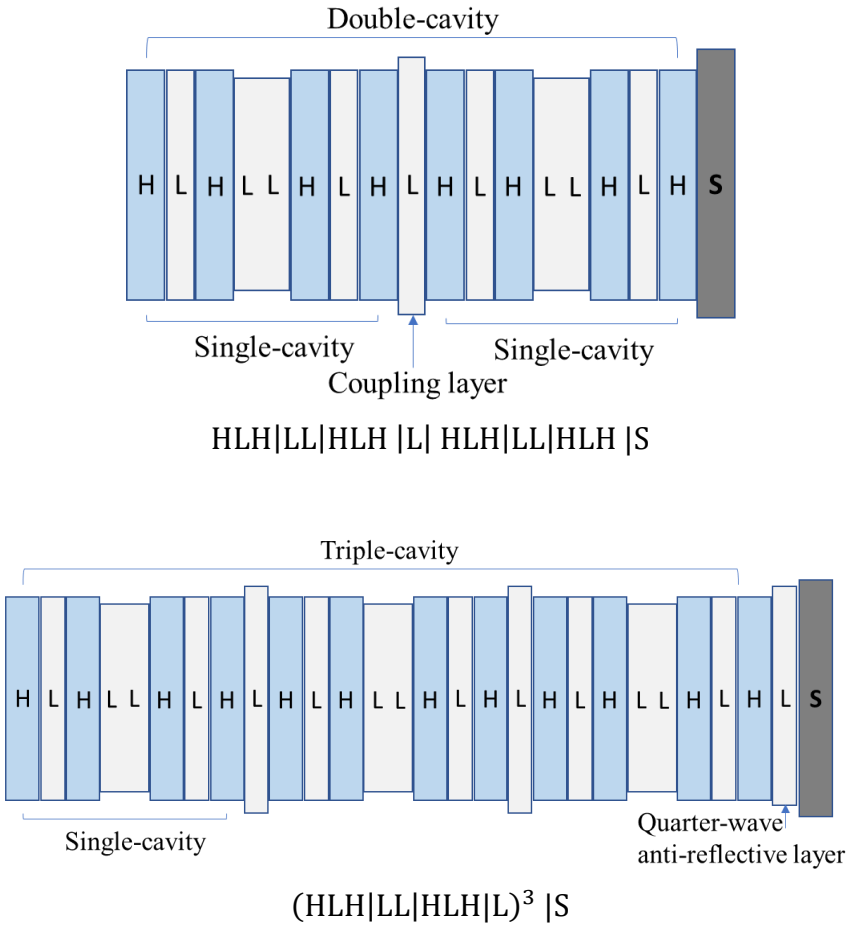

Figure 7.5. Structure of all-dielectric multi-cavity filters. (A) Double cavity, (B) Triple cavity.

7.4 Results

The optical constants (n, k) used for SiO_2, HfO_2, Al_2O_3, and AlF_3 were determined with the modified Lorentz methods described in Chapter 5, Fig. 7.6. For AlF_3, $k = 0$ in the far UV wavelength.

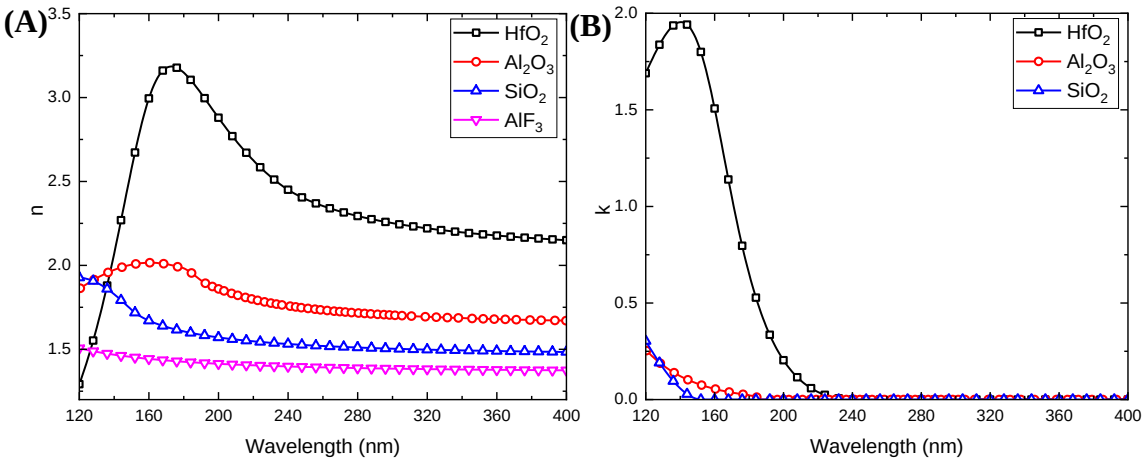

Figure 7.6. Optical constants used for the materials.

Bandpass filters were designed based on the single-cavity and multi-cavity structures in Fig. 7.4 and Fig. 7.5. These three filters use SiO_2, Al_2O_3, and HfO_2 as the high index layers, and AlF_3 as the low index layer, Fig. 7.6a. Based on the cut-off wavelength of each material, SiO_2/AlF_3 was used to design the coating with central wavelength 157 nm. Measurements showed both SiO_2 and AlF_3 have no absorption at 157 nm, Fig. 7.6b. Al_2O_3/AlF_3, and HfO_2/AlF_3 were used for the design with a central wavelength of 212 nm, and 248 nm. This is based on the same consideration that the cut-off wavelengths of both materials are below the central wavelength.

7.4.1 Bandpass Filter at 157 nm

A bandpass filter based on SiO_2/AlF_3 was designed with the single-cavity and multi-cavity structures. The reflector for the Fabry-Perot interferometer was design with multilayer high-reflectivity coating, Fig 7.2. The simulated reflectivity of the $(SiO_2/AlF_3)^m$ high-reflectivity coating was plotted in Fig. 7.7 (m denotes the number of the repeating

bilayers). The figure shows that with increasing of the number of layers, the reflectivity curves become sharper and higher. The peak reflectivity approaches the ultimate reflectivity R_k (with $m \to \infty$) which can be estimated by Eq. (7.4).[15] Here n_0 is the ambient refractive index, and (n, k) are the optical constants of the materials. The bandwidth $(\Delta\lambda)$ of the high-reflectivity coating can be estimated by Eq. (7.5).[16] It indicates that the bandwidth of designed high-reflectivity coating is directly proportional to the central wavelength λ_{cen}.

$$R_k = 1 - 2\pi n_0 \frac{k_H + k_L}{n_H^2 - n_L^2} \tag{7.4}$$

$$\Delta\lambda = \frac{4}{\pi} \sin^{-1}\left(\frac{n_H - n_L}{n_H + n_L}\right) \lambda_{\text{cen}} \tag{7.5}$$

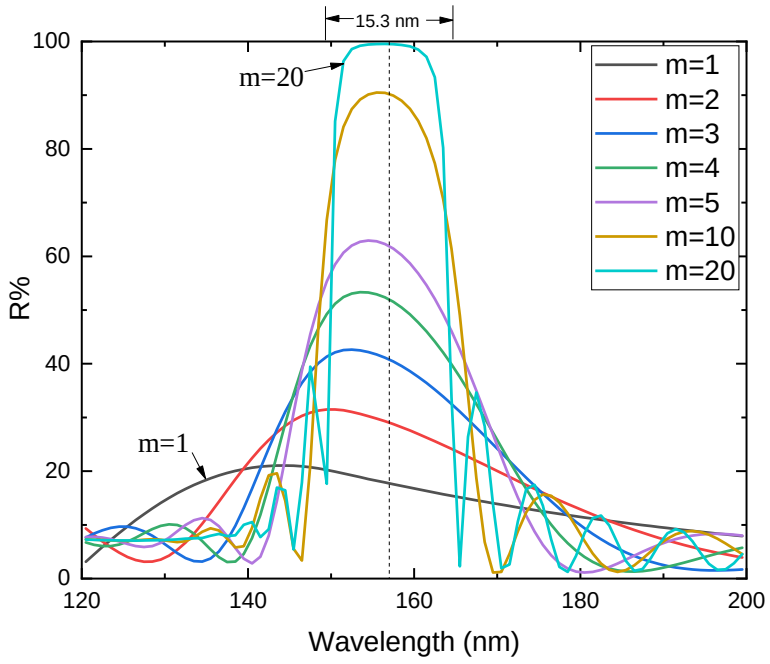

Figure 7.7. Simulated reflectivity for multilayer high-reflectivity coating $(SiO_2/AlF_3)^m$

A single-cavity bandpass filter based on SiO_2/AlF_3 was designed based on structure shown in Fig. 7.4. The substrate used for the design is fused silica. AlF_3 with half-wave

thickness is used as the spacer layer. The simulated transmission for this single-cavity filter is shown in Fig. 7.8. This figure shows with increasing thickness of the high-reflectivity coating, the bandwidth is reducing to less than 1 nm (0.2 nm for $m = 15$), while the peak transmission remains same for all the curves, with a constant value of 99.5%. As Eq. (7.3) shows, the peak transmission of the filters equals to the transmission of the fused silica substrate without any anti-reflective layer. In this design, a quarter-wave AlF_3 layer was deposited on the fused silica substrate before the filters, the peak transmission was enhanced from 91.8% (fused silica) to 99.5% (fused silica with anti-reflective coating).

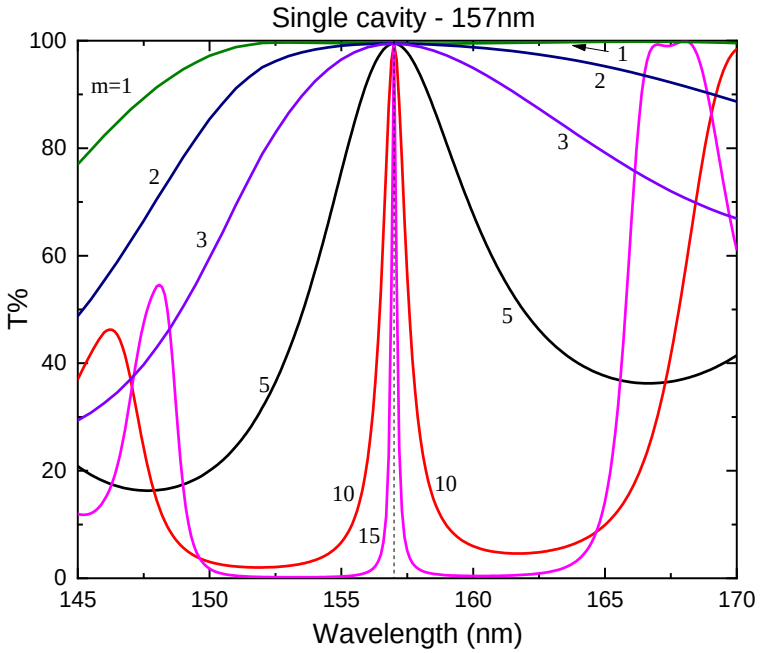

Figure 7.8. Simulated transmission for the single-cavity filter based on SiO_2/AlF_3, with structure $H(LH)^m|LL|(HL)^mH|LS$. "H" denotes SiO_2, "L" denotes AlF_3, "S" demotes fused silica substrate.

The bandwidth of the single-cavity filter can be calculated with Eq. (7.6). Here, m represents the number of repeating bilayers in the high-reflectivity coatings. "H" and "L" represent the high- and low-index layer. This equation indicates for m increased by 1, the

bandwidth of the resulted transmission curve will be $\left(\frac{n_L}{n_H}\right)^2$ of the previous one. In this design, $\left(\frac{n_L}{n_H}\right)^2 = 0.72$. This equation also shows that the bandwidth is directly proportional to the central wavelength, which is similar to the high-reflectivity coatings.

$$\Delta\lambda = \frac{4n_L^{2m+1}n_s}{\pi n_H^{2m+2}}\lambda_{\text{cen}} \qquad \text{(Eq. 7.6)}$$

Multi-cavity filters based on the structures in Fig. 7.4 have been designed based on SiO_2/AlF_3 for the use at 157 nm wavelength. The transmission curves have been simulated for the multi-cavity filters with 1, 2, 3, and 4 cavities, Fig. 7.9. It indicates that with increasing number of the cavities, the bandwidth reduces. The shape of the transmission curve becomes more rectangular, especially for the 4-cavity design in Fig. 7.9, this is different with the transmission curves for single-cavity design, Fig. 7.8. The peak transmission of all designs remains constant, is 95.5% at 157 nm wavelength.

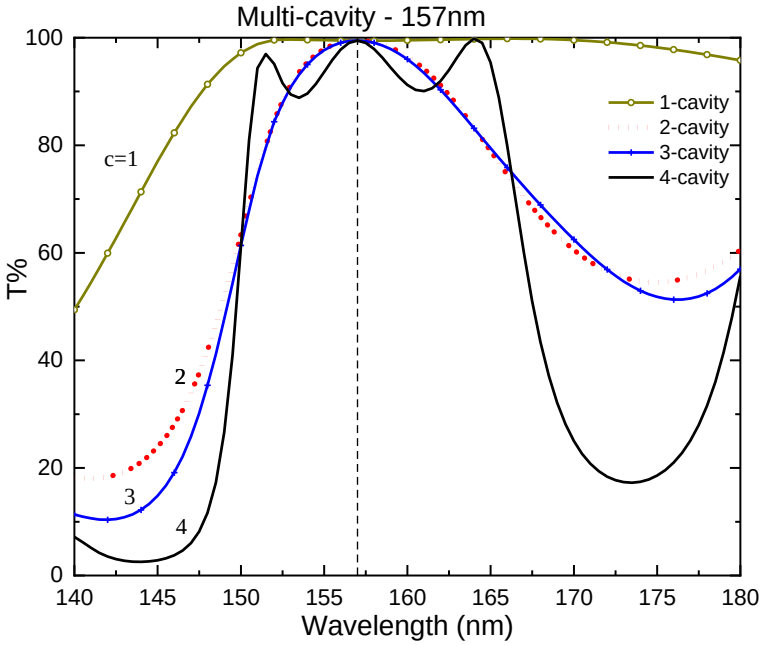

Figure 7.9. Simulated transmission for the multi-cavity filter based on SiO_2/AlF_3, with structure shown in Fig. 7.5. "c" denotes the number of the cavities in the filter.

7.4.2 Bandpass Filter at 212 nm

For the bandpass filter used at 212 nm, Al_2O_3 and AlF_3 layers were used for the design. Sapphire is used as the substrate. This is based on the consideration that both materials are transparent at this wavelength. The refractive index difference between Al_2O_3 and AlF_3 is greater than SiO_2 and AlF_3, which can reduce the total thickness used.[10] An high-reflectivity coating is designed at 212 nm, Fig. 7.10. The figure shows that the bandwidth (34.5 nm) is broader than the one used for 157 nm wavelength (15.3 nm), Fig. 7.7. This agrees with Eq. (7.5) that the bandwidth is directly proportional to the central wavelength.

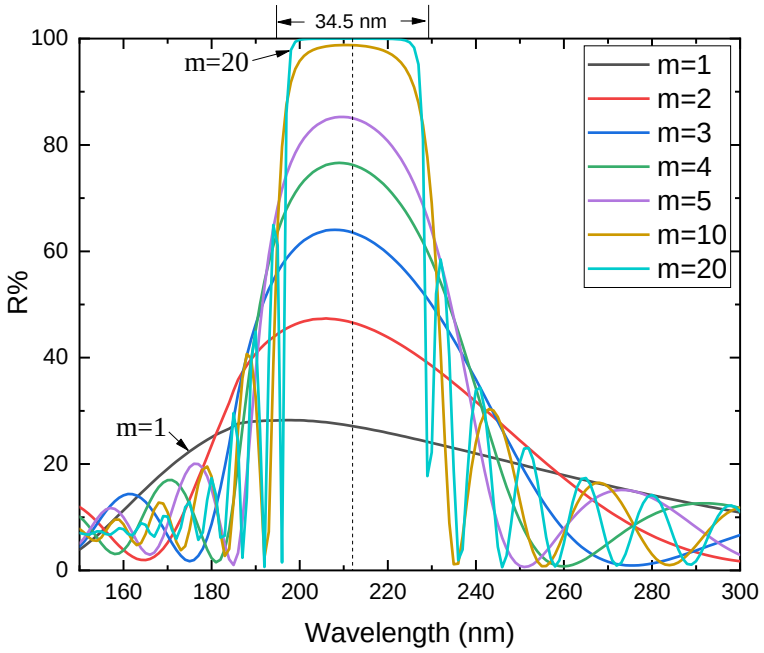

Figure 7.10. Simulated reflectivity for multilayer high-reflectivity coating $(Al_2O_3/AlF_3)^m$

The single and multiple cavity filters based on Al_2O_3/AlF_3 were design at 212nm wavelength, Fig. 7.11 and 7.12. This design also suggests that the multi-cavity design gives a better shape for the transmission curve. The bandwidth reduces with increasing number

of high-reflectivity coating and cavity number. The peak transmission for all design is 99.1% at 212 nm wavelength, this equals to the transmission of sapphire substrate with a half-wave AlF_3 anti-reflective layer.

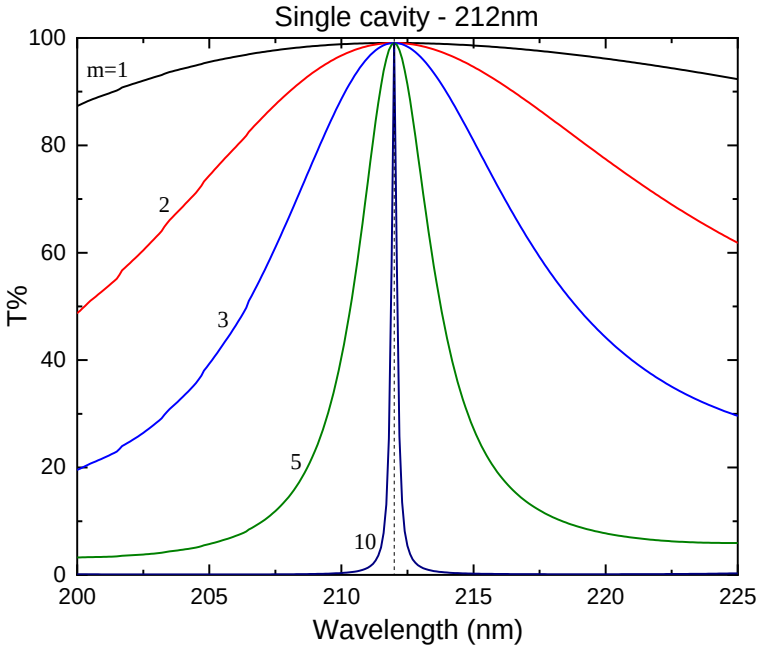

Figure 7.11. Simulated transmission for the single-cavity filter based on SiO_2/AlF_3, with structure $H(LH)^m|LL|(HL)^mH|LS$. "H" denotes Al_2O_3, "L" denotes AlF_3, "S" demotes sapphire substrate.

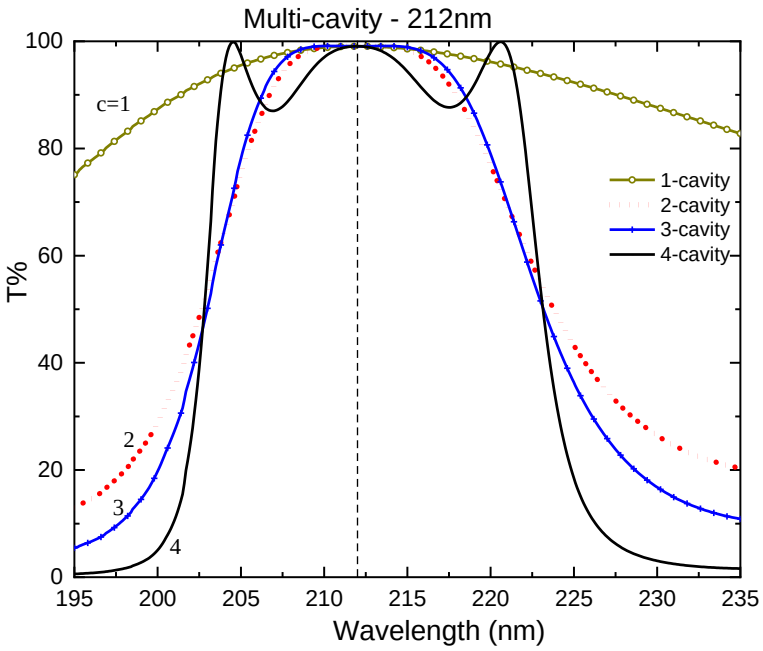

Figure 7.12. Simulated transmission for the multi-cavity filter based on Al_2O_3/AlF_3, with structure shown in Fig. 7.5. "c" denotes the number of the cavities in the filter.

7.4.3 Bandpass Filter at 248 nm

HfO_2 and AlF_3 layers were used to design the bandpass filters at 248 nm. HfO_2 has the highest refractive index among these materials used, Fig. 7.6. The simulated reflectivity for the high-reflectivity coating is shown in Fig. 7.13, the bandwidth increases with the increased central wavelength, Eq. (7.5). The simulated transmission curves for single-cavity and multi-cavity designs are shown in Fig. 7.14 and 7.15. The peak transmission is at 99.9% for all designs, which equals the transmission of sapphire coated with half-wave AlF_3 anti-reflective coating at 248 nm wavelength. It agrees the designs at 157 nm and 212 nm, that the multi-cavity design has a more rectangular shape for the transmission curve, which is better for the broadband bandpass filter design.

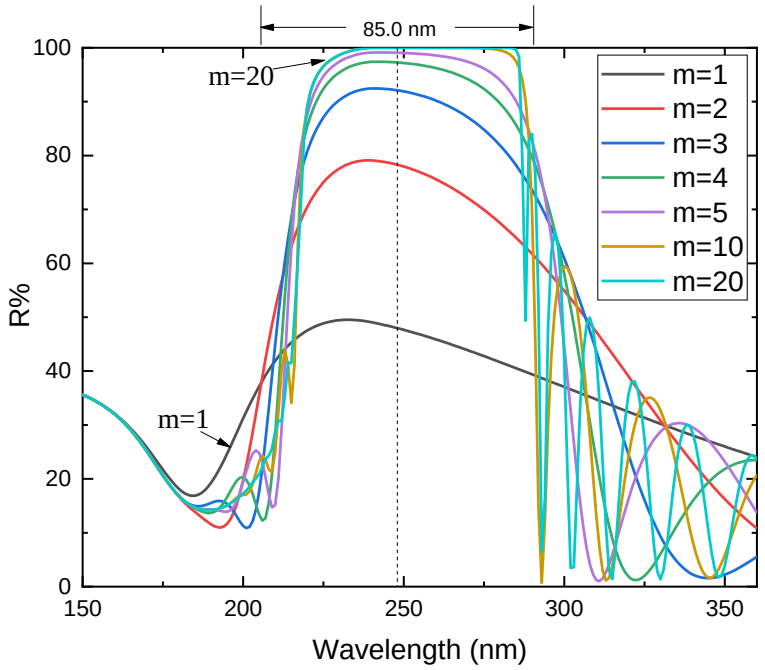

Figure 7.13. Simulated reflectivity for multilayer high-reflectivity coating $(HfO_2/AlF_3)^m$

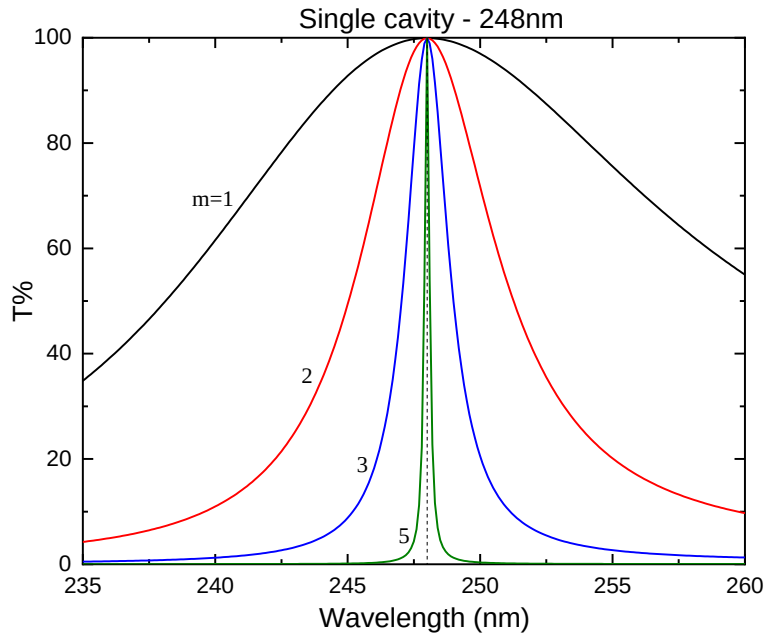

Figure 7.14. Simulated transmission for the single-cavity filter based on HfO_2/AlF_3, with structure $H(LH)^mLL(HL)^mH|LS$. "H" denotes HfO_2, "L" denotes AlF_3, "S" demotes sapphire substrate.

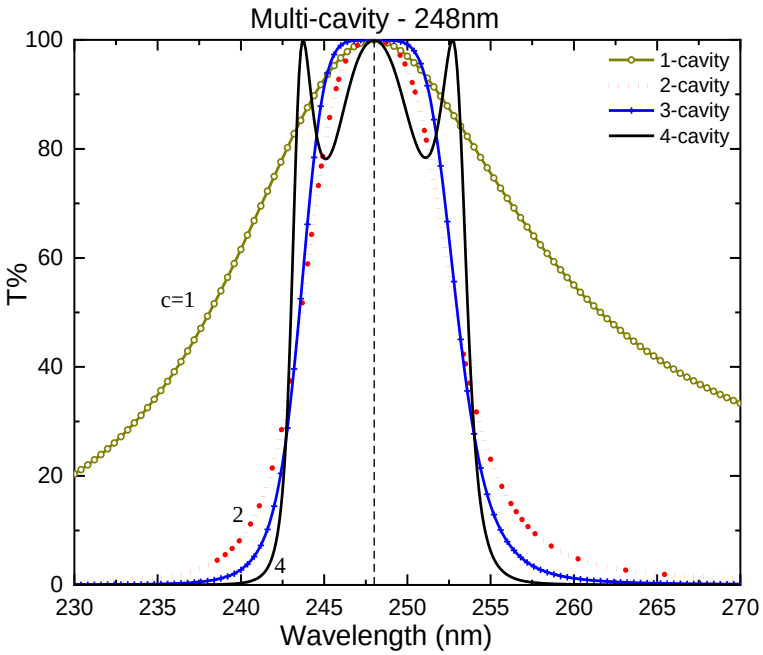

Figure 7.15. Simulated transmission for the multi-cavity filter based on HfO_2/AlF_3, with structure shown in Fig. 5. "c" denotes the number of the cavities in the filter.

7.5 Discussion

7.5.1 Comparison between Single- and Multi-cavity design

For a direct comparison between the single and multiple structure for the bandpass filter, simulations have been made for a 1-cavity and 3-cavity filter, which similar total thickness. For example, for the filter used at 157 nm wavelength. The 3-cavity structure, $(HLH|LL|HLH|L)^3\,|S$, gives a total thickness of 686.81 nm. The 1-cavity structure, $H(LH)^6|LL|(HL)^6H|LS$, gives a similar total thickness of 733.39 nm. This is to compare the difference on the transmission curves at a similar cost of material growth. Similar comparisons were made for the design at 212 nm and 248 nm, between 3-cavity and 1-cavity structures, with a similar total thickness. Since it is impossible to let the total

thickness identical between these two structures, the thickness of the 1-cavity design is slightly above the 3-cavity one.

The simulated transmission curves for all three designs are shown in Fig. 7.16. It shows that the 1-cavity design give a sharper shape for the transmission curve, while 3-cavity one gives a more rectangular shape. So, the 1-cavity structure may be used if a narrow bandpass filter is needed, and a multi-cavity design can be used for broad bandpass applications. Compared with the 3-cavity design, the 1-cavity design is more sensitive to non-idealities, as a small wavelength shift may cause significant transmission reduction at the central wavelength. The design at 248 nm, Fig. 7.16c, suggests that the transmission remains >99% from 246 to 250 nm for the 3-cavity design. For the 1-cavity, it is only >99% at 248 nm, while <12% at all other wavelengths. Thus, 1-cavity design requires stricter requirement for the actual fabrication process.

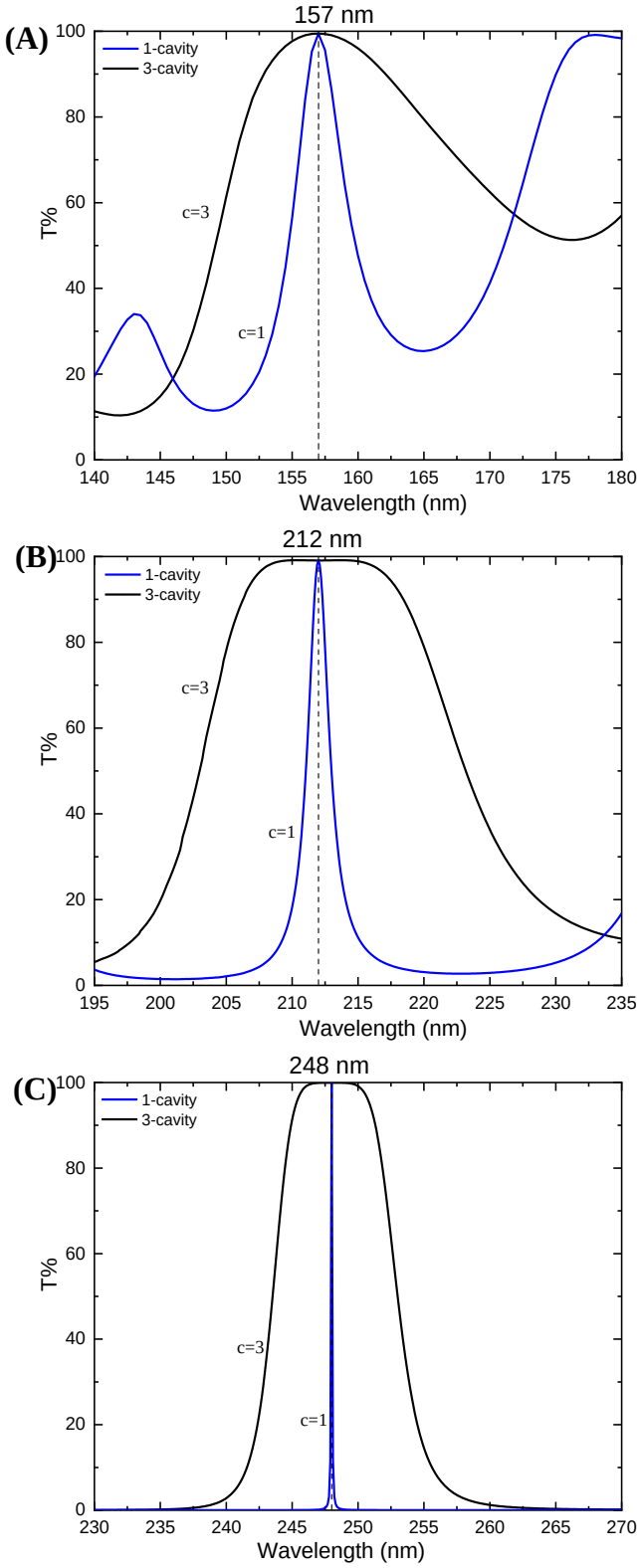

Figure 7.16. Comparison between 1-cavity and 3-cavity design with similar total thickness. Fabry-Perot filter used at (A) 157 nm, (B) 212 nm, and (C) 248 nm.

7.5.2 Comparison between Metal-Dielectric and All-Dielectric design

A metal-dielectric Fabry-Perot filter was designed as a comparison with the all-dielectric structure. SiO_2 and AlF_3 were used as the dielectric layers, and Al is used as the metallic reflectors. The structure is designed in Fig. 7.17. "H", and "L" represents SiO_2 and AlF_3. "M" is the Al metal. "S" is the fused silica substrate. In this design, the thickness of dielectrics is at quarter-wave thickness, while the Al thickness is 6.8 nm.[17] The total thickness of this filter is 341.6 nm.

Fig. 18 shows the comparison of the metal-dielectric and all-dielectric designs for the transmission curves. The main difference is that the peak transmission for the metal-dielectric structure is limited due to the light absorption in the Al metal used. For the all-dielectric design, the peak transmission is >99%. Besides, for the metal-dielectric structures, the shape of the transmission curves cannot be rectangular even with increasing the thickness of the filter.[10]

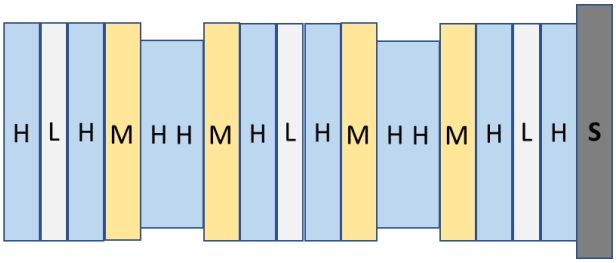

Figure 7.17. Metal-dielectric filter with 2 cavities.

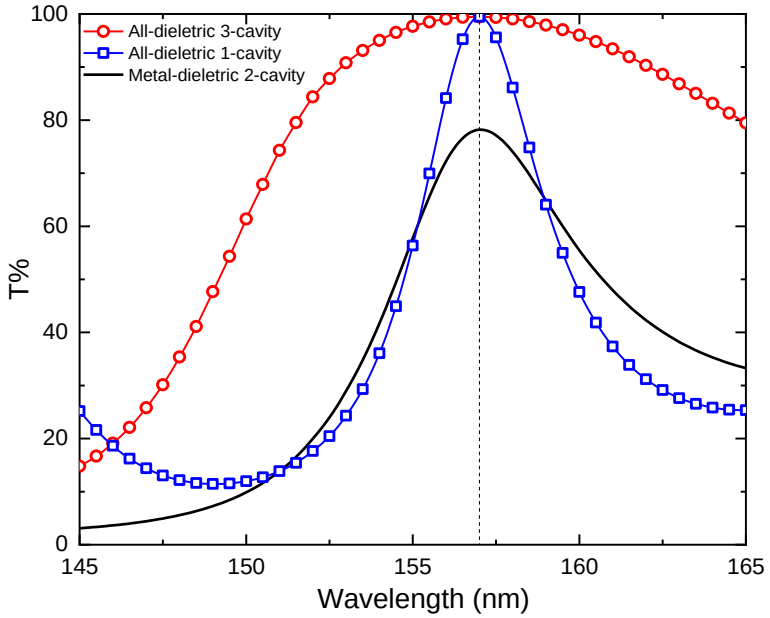

Figure 7.18. Comparison between metal-dielectric and all-dielectric designs.

7.5.3 Error Analysis for the Designed Filters

The error analysis on the designed filters was made to investigate the non-ideality effects on the optical performance of the filters. Error analysis for incident angle variation, thickness variation, roughness, inhomogeneity, and contaminations have been made to study the transmission curve changes. A 1-cavity and 3-cavity designs at 157 nm were used for the error analysis, with the ideal curves shown in Fig. 7.16a.

7.5.3.1 Incident Angle Variation

For bandpass filter, the design was made for normal incidence, i.e., incident angle θ=0°. In practice, there might be a variation of the angle from the light incidence. Fig. 7.19 shows the effects on the transmission curves from the variations of incident angles. It suggests for both 1-cavity and 3-cavity designs, the central wavelength shifts to lower wavelength with increasing incident angles. For the 1-cavity design, Fig. 7.19a, the central

wavelength shifts from 157 nm to 156.8 nm, at an incident angle θ=5°. The value of the peak transmission remains constant. For the 3-cavity design, Fig. 7.19b, at θ=5°, the central wavelength remains at 157 nm. This suggests that the transmission curves of the bandpass filters are not sensitive to the incident angle variation if it is less than 5° from the normal incidence.

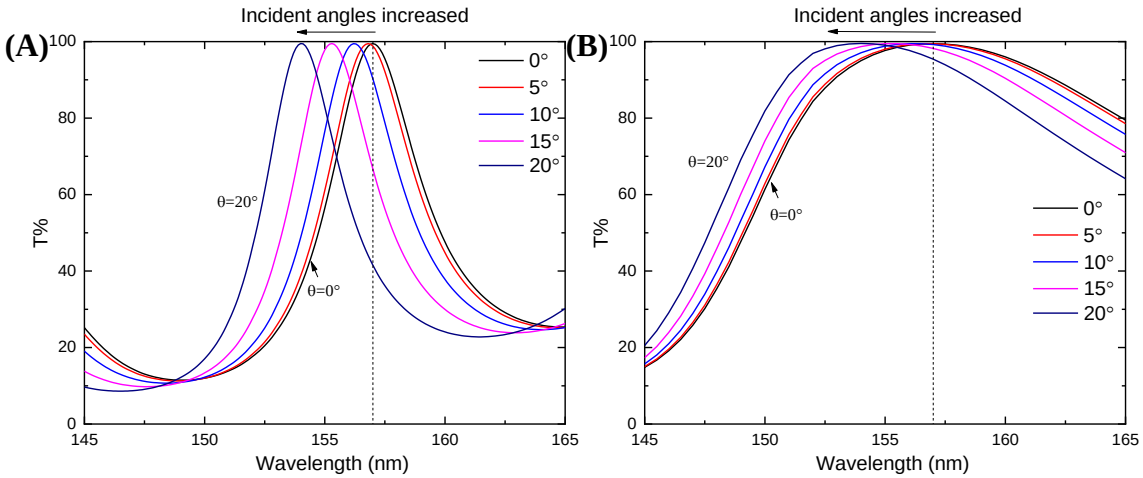

Figure 7.19. Incident angle variation on the transmission curves.
(A) 1-cavity filter design, (B) 3-cavity filter design.

7.5.3.2 Thickness Variation

During the actual process to fabricate the optical coatings, the thickness of each layer grown may differ from the values used in the design. This usually happens for the deposition methods with a fast growth rate, such as few angstroms to nanometers per second in the evaporation system. It is important to analyze the effects on the transmission curves from the variations of the thickness. This can be done with random numbers generated for the simulation of the thickness change. Fig. 7.20 shows the simulated transmission with thickness changes by 3% and 5% standard deviation. The error thickness

is generated by Eq. (7.4). In this analysis, 1000 random numbers were generated with Monte Carlo method, for both SiO_2 and AlF_3 layers. 1000 error thicknesses will be randomly generated, with a specified standard deviation.

Error thickness = Layer thickness + Layer thickness × Random numbers (Eq. 7.4)

Fig. 7.20 shows the mean value of the simulated 1000 curves with the varied thickness, for the 1-caivity and 3-caivty designs at 157 nm. Both showed that the peak transmission has been reduced with thickness variation. For the 1-cavity structure, the peak transmission reduces from 99.5% to 86.2% and 76.6% for the thickness standard deviation of 0.03 and 0.05, respectively. As for the 3-cavity structure, the peak transmission reduces from 99.5% to 97.9% and 95.4% for each case. This suggests that the 1-cavity design is more sensitive to the thickness variation. Even though the peak transmission decreases for both designs, the central wavelength remains constants if the thickness changes are random with a constant standard deviation for each layer.

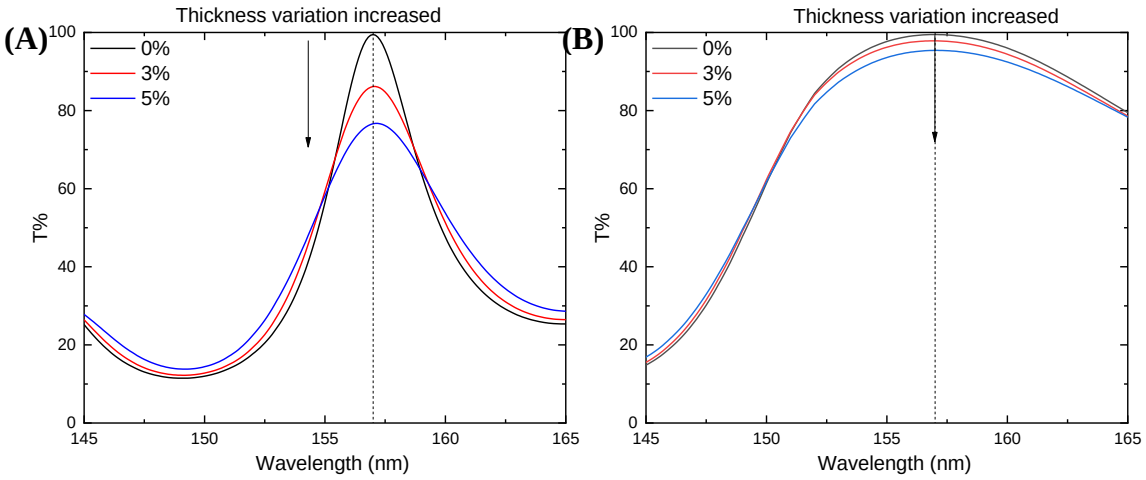

Figure 7.20. Thickness variation on the transmission curves.
(A) 1-cavity filter design, (B) 3-cavity filter design.

7.5.3.3 Interface and Surface Roughness

Besides the thickness deviation in the material growth, the interfaces between adjacent layers are usually rough for fast growth method. The rough interfaces and surfaces will cause light scattering and reduce the light transmission. Thus, it is important to investigate the effects from roughness on the transmission curves. 1-cavity and 3-cavity designs at 157 nm were used for the study. Fig. 7.21 shows the simulated transmission curves with different values of the roughness between the multilayer interfaces and on the surfaces. The roughness layer was simulated as an intermediate mixture of the adjacent layers, SiO_2 and AlF_3 in this case. The refractive index of the roughness layer equals to the Bruggeman appropriation of the SiO_2 and AlF_3 indices. The thickness of the roughness layer comes from the adjacent layers; thus, the total thickness of the designed filters remains constant.

Fig. 7.21 shows with the increasing interfacial roughness, the peak transmission reduces while the central wavelengths remain the same. Both designs showed that if the roughness is less than 1 nm, there is minimal deviation of the transmission curves. With a roughness of 2 nm, the peak transmission reduces from 99.5% to 98.7% for the 1-cavity design, and to 99.0% for the 3-cavity design. This suggests that both designs are not sensitive to the interface roughness if the roughness is less than 2 nm. For the commonly used techniques, the roughness of the growth can usually be reduced to be less than 1-2 nm.

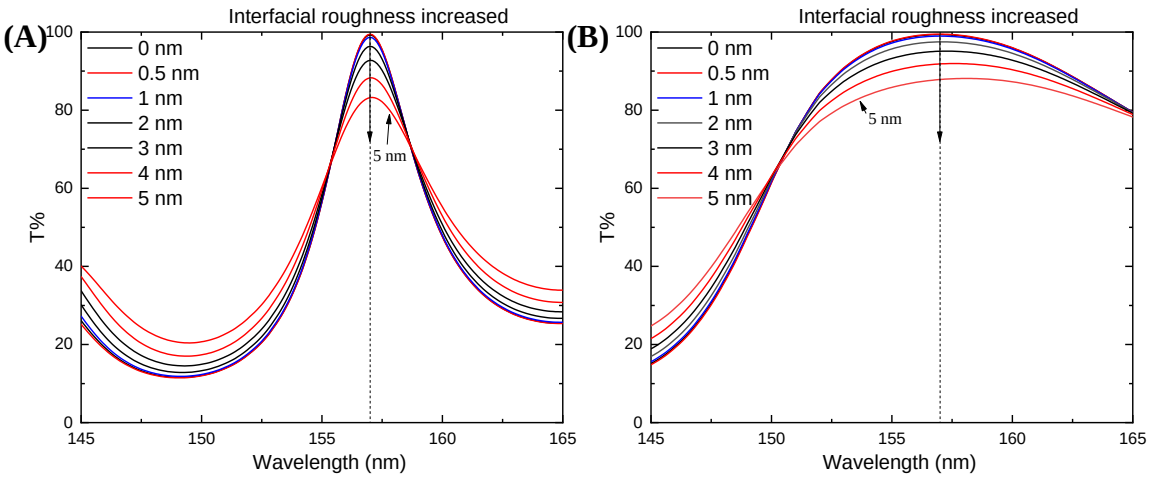

Figure 7.21. Interfacial roughness on the transmission curves.
(A) 1-cavity filter design, (B) 3-cavity filter design.

7.5.3.4 Refractive Index Inhomogeneity

During the material growth for the amorphous thin films, the density usually varies with the thickness. The films usually have higher density toward the substrate, while a lower density toward the surface. This packing density variation will cause the inhomogeneity of the refractive index along the films. The error analysis of the index inhomogeneity can be done by assuming a linear change of the refractive index along the depth of the films. The inhomogeneity factor (IF) is defined as the deviation of the refractive index change. In this design, the refractive index of the films on the substrate side is estimated to be, $n_+ = n_0(1 + \frac{\mathrm{IF}}{2})$; while the index on the surface side is estimated to be, $n_- = n_0(1 - \frac{\mathrm{IF}}{2})$. This ensures the average index of the films equals to be original value n_0, with a linear increase from the surface side to the bottom side. 1-cavity and 3-cavity filters at 157 nm were used for this error analysis. Fig. 7.22 shows the simulated transmission with different values of the inhomogeneity factor. Both designs showed that

with an “IF” factor equals to 0.2, the peak transmission increased a little bit from 99.5% to 99.9% for both designs. In practice, a film grown with “IF” = 0.2 is uncommon, and it usually should be less. This suggests that both designs are not sensitive the linear variation of the refractive index in the films.

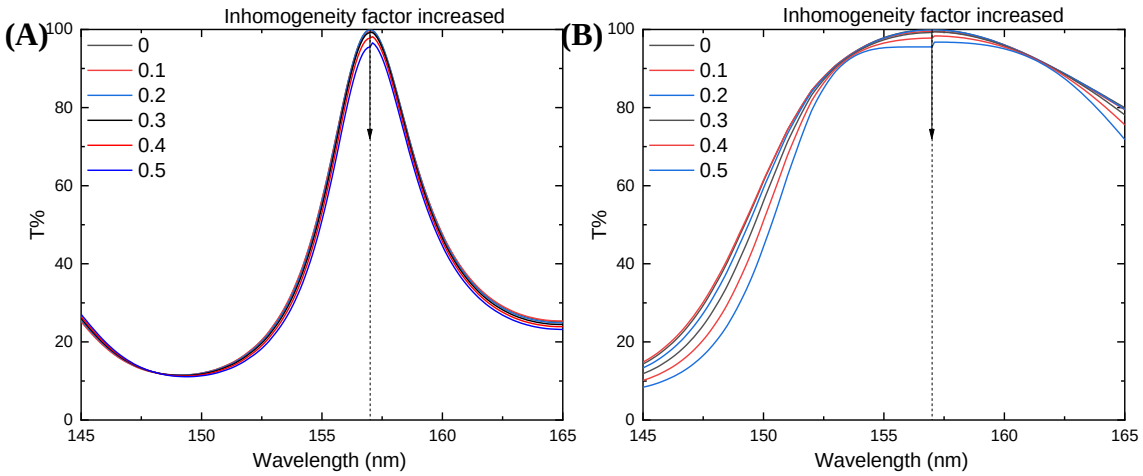

Figure 7.22. Refractive index inhomogeneity on the transmission curves. (A) 1-cavity filter design, (B) 3-cavity filter design.

7.5.3.5 Atmospheric Impurities

For a deposition of a stack of two materials in different chambers, the sample absorb atmospheric contaminations during the external sample transfer. Materials such as AlF_3 has reported will oxidize in the atmosphere with a thin Al_2O_3 layer on the surface.[18] It is also common that the surface of the materials will form a thin layer containing water and carbon picked from the atmosphere. It is important to study the effects from the ex-situ contamination and reactions on the transmission curves of the designed filters. In this analysis, 1-cavity and 3-cavity filter at 157 nm were used. For the AlF_3 layer, we assume the top 1 nm layer is oxidized, based on the experimental observation. For both AlF_3 and

SiO_2, the carbon impurity from atmosphere is also considered. The total thickness of the filter is fixed.

Fig. 7.23 shows the simulated transmission for both designs. It shows that the central wavelength will be shifted for the impurities considered. With increasing volume concentration of the carbon, peak transmission reduced. For the 1-cavity design, with 1% carbon considered, the central wavelength was shifted from 157 nm to 158.2 nm. The transmission at 157 nm was shifted from 99.5% to 67.6%. For the 3-cavity design, the central wavelength was shifted from 157 nm to 159.3 nm. The transmission at 157 nm was shifted from 99.5% to 86.2%. This suggests that both designs are sensitive to atmospheric impurities, especially, the oxidation of AlF_3 will introduce a large absorption in far UV wavelength. This absorption will cause the central wavelength shift and the transmission reduction.

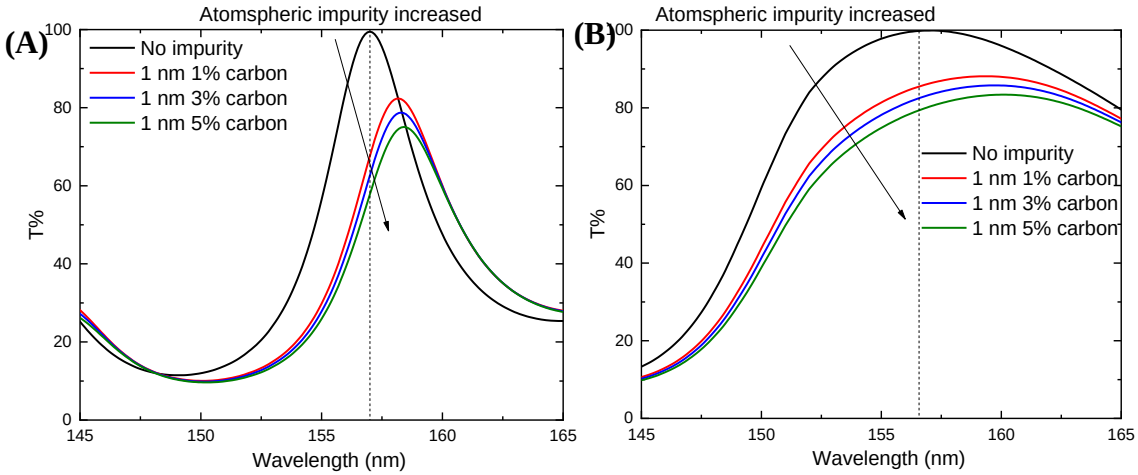

Figure 7.23. Atmospheric impurities on the transmission curves.
(A) 1-cavity filter design, (B) 3-cavity filter design.

7.6 Summary and Future Work

In this work, we have designed the ultraviolet bandpass interference filters based on all-dielectric single- and multi-cavity Fabry-Perot structures. Three different filters were designed for the use at 157 nm, 212 nm, and 248 nm wavelength. Three different combinations of the dielectrics, SiO_2/AlF_3, Al_2O_3/AlF_3, and HfO_2/AlF_3 were used at each wavelength based on their cut-off wavelength and refractive index. The results showed that the filters with multi-cavity structures have a more rectangular shape of the transmission curves, which are less sensitive to the wavelength shift caused by the non-idealities. The comparative study between the 1-cavity and 3-cavity structures suggests that the multi-layer design is better for broad bandpass filters, while 1-cavity for narrow bandpass applications.

A thorough error analysis was made to study the effects from the non-idealities on the transmission curves. Non-idealities include incident angle variation, thickness variation, roughness, refractive index inhomogeneity, and atmospheric impurities were investigated for both 1-cavity and 3-cavity designs at 157 nm. The analysis shows that both designs are not sensitive to the changes in the case of i). the incident angle is within 5° from the normal; and ii). the roughness is less than 2 nm; and iii). the refractive index is linearly varying along the films. However, thickness variation and atmospheric impurities can cause a significant amount of transmission reduction, and potential central wavelength shift, for both designs. This suggests that precise thickness control and in-situ deposition capabilities are needed for the bandpass filter fabrications.

In our lab, we have the capabilities to in-situ grow SiO_2, Al_2O_3, HfO_2, and AlF_3 materials, without atmospheric contaminations or reactions. Besides, the atomic layer

deposition techniques allow precise thickness control due to its unique self-limiting growth mechanism. The growth rate for ALD is around 1 Å per cycle, which ensures the uniformity and conformality of the materials grown. Future work includes using the ALD for fabrication of the designed bandpass filter, as a verification of the optical design, for example, the filter based on Al_2O_3/AlF_3. Besides, consideration of metal fluorides would be interesting, as they may push the central wavelength of the bandpass filter as low as ~120nm.

In conclusion, this work performed the bandpass interference filter design with all-dielectric structures. A thorough error analysis has been made to investigate the non-idealities effects on optical performance of the designed filters. A direct comparison between a single- and multi-cavity filters was made to investigate the limitations and applications for both structures. This work is expected to provide referential information for the bandpass interference filters used at shorter wavelength, including materials, designs, error analysis, and growth methods.

References

[1] G. A. Gary, E. A. West, D. Rees, J. A. Mckay, M. Zukic and P. Herman, "Solar CIV vacuum-ultraviolet Fabry-Perot interferometers," Astron. Astrophys. **461**, 707 (2007).

[2] P. Ribes-Pleguezuelo, F. Keller and M. Taccola, "UV astronomy with small satellites," arXiv:2006.14967 [astro-ph.IM] (2020).

[3] B. Q. Wua and A. Kumar, "Extreme ultraviolet lithography: A review," J. Vac. Sci. Technol., B **25**, 1743 (2007).

[4] P. R. Chalker, P. A. Marshall, K. Dawson, I. F. Brunell, C. J. Sutcliffe and R. J. Potter, "Vacuum ultraviolet photochemical selective area atomic layer deposition of Al2O3 dielectrics," AIP Adv. **5**, (2015).

[5] E. S. Field, J. C. Bellum and D. E. Kletecka, "Laser damage comparisons of broad-bandwidth, high-reflection optical coatings containing TiO_2, Nb_2O_5, or Ta_2O_5 high index layers," Proc. SPIE **8885**, 88851X (2013).

[6] M. L. Grilli, F. Menchini, A. Piegari, D. Alderighi, G. Toci and M. Vannini, "Al2O3/SiO2 and HfO2/SiO2 dichroic mirrors for UV solid-state lasers," Thin Solid Films **517**, 1731 (2009).

[7] S. Kumar, A. Shankar, N. Kishore, C. Mukherjee, R. Kamparath and S. Thakur, "Laser-induced damage threshold study on TiO2/SiO2 multilayer reflective coatings," Indian J. Phys. **94**, 105 (2020).

[8] K. Marszalek, A. Malek and P. Winkowski, "The GdF3/MgF2 bilayer as an antireflective narrow-band ultraviolet filter," Optica Applicata **46**, 187 (2016).

[9] J. I. Larruquert, "*Optical properties of thin film materials at short wavelengths*," in Optical Thin Films and Coatings, Ch. 7, edited by A. Piegari and F. Flory (Woodhead Publishing, 2018).

[10] H. A. Macleod, "Thin-Film Optical Filters."

[11] E. D. Palik, *Handbook of Optical Constants of Solids*. (Academic Press, 1985).

[12] H. A. Macleod, "*Multilayer high-reflectance coatings*," in Thin-Film Optical Filters, Ch. 6, edited by E. R. Pike and R. G. W. Brown (CRC Press, Boca Raton, 2018).

[13] A. Macleod and C. Clark, *Optical Coating Design with the Essential Macleod*. (Thin Film Center Inc, Tucson, AZ).

[14] H. K. Raut, V. A. Ganesh, A. S. Nair and S. Ramakrishna, "Anti-reflective coatings: A critical, in-depth review," Energy Environ. Sci. **4**, 3779 (2011).

[15] M. Zukic, D. G. Torr, J. M. Kim, J. F. Spann and M. R. Torr, "Filters for the International Solar Terrestrial Physics Mission far-ultraviolet imager," Opt. Eng. **32**, 3069 (1993).

[16] X. D. Wang, B. Chen and L. Yao, "Design and fabrication of Far-ultraviolet reflective broadband filter based on dielectric materials," Appl. Spectrosc. **72**, 943 (2018).

[17] N. D. Goldina, "Design of Metal-Dielectric Filters in Transmitted Ultraviolet Light," Optoelectronics, Instrumentation and Data Processing **55**, 550 (2019).

[18] C. C. Lee, M. C. Liu, M. Kaneko, K. Nakahira and Y. Takano, "Characterization of AlF3 thin films at 193 nm by thermal evaporation," Appl. Opt. **44**, 7333 (2005).

CHAPTER 8

MULTILAYER ULTRAVIOLET REFLECTIVE COATING BASED ON ATOMIC LAYER DEPOSITED ALUMINUM OXIDE AND FLUORIDE[2]

8.1 Abstract

Ultraviolet optical coatings employ wide bandgap dielectric materials due to their characteristic low absorption. High-reflectivity and anti-reflective coatings are essential for optical devices, which can be achieved by alternately depositing two dielectrics with different refractive indices. In this research, a multilayer high-reflectivity coating has been designed for middle UV wavelengths using Al_2O_3 and AlF_3 layers on a sapphire (0001) substrate, and the initial two layer structure has been fabricated by atomic layer deposition. The surface morphology and roughness of the coating was measured by atomic force microscopy after each deposition step. Ultraviolet spectroscopy and spectroscopic ellipsometry were used to characterize the optical performance of the single and multilayer coatings. Monochromatic X-ray photoemission spectroscopy was used to study the film composition, bonding, and impurities. A bilayer reflective coating was demonstrated, with a smooth surface (R_q <1nm), and peak reflectance of 25%-30% at a wavelength of 196 nm. The measured reflectance deviated from the simulations in middle UV range, and an analysis of the AlF_3 layer prepared by plasma enhanced atomic layer deposition (PEALD) indicated the presence of Al-rich clusters, which were associated with the UV absorption.

[2] The work in this Chapter has been submitted to Journal of Vacuum Science and Technology A and is currently under review.

A thermal atomic layer deposition (ALD) process for AlF_3 deposition showed reduced absorption, which could be more effective for shorter wavelength designs.

8.2 Introduction

Thin-film optical coatings, especially for high-reflectivity (HR), and anti-reflective (AR) applications, are commonly used in fields of space science,[1-5] laser physics,[6, 7] and photonic devices.[8-10] Optical coatings applied in the ultraviolet (UV) wavelength regime are more challenging than those in the visible or near infrared, as most of the coating materials suffer from significant absorption in the UV. HR coatings are fundamental for optical filters.[11] Specifically, for UV band-pass filters based on a Fabry-Perot interferometric design, the metal reflective layers can be replaced by dielectric layers with lower absorption.[5, 11] Thus, low-absorption high-reflectivity coatings are key for the design and fabrication of UV-based optical devices. The search for materials meeting these requirements has gained interest in the optics and material physics communities. [11-14]

Dielectrics, especially metal fluorides, have garnered much attention in UV optics, due to their wide band gaps and low cut-off wavelengths.[2-4, 15] One method to achieve AR or HR coatings, is to alternatively deposit two dielectrics with different refractive indices.[11] In the visible and near infrared regime, metal oxides have been largely used, with the high refractive index layers (H-layers) of Al_2O_3,[7, 16, 17] Ta_2O_5,[10, 18, 19] ZrO_2,[18] HfO_2,[6, 9, 20] or TiO_2,[19] while the low refractive index layers (L-layers) are normally SiO_2. [9, 17, 18]

However, most metal oxides display poor UV optical performance due to absorption below each oxide's cutoff wavelength, typically below 250nm. To extend the

use of oxides into the UV, metal fluorides have been identified as a key material for next generation UV coatings and optical systems.[3, 4, 15] For UV optical coatings, BaF_2,[12] LaF_3,[7, 12, 21] or GdF_3,[22] have been used as H-layers, while MgF_2,[7, 12, 21] and AlF_3[16, 22] have been used as L-layers. It is also worth noting that the definition of H- and L-layers is not strict, for example, low-index oxides, e.g. SiO_2, have also been used as H-layers when paired with metal fluorides, such as MgF_2.[12] Besides oxides and fluorides, UV optical coatings have also been reported to employ nitrides and carbides including AlN,[23] Si_3N_4,[1] and SiC.[24] A plot of refractive index, n, vs. wavelength for frequently used UV optical coating materials, is shown in Fig. 8.1. Values shown in Fig. 8.1, are obtained from various references.[25-31]

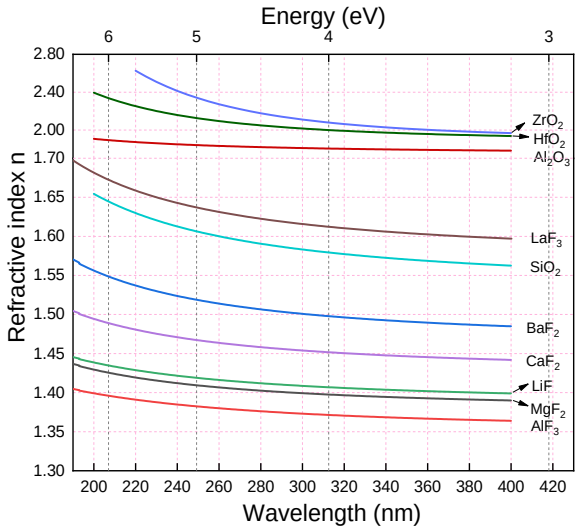

Figure 8.1. Refractive index vs wavelength for UV coating materials.

Common deposition techniques for the optical coating industry include physical vapor deposition (PVD) and chemical vapor deposition (CVD).[32] However, atomic layer deposition (ALD), a subset of CVD, has emerged to be a leading technique for modern semiconductor fabrication requiring ultrathin high-κ dielectric layers.[33, 34] Compared with

other thin-film deposition tools, ALD has the advantage of precise thickness control, high conformality and uniformity, and sub-nanometer root-mean-square surface roughness (R_q), which are all at least partially due to the unique self-limiting ALD growth process.[32, 33, 35-37] Plasma enhanced ALD (PEALD) is an energy-enhanced variation of ALD utilizing plasma radicals to drive surface reactions and reduce the number of surface species prior to initiating each cycle or half-cycle.[38, 39]

For UV coating applications, surface roughness becomes increasingly important as surface scattering can significantly degrade the optical performance of the designed coating.[14] Even though ultra-smooth surfaces ($R_q \approx 0.2\text{nm}$) have been achieved using techniques such as sputtering, incorporation of unwanted impurities may occur.[40] However, the self-limiting growth mechanism for ALD allows for minimal build-up of roughness for amorphous oxide and fluoride films.[41] The smooth surface and precise thickness control benefits thin-film coating design, fabrication, and characterization. As discrete precursor exposures are used in ALD to obtain self-limiting surface reactions, longer deposition times are to be expected in comparison to other growth methods.[32, 37]

In this study, a reflective coating consisting of single-crystal Al_2O_3 (sapphire) substrate, and amorphous Al_2O_3 and AlF_3 layers has been modeled and demonstrated for optical applications in the middle UV (200-300nm) range. The AlF_3 layers were deposited by PEALD and the Al_2O_3 layers by thermal ALD (tALD). The coating was characterized at each step of fabrication using atomic force microscopy (AFM), UV spectroscopy, and spectroscopic ellipsometry. A smooth bilayer reflective coating with UV reflectance of 25%-30%, centered at 196nm, has been achieved.

However, the properties of the PEALD AlF_3 layer were related to a deviation from the predicted optical performance. *In-situ* X-ray photoelectron spectroscopy (XPS) and *ex-situ* spectroscopic ellipsometry (SE) were used to characterize a set of PEALD, and tALD AlF_3 films to determine the composition, bonding, and defect configurations. Modified simulations could account for the optical performance deviation based on the inclusion of Al-rich clusters in the AlF_3 layer.

8.3 Optical Coating Design

A multilayer high-reflectivity coating can be constructed based on the traditional Bragg reflector design. In this design, a stack of dielectric layers with alternate high and low refractive indices are used, with each layer fixed at quarter-wavelength optical thickness (QWOT), i.e., $\lambda_{cen}/4n$.[11] Here, λ_{cen} is the central wavelength where the reflectance maxima occurs, and n is the refractive index at λ_{cen}. The ultimate reflectance R_k of the multilayer coating can be estimated using Eq. (8.1)[42] :

$$R_k = 1 - 2\pi n_0 \frac{k_H + k_L}{n_H^2 - n_L^2} \tag{8.1}$$

where n_0 is the refractive index of incident medium, and *H* and *L* denote high- and low-index layers. Eq. (8.1) shows that, for transparent materials ($k_H = k_L = 0$), the ultimate reflectance can theoretically reach 100%. For the case of $k_H + k_L \neq 0$, the larger the difference of the refractive index, the higher the ultimate reflectance of the coating.

Based on these considerations, the materials for UV reflective coatings, should satisfy two conditions: (1) The materials should have relatively large bandgaps, in order to minimize the absorption, and (2) The H-L refractive index contrast should be maximized

for ultimate reflectance. In this research, the cut-off wavelength, λ_c, of the materials should be below 300nm, for middle UV optical applications.

8.3.1 High- and Low-index Materials Selection

The refractive index, and cut-off wavelength, λ_c, for select UV coating materials, are respectively shown in Fig. 8.1 and 8.2. As indicated in Fig. 8.2, the refractive index increases with λ_c, which agrees with the energy gap-refractive index correlations described by the Moss relation, Eq. 8.2a, and the Herve-Vandamme relation, Eq. 8.2b[43] :

$$\text{Moss relation:} \quad n^4 E_g = 95 \text{ eV} \tag{2a}$$

$$\text{Herve–Vandamme relation:} \quad n^2 = 1 + \left(\frac{13.6 \text{ eV}}{E_g + 3.47 \text{ eV}}\right)^2 \tag{2b}$$

where n and E_g are the refractive index and energy gap, respectively. Values shown in Fig. 8.2 are obtained from various references. [14, 25-31, 44-55]

For the selection of H-layer materials, evidently, the commonly used TiO_2, Ta_2O_5, and Nb_2O_5, are no longer feasible, due to their lower band gap energies. In this study Al_2O_3 was chosen as the H-layer, because of its wider bandgap (6.7 eV), and lower UV absorption compared to other high-index materials, such as ZrO_2, HfO_2, and Y_2O_3.[54, 55] As for the L-layers, the commonly used SiO_2 in the visible range, can be replaced by metal fluorides. Specifically, AlF_3 or MgF_2 have significantly lower index and larger band gap (both 10-11 eV)[44, 56, 57] than SiO_2. These fluorides are projected to be transparent down to 115nm with refractive indices of ~1.4. To minimize the number of layers for the UV coating, AlF_3, Al_2O_3 and (0001) sapphire were chosen as low-index layer, the high-index layer and the substrate, respectively.

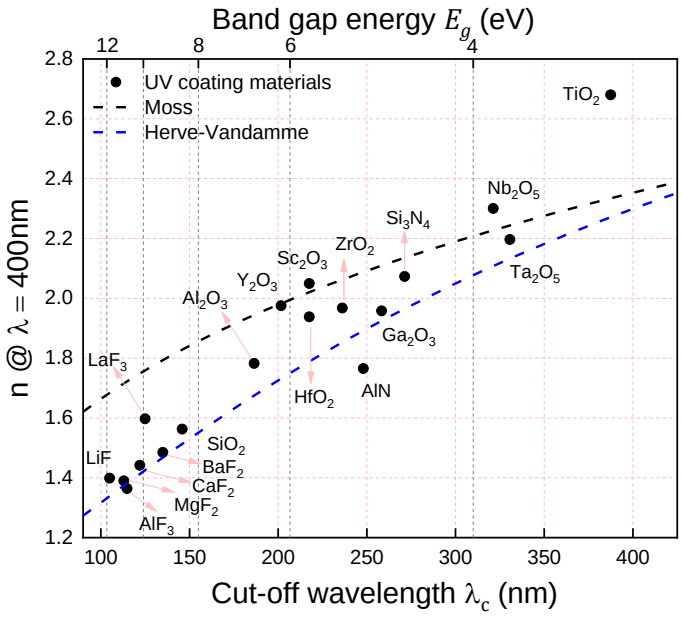

Figure 8.2. Refractive index (at $\lambda = 400\text{nm}$) vs λ_c and E_g for UV coating materials.

8.3.2 Optical Coating Modelling

The structure of the reflective coating, which is based on quarter-wavelength optical thickness (QWOT) Al_2O_3 and AlF_3 layers, was designed as vacuum/$(Al_2O_3/AlF_3)^m$/sapphire, where *m* denotes the number of repeating bilayers, Fig. 8.3b. For the quarter-wave HR coatings, the top layer must be an H-layer for constructive interference,[11] thus the lowest order reflective coating is a bilayer structure, i.e. $m = 1$. This coating was designed to be used at wavelengths between 200-250nm with a reflectance maximum, and central wavelength, at 225nm. The optical constants used for ALD Al_2O_3 were measured by SE, from a 52nm thick Al_2O_3 layer prepared by tALD. A transparent Cauchy model,

$$n = \mathrm{A} + \frac{\mathrm{B}}{\lambda^2} + \frac{\mathrm{C}}{\lambda^4} \ (\lambda \text{ in } \mu\text{m}) \qquad (8.3)$$

was used to describe the Al_2O_3 index of refraction. As for the AlF_3 layer, the Cauchy parameters for a 50 nm tALD AlF_3 layer, reported by Hennessy *et al*, [31] were used for the modelling. Table 8.1 lists the Cauchy parameters used for the sapphire substrate, ALD Al_2O_3, and ALD AlF_3, which are also plotted in Fig. 8.3a. The refractive index for sapphire is from Dodge.[27]

Table 8.1 Cauchy parameters used for UV reflective coating design.

Growth method	Material	A	B	C
Thermal ALD	Al_2O_3	1.636	0.0041	1.79×10^{-4}
Thermal ALD	AlF_3	1.352	0.0019	0
	Sapphire	1.757	0.0046	8.36×10^{-5}

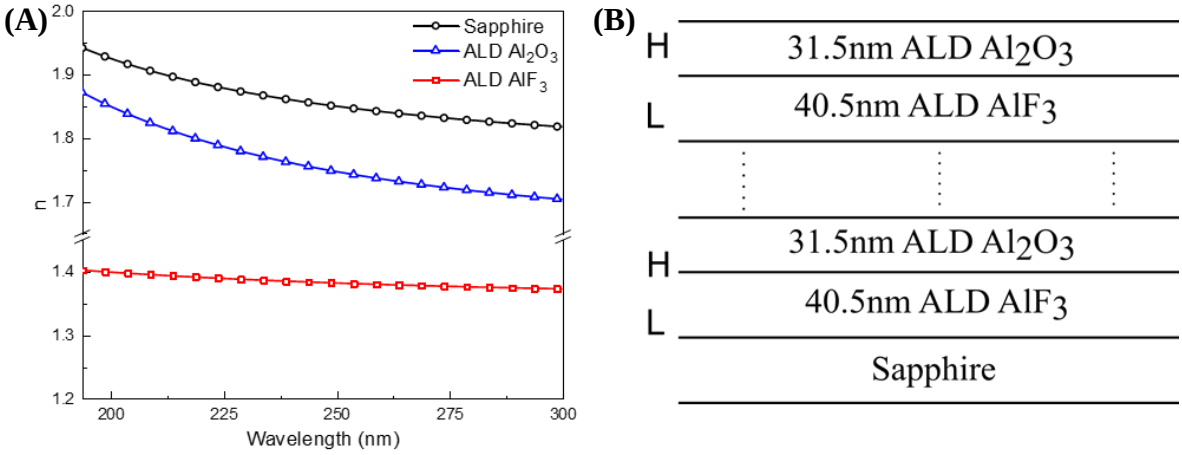

Figure 8.3. Design of the Al_2O_3/AlF_3 HR coating. (A) Refractive index of each layer used for the simulation, (B) Structure of the coating with thickness of each layer fixed at quarter-wavelength optical thickness (QWOT). H and L denote H-index, and L-index, respectively.

The reflectance of the designed coating was simulated using ellipsometry software (J. A. Woollam, CompleteEASE v6.51), which is based on the transfer matrix method (TMM).[58, 59] The simulated result, Fig. 8.4, shows that with increasing number of the repeating bilayers, the ultimate reflectance approaches 100% (in agreement with Eq. 8.1),

and the ultimate bandwidth ($\Delta\lambda$) approaching the theoretical value of 36nm given by Eq. (8.4).[21]

$$\Delta\lambda = \frac{4}{\pi}\sin^{-1}\left(\frac{n_H - n_L}{n_H + n_L}\right)\lambda_{\text{cen}} \tag{8.4}$$

In this study, an $m = 1$ reflective coating was fabricated and characterized, and the optical properties were compared to the simulation results.

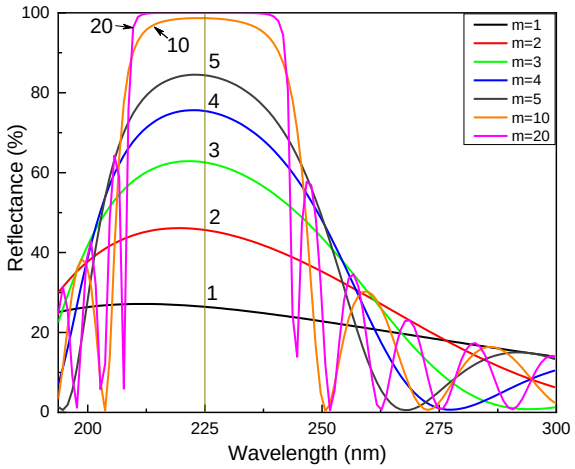

Figure 8.4. Simulated reflectance with different numbers of the repeating bilayers, with $\lambda_{\text{cen}} = 225\text{nm}$ and $\Delta\lambda = 36\text{nm}$.

8.4 Experimental Methods

The experiments involved ALD AlF_3 layers on passivated Si surfaces and also on sapphire substrates to be used as a UV reflective filter following the design in Fig. 8.4. During the optical measurements, it was recognized that the PEALD AlF_3 layers exhibited additional UV absorption. Consequently, an alternative thermal ALD process was studied and compared to confirm the effect and explore alternatives. The experimental description presents the experimental details for both the plasma and thermal ALD AlF_3 processes.

AlF_3 films were deposited, by plasma-enhanced ALD (PEALD) or thermal ALD (tALD), using a custom-built reactor integrated into an ultra-high vacuum (UHV) cluster tool allowing for *in-situ* characterization. Initial PEALD and tALD layers were on 25.4 mm diameter boron-doped silicon wafers (100) (Virginia Semiconductor) passivated with a 33 nm coating of tALD amorphous Al_2O_3. The tALD Al_2O_3 layers were prepared using a commercial tool (Cambridge, Savannah S100) with TMA and H_2O, as precursors, and a substrate temperature of 185°C. Sample surfaces were cleaned using a 10-minute UV-ozone exposure and then placed into a load-locked UHV cluster tool prior to initial characterization.

The plasma and thermal ALD AlF_3 layers were deposited in the same chamber, which is part of the UHV cluster tool described in a previous report.[60] For PEALD, the system is equiped with a 13.56 MHz radiofrequency (RF) inducitvely coupled plasma (ICP) for generating hydrogen radicals. The ALD AlF_3 reactions were performed using trimethylaluminum (TMA) (STREM, 97%), hydrogen fluoride-pyridine (HF-P) (Alfa-Asear, 70% w.t. HF), and $H_{2(g)}$ (Matherson Tri-Gas, 5N) as Al, F, and H precursors, respectively. The ALD process used a substrate temperature of 100°C. HF-P was chosen based on results of a prior AlF_3 ALD study where HF-P was shown to be a convenient, less-volatile alternative to handling anhydrous HF (AHF).[56, 61] Each ALD half-cycle consisted of a precursor exposure and Ar purge. For the PEALD AlF_3 process, an H-plasma step was included after each HF step.

Film surface composition, chemical-bonding states, and defect configurations were determined by *in-situ* X-ray photoelectron spectroscopy (XPS). The XPS instrument (VG Scientia, R3000) uses a monochromatic Al K_α X-ray source with a photon energy of 1482

eV. Data acquisition was performed using the manufacturer supplied software (VG Scientia, SES Software). The system pressure was below 7×10^{-10} Torr during measurements. High resolution scans of the Al 2p core level were acquired using a pass energy of 200 eV, step size of 0.050 eV, and energy resolution of 0.30 eV. Peak analysis was performed using an XPS software package (Casa Software LTD, CasaXPS). All photoelectron transitions were modeled with Gaussian-Lorentzian line shapes with Tougaard backgrounds.[62] Relative atomic concentrations were calculated using a standard method based on the ratio of peak areas and atomic sensitivity factors. This method had an accuracy of 10-20%.[63]

A custom-built vacuum UV spectrometer, with a base pressure 4×10^{-7} Torr, was used for *in-situ* characterization of the optical properties spanning 120-300nm. The UV spectrometer, described previously,[60] has three primary components: UV light source, monochromator, and detector. The light source used is a water-cooled deuterium lamp (Hamamatsu Photonics, L1835) with a MgF_2 window. The monochromator (McPherson Inc, Model 234/302), based on the aberration corrected Seya-Namioka design,[64] allows for a simple rotation of the diffraction grating (Al overcoated MgF_2 with 1200 g/mm) to continuously vary the wavelength. A stepper drive system (McPherson Inc, Model 789A) was used to control the wavelength output. A National Institute of Standards and Technology (NIST) calibrated silicon photodiode detector (McPherson Inc, AXUV100G) connected with a picoammeter (Keithley Instruments, Model 6485) was used to detect the intensity of the transmitted or reflected light beams. An incident angle of 20° (from normal), which was the smallest available for reflectance, was used in this research.

Surface morphology was characterized ex-situ using an atomic force microscope (Asylum Research, MFP-3D) in alternating contact mode. Scans were taken over a 5 μm × 5 μm area with a scan rate of 0.5 Hz and 1024 points and lines. The cantilever used was n-type Si (AppNano, ACT-200) with a tip radius less than 10 nm. The root mean square (rms) roughness, R_q, is defined by $R_q = \sqrt{\frac{1}{n}\sum_{i=1}^{n} y_i^2}$, where n is the total number of points and y_i is the height, of the *i*-th point, relative to the mean line of the roughness profile.

Ex-situ spectroscopic ellipsometry (SE) was used to deduce the optical constants (i.e. refractive index, n, extinction coefficient, k), and the layer thicknesses. The ratio of the complex reflectance ρ, of the mutually perpendicular components of the light beam (s-, and p-waves) can be measured by the SE, and is defined as $\rho = \frac{R_p}{R_s} = \tan\Psi\, e^{i\Delta}$, where Ψ and Δ are related to the change in amplitude, and phase shift, respectively.[65] The ellipsometer (J. A. Woollam, M-2000DI) allows for use of wavelengths ranging from 193.7nm to 1689.4nm with incident angles spanning 45°-85°. Multiple incident angles, around the substrate Brewster angle, are used for more accurate measurements. An ellipsometry software package (J. A. Woollam, CompleteEASE v6.51) was used to analyze Ψ and Δ, for the determination of thickness, and optical constants. Cauchy and B-Spline dispersion models are applied for transparent and absorbing films, respectively. The root mean square error (RMSE) was used to quantify the "goodness of fit" where an RMSE of 1 indicates an ideal fit.[66]

8.5 Results

8.5.1 UV Reflective Coating

8.5.1.1 Surface Morphology

The surface morphology of the reflective Al_2O_3/AlF_3/sapphire coating was studied by AFM. The initial sapphire surface had a rms roughness of 0.70 nm and showed polishing marks. After the deposited AlF_3 layer, the rms roughness decreased to 0.49 nm but showed specks, thought to be dust from *ex-situ* transfer, and pits from growth. After the final tALD Al_2O_3 layer, the surface showed a slight increase in roughness to 0.68 nm, with additional particles on the surface. The results indicate the deposition did not roughen the surface.

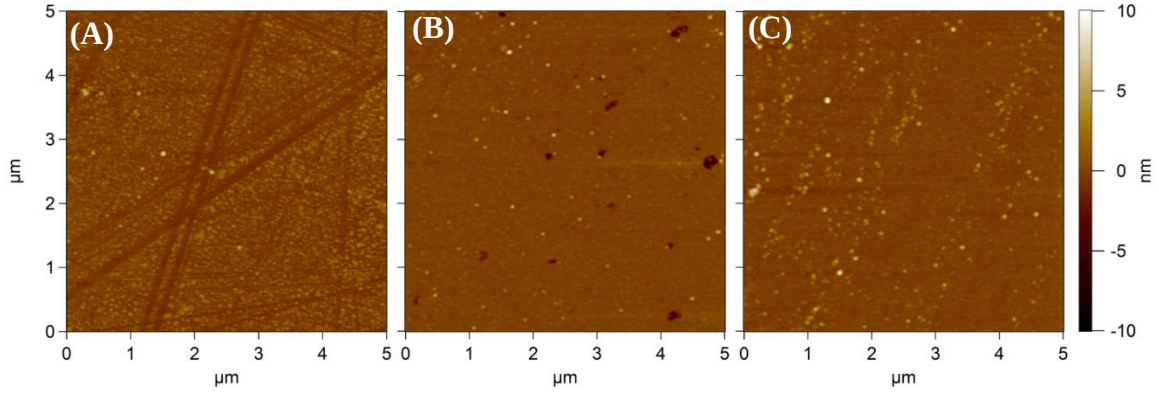

Figure 8.5. Atomic Force Microscopy (AFM) comparison of the middle UV coating at various stages of fabrication. (A) As received sapphire wafer showing polishing marks, $R_q = 0.70$ nm, (B) 42.8 nm of PEALD AlF_3, $R_q = 0.49$ nm, and (C) the completed coating with 32.8 nm Al_2O_3 deposited on top, $R_q = 0.68$ nm.

8.5.1.2 Optical Performance

The reflective coating was then characterized by UV spectroscopy and SE. The reflectance curves, Fig. 8.6, were measured *in-situ* with the UV spectrometer (120 – 300

nm) and *ex-situ* with the SE (193-400nm) using incident angles of 33° and 45°, respectively. As the UV spectrometer was fixed, the ellipsometry software was used to convert from 45° to 33°. Measurements from both systems agree with each other, however, both measurements have a discrepancy with the original design in the middle UV.

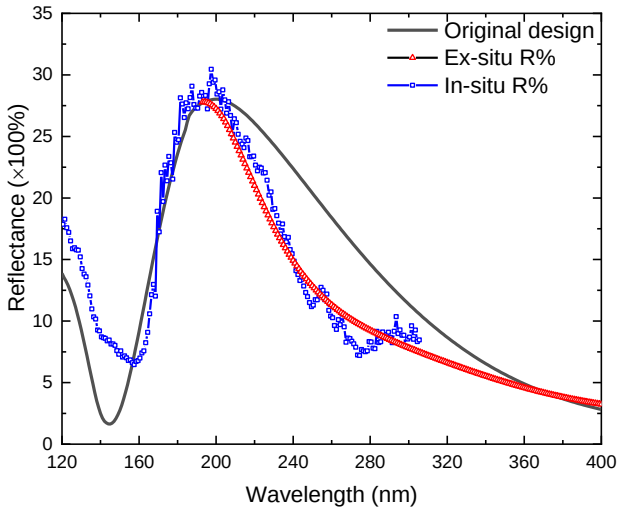

Figure 8.6. Unpolarized reflectance measured using the M-2000 SE and UV spectrometer.

A two-term Cauchy dispersion model, with $C = 0$ in Eq. 8.3, was applied to characterize the refractive index of PEALD AlF_3 layer, prior the deposition of ALD Al_2O_3. An unexpected large discrepancy between the Cauchy model and the SE data, at UV wavelengths, is shown in Fig. 8.7. As for the tALD grown AlF_3, the two-term Cauchy model worked well, see Fig. 8.4 in Hennessy et al,[31] and the measured extinction coefficient, k, at $\lambda = 200nm$ is below 2.5×10^{-4}.[31, 56, 67] The failure of the Cauchy model to describe PEALD AlF_3 suggests the presence of impurities or defects, which are not present to the same extent in thermal ALD AlF_3.

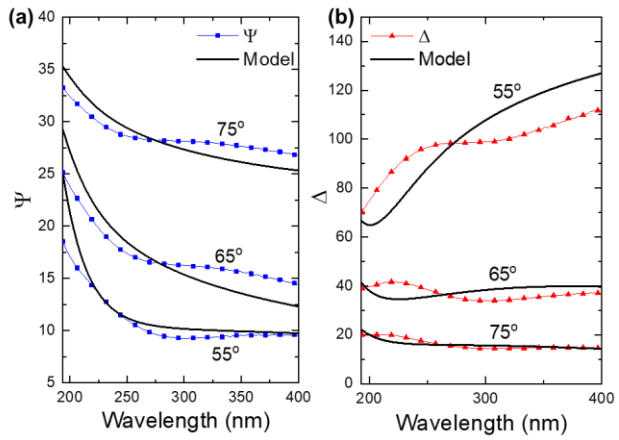

Figure 8.7. Ellipsometry data Ψ and Δ for PEALD AlF_3 on sapphire.

Table 8.2 Cauchy parameters characterized for ALD AlF_3.

Reference	Method	A	B	RMSE
This work	PEALD	1.418 ±0.005	0.0187 ±0.0019	29.358
Hennessy *et al* [31]	tALD	1.352 ±0.005	0.0019 ±0.0002	N/A

To account for the absorption in the PEALD AlF_3 layer, a B-Spline model[68] was used to further characterize the refractive index. The measured refractive index of $n = 1.44$ at 589nm, is higher than $n = 1.36$ reported by several other groups for ALD AlF_3,[31, 56, 67, 69] and $n = 1.38$ for bulk AlF_3.[70] The resulting extinction coefficient k was identified to start increasing at 400 nm, and reach a maxima at ~221nm, Fig. 8.8.

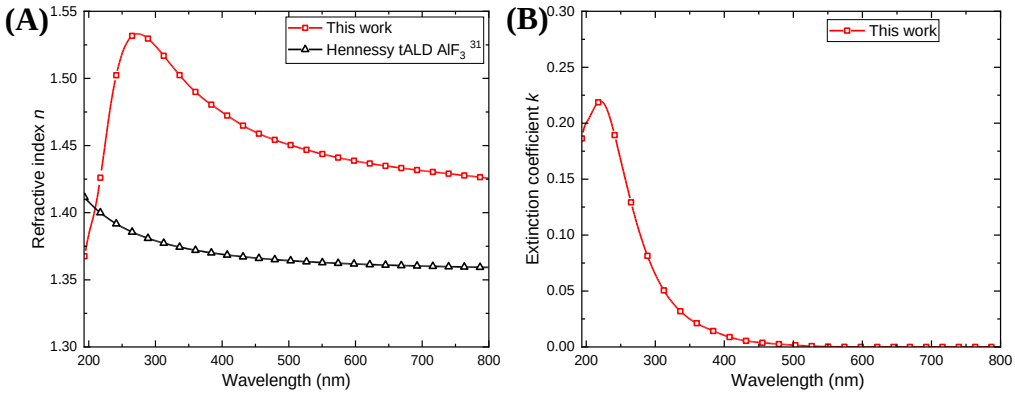

Figure 8.8. Optical constants of PEALD AlF_3, determined by B-Spline model. (A) Refractive index n, (B) extinction coefficient k.

As for the tALD Al_2O_3 layer, the determined Cauchy parameters are $A = 1.628$, $B = 0.00505$, and $C = 0.00014339$. The measured refractive index, $n = 1.64$ at 630 nm agrees with $n = 1.65$-1.66 for tALD Al_2O_3.[71, 72] The determined thickness of each layer, are 42.8 nm for PEALD AlF_3, and 32.8 nm for tALD Al_2O_3. The determined thickness is slightly different from the target value, Fig. 8.3b, which is most likely due to the deposition with inaccurate growth rate determined for PEALD AlF_3. Regardless of the unexpected absorption in the AlF_3 layer, the UV reflectance, Fig. 8.6, shows a peak reflectance of 25%-30% at 196nm, with bandwidth of about 50 nm.

8.5.2 Origin of Absorption in PEALD AlF_3

8.5.2.1 X-ray Photoelectron Spectroscopy

The optical measurements on the UV filter suggested defects in the PEALD AlF_3 that exist to a greater extent than thermal ALD AlF_3. Consequently a careful comparison of the chemical bonding of PEALD and tALD AlF_3 films was initiated using XPS. As

noted previously the PEALD and tALD AlF_3 films were on Si substrates passivated with Al_2O_3. 40 cycles of ALD was performed for each AlF_3 film. The Al 2p scans for the layers are compared in Fig. 8.9. The different peaks are associated with the chemical shifts of Al atoms bonded to O, F, and Al. The peak parameters from the scans are listed in Table 8.3.

XPS spectra of the Al 2p region is shown in Fig. 8.9 for both ALD AlF_3 films. The PEALD AlF_3 Al 2p scan showed the presence of a third, low binding energy peak interpreted as an Al-Al chemical state, Fig. 8.9(b). This Al-Al chemical state was not observed for the tALD film and is thought to occur during the H-plasma step. The Al-Al chemical state could indicate the presence of Al-rich clusters in the PEALD AlF_3 layer at 4.8±0.95 %, by peak area. Additionally, a change in peak profile was observed for the PEALD AlF_3 Al-F chemical state, Table 8.3. The change in peak position and FWHM is likely related to the presence of Al-rich clusters.

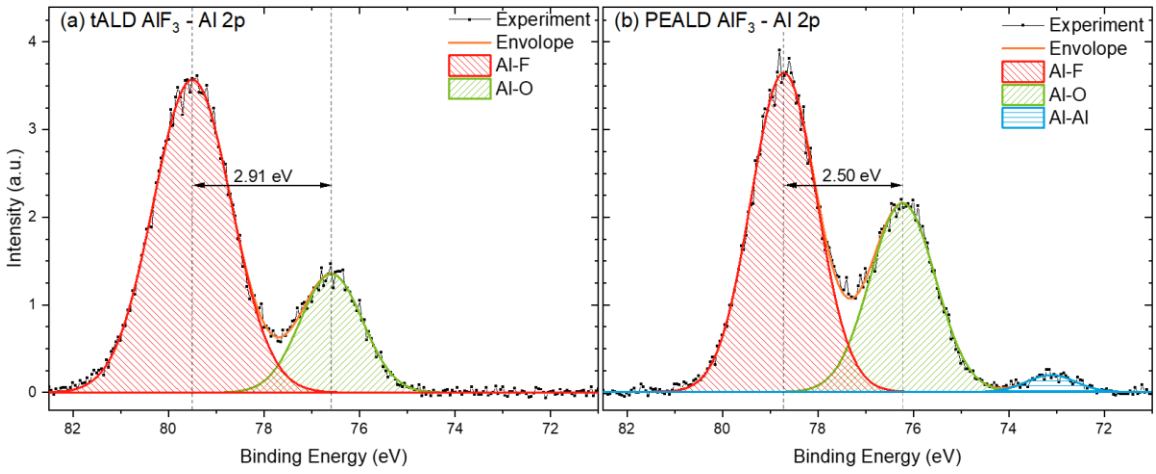

Figure 8.9. XPS Al 2p spectra of ALD AlF_3 films on 33 nm tALD Al_2O_3. The peaks associated with AlF_3 (red), Al_2O_3 (green), and Al clusters (blue) are shown. (b) PEALD AlF_3 shows the presence of an Al-Al bonding that is absent for (a) tALD AlF_3.

Table 8.3. Comparison of the Al 2p XPS peak parameters for before and after deposition of tALD and PEALD AlF_3 film. Errors are calculated from peak fitting and instrument resolution. Unless listed, errors were less than 0.1 eV.

		Chemical State (Al 2p)	Peak Energy (eV)	Peak Width FWHM (eV)	Peak Area (eV-cts/s)
tALD	Before	Al-O	76.0	1.5	10.6
	After	Al-O	76.6 ± 0.1	1.5	2.2
		Al-F	79.5	1.9	7.3
PEALD	Before	Al-O	75.9	1.5	11.3
	After	Al-O	76.2	1.6	3.7
		Al-F	78.7	1.6	6.3
		Al-Al	73.1 ± 0.1	1.2 ± 0.2	0.3

The presence of carbon and oxygen in the AlF_3 films was also analysized by XPS. Some carbon (~3 at. %) was observed in the tALD passivating Al_2O_3 layer prior to growth of the AlF_3. Additiona carbon was not detected after tALD or PEALD AlF_3 film growth. Additionally, both tALD and PEALD AlF_3 films showed the presence of a second peak in the F 1s and O 1s spectra thought to indicate the presence of an AlO_xF_y layer. In a study of water adsorption on AlF_3 surfaces, correcponding additional peaks were observed.[31, 73] We speculate that the AlO_xF_y layer could be at the Al_2O_3-AlF_3 interface or on the AlF_3 surface. Comparison of the F 1s peak fitted areas suggests the AlO_xF_y layer is ~ 0.2 ML for both thermal and PEALD AlF_3 on Al_2O_3.

The XPS results indicated that neither the plasma enhanced or thermal ALD AlF_3 films showed a detectable increase in carbon after ALD. Both films seemed to show the presence of interfacial Al-O-F with sub-monolayer thickness. The PEALD AlF_3 film showed a third peak, in the Al 2p region, interpreted as Al-Al bonding. The Al-Al bonds are thought to correspond to Al-rich clusters. The relative concentration of the Al-rich

clusters was calculated, based on the ratio of Al-F to Al-Al peak areas. The results indicated the Al-rich clusters composed 4.8±0.95 % of the AlF_3 layer. It is likely that this component is responsible for the observed absorption in the mid-UV.

8.5.2.2 Optical Characterization

This section considers the optical properties of the PEALD and tALD AlF_3 films deposited on 33nm tALD Al_2O_3/Si which were characterized by SE. Using a B-spline model, the maximum extinction coefficient, k_{m} , of the tALD AlF_3 film was determined to be 0.02, at wavelengths between 193.7 – 400 nm. For PEALD AlF_3 film, k_{m} is 0.26 over the same range. Combined with the XPS analysis, Fig. 8.9, it is evident that the Al-rich clusters component, observed in the PEALD AlF_3 film, contributes to the observed absorption.

SE was further used to study the Al clusters concentration within the PEALD AlF_3 films on sapphire by employing the effective medium approximations (EMA) method.[74] In EMA theory, an effective dielectric function ($\varepsilon_{\mathrm{EMA}}$) is used to describe a composite with two constituents, where $\varepsilon_{\mathrm{EMA}} = f_a\varepsilon_a + f_b\varepsilon_b$ with the constraint $f_a + f_b = 1$. Here (f_a, f_b) and $(\varepsilon_a, \varepsilon_b)$ are the volume fraction and dielectric functions of each constituent, respectively. The measured optical constants of PEALD AlF_3 (Fig. 8.8), were fit using the Bruggeman EMA method[68, 74] (Fig. 8.10a) to determine the volume fraction of the Al-rich clusters. The optical constants used for AlF_3 and Al are from the results for thermal ALD AlF_3 (193.7-400nm),[31] and evaporated Al metal (138 – 400 nm),[75] respectively, Fig. 8.10b. For AlF_3, the refractive index at wavelengths 138 – 193.7 nm is obtained by extending the Cauchy model for thermal ALD AlF_3, by assuming the absorption is

negligible in this wavelength range. This assumption is reasonable as the extinction coefficient for thermally evaporated AlF_3, is reported to be below 8×10^{-3} in the region of interest.[76] From the Bruggeman EMA analysis, the volume fraction of the Al-rich clusters was found to be 2.4±0.02%. Consequently, including 2.4% Al clusters in the PEALD AlF_3 layers, the RMSE of the fitting in Fig. 8.7, has been reduced from 29.36 to 5.01. To simulate the reflectivity at wavelengths 138-193.7nm, the optical constants of PEALD AlF_3 were generated by mixing the optical constants of pure Al and AlF_3, using the Bruggeman EMA method. The simulated reflectivity in the wavelength range 138 – 400 nm is shown in Fig. 8.11a.

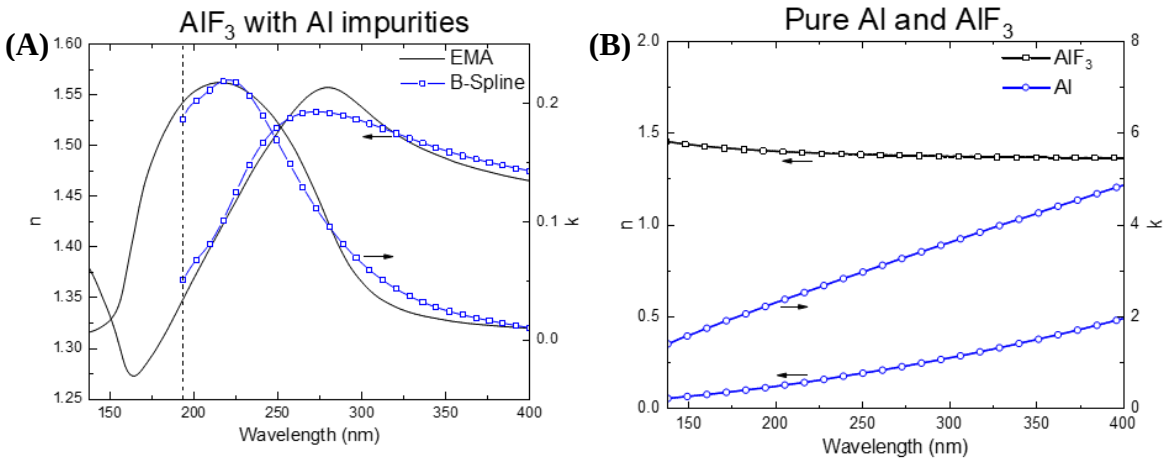

Figure 8.10. Bruggeman EMA analysis for PEALD AlF_3. B-Spline curve corresponds to the experimental data measured by SE. (A) Effective optical constants obtained with 2.4% Al clusters in the AlF_3 films, at wavelengths between 138 – 400 nm. (B) Optical constants of pure AlF_3[31] and Al[75].

8.6 Discussion

8.6.1 XPS Results for AlF_3

The most significant observation is the presence of Al-rich clusters in the PEALD layer at a level of 4.8±0.95 % of the layer, which is close to the 2.4±0.02% determinded by SE analysis. Additionally, the AlF_3 showed the presence of AlO_xF_y with sub-monolayer thickness. Additional carbon was not detected after PEALD AlF_3 growth, which likely precludes carbon as the source of the optical absorption. The mechansim for the formation of these Al-rich clusters is not understood but is thought originate during the H-plasma step.

8.6.2 Optical Performance for the Reflective Coating

The presence of the Al-rich clusters will affect the optical properties of the layer and multilayer filter. Fig. 8.10a shows the modeled reflectance curve of the UV coating in the wavelength range of 138 – 400 nm, using the EMA optical constants of PEALD AlF_3 in Fig. 8.10a. The simulation for the multilayer reflective coating updated with the optical constants from Fig. 8.8, is shown in Fig. 8.11b. The ultimate reflectance has been degraded from 100% to 43%, and the central wavelength also varies with the number of repeating bilayers, which is different from the original design shown in Fig. 8.4. This implies that reducing or eliminating Al-rich clusters in the AlF_3 deposition should enable filters with greater reflectivity.

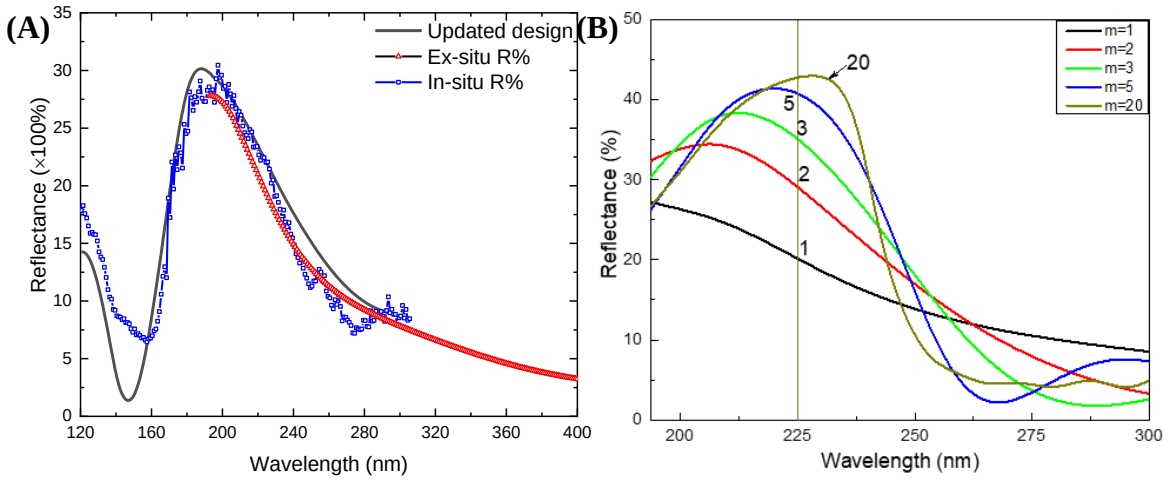

Figure 8.11. Optical modelling of the reflective coating. (A) Modeling of the reflectance below 193.7nm, with 2.4% Al clusters considered in the AlF_3 films, (B) Simulated reflectance of the reflective coating with the updated optical constants from Fig. 8.8.

8.7 Summary and Future Work

A multilayer high-reflective coating, based on AlF_3 and Al_2O_3, has been designed and fabricated. SE measurements of the reflective coating suggested the presence of an absorbing compound inside the PEALD AlF_3 layer. To determine the cause of absorption, a set of PEALD and tALD AlF_3 films were grown and characterized by XPS and SE. The results implied the existence of Al-rich clusters in the PEALD AlF_3 films. Optical simulations suggest that incorporation of Al-rich clusters (~2.4%) into the AlF_3 layer would cause a shift in central wavelength similar to the observed shift (from 225nm to 196nm).

Further studies are needed to determine the cause of Al-cluster formation and a method to mitigate their formation in PEALD AlF_3 films. Otherwise, tALD AlF_3 would be preferred for UV optical coatings. Additionally, the ALD interface impurities could be reduced by combining the AlF_3 and Al_2O_3 depositions in the same reactor or interconnected chambers. Besides Al_2O_3 and AlF_3, other dielectric materials, including HfO_2, MgF_2 and

LiF, could be applied to UV optics. Further improvement of the optical modelling could be achieved by determination of the film UV optical constants.

In summary, this work demonstrated the use of ALD to fabricate an all-dielectric high-reflective mid-UV coating. The work supports a path forward for mid and even far UV optical filters and devices. Various issues have been identified with solutions proposed for future research of materials for UV optics.

References

[1] G. Christidis, U. Koch, E. Poloni, E. De Leo, B. J. Cheng, S. M. Koepfli, A. Dorodnyy, F. Bouville, Y. Fedoryshyn, V. Shklover and J. Leuthold, "Broadband, high-temperature stable reflector for aerospace thermal radiation protection," ACS Appl. Mater. Interfaces **12**, 9925 (2020).

[2] H. W. Moos, W. C. Cash, L. L. Cowie, A. F. Davidsen, A. K. Dupree, *et al.*, "Overview of the Far Ultraviolet Spectroscopic Explorer Mission," Astrophys. J. **538**, L1 (2000).

[3] P. Ribes-Pleguezuelo, F. Keller and M. Taccola, "UV astronomy with small satellites," arXiv:2006.14967 [astro-ph.IM] (2020).

[4] B. Fleming, M. Quijada, J. Hennessy, A. Egan, J. Del Hoyo, B. A. Hicks, J. Wiley, N. Kruczek, N. Erickson and K. France, "Advanced environmentally resistant lithium fluoride mirror coatings for the next generation of broadband space observatories," Appl. Opt. **56**, 9941 (2017).

[5] G. A. Gary, E. A. West, D. Rees, J. A. Mckay, M. Zukic and P. Herman, "Solar CIV vacuum-ultraviolet Fabry-Perot interferometers," Astron. Astrophys. **461**, 707 (2007).

[6] L. Yuan, Y. N. Zhao, C. J. Wang, H. B. He, Z. X. Fan and J. D. Shao, "Effect of SiO_2 protective layer on the femtosecond laser-induced damage of HfO_2/SiO_2 multilayer high-reflective coatings," Appl. Surf. Sci. **253**, 3450 (2007).

[7] S. Gunster, D. Ristau, A. Gatto, N. Kaiser, M. Trovo and M. Danailov, "Storage ring free-electron lasing at 176 nm-dielectric mirror development for vacuum ultraviolet free-electron lasers," Appl. Opt. **45**, 5866 (2006).

[8] M. S. Alias, A. Y. Alyamani, B. S. Ooi, A. A. Alatawi, W. K. Chong, M. Tangi, J. A. Holguin-Lerma, E. Stegenburgs, M. K. Shakfa, T. K. Ng and A. M. Albadri, "High reflectivity YDH/SiO_2 distributed Bragg reflector for UV-C wavelength regime," IEEE Photonics J. **10**, 1 (2018).

[9] F. Réveret, L. Bignet, W. Zhigang, X. Lafosse, G. Patriarche, P. Disseix, F. Médard, M. Mihailovic, J. Leymarie, J. Zúñiga-Pérez and S. Bouchoule, "High reflectance dielectric distributed Bragg reflectors for near ultra-violet planar microcavities: SiO_2/HfO_2 versus SiO_2/SiNx," J. Appl. Phys. **120**, 093107 (2016).

[10] T. Sertel, Y. Ozen, V. Baran and S. Ozcelik, "Effect of single-layer Ta_2O_5 and double-layer SiO_2/Ta_2O_5 anti-reflective coatings on GaInP/GaAs/Ge triple-junction solar cell performance," J. Alloys Compd. **806**, 439 (2019).

[11] H. A. Macleod, "*Multilayer high-reflectance coatings*," in Thin-Film Optical Filters, Ch. 6, edited by E. R. Pike and R. G. W. Brown (CRC Press, Boca Raton, 2018).

[12] M. Zukic, D. G. Torr, J. F. Spann and M. R. Torr, "Vacuum ultraviolet thin-films. 2: Vacuum ultraviolet all-dielectric narrowband filters," Appl. Opt. **29**, 4293 (1990).

[13] M. Zukic and D. G. Torr, "Multiple reflectors as narrow-band and broadband vacuum ultraviolet filters," Appl. Opt. **31**, 1588 (1992).

[14] J. I. Larruquert, "*Optical properties of thin film materials at short wavelengths*," in Optical Thin Films and Coatings, Ch. 7, edited by A. Piegari and F. Flory (Woodhead Publishing, 2018).

[15] M. Beasley, F. Greer and S. Nikzad, "Progress in new ultraviolet reflective coating techniques," Proc. SPIE **8443**, 84433Q (2012).

[16] J. Sun, X. Li, W. L. Zhang, K. Yi and J. D. Shao, "High-reflectivity mirrors by Al_2O_3, LaF_3 and AlF_3 for 193 nm application," Opt. Laser Technol. **56**, 65 (2014).

[17] V. S. P. Kumar, M. Kumar, N. Kumari, V. Karar and A. L. Sharma, "Fabrication of Al_2O_3/SiO_2 multilayer reflective filters with excellent uniformity for demanding optical interference filters," Mater. Res. Express **6**, 066410 (2019).

[18] S. F. Pellicori, C. L. Martinez, P. Hausgen and D. Wilt, "Development and testing of coatings for orbital space radiation environments," Appl. Opt. **53**, A339 (2014).

[19] E. S. Field, J. C. Bellum and D. E. Kletecka, "Laser damage comparisons of broad-bandwidth, high-reflection optical coatings containing TiO_2, Nb_2O_5, or Ta_2O_5 high index layers," Proc. SPIE **8885**, 88851X (2013).

[20] P. Torchio, A. Gatto, M. Alvisi, G. Albrand, N. Kaiser and C. Amra, "High-reflectivity HfO_2/SiO_2 ultraviolet mirrors," Appl. Opt. **41**, 3256 (2002).

[21] X. D. Wang, B. Chen and L. Yao, "Design and fabrication of Far-ultraviolet reflective broadband filter based on dielectric materials," Appl. Spectrosc. **72**, 943 (2018).

[22] M. C. Liu, C. C. Lee, B. H. Liao, M. Kaneko, K. Nakahira and Y. Takano, "Fluoride antireflection coatings deposited at 193 nm," Appl. Opt. **47**, C214 (2008).

[23] T. Nakashima, K. Takeda, H. Shinzato, M. Iwaya, S. Kamiyama, T. Takeuchi, I. Akasaki and H. Amano, "Combination of Indium-Tin oxide and SiO_2/AlN dielectric multilayer reflective electrodes for ultraviolet-light-emitting diodes," Jpn. J. Appl. Phys. **52**, (2013).

[24] M. Fernandez-Perea, M. Vidal-Dasilva, J. I. Larruquert, J. A. Mendez and J. A. Aznarez, "Novel narrow filters for imaging in the 50-150 nm VUV range," Astrophys. Space Sci. **320**, 243 (2009).

[25] M. Jerman, Z. Qiao and D. Mergel, "Refractive index of thin films of SiO2, ZrO2, and HfO2 as a function of the films' mass density," Applied Optics **44**, 3006 (2005).

[26] M. F. Al-Kuhaili, "Optical properties of hafnium oxide thin films and their application in energy-efficient windows," Opt. Mater. **27**, 383 (2004).

[27] M. J. Dodge, "*Refractive index*," in Handbook of Laser Science and Technology, Vol. IV, pp. 30 (CRC Press, Boca Raton, 1986).

[28] G. Ghosh, "Dispersion-equation coefficients for the refractive index and birefringence of calcite and quartz crystals," Optics Communications **163**, 95 (1999).

[29] L. V. Rodriguez-de Marcos, J. I. Larruquert, J. A. Mendez and J. A. Aznarez, "Self-consistent optical constants of MgF_2, LaF_3, and CeF_3 films," Opt. Mater. Express **7**, 989 (2017).

[30] H. H. Li, "Refractive index of alkaline earth halides and its wavelength and temperature derivatives," Journal of Physical and Chemical Reference Data **9**, 161 (1980).

[31] J. Hennessy, A. Jewell, K. Balasubramanian and S. Nikzad, "Ultraviolet optical properties of aluminum fluoride thin films deposited by atomic layer deposition," J. Vac. Sci. Technol., A **34**, 01A120 (2016).

[32] P. O. Oviroh, R. Akbarzadeh, D. Pan, R. A. M. Coetzee and T.-C. Jen, "New development of atomic layer deposition: processes, methods and applications," Sci. Technol. Adv. Mater. **20**, 465 (2019).

[33] S. M. George, "Atomic layer deposition: an overview," Chem. Rev. **110**, 111 (2010).

[34] J. Robertson, "High dielectric constant oxides," The European Physical Journal Applied Physics **28**, 265 (2004).

[35] R. W. Johnson, A. Hultqvist and S. F. Bent, "A brief review of atomic layer deposition: from fundamentals to applications," Mater. Today **17**, 236 (2014).

[36] P. French, G. Krijnen and F. Roozeboom, "Precision in harsh environments," Microsyst. Nanoeng. **2**, 16048 (2016).

[37] S. Zhuiykov, T. Kawaguchi, Z. Hai, M. Karbalaei Akbari and P. M. Heynderickx, "Interfacial engineering of two-dimensional nano-structured materials by atomic layer deposition," Appl. Surf. Sci. **392**, 231 (2017).

[38] B. Groven, M. Heyne, A. Nalin Mehta, H. Bender, T. Nuytten, J. Meersschaut, T. Conard, P. Verdonck, S. Van Elshocht, W. Vandervorst, S. De Gendt, M. Heyns, I. Radu, M. Caymax and A. Delabie, "Plasma-enhanced atomic layer deposition of two-dimensional WS_2 from WF_6, H_2 plasma, and H_2S," Chem. Mater. **29**, 2927 (2017).

[39] H. B. Profijt, S. E. Potts, M. C. M. van de Sanden and W. M. M. Kessels, "Plasma-Assisted Atomic Layer Deposition: Basics, Opportunities , and Challenges," J. Vac. Sci. Technol., A **29**, 050801 (2011).

[40] C. Q. Hu, J. Z. Cai, Y. K. Li, C. B. Bi, Z. Q. Gu, J. Q. Zhu, J. F. Zang and W. T. Zheng, "In situ growth of ultra-smooth or super-rough thin films by suppression of vertical or horizontal growth of surface mounds," J. Mater. Chem. C **8**, 3248 (2020).

[41] P. A. Premkumar, A. Delabie, L. N. J. Rodriguez, A. Moussa and C. Adelmann, "Roughness evolution during the atomic layer deposition of metal oxides," J. Vac. Sci. Technol., A **31**, 061501 (2013).

[42] M. Zukic, D. G. Torr, J. M. Kim, J. F. Spann and M. R. Torr, "Filters for the International Solar Terrestrial Physics Mission far-ultraviolet imager," Opt. Eng. **32**, 3069 (1993).

[43] S. K. Tripathy, "Refractive indices of semiconductors from energy gaps," Opt. Mater. **46**, 240 (2015).

[44] D. König, R. Scholz, D. R. T. Zahn and G. Ebest, "Band diagram of the $AlF_3/SiO_2/Si$ system," J. Appl. Phys. **97**, 093707 (2005).

[45] A. Belosludtsev, K. Juškevičius, L. Ceizaris, R. Samuilovas, S. Stanionytė, V. Jasulaitienė and S. Kičas, "Correlation between stoichiometry and properties of scandium oxide films prepared by reactive magnetron sputtering," Appl. Surf. Sci. **427**, 312 (2018).

[46] R. K. Choudhary, P. Mishra, A. Biswas and A. C. Bidaye, "Structural and Optical Properties of Aluminum Nitride Thin Films Deposited by Pulsed DC Magnetron Sputtering," ISRN Materials Science **2013**, 1 (2013).

[47] I. Bhaumik, R. Bhatt, S. Ganesamoorthy, A. Saxena, A. K. Karnal, P. K. Gupta, A. K. Sinha and S. K. Deb, "Temperature-dependent index of refraction of monoclinic Ga_2O_3 single crystal," Appl. Opt. **50**, 6006 (2011).

[48] S.-L. Ku and C.-C. Lee, "Optical and structural properties of silicon nitride thin films prepared by ion-assisted deposition," Optical Materials **32**, 956 (2010).

[49] K.-N. Chen, C.-M. Hsu, J. Liu, Y.-C. Liou and C.-F. Yang, "Investigation of Antireflection Nb_2O_5 Thin Films by the Sputtering Method under Different Deposition Parameters," Micromachines **7**, 151 (2016).

[50] T. Siefke, S. Kroker, K. Pfeiffer, O. Puffky, K. Dietrich, D. Franta, I. Ohlídal, A. Szeghalmi, E. B. Kley and A. Tünnermann, "Materials Pushing the Application Limits of Wire Grid Polarizers further into the Deep Ultraviolet Spectral Range," Adv. Opt. Mater. **4**, 1780 (2016).

[51] F. Z. Tepehan, F. E. Ghodsi, N. Ozer and G. G. Tepehan, "Determination of optical properties of amorphous Ta_2O_5 films deposited by spin- and dip-coating methods," Sol. Energy Mater. Sol. Cells **46**, 311 (1997).

[52] L. V. Rodríguez-de Marcos, J. I. Larruquert, J. A. Méndez and J. A. Aznárez, "Self-consistent optical constants of SiO_2 and Ta_2O_5 films," Opt. Mater. Express **6**, 3622 (2016).

[53] J.-K. Yang, W. S. Kim and H.-H. Park, "Chemical bonding states and energy band gap of SiO_2-incorporated La_2O_3 films on n-GaAs (001)," Thin Solid Films **494**, 311 (2006).

[54] M. L. Huang, Y. C. Chang, C. H. Chang, T. D. Lin, J. Kwo, T. B. Wu and M. Hong, "Energy-band parameters of atomic-layer-deposition Al_2O_3 / InGaAs heterostructure," Appl. Phys. Lett. **89**, 012903 (2006).

[55] E. R. Zakirov, V. G. Kesler, G. Y. Sidorov, I. P. Prosvirin, A. K. Gutakovsky and V. I. Vdovin, "XPS investigation of the ALD Al_2O_3/HgCdTe heterointerface," Semicond. Sci. Technol. **34**, 065007 (2019).

[56] Y. Lee, J. W. DuMont, A. S. Cavanagh and S. M. George, "Atomic Layer Deposition of AlF_3 Using Trimethylaluminum and Hydrogen Fluoride," J. Phys. Chem. C **119**, 14185 (2015).

[57] J. Hennessy and S. Nikzad, "Atomic Layer Deposition of Lithium Fluoride Optical Coatings for the Ultraviolet," Inorganics **6**, 46 (2018).

[58] C. C. Katsidis and D. I. Siapkas, "General transfer-matrix method for optical multilayer systems with coherent, partially coherent, and incoherent interference," Appl. Opt. **41**, 3978 (2002).

[59] B. Harbecke, "Coherent and incoherent reflection and transmission of multilayer structures," Appl. Phys. B **39**, 165 (1986).

[60] P. Scowen, D. C. Messina, Z. Huang, B. Eller, R. J. Nemanich, H. Yu, T. Mooney and M. Beasley. "Building a Better ALD: Use of Plasma-Enhanced ALD to Construct Efficient Interference Filters for the FUV." http://www.astrostrategictech.us/pdf/projectfiles/Reports/14-SAT14-0023_AR_Scowen_Paul_2019_06.pdf (accessed 8/10/2020)

[61] G. A. Olah, J. T. Welch, Y. D. Vankar, M. Nojima, I. Kerekes and J. A. Olah, "Synthetic methods and reactions. 63. Pyridinium poly(hydrogen fluoride) (30% pyridine-70% hydrogen fluoride): a convenient reagent for organic fluorination reactions," The Journal of Organic Chemistry **44**, 3872 (1979).

[62] S. Tougaard, "Universality Classes of Inelastic Electron Scattering Cross-sections " Surf. Interface Anal. **25**, 137 (1997).

[63] J. F. Moulder, W. F. Stickle, P. E. Sobol and K. D. Bomben, "*Handbook of X-ray Photoelectron Spectroscopy*," Ch. 1, pp. 25 (Perkin-Elmer Corporation, Eden Prairie, Minnesota, USA 1979).

[64] T. Namioka, "Theory of the Concave Grating. III. Seya-Namioka Monochromator," J. Opt. Soc. Am. **49**, 951 (1959).

[65] H. Fujiwara, "*Principles of Ellipsometry*," in Spectroscopic Ellipsometry for Photovoltaics, Vol. 1, Ch. 1.1.1, edited by H. Fujiwara and R. W. Collins (Springer International Publishing AG, Cham, Switzerland, 2018).

[66] J. A. W. Co., "*"Goodness" of Fit: definition of the MSE*," in CompleteEASE Software Manual, Ch. 3.1 (J.A. Woollam Co., Lincoln, NE, 2014).

[67] M. F. J. Vos, H. C. M. Knoops, R. A. Synowicki, W. M. M. Kessels and A. J. M. Mackus, "Atomic layer deposition of aluminum fluoride using $Al(CH_3)_3$ and SF_6 plasma," Appl. Phys. Lett. **111**, 113105 (2017).

[68] J. A. W. Co., "*Absorbing Thin Films (B-Spline)*," in CompleteEASE Software Manual, Ch. 4.3 (J.A. Woollam Co., Lincoln, NE, 2014).

[69] M. Mäntymäki, M. J. Heikkilä, E. Puukilainen, K. Mizohata, B. Marchand, J. Räisänen, M. Ritala and M. Leskelä, "Atomic Layer Deposition of AlF_3 Thin Films Using Halide Precursors," Chem. Mater. **27**, 604 (2015).

[70] Eugene. Staritzky and L. B. Asprey, "Crystallographic Data. 159. Aluminum Trifluoride, AlF_3," Anal. Chem. **29**, 984 (1957).

[71] C. Barbos, D. Blanc-Pelissier, A. Fave, C. Botella, P. Regreny, G. Grenet, E. Blanquet, A. Crisci and M. Lemiti, "Al2O3 thin films deposited by thermal atomic layer deposition: Characterization for photovoltaic applications," Thin Solid Films **617**, 108 (2016).

[72] M. Broas, O. Kanninen, V. Vuorinen, M. Tilli and M. Paulasto-Kröckel, "Chemically Stable Atomic-Layer-Deposited Al_2O_3 Films for Processability," ACS Omega **2**, 3390 (2017).

[73] A. Makarowicz, C. L. Bailey, N. Weiher, E. Kemnitz, S. L. M. Schroeder, S. Mukhopadhyay, A. Wander, B. G. Searle and N. M. Harrison, "Electronic structure of Lewis acid sites on high surface area aluminium fluorides: a combined XPS and ab initio investigation," Physical Chemistry Chemical Physics **11**, 5664 (2009).

[74] J. N. Hilfiker, J. Sun and N. Hong, "*Data Analysis*," in Spectroscopic Ellipsometry for Photovoltaics, Vol. 1, Ch. 3, edited by H. Fujiwara and R. W. Collins (Springer International Publishing AG, Cham, Switzerland, 2018).

[75] D. Y. Smith, E. Shiles and M. Inokuti, "*The Optical Properties of Metallic Aluminum*," in Handbook of Optical Constants of Solids, Vol. 1, pp. 369 (Elsevier, 1997).

[76] S. Günstera, H. Blaschkea, D. Ristaua, M. Danailovb, M. Trovób, A. Gattoc, N. Kaiserc, F. Sartod, D. Florid and F. Menchinid, "Radiation resistance of single-

and multilayer coatings against synchrotron radiation," Proc. SPIE **5250**, 146 (2004).

CHAPTER 9

SUMMARY AND FUTURE WORK

9.1 Summary of current work

In this study, a set of dielectric thin films, including Ga_2O_3, Al_2O_3, HfO_2, and AlF_3, were grown on silicon wafers by atomic layer deposition. Far UV reflectance and spectroscopic ellipsometry measurements have been completed for each material. The optical calculation methods based on the iso-reflectivity curve and optical dispersion model have been developed and used to determine the optical properties in the far UV wavelength (120 – 200 nm). For each material, the optical constants (n, k), dielectric constants (ε_1, ε_2), and cut-off wavelengths were determined. The results determined using different methods were consistent and agree with the reports from the literature. From the measured imaginary dielectric constant ε_2, the inter-band transitions for each material were discussed.

A method based on far UV spectroscopy was developed for the analysis of material mixtures. This method can be used to quantitatively determine the volume concentration of each constitute in the composite materials. AlF_3/Al and h-BN/c-BN mixtures have been used as examples. For the AlF_3/Al mixtures, the Al-clusters concentration was determined to be 1.6±0.16 vol. % from the far UV reflectance data, which agrees with the 2.6±0.01 vol. % using spectroscopic ellipsometry and 4.8±0.95 at. % using the XPS. For the h-BN/c-BN mixtures, the method for distinguishing the phases based on the inter-band transitions was proposed and verified with experiments. Raman spectroscopy and XRD were used to identify the h-BN phase grown on silicon, and SE was used to measure the anisotropic refractive index in the transparent range.

Ultraviolet bandpass interference filters based on all-dielectric single- and multi-cavity Fabry-Perot structures were designed. Three different filters were designed for use at 157 nm, 212 nm, and 248 nm. Three different combinations of the dielectrics, SiO_2/AlF_3, Al_2O_3/AlF_3, and HfO_2/AlF_3 were used at each wavelength based on their cut-off wavelength and refractive index. The results showed that the filters with multi-cavity structures have a more rectangular shape of the transmission curves, which are less sensitive to wavelength shifts caused by non-idealities. A comparative study between the 1-cavity and 3-cavity structures suggests that the multi-layer design is better for broad bandpass filters, while 1-cavity is better for narrow bandpass applications.

For the designed bandpass filters, a thorough error analysis was made to study the effects from the non-idealities on the transmission curves. Non-idealities include incident angle variation, thickness variation, roughness, refractive index inhomogeneity, and atmospheric impurities were investigated for both 1-cavity and 3-cavity designs at 157 nm. The analysis shows that both designs are not sensitive to changes for the following conditions i). the incident angle is within 5° from the normal; ii). the roughness is less than 2 nm; and iii). the refractive index varies but with a linear distribution. However, thickness variation and atmospheric impurities can cause a significant amount of transmission reduction, and potential central wavelength shift, for both designs. This suggests that precise thickness control and in-situ deposition capabilities are needed for bandpass filter fabrication.

A multilayer high-reflective coating, based on AlF_3 and Al_2O_3, was designed and fabricated. Spectroscopic ellipsometry (SE) measurements of the reflective coating suggested the presence of an absorbing compound inside the plasma enhanced ALD

(PEALD) AlF_3 layer. To determine the cause of the absorption, a set of PEALD and thermal ALD AlF_3 films were grown and characterized by XPS and SE. The results implied the existence of Al-rich clusters in the PEALD AlF_3 films. Optical simulations suggest that incorporation of Al-rich clusters (~2.4 vol. %) into the AlF_3 layer would cause a shift in central wavelength similar to the observed shift (from 225nm to 196nm).

9.2 Outline of future work

Based on the current study, the future work can be extended into the detailed study of cubic and hexagonal BN, including the far UV optical constants measurements and volume concentration determination. Besides, the optical coatings and filters design can be further improved using more complex structures and analysis methods. Finally, the fabrication of designed filters is needed to verify the optical modelling results.

9.2.1 Far UV optical constants measurements

For measurements of the far UV optical constants, it is important to measure the as-grown thin films in vacuum. For current measurements, the thin films were stored at atmosphere for several days. The atmospheric impurities on the surface, including water and carbon, will affect the accuracy of the determined optical constants. For the AlF_3 films, it could be oxidized in atmosphere. To improve the accuracy, the reflectance measurements should be conducted right after the films are grown, without exposure to atmosphere. For the dielectric thin films, the measurements showed there is a peak at ~ 9 eV on the imaginary dielectric constant ε_2 curve, the next step is to investigate the origin of this peak. If it is related to inter-band transition, a close look at the band structure is necessary.

The measurements for cubic BN have not been done yet. For the future work, a thin BN film with pure c-BN phase should be grown. The reflectance measurement should be done for the as-grown films in vacuum, at variable angles. The optical constants can be determined with the methods used for dielectric thin films. For h-BN, determination of the anisotropic refractive index is challenging. The next step is to develop a method to determine the anisotropic refractive index of h-BN, based on the complementary use of far UV spectroscopy and spectroscopic ellipsometry.

9.2.2 Far UV optical coatings design

The designs of optical coatings and filters have been made based on common structures. To maximize the optical performance and minimize the total thickness needed, more complex structures and designs should be considered. Currently, the layer thickness in the design is fixed at quarter-wave thickness, however, it is also reported that the non-quarter-wave structure was also used in the design and fabrication. A more complex design method, such as needle synthesis, should be considered in the design process. This can be achieved with the commercially available software program, Essential MacLeod.[1]

Besides, a more detailed error analysis of the coatings and filters design should be made. Currently, a random thickness variation was considered for the analysis. However, for some material growth systems, there could be a systematic error of the thickness, especially in evaporation system with faster growth rates. A detailed study of the deposition methods and their characteristics is needed to improve the reliability of the error analysis. The refractive index inhomogeneity was considered with a linear deviation along the thickness; however, this relation could be more complex. Different models should be

considered to model the refractive index variation in the thin films. For the atmospheric contamination, we only consider a 1 nm layer containing 1 – 5 % carbon. More surface contamination needs to be considered to better analyze the non-idealities.

9.2.3 Far UV optical coating growth

Currently, only a bilayer reflective coating based on Al_2O_3 and AlF_3 was fabricated. The Al-rich clusters in the plasma enhanced ALD AlF_3 films degrade the performance of the coatings. The next step includes growing a reflectance coating based on thermal ALD AlF_3, which contains reduced or negligible density of Al clusters as confirmed by X-ray photoelectron spectroscopy and spectroscopic ellipsometry. Besides the Al_2O_3/AlF_3 structure, the fabrication of other designed coatings, include SiO_2/AlF_3, and HfO_2/AlF_3 are also interesting. With optical measurements of the deposited coatings, the optical designs can be further improved to match the experimental results.

References

[1] A. Macleod and C. Clark, *Optical Coating Design with the Essential Macleod*. (Thin Film Center Inc, Tucson, AZ).

REFERENCES

[1] H. G. Tompkins and J. N. Hilfiker, *Spectroscopic Ellipsometry: Practical Application to Thin Film Characterization*. (Momentum Press, LLC, New York, 2016).

[2] D. E. Aspnes, "Spectroscopic ellipsometry — Past, present, and future," Thin Solid Films **571**, 334 (2014).

[3] H. Fujiwara, "*Principles of Ellipsometry*," in Spectroscopic Ellipsometry for Photovoltaics, Vol. 1, Ch. 1.1.1, edited by H. Fujiwara and R. W. Collins (Springer International Publishing AG, Cham, Switzerland, 2018).

[4] J. I. Larruquert, "*Optical properties of thin film materials at short wavelengths*," in Optical Thin Films and Coatings, Ch. 7, edited by A. Piegari and F. Flory (Woodhead Publishing, 2018).

[5] R. E. Hummel, "*The Optical Constants*," in Electronic Properties of Materials, Ch. 10, pp. 215, edited by R. E. Hummel (Springer 2010).

[6] R. E. Hummel, "*Quantum Mechanical Treatment of the Optical Properties*," in Electronic Properties of Materials, Ch. 12, pp. 247, edited by R. E. Hummel (Springer, 2010).

[7] M. Tryus, "Extreme Ultraviolet Reflectometry for Structural and Optical Characterization of Thin Films and Layer Systems," RWTH Aachen University, 2018.

[8] P. Y. Yu and M. Cardona, "*Optical Properties I*," in Fundamentals of Semiconductors - Physics and Materials Properties, Ch. 6, pp. 243, edited by P. Y. Yu and M. Cardona (Springer, 2010).

[9] M. Fox, "*Interband absorption*," in Optical Properties of Solids, Ch. 3, pp. 62 (Oxford University Press, 2010).

[10] M. Fox, "*Excitons*," in Optical Properties of Solids, Ch. 4, pp. 95 (Oxford University Press, 2010).

[11] A. Delin, P. Ravindran, O. Eriksson and J. M. Wills, "Full-potential optical calculations of lead chalcogenides," Int. J. Quantum Chem. **69**, 349 (1998).

[12] G. E. Jellison and F. A. Modine, "Parameterization of the optical functions of amorphous materials in the interband region," Appl. Phys. Lett. **69**, 371 (1996).

[13] J. L. Navarro, E. A. Albanesi, R. Vidal and J. Ferrón, "A study on the structural, electronic and optical properties of the α-AlF3 compound," Mater. Res. Bull. **83**, 615 (2016).

[14] E. S. Field, J. C. Bellum and D. E. Kletecka, "Laser damage comparisons of broad-bandwidth, high-reflection optical coatings containing TiO_2, Nb_2O_5, or Ta_2O_5 high index layers," Proc. SPIE **8885**, 88851X (2013).

[15] B. Fleming, M. Quijada, J. Hennessy, A. Egan, J. Del Hoyo, B. A. Hicks, J. Wiley, N. Kruczek, N. Erickson and K. France, "Advanced environmentally resistant lithium fluoride mirror coatings for the next generation of broadband space observatories," Appl. Opt. **56**, 9941 (2017).

[16] J. A. W. Co., "*"Goodness" of Fit: definition of the MSE*," in CompleteEASE Software Manual, Ch. 3.1 (J.A. Woollam Co., Lincoln, NE, 2014).

[17] M. Jerman, Z. Qiao and D. Mergel, "Refractive index of thin films of SiO_2, ZrO_2, and HfO_2 as a function of the films' mass density," Appl. Opt. **44**, 3006 (2005).

[18] M. F. Al-Kuhaili, "Optical properties of hafnium oxide thin films and their application in energy-efficient windows," Opt. Mater. **27**, 383 (2004).

[19] M. J. Dodge, "*Refractive index*," in Handbook of Laser Science and Technology, Vol. IV, pp. 30 (CRC Press, Boca Raton, 1986).

[20] G. Ghosh, "Dispersion-equation coefficients for the refractive index and birefringence of calcite and quartz crystals," Opt. Commun. **163**, 95 (1999).

[21] L. V. Rodriguez-de Marcos, J. I. Larruquert, J. A. Mendez and J. A. Aznarez, "Self-consistent optical constants of MgF_2, LaF_3, and CeF_3 films," Opt. Mater. Express **7**, 989 (2017).

[22] H. H. Li, "Refractive index of alkaline earth halides and its wavelength and temperature derivatives," Journal of Physical and Chemical Reference Data **9**, 161 (1980).

[23] J. Hennessy, A. Jewell, K. Balasubramanian and S. Nikzad, "Ultraviolet optical properties of aluminum fluoride thin films deposited by atomic layer deposition," J. Vac. Sci. Technol., A **34**, 01A120 (2016).

[24] D. König, R. Scholz, D. R. T. Zahn and G. Ebest, "Band diagram of the $AlF_3/SiO_2/Si$ system," J. Appl. Phys. **97**, 093707 (2005).

[25] A. Belosludtsev, K. Juškevičius, L. Ceizaris, R. Samuilovas, S. Stanionytė, V. Jasulaitienė and S. Kičas, "Correlation between stoichiometry and properties of scandium oxide films prepared by reactive magnetron sputtering," Appl. Surf. Sci. **427**, 312 (2018).

[26] R. K. Choudhary, P. Mishra, A. Biswas and A. C. Bidaye, "Structural and Optical Properties of Aluminum Nitride Thin Films Deposited by Pulsed DC Magnetron Sputtering," ISRN Materials Science **2013**, 1 (2013).

[27] I. Bhaumik, R. Bhatt, S. Ganesamoorthy, A. Saxena, A. K. Karnal, P. K. Gupta, A. K. Sinha and S. K. Deb, "Temperature-dependent index of refraction of monoclinic Ga_2O_3 single crystal," Appl. Opt. **50**, 6006 (2011).

[28] S.-L. Ku and C.-C. Lee, "Optical and structural properties of silicon nitride thin films prepared by ion-assisted deposition," Opt. Mater. **32**, 956 (2010).

[29] K.-N. Chen, C.-M. Hsu, J. Liu, Y.-C. Liou and C.-F. Yang, "Investigation of Antireflection Nb_2O_5 Thin Films by the Sputtering Method under Different Deposition Parameters," Micromachines **7**, 151 (2016).

[30] T. Siefke, S. Kroker, K. Pfeiffer, O. Puffky, K. Dietrich, D. Franta, I. Ohlídal, A. Szeghalmi, E. B. Kley and A. Tünnermann, "Materials Pushing the Application Limits of Wire Grid Polarizers further into the Deep Ultraviolet Spectral Range," Adv. Opt. Mater. **4**, 1780 (2016).

[31] F. Z. Tepehan, F. E. Ghodsi, N. Ozer and G. G. Tepehan, "Determination of optical properties of amorphous Ta_2O_5 films deposited by spin- and dip-coating methods," Sol. Energy Mater. Sol. Cells **46**, 311 (1997).

[32] L. V. Rodríguez-de Marcos, J. I. Larruquert, J. A. Méndez and J. A. Aznárez, "Self-consistent optical constants of SiO_2 and Ta_2O_5 films," Opt. Mater. Express **6**, 3622 (2016).

[33] J.-K. Yang, W. S. Kim and H.-H. Park, "Chemical bonding states and energy band gap of SiO_2-incorporated La_2O_3 films on n-GaAs (001)," Thin Solid Films **494**, 311 (2006).

[34] M. L. Huang, Y. C. Chang, C. H. Chang, T. D. Lin, J. Kwo, T. B. Wu and M. Hong, "Energy-band parameters of atomic-layer-deposition Al_2O_3/InGaAs heterostructure," Appl. Phys. Lett. **89**, 012903 (2006).

[35] E. R. Zakirov, V. G. Kesler, G. Y. Sidorov, I. P. Prosvirin, A. K. Gutakovsky and V. I. Vdovin, "XPS investigation of the ALD Al_2O_3/HgCdTe heterointerface," Semicond. Sci. Technol. **34**, 065007 (2019).

[36] A. S. Ferlauto, G. M. Ferreira, J. M. Pearce, C. R. Wronski, R. W. Collins, X. Deng and G. Ganguly, "Analytical model for the optical functions of amorphous semiconductors from the near-infrared to ultraviolet: Applications in thin film photovoltaics," J. Appl. Phys. **92**, 2424 (2002).

[37] G. E. Jellison and F. A. Modine, "Erratum: ‘‘Parameterization of the optical functions of amorphous materials in the interband region’’ [Appl. Phys. Lett. 69, 371 (1996)]," Appl. Phys. Lett. **69**, 2137 (1996).

[38] M. T. Aguilar-Gama, E. Ramírez-Morales, Z. Montiel-González, A. Mendoza-Galván, M. Sotelo-Lerma, P. K. Nair and H. Hu, "Structure and refractive index of thin alumina films grown by atomic layer deposition," Journal of Materials Science: Materials in Electronics **26**, 5546 (2015).

[39] W. R. Hunter, "Measurement of optical properties of materials in the vacuum ultraviolet spectral region," Appl. Opt. **21**, 2103 (1982).

[40] S. J. Byrnes, "Multilayer optical calculations," arXiv:1603.02720 (2016).

[41] M. Vidal-Dasilva, A. L. Aquila, E. M. Gullikson, F. Salmassi and J. I. Larruquert, "Optical constants of magnetron-sputtered magnesium films in the 25-1300 eV energy range," J. Appl. Phys. **108**, (2010).

[42] "Lambda 650/850/950 Hardware Guide." https://cmdis.rpi.edu/sites/default/files/UVVis-PerkinElmer-Lambda950-HardwareGuide.pdf (accessed 4/2/2021)

[43] W. Neumann, "*Spectrometer Concepts*," in Fundamentals of dispersive optical spectroscopy systems, Ch. 2, pp. 13, edited by W. Neumann (SPIE—The International Society for Optical Engineering, 2014).

[44] J. A. Samson and David L. EDERER, *Vacuum Ultraviolet Spectroscopy*. (Academic Press, 1998).

[45] T. Namioka, "Theory of the Concave Grating. III. Seya-Namioka Monochromator," J. Opt. Soc. Am. **49**, 951 (1959).

[46] Y. Ozaki, Y. Saito and S. Kawata, "*Introduction to FUV and DUV Spectroscopy*," in Far and Deep Ultraviolet Spectroscopy, Ch. 1, pp. 1, edited by Y. Ozaki and S. Kawata (Springer 2015).

[47] H. A. Macleod, "Thin-Film Optical Filters."

[48] J. Sun, X. Li, W. L. Zhang, K. Yi and J. D. Shao, "High-reflectivity mirrors by Al_2O_3, LaF_3 and AlF_3 for 193 nm application," Opt. Laser Technol. **56**, 65 (2014).

[49] S. Gunster, D. Ristau, A. Gatto, N. Kaiser, M. Trovo and M. Danailov, "Storage ring free-electron lasing at 176 nm-dielectric mirror development for vacuum ultraviolet free-electron lasers," Appl. Opt. **45**, 5866 (2006).

[50] V. S. P. Kumar, M. Kumar, N. Kumari, V. Karar and A. L. Sharma, "Fabrication of Al_2O_3/SiO_2 multilayer reflective filters with excellent uniformity for demanding optical interference filters," Mater. Res. Express **6**, 066410 (2019).

[51] P. Torchio, A. Gatto, M. Alvisi, G. Albrand, N. Kaiser and C. Amra, "High-reflectivity HfO_2/SiO_2 ultraviolet mirrors," Appl. Opt. **41**, 3256 (2002).

[52] L. Yuan, Y. N. Zhao, C. J. Wang, H. B. He, Z. X. Fan and J. D. Shao, "Effect of SiO_2 protective layer on the femtosecond laser-induced damage of HfO_2/SiO_2 multilayer high-reflective coatings," Appl. Surf. Sci. **253**, 3450 (2007).

[53] F. Réveret, L. Bignet, W. Zhigang, X. Lafosse, G. Patriarche, P. Disseix, F. Médard, M. Mihailovic, J. Leymarie, J. Zúñiga-Pérez and S. Bouchoule, "High reflectance dielectric distributed Bragg reflectors for near ultra-violet planar microcavities: SiO_2/HfO_2 versus $SiO_2/SiNx$," J. Appl. Phys. **120**, 093107 (2016).

[54] S. F. Pellicori, C. L. Martinez, P. Hausgen and D. Wilt, "Development and testing of coatings for orbital space radiation environments," Appl. Opt. **53**, A339 (2014).

[55] M. Zukic, D. G. Torr, J. F. Spann and M. R. Torr, "Vacuum ultraviolet thin-films. 2: Vacuum ultraviolet all-dielectric narrowband filters," Appl. Opt. **29**, 4293 (1990).

[56] X. D. Wang, B. Chen and L. Yao, "Design and fabrication of Far-ultraviolet reflective broadband filter based on dielectric materials," Appl. Spectrosc. **72**, 943 (2018).

[57] M. C. Liu, C. C. Lee, B. H. Liao, M. Kaneko, K. Nakahira and Y. Takano, "Fluoride antireflection coatings deposited at 193 nm," Appl. Opt. **47**, C214 (2008).

[58] R. Thielsch, "*Optical Coatings for the DUV/VUV*," in Optical Interference Coatings, pp. 257, edited by N. Kaiser and H. K. Pulker (Springer, 2003).

[59] H. K. Raut, V. A. Ganesh, A. S. Nair and S. Ramakrishna, "Anti-reflective coatings: A critical, in-depth review," Energy Environ. Sci. **4**, 3779 (2011).

[60] M. Keshavarz Hedayati and M. Elbahri, "Antireflective Coatings: Conventional Stacking Layers and Ultrathin Plasmonic Metasurfaces, A Mini-Review," Materials **9**, 497 (2016).

[61] M. H. Yang, A. Gatto and N. Kaiser, "Design and deposition of vacuum-ultraviolet narrow-bandpass filters for analytical chemistry applications," Appl. Opt. **45**, 1359 (2006).

[62] S. M. George, "Atomic layer deposition: an overview," Chem. Rev. **110**, 111 (2010).

[63] P. O. Oviroh, R. Akbarzadeh, D. Pan, R. A. M. Coetzee and T.-C. Jen, "New development of atomic layer deposition: processes, methods and applications," Sci. Technol. Adv. Mater. **20**, 465 (2019).

[64] P. French, G. Krijnen and F. Roozeboom, "Precision in harsh environments," Microsyst. Nanoeng. **2**, 16048 (2016).

[65] S. Zhuiykov, T. Kawaguchi, Z. Hai, M. Karbalaei Akbari and P. M. Heynderickx, "Interfacial engineering of two-dimensional nano-structured materials by atomic layer deposition," Appl. Surf. Sci. **392**, 231 (2017).

[66] C. Q. Hu, J. Z. Cai, Y. K. Li, C. B. Bi, Z. Q. Gu, J. Q. Zhu, J. F. Zang and W. T. Zheng, "In situ growth of ultra-smooth or super-rough thin films by suppression of vertical or horizontal growth of surface mounds," J. Mater. Chem. C **8**, 3248 (2020).

[67] P. A. Premkumar, A. Delabie, L. N. J. Rodriguez, A. Moussa and C. Adelmann, "Roughness evolution during the atomic layer deposition of metal oxides," J. Vac. Sci. Technol., A **31**, 061501 (2013).

[68] S. Tougaard, "Universality Classes of Inelastic Electron Scattering Cross-sections " Surf. Interface Anal. **25**, 137 (1997).

[69] J. F. Moulder, W. F. Stickle, P. E. Sobol and K. D. Bomben, "*Handbook of X-ray Photoelectron Spectroscopy*," Ch. 1, pp. 25 (Perkin-Elmer Corporation, Eden Prairie, Minnesota, USA 1979).

[70] C. C. Katsidis and D. I. Siapkas, "General transfer-matrix method for optical multilayer systems with coherent, partially coherent, and incoherent interference," Appl. Opt. **41**, 3978 (2002).

[71] B. Harbecke, "Coherent and incoherent reflection and transmission of multilayer structures," Appl. Phys. B **39**, 165 (1986).

[72] F. Bridou, M. Cuniot-Ponsard and J.-M. Desvignes, "Experimental determination of optical constants in the vacuum ultra violet wavelength region between 80 and 140nm: A reflectance versus thickness method and its application to ZnSe," Opt. Commun. **271**, 353 (2007).

[73] F. Bridou, M. Cuniot-Ponsard, J.-M. Desvignes, M. Richter, U. Kroth and A. Gottwald, "Experimental determination of optical constants of MgF2 and AlF3 thin films in the vacuum ultra-violet wavelength region (60–124nm), and its application to optical designs," Opt. Commun. **283**, 1351 (2010).

[74] O. Stenzel, "*Basic Knowledge on Optical Constants*," in Optical Coatings Material Aspects in Theory and Practice, Ch. 2, pp. 21, edited by O. Stenzel (Springer 2014).

[75] [Online] Available: https://mcphersoninc.com/

[76] "Responsivity." Wikipedia. https://en.wikipedia.org/wiki/Responsivity (accessed)

[77] E. D. Palik, *Handbook of Optical Constants of Solids*. (Academic Press, 1985).

[78] in *Handbook of Optical Constants of Solids*, edited by E. D. Palik (1991), Vol. 2, pp. 3.

[79] Z.-Y. Wang, R.-J. Zhang, H.-L. Lu, X. Chen, Y. Sun, Y. Zhang, Y.-F. Wei, J.-P. Xu, S.-Y. Wang, Y.-X. Zheng and L.-Y. Chen, "The impact of thickness and thermal annealing on refractive index for aluminum oxide thin films deposited by atomic layer deposition," Nanoscale Res. Lett. **10**, (2015).

[80] C. C. Lee, M. C. Liu, M. Kaneko, K. Nakahira and Y. Takano, "Influence of thermal annealing and ultraviolet light irradiation on LaF3 thin films at 193 nm," Appl. Opt. **44**, 6921 (2005).

[81] S. Shi, S. Qian, X. Hou, J. Mu, J. He and X. Chou, "Structural and optical properties of amorphous Al2O3 thin film deposited by atomic layer deposition," Adv. Condens. Matter Phys. **2018**, (2018).

[82] C. Barbos, D. Blanc-Pelissier, A. Fave, C. Botella, P. Regreny, G. Grenet, E. Blanquet, A. Crisci and M. Lemiti, "Al2O3 thin films deposited by thermal atomic layer deposition: Characterization for photovoltaic applications," Thin Solid Films **617**, 108 (2016).

[83] C. C. Lee, M. C. Liu, M. Kaneko, K. Nakahira and Y. Takano, "Characterization of AlF3 thin films at 193 nm by thermal evaporation," Appl. Opt. **44**, 7333 (2005).

[84] D. J. Comstock and J. W. Elam, "Atomic Layer Deposition of Ga2O3 Films Using Trimethylgallium and Ozone," Chem. Mater. **24**, 4011 (2012).

[85] K. M. Kim, J. S. Jang, S. G. Yoon, J. Y. Yun and N. K. Chung, "Structural, Optical and Electrical Properties of HfO2 Thin Films Deposited at Low-Temperature Using Plasma-Enhanced Atomic Layer Deposition," Materials (Basel) **13**, (2020).

[86] C. Barbos, D. Blanc-Pelissier, A. Fave, E. Blanquet, A. Crisci, E. Fourmond, D. Albertini, A. Sabac, K. Ayadi, P. Girard and M. Lemiti, "Characterization of Al2O3 Thin Films Prepared by Thermal ALD," Energy Procedia **77**, 558 (2015).

[87] Y. Lee, J. W. DuMont, A. S. Cavanagh and S. M. George, "Atomic Layer Deposition of AlF_3 Using Trimethylaluminum and Hydrogen Fluoride," J. Phys. Chem. C **119**, 14185 (2015).

[88] J. Hennessy, K. Balasubramanian, C. S. Moore, A. D. Jewell, S. Nikzad, K. France and M. Quijada, "Performance and prospects of far ultraviolet aluminum mirrors protected by atomic layer deposition," Journal of Astronomical Telescopes Instruments and Systems **2**, (2016).

[89] S. Günstera, H. Blaschkea, D. Ristaua, M. Danailovb, M. Trovób, A. Gattoc, N. Kaiserc, F. Sartod, D. Florid and F. Menchinid, "Radiation resistance of single- and multilayer coatings against synchrotron radiation," Proc. SPIE **5250**, 146 (2004).

[90] R. H. French, H. Müllejans and D. J. Jones, "Optical Properties of Aluminum Oxide: Determined from Vacuum Ultraviolet and Electron Energy-Loss Spectroscopies," J. Am. Ceram. Soc. **81**, 2549 (2005).

[91] Y.-N. Xu and W. Y. Ching, "Self-consistent band structures, charge distributions, and optical-absorption spectra in MgO, α-Al2O3, andMgAl2O4," Physical Review B **43**, 4461 (1991).

[92] F. Naumann, J. Reck, H. Gargouri, B. Gruska, A. Blümich, A. Mahmoodinezhad, C. Janowitz, K. Henkel and J. I. Flege, "In situ real-time and ex situ spectroscopic analysis of Al2O3 films prepared by plasma enhanced atomic layer deposition," J. Vac. Sci. Technol., B **38**, (2020).

[93] Bernhard von Blanckenhagen, Diana Tonova and J. Ullmann, "Application of the Tauc–Lorentz formulation to the interband absorption of optical coating materials," Appl. Opt. **41**, 3137 (2002).

[94] A. Duparré, R. Geyl, D. Franta, D. Nečas, I. Ohlídal and A. Giglia, in *Optical Systems Design 2015: Optical Fabrication, Testing, and Metrology V* (2015).

[95] M. Balog, M. Schieber, M. Michman and S. Patai, "Chemical vapor deposition and characterization of HfO2 films from organo-hafnium compounds," Thin Solid Films **41**, 247 (1977).

[96] T. Tan, Z. Liu and Y. Li, "First-principles calculations of electronic and optical properties of Ti-doped monoclinic HfO2," J. Alloys Compd. **510**, 78 (2012).

[97] J. C. Garcia, presented at the AIP Conference Proceedings, 2005 (unpublished).

[98] R. Drazdys, L. Stasiūnas, K. Leinartas, R. Buzelis, T. Tolenis, K. Juškevičius, U. Gimževskis, A. Selskis and V. Jasulaitienė, "Optical Properties of HfO2 Thin Films Grown by Atomic Layer Deposition," Optical Interference CoatingsWB.2 (2016).

[99] D. Franta, D. Necas and I. Ohlidal, "Universal dispersion model for characterization of optical thin films over a wide spectral range: application to hafnia," Appl Opt **54**, 9108 (2015).

[100] S. Li, Y. Zhang, D. Yang, W. Yang, X. Chen, H. Zhao, J. Hou and P. Yang, "Structure and optical properties of HfO2 films on Si (100) substrates prepared by ALD at different temperatures," Physica B **584**, 412065 (2020).

[101] H. Xue, Q. He, G. Jian, S. Long, T. Pang and M. Liu, "An Overview of the Ultrawide Bandgap Ga2O3 Semiconductor-Based Schottky Barrier Diode for Power Electronics Application," Nanoscale Res. Lett. **13**, (2018).

[102] K. Yamaguchi, "First principles study on electronic structure of β-Ga2O3," Solid State Commun. **131**, 739 (2004).

[103] D. F. Edwards, "*Beta-Gallium Oxide (β-Ga2O3)*," in Handbook of Optical Constants of Solids, pp. 753 (Elsevier, 1997).

[104] S. Ghose, S. Rahman, L. Hong, J. S. Rojas-Ramirez, H. Jin, K. Park, R. Klie and R. Droopad, "Growth and characterization of β-Ga2O3 thin films by molecular beam epitaxy for deep-UV photodetectors," J. Appl. Phys. **122**, 095302 (2017).

[105] S. J. Hao, M. Hetzl, F. Schuster, K. Danielewicz, A. Bergmaier, G. Dollinger, Q. L. Sai, C. T. Xia, T. Hoffmann, M. Wiesinger, S. Matich, W. Aigner and M. Stutzmann, "Growth and characterization of β-Ga2O3 thin films on different substrates," J. Appl. Phys. **125**, 105701 (2019).

[106] J. Y. Tsao, S. Chowdhury, M. A. Hollis, D. Jena, N. M. Johnson, *et al.*, "Ultrawide-Bandgap Semiconductors: Research Opportunities and Challenges," Adv. Electron. Mater. **4**, 1600501 (2018).

[107] W. C. Walker and J. Osantowski, "Ultraviolet Optical Properties of Diamond," Physical Review **134**, A153 (1964).

[108] C. Tarrio and S. E. Schnatterly, "Interband transitions, plasmons, and dispersion in hexagonal boron nitride," Physical Review B **40**, 7852 (1989).

[109] K. P. Loh, I. Sakaguchi, M. Nishitani-Gamo, T. Taniguchi and T. Ando, "Surface structure of single-crystal cubic boron nitride (111) studied by LEED, EELS, and AES," Physical Review B **56**, R12791 (1997).

[110] D. A. Evans, A. G. Mcglynn, B. M. Towlson, M. Gunn, D. Jones, T. E. Jenkins, R. Winter and N. R. J. Poolton, "Determination of the optical band-gap energy of cubic and hexagonal boron nitride using luminescence excitation spectroscopy," J. Phys.: Condens. Matter **20**, 075233 (2008).

[111] J. N. Hilfiker, J. Sun and N. Hong, "*Data Analysis*," in Spectroscopic Ellipsometry for Photovoltaics, Vol. 1, Ch. 3, edited by H. Fujiwara and R. W. Collins (Springer International Publishing AG, Cham, Switzerland, 2018).

[112] J. Shammas, "Characterization of Cubic Boron Nitride Interfaces with in situ Photoelectron Spectroscopy," Arizona State University, 2016.

[113] J. Shammas, Y. Yang, X. Wang, F. A. M. Koeck, M. R. McCartney, D. J. Smith and R. J. Nemanich, "Band offsets of epitaxial cubic boron nitride deposited on polycrystalline diamond via plasma-enhanced chemical vapor deposition," Appl. Phys. Lett. **111**, (2017).

[114] M. Chubarov, H. Pedersen, H. Högberg, S. Filippov, J. A. A. Engelbrecht, J. O'Connel and A. Henry, "Boron nitride: A new photonic material," Physica B **439**, 29 (2014).

[115] R. Haubner, M. Wilhelm, R. Weissenbacher and B. Lux, "*Boron Nitrides — Properties, Synthesis and Applications*," in Struct. Bond., pp. 1 (Springer Berlin Heidelberg, 2002).

[116] Y. N. Xu and W. Y. Ching, "Calculation of ground-state and optical properties of boron nitrides in the hexagonal, cubic, and wurtzite structures," Phys Rev B Condens Matter **44**, 7787 (1991).

[117] S. Adachi, *Optical Constants of Crystalline and Amorphous Semiconductors*. (1999).

[118] M. Schubert, B. Rheinländer, E. Franke, H. Neumann, J. Hahn, M. Röder and F. Richter, "Anisotropy of boron nitride thin-film reflectivity spectra by generalized ellipsometry," Appl. Phys. Lett. **70**, 1819 (1997).

[119] M. Ye and M. P. Delplancke-Ogletree, "Formation of cubic boron nitride thin films using ECR plasma enhanced CVD," Diamond Relat. Mater. **9**, 1336 (2000).

[120] G. A. Gary, E. A. West, D. Rees, J. A. Mckay, M. Zukic and P. Herman, "Solar CIV vacuum-ultraviolet Fabry-Perot interferometers," Astron. Astrophys. **461**, 707 (2007).

[121] P. Ribes-Pleguezuelo, F. Keller and M. Taccola, "UV astronomy with small satellites," arXiv:2006.14967 [astro-ph.IM] (2020).

[122] B. Q. Wua and A. Kumar, "Extreme ultraviolet lithography: A review," J. Vac. Sci. Technol., B **25**, 1743 (2007).

[123] P. R. Chalker, P. A. Marshall, K. Dawson, I. F. Brunell, C. J. Sutcliffe and R. J. Potter, "Vacuum ultraviolet photochemical selective area atomic layer deposition of Al2O3 dielectrics," AIP Adv. **5**, (2015).

[124] M. L. Grilli, F. Menchini, A. Piegari, D. Alderighi, G. Toci and M. Vannini, "Al2O3/SiO2 and HfO2/SiO2 dichroic mirrors for UV solid-state lasers," Thin Solid Films **517**, 1731 (2009).

[125] S. Kumar, A. Shankar, N. Kishore, C. Mukherjee, R. Kamparath and S. Thakur, "Laser-induced damage threshold study on TiO2/SiO2 multilayer reflective coatings," Indian J. Phys. **94**, 105 (2020).

[126] K. Marszalek, A. Malek and P. Winkowski, "The GdF3/MgF2 bilayer as an antireflective narrow-band ultraviolet filter," Optica Applicata **46**, 187 (2016).

[127] H. A. Macleod, "*Multilayer high-reflectance coatings*," in Thin-Film Optical Filters, Ch. 6, edited by E. R. Pike and R. G. W. Brown (CRC Press, Boca Raton, 2018).

[128] A. Macleod and C. Clark, *Optical Coating Design with the Essential Macleod*. (Thin Film Center Inc, Tucson, AZ).

[129] M. Zukic, D. G. Torr, J. M. Kim, J. F. Spann and M. R. Torr, "Filters for the International Solar Terrestrial Physics Mission far-ultraviolet imager," Opt. Eng. **32**, 3069 (1993).

[130] N. D. Goldina, "Design of Metal-Dielectric Filters in Transmitted Ultraviolet Light," Optoelectronics, Instrumentation and Data Processing **55**, 550 (2019).

[131] G. Christidis, U. Koch, E. Poloni, E. De Leo, B. J. Cheng, S. M. Koepfli, A. Dorodnyy, F. Bouville, Y. Fedoryshyn, V. Shklover and J. Leuthold, "Broadband, high-temperature stable reflector for aerospace thermal radiation protection," ACS Appl. Mater. Interfaces **12**, 9925 (2020).

[132] H. W. Moos, W. C. Cash, L. L. Cowie, A. F. Davidsen, A. K. Dupree, *et al.*, "Overview of the Far Ultraviolet Spectroscopic Explorer Mission," Astrophys. J. **538**, L1 (2000).

[133] M. S. Alias, A. Y. Alyamani, B. S. Ooi, A. A. Alatawi, W. K. Chong, M. Tangi, J. A. Holguin-Lerma, E. Stegenburgs, M. K. Shakfa, T. K. Ng and A. M. Albadri, "High reflectivity YDH/SiO_2 distributed Bragg reflector for UV-C wavelength regime," IEEE Photonics J. **10**, 1 (2018).

[134] T. Sertel, Y. Ozen, V. Baran and S. Ozcelik, "Effect of single-layer Ta_2O_5 and double-layer SiO_2/Ta_2O_5 anti-reflective coatings on GaInP/GaAs/Ge triple-junction solar cell performance," J. Alloys Compd. **806**, 439 (2019).

[135] M. Zukic and D. G. Torr, "Multiple reflectors as narrow-band and broadband vacuum ultraviolet filters," Appl. Opt. **31**, 1588 (1992).

[136] M. Beasley, F. Greer and S. Nikzad, "Progress in new ultraviolet reflective coating techniques," Proc. SPIE **8443**, 84433Q (2012).

[137] T. Nakashima, K. Takeda, H. Shinzato, M. Iwaya, S. Kamiyama, T. Takeuchi, I. Akasaki and H. Amano, "Combination of Indium-Tin oxide and SiO_2/AlN dielectric multilayer reflective electrodes for ultraviolet-light-emitting diodes," Jpn. J. Appl. Phys. **52**, (2013).

[138] M. Fernandez-Perea, M. Vidal-Dasilva, J. I. Larruquert, J. A. Mendez and J. A. Aznarez, "Novel narrow filters for imaging in the 50-150 nm VUV range," Astrophys. Space Sci. **320**, 243 (2009).

[139] J. Robertson, "High dielectric constant oxides," The European Physical Journal Applied Physics **28**, 265 (2004).

[140] R. W. Johnson, A. Hultqvist and S. F. Bent, "A brief review of atomic layer deposition: from fundamentals to applications," Mater. Today **17**, 236 (2014).

[141] B. Groven, M. Heyne, A. Nalin Mehta, H. Bender, T. Nuytten, J. Meersschaut, T. Conard, P. Verdonck, S. Van Elshocht, W. Vandervorst, S. De Gendt, M. Heyns, I. Radu, M. Caymax and A. Delabie, "Plasma-enhanced atomic layer deposition of two-dimensional WS_2 from WF_6, H_2 plasma, and H_2S," Chem. Mater. **29**, 2927 (2017).

[142] H. B. Profijt, S. E. Potts, M. C. M. van de Sanden and W. M. M. Kessels, "Plasma-Assisted Atomic Layer Deposition: Basics, Opportunities , and Challenges," J. Vac. Sci. Technol., A **29**, 050801 (2011).

[143] S. K. Tripathy, "Refractive indices of semiconductors from energy gaps," Opt. Mater. **46**, 240 (2015).

[144] J. Hennessy and S. Nikzad, "Atomic Layer Deposition of Lithium Fluoride Optical Coatings for the Ultraviolet," Inorganics **6**, 46 (2018).

[145] P. Scowen, D. C. Messina, Z. Huang, B. Eller, R. J. Nemanich, H. Yu, T. Mooney and M. Beasley. "Building a Better ALD: Use of Plasma-Enhanced ALD to Construct Efficient Interference Filters for the FUV." http://www.astrostrategictech.us/pdf/projectfiles/Reports/14-SAT14-0023_AR_Scowen_Paul_2019_06.pdf (accessed 8/10/2020)

[146] G. A. Olah, J. T. Welch, Y. D. Vankar, M. Nojima, I. Kerekes and J. A. Olah, "Synthetic methods and reactions. 63. Pyridinium poly(hydrogen fluoride) (30% pyridine-70% hydrogen fluoride): a convenient reagent for organic fluorination reactions," The Journal of Organic Chemistry **44**, 3872 (1979).

[147] M. F. J. Vos, H. C. M. Knoops, R. A. Synowicki, W. M. M. Kessels and A. J. M. Mackus, "Atomic layer deposition of aluminum fluoride using $Al(CH_3)_3$ and SF_6 plasma," Appl. Phys. Lett. **111**, 113105 (2017).

[148] J. A. W. Co., "*Absorbing Thin Films (B-Spline)*," in CompleteEASE Software Manual, Ch. 4.3 (J.A. Woollam Co., Lincoln, NE, 2014).

[149] M. Mäntymäki, M. J. Heikkilä, E. Puukilainen, K. Mizohata, B. Marchand, J. Räisänen, M. Ritala and M. Leskelä, "Atomic Layer Deposition of AlF_3 Thin Films Using Halide Precursors," Chem. Mater. **27**, 604 (2015).

[150] Eugene. Staritzky and L. B. Asprey, "Crystallographic Data. 159. Aluminum Trifluoride, AlF_3," Anal. Chem. **29**, 984 (1957).

[151] M. Broas, O. Kanninen, V. Vuorinen, M. Tilli and M. Paulasto-Kröckel, "Chemically Stable Atomic-Layer-Deposited Al_2O_3 Films for Processability," ACS Omega **2**, 3390 (2017).

[152] A. Makarowicz, C. L. Bailey, N. Weiher, E. Kemnitz, S. L. M. Schroeder, S. Mukhopadhyay, A. Wander, B. G. Searle and N. M. Harrison, "Electronic structure of Lewis acid sites on high surface area aluminium fluorides: a combined XPS and ab initio investigation," Physical Chemistry Chemical Physics **11**, 5664 (2009).

[153] D. Y. Smith, E. Shiles and M. Inokuti, "*The Optical Properties of Metallic Aluminum*," in Handbook of Optical Constants of Solids, Vol. 1, pp. 369 (Elsevier, 1997).

[154] J. Barth, R. L. Johnson and M. Cardona, "*Spectroscopic Ellipsometry in the 6–35 eV Region*," in Handbook of Optical Constants of Solids, pp. 213 (Elsevier, 1997).

[155] U. Finkenzeller and D. Labs, "Deuterium lamp as a UV continuum source from 160 nm to 320 nm for space applications," Appl. Opt. **18**, 3938 (1979).

[156] W. Zheng, L. Jia and F. Huang, "Vacuum-Ultraviolet Photon Detections," iScience **23**, 101145 (2020).

[157] "VUV system: Detector." Horiba Ltd. https://www.horiba.com/gbr/technology/measurement-and-control-techniques/spectroscopy/vacuum-ultra-violet-spectroscopy/vuv-system-detector/ (accessed)

[158] L. Jia, W. Zheng and F. Huang, "Vacuum-ultraviolet photodetectors," PhotoniX **1**, (2020).

[159] "Si Photodiodes Selection Guide - April 2020." Hamamatsu Photonics K.K. https://www.hamamatsu.com/resources/pdf/ssd/si_pd_kspd0001e.pdf (accessed)

[160] M. Richter, U. Kroth, A. Gottwald, C. Gerth, K. Tiedtke, T. Saito, I. Tassy and K. Vogler, "Metrology of pulsed radiation for 157-nm lithography," Appl. Opt. **41**, 7167 (2002).

[161] "Photomultiplier Tube." Wikipedia. https://en.wikipedia.org/wiki/Photomultiplier_tube (accessed)

[162] "Charge-coupled device." Wikipedia. https://en.wikipedia.org/wiki/Charge-coupled_device (accessed)

[163] "What is a CCD Detector?" Horiba Ltd. https://www.horiba.com/en_en/technology/measurement-and-control-techniques/spectroscopy/detectors/what-is-a-ccd-detector/ (accessed)

[164] "Windowless, back illuminated CCD." McPherson Inc. https://mcphersoninc.com/detectors/directDetectionCCD.html (accessed)

[165] "Reflectance." Wikipedia. https://en.wikipedia.org/wiki/Reflectance (accessed)

[166] H. A. MacEwen, J. B. Breckinridge, K. Balasubramanian, J. Hennessy, N. Raouf, S. Nikzad, M. Ayala, S. Shaklan, P. Scowen, J. Del Hoyo and M. Quijada, in *UV/Optical/IR Space Telescopes and Instruments: Innovative Technologies and Concepts VII* (2015).

[167] M.F.J. Vos, A. J. M. Mackus and W. M. M. Kessels. "Atomic Layer Deposition Process Development – 10 steps to successfully develop, optimize and characterize ALD recipes." Atomic Limits. https://www.atomiclimits.com/2019/02/12/atomic-layer-deposition-process-development-10-steps-to-successfully-develop-optimize-and-characterize-ald-recipes/ (accessed)

[168] N. Hong. "1A: Introduction to WVASE Data Analysis." J. A. Woollam Co., Inc. https://www.seas.upenn.edu/~nanosop/documents/Session1A_UPenn_WVASE_Feb_2014.pdf (accessed)

[169] "AFM scanning modes." MAX IV Laboratory. https://www.maxiv.lu.se/accelerators-beamlines/support-labs-microscopy/atomic-force-microscopy/afm-scanning-modes/ (accessed)

[170] L. C. d. Carvalho. "X-ray photoelectron spectroscopy - Basic components of a monochromatic XPS system." Wikipedia. https://en.wikipedia.org/wiki/X-ray_photoelectron_spectroscopy (accessed)

[171] "High Intensity, 150 W Type, Vacuum UV (from 115 nm) Light Source - L1835." Hamamatsu Photonics K.K. https://www.hamamatsu.com/resources/pdf/etd/L1314_L1835_TLSO1012E.pdf (accessed)

[172] "Aberration Corrected Vacuum Monochromator." McPherson Inc. https://mcphersoninc.com/spectrometers/vuvuvvis/model234302.html (accessed)

[173] "Model 789A-3 Scan Controller." McPherson Inc. https://nstx.pppl.gov/nstxhome/DragNDrop/Operations/Diagnostics_&_Support_Sys/DIMS/789A3%20Manual.pdf (accessed)

[174] "Toroidal Mirrors (Definitions)." ZILTA Co., Inc. http://www.lasertechn.com/index.php/toroidal-mirrors (accessed)

[175] "VUV Si Detector." McPherson Inc. https://mcphersoninc.com/detectors/vuv-si-diode.html (accessed)

APPENDIX A

MAINTENANCE ON THE FAR UV SPECTROMETER

This section covers the general procedures for the maintenance on the *in-situ* variable angle Far UV spectrometer, described in Chapter 4. The procedures on vacuum vent/pump, diffraction grating calibration, and deuterium lamp window cleaning will be described.

A.1. Vacuum vent/pump

In some situations, the system needs to be vented to atmosphere. To do so, make sure the gate valves are all open in this system. Then, turn off the turbomolecular pumps first. After about 20-30 minutes, close the valves on the roughing pumps. Next, open the knobs on the monochromator and the toroidal mirror, slightly open the UHP N_2 gas valve. When the pressure is close to the atmosphere, the caps on the monochromator and the toroidal can be opened.

A.2. Diffraction grating calibration

If the emission spectrum measured for the lamp is shifted a lot (+/- 10nm) compared with the reference spectrum, the grating needs to be calibrated. To do so, the chambers need to be vented following the procedures shown in A1.

The procedures for calibrating the gratings are shown below. The configuration of the diffraction grating, Fig. A1, should be used along with the procedures described below.

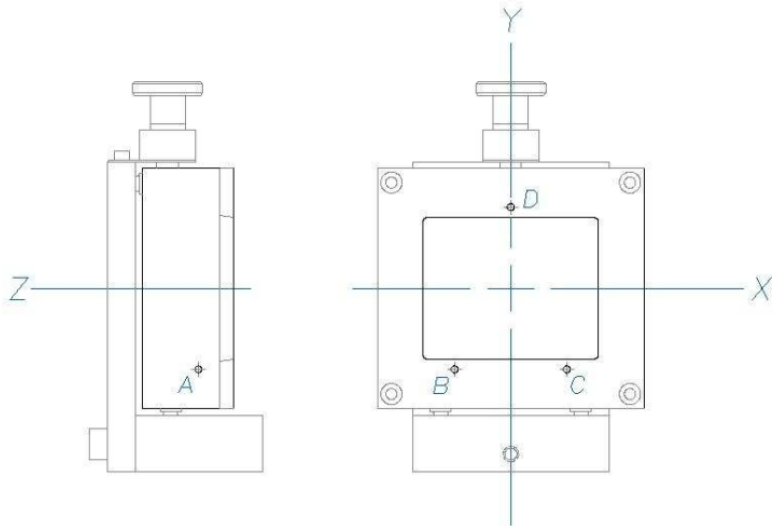

Figure A1. Diffraction grating configuration. Copyright © 2021, McPherson Inc.

I. First check the image position height wise. Set entrance and exit slit heights to the same value (4 mm). Find the zero order on the exit slit and by positioning your eye further away from the slit on the optical axis check if white light fills entire slit (slits can be wide open). If the image is high loosen screw D, otherwise tighten screw D (Fig. A1). This shifts all wavelengths up and down accordingly.

II. After the height is set check the wavelength position. Move the leadscrew to "00000" position and by looking inside the instrument determine the position of the white light. If the light is between two slits tighten screw C or loosen screw B (Fig. A1) until light gets through the exit slit jaws. If the light is on the other side of exit slit tighten screw B or loosen screw C (Fig. A1). This procedure will bring you close to the final alignment.

III. Check the image position height wise again and if it is ok put your detector on and using scan controller scan zero order. Make sure that when you do

that software counter value and actual counter reading are set to zero. If the scanned zero order is below “0” tighten screw C or loosen screw B, if scanned zero order is above “0” tighten screw B or loosen screw C (Fig. A1) until scanned line coincide with “0” reading. Once zero order is on “0” all other wavelengths should be in their positions. The grating sent with the instrument can be used as a master grating.

IV. Last thing to check is focus. If the focus is not satisfactory, bring the grating out by loosening screws B, C and D (Fig. A1) by the same amount. Scan the line and check FWHM. If focus gets worse rotate screws in opposite direction. Check the image position height wise and wavelength wise again.

Note: Adjust screws B, C and D by very little (1/8 of the turn). Small screw adjustments cause big shifts in image position.

A.3. Deuterium lamp window cleaning

Sometimes, the deuterium lamp MgF_2 window needs to be polished. The polishing procedures are shown as below:

If previously used in air:

A wipe with absolute alcohol on a fresh paper tissue untouched by hand is sufficient. Ethanol or methanol can be used. Methanol, although it is poisonous, is preferred because its vapor has no absorption bands in the air UV.

If previously used in a vacuum system:

All vacuum system will cause lamp degradation because of polymerization of vacuum greases and oils on the window. These should be removed each time the lamp is used and is most readily achieved by repolishing using 0.05-micron alumina polishing powder using the following procedure:

I. Place a small quantity of the alumina powder in a suitable clean container and add enough de-ionized (or distilled) water to make a thick slurry or paste. Take a small piece of cotton wool and twist and fold it so that it produces a small pad 10mm to 15mm diameter, hold it in your fingers, using gloves.

II. Dip the pad in the slurry and rub over the window keeping the pad moving in a circular pattern. Light pressure, like that used when writing a pencil, should be applied and the polishing should continue for one minute. Re-coat the pad with alumina pastes if necessary, as the alumina tends to work its way into the cotton wool and over the edge of the window.

III. Wipe the window free of alumina powder with a pad of cotton wool moistened with de-ionized water. Do this twice.

IV. Clean by placing a few drops of methyl alcohol on the windows and wipe the surface with a fresh lens cleaning tissue using a circular motion. Place a few more of alcohol on the window and wipe off.

Degradation in vacuum may be reversed to a certain degree by operating the lamp with air in front of the window using the ozone cleaning effect, oxidizing the hydrocarbons on the window surfaces.

APPENDIX B

OPERATION PROCEDURES OF THE FAR UV SPECTROMETER

This section covers the general operation procedures for the *in-situ* variable angle Far UV spectrometer, described in Chapter 4.

B.1 System Check

Before use of the spectrometer for the measurements, make sure the following things:

I. Vacuum pressure is normal ($<10^{-6}$ torr) and the displayed current on the turbomolecular pump controller is normal (0.07-0.09 mA). Make sure the cooling water on the deuterium lamp is on. The black caps on the view port windows should be covered, make sure there are no external light into the sample chamber. The gate valve between the sample chamber and the toroidal mirror should be open, otherwise the light will not be in. If everything is normal, move on to next step.

II. Turn off the cold cathode gauge. Turn on the pico-ammeter, leave it on 10-30 minutes for warm-up. The baseline measurements should be done first, with the detector rotated to the position with a white marker on the detector manipulator stage. As for the sample stage, the *z*-height should be adjusted to the position of 0 cm. Next, turn on the spectrometer control software, check the displayed output wavelength shown in Fig. 4.9b. If it is not the wanted value, use Go to wavelength function in the control software.

    Then, turn on the deuterium lamp power supply, leave it for 20 s warm-up. Click the CONFIGUE button as shown in Fig. 7. The displayed current should be around 8×10^{-7} mA. If not, wait a little longer for the lamp to be operational. Click it again to close it.

B.2 Data Collection

After the system check is ready, one can follow the next steps to start the actual measurements.

III. Baseline measurements. Clearly specify the Begin, End, and Point Increment under the Motion Parameters on the control software. Make sure the Current Position and Counter Reading under Monochromator 1 are same, and both are same with the Begin position you specified. If not, manually change the Counter Reading to be the same number with the Begin position. Then, choose Voltage under the Application, with Delay Second specified, one can click Scan to start the baseline intensity measurements.

IV. Reflectance measurements. After the baseline measurement is done, save the file. Next, adjust the z-height of the sample stage back to 3.5 cm. For the measurement with the incident angle of 75°, the sample stage should be rotated to the angle of 120°, shown in Fig. 4.11a, and rotate the detector to the red marker on the manipulator stage. For the measurement with incident angle of 33°, the sample stage should be rotated to the angle of 67.5° and adjust the detector position to the black marker on the rotational stage. Then, use the software to move back to the Begin wavelength, and choose Reflectance under Application, and click Scan to load the Baseline file for the reflectance measurements. The reflectance of the sample will be internally calculated by the software with the Eq. 4.3 shown below. The transmission measurements can also be made without changing the angles of the sample and the detector.

APPENDIX C

COPYRIGHT PERMISSION

Copyright permissions for the re-use/re-print of the following figures were obtained or requested from the publishers. The detailed permission agreement for each figure with copyright statement in the text can be provided upon request. Please contact me at: Zhiyu.Huang@asu.edu if there is any copyright violation in this Dissertation.

C. 1 Permission Agreement Obtained for Following Figures:

Figure 2.1: Reproduced with permission of Cambridge University Press through PLSclear, Soft X-Rays and Extreme Ultraviolet Radiation by David Attwood, Copyright © 1999, Cambridge University Press.

Figure 2.2: Reprinted/adapted by permission from [Springer Nature]: [Springer] [The Optical Constants] by [Rolf E. Hummel] [Copyright © 2011, Springer Science Business Media, LLC]

Figure 2.3: Reprinted/adapted by permission from [Springer Nature]: [Springer] [Quantum Mechanical Treatment of the Optical Properties] by [Rolf E. Hummel] [Copyright © 2011, Springer Science Business Media, LLC]

Figure 2.4: Reproduced with permission of Oxford University Press through PLSclear, Optical Properties of Solids by Mark Fox, Copyright © 2010, Oxford University Press.

Figure 2.5: Reproduced with permission of Oxford University Press through PLSclear, Optical Properties of Solids by Mark Fox, Copyright © Oxford University Press 2010.

Figure 2.10: Reprinted/adapted by permission from [Springer Nature]: [Springer] [Atomistic Theory of the Optical Properties] by [Rolf E. Hummel] [Copyright © 2011, Springer Science Business Media, LLC]

Figure 2.11: [Atomistic Theory of the Optical Properties] by [Rolf E. Hummel] [Copyright © 2011, Springer Science Business Media, LLC]

Figure 2.21 and **2.22**: Copyright © 2014 Society of Photo-Optical Instrumentation Engineers (SPIE)

Figure 2.23 and **2.24**: Copyright © 1999 Elsevier Inc.

Figure 2.25: Reprinted/adapted by permission from [Springer Nature]: [Springer] [Introduction to FUV and DUV Spectroscopy] by [Yukihiro Ozaki, Yuika Saito, Satoshi Kawata] [Copyright © 2015, Springer Japan]

Figure 2.28a: Reprinted/adapted by permission from [Springer Nature]: [Springer] [Optical Coatings for the DUV/VUV] by [Roland Thielsch] [Copyright © 2003, Springer-Verlag Berlin Heidelberg 2003]

Figure 2.28b: Copyright © 2018, Elsevier Ltd.

Figure 2.30: Reprinted/adapted by permission from [Springer Nature]: [Springer] [Optical Coatings for the DUV/VUV] by [Roland Thielsch] [Copyright © 2003, Springer-Verlag Berlin Heidelberg 2003]

Figure 2.32 and **2.33**: Republished with permission of Taylor & Francis Group LLC - Books, from [Thin-Film Optical Filters, H. Angus Macleod, 4th edition, and Copyright © 2010]; permission conveyed through Copyright Clearance Center, Inc.

Figure 5.1, and **5.2**: Copyright © 2016, Elsevier.

Figure 5.12: Copyright © 2011, Elsevier B.V.

Figure 5.17: Copyright © 2004, Elsevier Ltd.

C. 2 No Permission Required for Following Figures:

Figure 2.26: Copyright © CC BY-SA 3.0

Figure 3.5: Public domain

C. 3 Permission Agreement Requested for Following Figures:

As of April 30, 2021, the copyright permission agreements for following figures are requested. The detailed agreement can be provided if issued. If any of the following figures violates the copyright permission of the publishers, the figures will be permanently removed. Unless further modification request sent to ProQuest, there are no copyright issues for following figures. Please contact me at Zhiyu.Huang@asu.edu for any questions about the copyright issues.

Figure 2.20 and **Table 2.2**: Copyright © 2004 PerkinElmer, Inc.

Figure 2.35: Copyright © The Optical Society, 2006.

Figure 3.1: Copyright © Atomic Limits, 2019.

Figure 3.4: Copyright © MAX IV, 2021.

Figure 3.11: Copyright © 2014, Springer-Verlag Berlin Heidelberg.

Figure 4.4: Copyright © 1998, Hamamatsu Photonics K.K.

Figure 4.6, **4.9**, **4.13**, **4.14**, and **A1**: Copyright © 2021, McPherson Inc.

Figure 4.11: Copyright © 2019, Lithuania European Union.

Figure 5.6, **5.11**, **6.5**, and **6.6**: Copyright © 1991, American Physics Society.

Figure 6.7: Copyright © 1964, The American Physics Society.

Figure 6.8: Copyright © 1997, American Institute of Physics.

Figure 7.1: Copyright © 2010, Taylor & Francis Group LLC – Books.